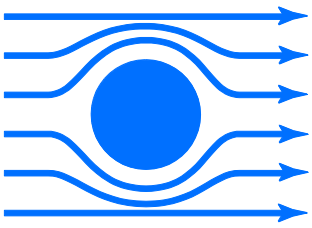

Walther-Meißner-Institut
für
Tieftemperaturforschung

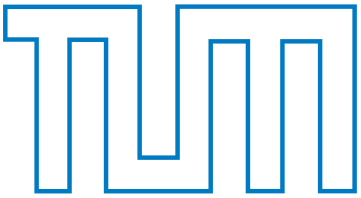

Technische Universität
München

Bayerisch Akademie
der Wissenschaften

Superconductivity and competing ordered states in layered organic metals

Dissertation

Michael Kunz

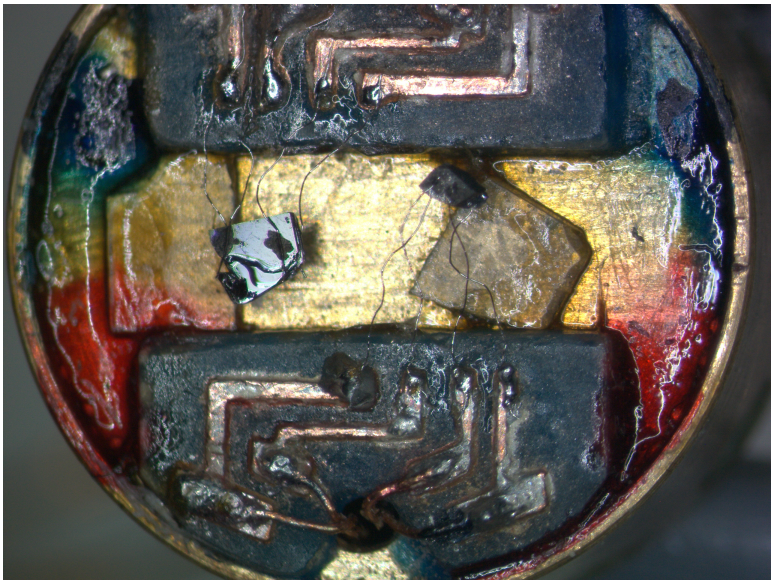

TECHNISCHE UNIVERSITÄT MÜNCHEN

Fakultät für Physik

Lehrstuhl E23 für Technische Physik

Walther-Meißner-Institut für Tieftemperaturforschung
der Bayerischen Akademie der Wissenschaften

Superconductivity and competing ordered states in layered organic metals

Michael Kunz

Vollständiger Abdruck der von der Fakultät für Physik der Technischen Universität München zur Erlangung des akademischen Grades eines

Doktors der Naturwissenschaften

genehmigten Dissertation.

Vorsitzende:		Univ.-Prof. Dr. M. Brambilla
Prüfer der Dissertation:	1.	Univ.-Prof. Dr. R. Gross
	2.	Univ.-Prof. Chr. Pfleiderer, Ph.D.

Die Dissertation wurde am 26.07.2016 bei der Technischen Universität München eingereicht und durch die Fakultät für Physik am 04.10.2016 angenommen.

Kurze Zusammenfassung

Diese Arbeit präsentiert experimentelle Studien zweier unterschiedlicher Familien organischer Metalle, in denen Supraleitung in der Nähe von anderen geordneten elektronischen Zuständen auftritt. In den Ladungsdichtewellensupraleitern α-(BEDT-TTF)$_2$MHg(SCN)$_4$, wobei M = K, Tl, wurde die Anisotropie der kritischen Felder des supraleitenden Zustands untersucht, unter der Verwendung von Druck als Kontrollparameter für den Grundzustand. In den antiferromagnetischen Supraleitern κ-(BETS)$_2$FeX$_4$, wobei X = Cl, Br, wurde das Zusammenspiel von lokalisierten magnetischen und leitfähigen Untersystemen durch Studien magnetoresistiver Effekte erforscht.

Abstract

This work presents experimental studies of two families of organic metals, in which superconductivity occurs in the vicinity to other ordered electronic states. In the charge-density wave superconductors α-(BEDT-TTF)$_2$MHg(SCN)$_4$, where M = K, Tl, the critical field anisotropy of the superconducting state was investigated, using pressure as a parameter controlling the ground state. In the antiferromagnetic superconductors κ-(BETS)$_2$FeX$_4$, where X = Cl, Br, the interplay of localised magnetic and conducting subsystems was examined by studies of magnetoresistive effects.

Contents

Part I

Introduction and presentation of the basic knowledge about the topic

1 Introduction

One of the big milestones in the field of organic metals was the discovery of the so called Bechgaard salts. They are named after K. Bechgaard, who, together with his chemistry group, was the first to synthesize charge transfer salts containing the organic donor molecule TMTSF [1]. In 1980 D. Jérome *et al.* discovered superconductivity in $(TMTSF)_2PF_6$ [2] under high hydrostatic pressure of a few kilobar with a critical temperature $T_c = 0.9\,\mathrm{K}$, which started an increasing interest in this class of compounds. One year later with $(TMTSF)_2ClO_4$ the first salt showing superconductivity at ambient pressure was discovered [3]. Soon other organic donor molecules were found to yield metallic salts. Among them was the molecule BEDT-TTF [4]. With this donor molecule the synthesis of layered charge-transfer salts with a wide variety of anions and stacking patterns became possible. In particular the first ambient pressure layered organic superconductor β-$(BEDT\text{-}TTF)_2I_3$ [5].

The organic metals can be tuned to feature a large number of different ground states like superconductivity, spin- and charge-density waves, antiferromagnetism, Mott-insulating, spin-liquids and various other [6–11]. This allows the study of a lot of different kinds of interactions in one class of compounds. Superconductivity was found with T_c at around 10 K and higher like for example in the compound κ-$(BEDT\text{-}TTF)_2Cu(NCS)_2$ [12, 13]. Later the first compounds with the very similar molecule BEDT-TSF or shorter BETS were discovered [14], which feature a larger π-orbital and, therefore, have a more stable metallic state.

Another big advantage of the organic charge transfer salts lies in their chemical nature. Due to the crystal structure, these compounds feature quasi-one-dimensional (q1D) and quasi-two-dimensional (q2D) electron systems. The low dimensionality together with the fact that these compounds are of stoichiometric (e.g. undoped) nature gives rise to a lot of geometrical electronic and quantum magnetoresistive effects becoming visible even at relatively high temperatures and low magnetic fields. Among these are magnetic quantum oscillations and angular magnetoresistance oscillations (AMRO) [9]. This provides access to the structure of the Fermi surface from experimental studies.

Recently especially multifunctional materials, featuring more than one kind of ground state, have become the center of interest. In these compounds the correlation of different interaction mechanisms can be studied in order to better understand the microscopic behaviour of these interactions. Such multifunctional materials are relatively easy to realise with the organic charge transfer salts by the use of different kinds of organic donors and inorganic acceptors. Among this class of compounds are the $(BETS)_2FeX_4$ salts where X = Cl, Br. Here the FeX_4-ions offer localised magnetic moments, while the $BETS^+$ radical cations offer a conducting π-electron system [10]. The most extensively studied compound from this family is λ-$(BETS)_2FeCl_4$ (λ-FeCl), which shows especially interesting manifestations of magnetic interactions in the formation of the electronic

ground state: At low temperatures the material is in an insulating state where both subsystems are antiferromagnetically ordered [15–17]. Under an applied magnetic field the insulating antiferromagnetic (AFM) state becomes suppressed at about 10 T [17], leading to a reentrance into the metallic paramagnetic (PM) state and – most exciting – the system enters a field induced superconducting (FISC) state for magnetic fields higher than 17 T [18], when applied parallel to the layers. It is very intriguing to see, how the magnetic system, which is carried by localised spins at the Fe^{3+} ions is able to drive the conducting system through different ground states. This is realised because of a strong π-d interaction in the system. Application of pressure also leads to a suppression of the insulating ground state and a formation of a zero field SC state. However, it can be shown that the AFM interaction still is present under pressure [19]. This shows that the interactions can be tuned with pressure allowing careful studies about the relation of the interaction strengths and the resulting ground states.

The isomer κ-$(BETS)_2FeCl_4$ (κ-FeCl) and its sister compound κ-$(BETS)_2FeBr_4$ (κ-FeBr) also show magnetic ordering [15, 20] (λ and κ indicate the packing structure of the BETS molecules), however, with notable differences in the coupling between the magnetic and conducting subsystems. In κ-FeBr we already observe a weaker interaction, which manifests in a lower Néel temperature T_N and, especially interesting, a metallic behaviour of the conduction electrons in the AFM state and the formation of a zero field SC state [21, 22]. Still a clear influence of the magnetic moments on the conduction electrons can be observed, since the AFM transition is reflected in the compound's interlayer resistance and also for κ-FeBr a FISC state was discovered [22]. The much lower transition fields of the FISC state give a clear indication about the weaker magnetic interaction. Another proof for the coupling between magnetic and conducting subsystems is a Fermi surface (FS) reconstruction taking place at the AFM transition, which was revealed by measurements of Shubikov-de Haas (SdH) oscillations inside and outside of the AFM state [23].

About κ-FeCl much less is known than for its sister compound κ-FeBr. κ-FeCl is believed to show an even weaker interaction between the localised moments and a smaller coupling to the conduction electrons, indicated by an even lower T_N than κ-FeBr [21]. A signature of superconductivity in κ-FeCl was reported for AC-susceptibility measurements [21] and in muon spin-rotation (μSR) studies [24], while other measurement techniques like resistance and specific heat did not show an indication for superconductivity [21].

Thus the family of $(BETS)_2FeX_4$ offers a playground, where fine tuning of specific interactions is possible by chemical substitution and pressure, yielding a possibility to better understand the influence of the different interactions on the behaviour of the electrons in the system and, hopefully, provide some advance in understanding the mechanisms behind unconventional superconductivity. Therefore a major topic in this thesis was an extensive study of the electronic properties of κ-FeCl, in order to get a better understanding of the impact of the localised AFM ordering on the conduction electron system. One focus was the anisotropy of the AFM and SC states in magnetic field. Another focus was the study of the exchange interaction by measurements of SdH oscillations. Further, the FS of κ-FeCl was mapped by the use of AMRO.

Even though κ-FeBr was already extensively studied to date, a number of interesting questions remain. For that reason also κ-FeBr was investigated during this thesis. A focus was thereby set on a study of the SdH oscillations in the PM and AFM states and a comparison of the two and with the results on κ-FeCl. Further the effect of pressures on the AFM ordering in κ-FeBr was studied. From all of this a more clear picture of the interaction between the localised spin system and the conduction electrons was obtained. The measurements on κ-FeBr were mainly performed jointly with L. Schaidhammer in the course of his master's thesis [25] and with F. Kollmansberger in the framework of his bachelor's thesis [26].

Like the aforementioned BETS compounds, many organic charge transfer salts show superconductivity in the vicinity of other ordering phenomena. And since the microscopic interactions responsible for the formation of different ground states are a hot topic, it is of interest to also study the SC properties of these materials. For this the compounds α-(BEDT-TTF)$_2$KHg(SCN)$_4$ (α-KHg) and α-(BEDT-TTF)$_2$TlHg(SCN)$_4$ (α-TlHg) were investigated under hydrostatic pressure. (α-KHg) is a compound that was already extensively studied in the past. It has very interesting properties since it shows the lowest known transition temperature into a charge-density wave (CDW) state, $T_{\mathrm{CDW}} = 8\,\mathrm{K}$, which at even lower temperatures competes with a SC state [27]. When pressure is applied, the CDW state is weakened and at a sufficiently high pressure of $p_c \approx 2.6\,\mathrm{kbar}$ it becomes fully suppressed giving rise to a bulk SC state with a maximum critical temperature of $T_c = 110\,\mathrm{mK}$ [27]. The pressure dependence of the CDW state and its reaction to magnetic field have already been studied in detail [28–35] and an extensive summary of its properties can be found in the PhD thesis of D. Andres [36] and in [37].

During his diploma thesis S. Jakob [38] found out that the bulk SC state for slightly overcritical pressure shows an extremely strong anisotropy between inplane and out-of-plane magnetic fields. And also a significant inplane anisotropy was discovered. However, the pressure dependence of this anisotropy was still an open question. Therefore, the critical field anisotropy of α-KHg was studied at several higher pressures during this PhD-thesis. One focus was thereby set to the comparison of the inplane anisotropy between over- and undercritical pressures in order to obtain information about which electron systems are responsible for the formation of Cooper pairs in the CDW and normal metallic state, respectively.

For the comparison of the results, also the sister compound (α-TlHg) was investigated, which has a slightly higher CDW transition temperature of $\sim 10\,\mathrm{K}$. This material is much less investigated than α-KHg. Schegolev *et al.* [39] studied the pressure dependence of the CDW transition up to 3.5 kbar in the temperature range down to 1.3 K. Further Ito *et al.* [40] reported that α-TlHg also shows a transition into an inhomogenous SC state. Because of the higher CDW transition temperature at zero pressure, there was a hope that this compound would also show a bulk SC state with a higher T_c than the K-salt above the critical pressure. Therefore, the pressure dependence of the CDW and SC state was investigated jointly with L. Höhlein in the course of her master's thesis [41].

2 Theoretical background

In this section we present an overview of the theoretical basis required for understanding the phenomena given in the introduction to the compounds and used for analysing the data. This includes the observed magnetoresistive effects of magnetic quantum oscillations (MQO) and angular magnetoresistance oscillations (AMRO) as well as the theoretical description of the ground states of superconductivity and antiferromagnetism, which were studied in this thesis.

2.1 Magnetic quantum oscillations

2.1.1 The origin of quantum oscillations

In a magnetic field electrons become affected by the Lorentz force. This results in the electrons moving on closed orbits, where their energy spectrum becomes quantised due to the Bohr-Sommerfeld quantisation. L.D. Landau first suggested the existence of these orbits and derived the spectrum of a free electron gas in a magnetic field [42]

$$E(n, k_H) = \left(n + \frac{1}{2}\right)\hbar\omega_c + \frac{\hbar^2 k_H^2}{2m_e}, \tag{2.1}$$

where $n = 0, 1, 2, ...$, $\omega_c = \frac{eB}{m_e}$ is the cyclotron frequency of a free electron and k_H is the wave vector component parallel to the field $\mathbf{B}$, e is the elementary charge and m_e the free electron mass.

In $\mathbf{k}$-space the allowed states, therefore, are reduced to coaxial tubes, called Landau tubes, parallel to the magnetic field direction, causing a degeneracy of the states on each of the tubes. The cross section area of these Landau tubes increases with increasing field, following the Onsager relation [43]

$$S_n = \left(n + \frac{1}{2}\right)\frac{2\pi eB}{\hbar}. \tag{2.2}$$

A sketch of Landau tubes in a three-dimensional (3D) and a quasi-two-dimensional (q2D) warped FS is given in Fig. 2.1.

When the field is changing the Landau tubes move, crossing the FS with a constant period in B^{-1}-scale

$$\Delta\left(\frac{1}{B}\right) = \frac{2\pi e}{\hbar S_{\text{extr}}}, \tag{2.3}$$

with S_{extr} being the extremal cross section area. This results in an oscillation of the density of states close to the FS. As the density of states close to the FS influences a

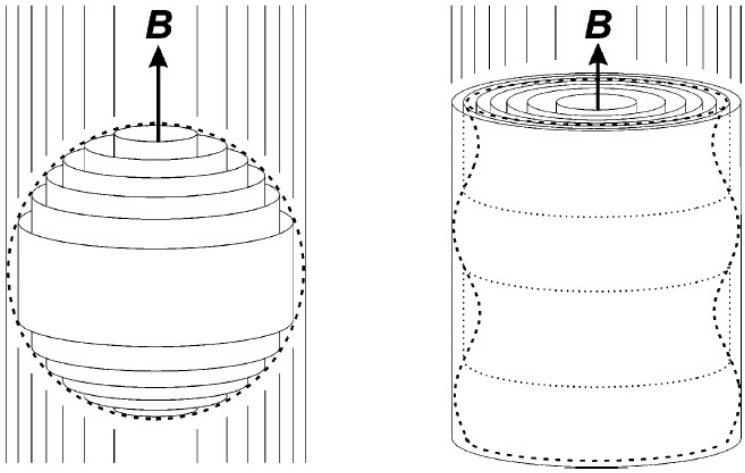

Figure 2.1: Schematic drawing of the Landau tubes for a 3D isotropic (left) and a q2D warped cylindrical Fermi surface (right) (taken from [9]).

lot of physical properties like magnetization, conductivity, heat capacity, thermoelectric power,... these properties also start to oscillate. The most important properties for investigating magnetic quantum oscillations are the magnetization, where the first oscillations have been discovered by W.J. de Haas and P.M. van Alphen [44] and electrical resistance, where the first oscillations were detected by L.W. Shubnikov and W.J. de Haas [45]. These oscillations in magnetization and resistance were, therefore, respectively called de Haas-van Alphen (dHvA) and Shubnikov-de Hass (SdH) oscillations. A more detailed overview of magnetic quantum oscillations is for example given in Ref. [46]. A summary with the relevant aspects for the field of organic superconductors can be found in [9].

2.1.2 Lifshitz-Kosevich formula

De Haas-van Alphen oscillations

The oscillations in magnetisation could first be fully described quantitatively for an arbitrary dispersion by I.M. Lifshitz and A.M. Kosevich [47] who formulated what has become the standard theory for the description of dHvA oscillations. The magnetization can be described as the field derivative of the Gibbs thermodynamic potential Ω at constant temperature T and constant chemical potential μ

$$\mathbf{M} = -\left(\frac{\partial\Omega}{\partial\mathbf{B}}\right)_{T,\mu} \tag{2.4}$$

Assuming that we have only one extremal cross section of the FS perpendicular to $\mathbf{B}$, the oscillatory part of the magnetization along $\mathbf{B}$ is given by the sum of the harmonics

$$\tilde{M}_{\parallel} = -\sqrt{\frac{e^5}{2\pi^5\hbar}}\frac{F\sqrt{B}}{m_c|S''|^{\frac{1}{2}}_{\text{extr}}}\sum_{r=1}^{\infty}R_D(r)R_T(r)R_S(r)\frac{1}{r^{\frac{3}{2}}}\sin\left[2\pi r\left(\frac{F}{B}-\frac{1}{2}\right)\pm\frac{\pi}{4}\right], \tag{2.5}$$

where $\tilde{M}_{\parallel}$ ist the oscillatory component of the magnetisation parallel to $\mathbf{B}$, r the harmonic index, m_c the cyclotron mass,

$$m_c = \frac{1}{2\pi}\left(\frac{\partial S}{\partial E}\right)_{k_H}, \tag{2.6}$$

and F the fundamental frequency

$$F = \frac{S_{\mathrm{extr}}\hbar}{2\pi e}. \tag{2.7}$$

$(S'')_{\mathrm{extr}} = (\partial^2 S/\partial k_H^2)_{\mathrm{extr}}$ characterises the FS curvature along $\mathbf{B}$ around the extremal cross section. The motion of the electrons along a closed orbit in $\mathbf{k}$-space is dependent on the cyclotron frequency, which in general is only characterised by the cyclotron mass

$$\omega_c = \frac{2\pi eB}{\partial S/\partial E_{k_H}} = \frac{eB}{m_c}. \tag{2.8}$$

Equation (2.5) is called the Lifshitz-Kosevich (LK) formula and describes the dHvA oscillations in a 3D metallic electron system. It contains the damping factors R_T, R_D and R_S describing the effects of finite temperature, scattering effects and Zeeman splitting, respectively. As $R_T(r)$ and $R_D(r)$ decrease exponentially with increasing harmonic index we will only consider the case of the fundamental harmonic, $r = 1$.

In the case of a q2D metal, where the warping of the cylindrical FS is smaller than the Landau level spacing, a large number of the charge carriers contribute to the oscillations in phase. This results in a strong enhancement of the oscillation amplitude and in extremely 2D cases it can even violate the standard theory [9]. In this case some changes have to be made to the LK formula given in Eq. (2.5). The resulting equation is then called the Lifshitz-Kosevich-Shoenberg (LKS) formula (also called the 2D LK formula), which has the form

$$\tilde{M}_{\parallel} = \frac{e^2}{2\pi^3\hbar}\frac{S}{m_c d}\sum_{r=1}^{\infty} R_D(r)R_T(r)R_S(r)\frac{(-1)^{r+1}}{r}\sin\left(2\pi r\frac{F}{B}\right). \tag{2.9}$$

Since the 2D description is probably more accurate for the description of our compounds, we will only use this version from now on.

Shubnikov-de Hass oscillations

The theory of the Shubnikov-de Haas (SdH) oscillations is more complicated than in the case of dHvA oscillations and not fully understood, because in principle it would be necessary to consider explicitely the problem of various scattering processes modified by a quantising magnetic field [48]. However, in most of the cases it is enough to follow Pippard's idea [49] that the scattering probability, hence, the resistivity are proportional to the density of states $D(\mu)$ around the Fermi level. Following from this, the oscillatory part of the conductivity can be expressed in the form

$$\frac{\tilde{\sigma}}{\sigma_0} \propto \frac{m_c}{d}\sum_{r=1}^{\infty} R_D(r)R_T(r)R_S(r)\cos\left(2\pi r\frac{F}{B}\right), \tag{2.10}$$

where σ_0 is the background conductivity. Due to the direct proportionality the influence of the reduction factors on the SdH oscillations is identical to that on the dHvA oscillations.

Reduction factors

The reduction factors are responsible for taking into account several real system properties, which are reducing the oscillation amplitude. The temperature damping factor R_T takes into account the influence of a finite temperature on the Fermi distribution function. Due to thermal excitation, the electrons near the Fermi energy E_F have slightly different energies meaning that their isoenergetic orbits in k-space have slightly different areas. This leads to a slight distribution of oscillation frequencies, which results in a smearing of the phase of the oscillations and, therefore, a decrease in amplitude. The temperature damping factor is expressed by [47]:

$$R_T = \frac{Km^*\frac{T}{B}}{\sinh(Km^*\frac{T}{B})}, \tag{2.11}$$

where K is a constant

$$K = \frac{2\pi^2 k_B m_e}{\hbar e} \approx 14.7\frac{\mathrm{T}}{\mathrm{K}} \tag{2.12}$$

and $m^* = m_c/m_e$ is the cyclotron mass normalised to the free electron mass. Because of this dependence, it is possible to determine the effective cyclotron mass from the temperature dependence of the oscillation amplitude by fitting Eq. (2.11) to the experimental data [46].

The so called Dingle damping factor R_D takes into account the effect of a finite scattering time τ caused by imperfections and impurities in the crystal lattice. The existence of additional scattering centers broadens the Landau tubes causing a less sharp change in the density of states at the Fermi level. R.B. Dingle argued that the broadening can be described by a Lorentzian distribution function with half width $\Gamma = \hbar/2\tau$ [50]. This leads to the following expression for the Dingle damping factor

$$R_D = \exp\left(-Km^*\frac{T_D}{B}\right), \tag{2.13}$$

with the Dingle temperature

$$T_D = \frac{\hbar}{2\pi k_B \tau}. \tag{2.14}$$

After extracting the cyclotron mass m^* from the temperature damping factor the relaxation time can be calculated by fitting the B-dependence of the oscillations with the Dingle factor (Eq. (2.13)). It should be noted that the relaxation time derived from the Dingle damping factor is usually smaller than the usual transport relaxation time, since the quantum oscillations are much stronger effected by long-range scattering defects like, for example, dislocations.

The spin damping factor R_S, finally, regards the effect of the Zeeman spin splitting. Each Landau level is split into two sub-bands depending on the electron spin that are separated by the energy gap

$$\Delta E = g\mu_B B, \tag{2.15}$$

where g is the Landé factor ($g \approx 2$ for free electrons) and $\mu_B = e\hbar/2m_e$ is the Bohr magneton. As these two sub-bands contribute to the oscillations with very similar frequency but with a slightly shifted phase the resulting oscillation amplitude is reduced according to

$$R_S = \cos\left(\frac{\pi}{2} g m^*\right). \tag{2.16}$$

From Eq. (2.16) follows that the interference of the two sub-bands oscillatory components is constructive or destructive depending on the values of g and m^*. As the value of the cyclotron mass in layered metals is angle-dependent $m^*(\theta) = \frac{m^*(0)}{\cos\theta}$, g can be determined by plotting the oscillation amplitude as a function of θ. At the values of θ, where the interference becomes completely destructive (Zeeman splitting of the Landau tubes is exactly $n + 1/2$ times the distance between two Landau tubes) the oscillations vanish completely. Such angles are called "spin-zeros" [51]. In organic metals spin-zeros are often used as a tool to, for example, analyse the strength of many-body interactions in the system [52–54].

Magnetic breakdown

In all of our estimations in the LK theory above, we have assumed that the electrons move on well defined trajectories. This is true as long as the cyclotron energy $\hbar\omega_c$ is much smaller than the relative band energies $\sim E_F$. But in the case, where two conduction bands come close to each other near the Fermi energy this is no longer correct. In such a case for sufficiently high fields the electrons can tunnel through the small gap from one band into the other. This effect is called magnetic breakdown (MB) [55]. The probability P for such a tunneling process is given by

$$P = e^{-B_{\mathrm{MB}}/B}, \tag{2.17}$$

with the breakdown field

$$B_{\mathrm{MB}} \cong \frac{m}{e\hbar}\frac{\Delta_g^2}{E_F}, \tag{2.18}$$

where Δ_g is the interband gap at the MB junction. The conditions under which MB becomes relevant are given by the Blount criterium [56]:

$$\hbar\omega_c \gtrsim \Delta_g^2/E_F. \tag{2.19}$$

The quasiclassical approach is still valid for very low fields ($B \ll B_{\mathrm{MB}}$) and very high fields ($B \gg B_{\mathrm{MB}}$), because the electron trajectories are still well defined: In the low-field case the electrons stay on their respective orbitals and at high fields the electrons can freely pass through the MB junctions. The intermediate case ($B \sim B_{\mathrm{MB}}$), however, would need to be treated as a quantum mechanical problem [57]. However, Falicov and

Stachowiak [58] have shown that the quasiclassical approach still describes the system sufficiently well by considering all possible closed orbits. At each breakdown junction the initial electron wave is separated into a transmitted an a reflected part with respective amplitudes p and q,

$$p = \sqrt{P}; \quad q = \sqrt{1-P}. \tag{2.20}$$

The reflected and transmitted waves have a phase difference of $\pi/2$ because of the conservation of particles. Thereby the reflected phase is conventionally assumed to preserve its phase [59, 60]. Due to this distribution of the electron waves, the amplitude of a single oscillation frequency becomes an additional damping component. This is reflected in the MB reduction factor [58]

$$R_{\mathrm{MB}} = (ip)^{l_{1j}} q^{l_{2j}}, \tag{2.21}$$

where l_{1j} and l_{2j} are the numbers of points at which the electron encircling the j-th orbit must tunnel through and be reflected from a MB junction, respectively. The tunneling amplitude is ip because of the $\pi/2$ phase shift of the transmitted wave.

2.2 Angular magnetoresistance oscillations (AMRO)

In low-dimensional compounds in addition to quantum oscillations several other magnetoresistive oscillatory phenomena are observable. Among them are the angular magnetoresistance oscillations (AMRO). AMRO are semiclassical effects depending on the FS geometry [9]. Therefore, they can be used in order to obtain information on the FS. Due to the semiclassical nature it is often possible to observe them under conditions where quantum oscillations are no longer visible making them a powerful tool to study the FS. AMRO are a property of the coherent interlayer transport in the material.

2.2.1 Quasi-1-dimensional electron systems: Lebed magic angle (LMA) resonances

Among the AMRO effects resulting from a 1D FS are the Lebed magic angle (LMA) resonances. They originate from the fact that a high magnetic field applied perpendicular to the direction of the 1D conductivity causes the electrons to move along the open Fermi sheets, crossing many Brillouin zones. In a q1D system with the highly conducting direction being along x the dispersion relation is given as [9]

$$E(k) = \hbar v_F(|k_x| - k_F) - \sum_{m,n} t_{mn} \cos(m a_y k_y + n a_z k_z), \tag{2.22}$$

where $t_{mn} \ll E_F$ are the transfer integrals and a_x, a_y and a_z are the lattice constants in the respective directions. The frequencies of crossing one Brillouin zone in the k_y and k_z direction are [9]

$$\omega_y = a_y \left| \frac{\mathrm{d}k_y}{\mathrm{d}t} \right| = \frac{e v_F a_y}{\hbar} B \cos\theta \tag{2.23}$$

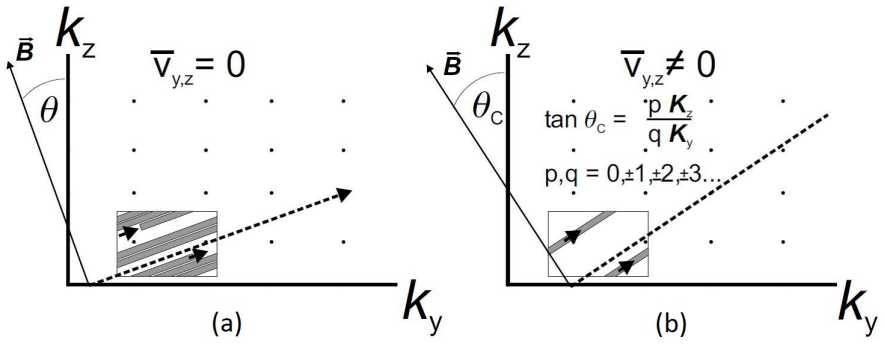

Figure 2.2: Electron trajectories within an open FS sheet for a q1D electron system with high conductivity direction along x. (a) For an arbitrary magnetic field direction the electron path covers the whole FBZ. (b) With a field direction along an integer number of a lattice vector the path consists only of a few lines. (Both taken from [36].)

$$\omega_z = a_z \left| \frac{\mathrm{d}k_z}{\mathrm{d}t} \right| = \frac{e v_F a_z}{\hbar} B \cos\theta. \tag{2.24}$$

In general these frequencies are different and the electron motion is aperiodic $v_z = \frac{1}{\hbar}\frac{\partial E}{\partial k_z}$ causing the average velocity $\bar{v}_z$ to zero. This is, however, not the case when the magnetic field is applied along a lattice vector, as first noted by A.G. Lebed [61]. There exist special angles θ

$$\tan\theta_{\mathrm{LMA}} = \frac{p}{q}\frac{a_y}{a_z}, \tag{2.25}$$

where the resistivity was experimentally found to show sharp dips, when the field is rotated in the plane of the 1D FS. Here p and q are integers. When we also take into account that the field is rotated in a plane that forms an angle φ to the plane of the 1D FS, the relation is expressed as:

$$\tan\theta_{\mathrm{LMA}} \cos\varphi = \frac{p}{q}\frac{a_y}{a_z}. \tag{2.26}$$

This behaviour can be explained by a model proposed by T. Osada *et al.* [62] and qualitatively interpreted by M.V. Kartsovnik *et al.* [63] and G.M. Lebed [64]. According to this model for an arbitrary value of θ the electron trajectories will completely cover the reduced Brillouin zone assuming the scattering time τ is sufficiently large as shown in Fig. 2.2(a), causing the mean interlayer velocity to zero as mentioned above. When the field is applied parallel to a low integer multiple of the lattice constants $\mathbf{K} = p\mathbf{K}_y + q\mathbf{K}_z$ the path of the electrons on the reduced FS consists of only a few lines. In this case the mean velocity $\bar{v}_z$ maintains a finite value at increasing B resulting in a constant interlayer conductivity.

2.2.2 Quasi-2-dimensional electron systems

Yamaji oscillations

Also q2D electron systems are known to show oscillatory effects on changing the angle of the magnetic field. In the presence of a cylindrical FS $R(\theta)$ shows characteristic peaks at certain θ. The first calculations for the θ positions of this kind of AMRO were done by K. Yamaji [65]. This kind of AMRO is, therefore, also called Yamaji oscillations.

The dispersion relation for a slightly corrugated cylindrical FS can be written in a simplified form

$$E(\mathbf{k}) = \frac{\hbar^2}{2m}(k_x^2 + k_y^2) - 2t_\perp \cos(k_z d), \tag{2.27}$$

where $t_\perp \ll E_F$ is the interlayer hopping energy and d the interlayer spacing constant. As Yamaji pointed out, the area difference ΔS between the largest and the smallest electron orbit on a weakly warped cylinder oscillates with the field direction:

$$\Delta S(\theta) \approx \frac{8\pi m t_\perp}{\cos\theta} J_0\left(k_F d \tan\theta\right). \tag{2.28}$$

As we can see, ΔS becomes zero for the zeros of the zeroth-order Bessel function J_0. At the corresponding θ all cross sections have the same area as schematically shown in Fig. 2.3(a). For $\tan\theta > 1$ these θ follow the "Yamaji's condition"

$$|\tan\theta_n| \approx \frac{\pi}{k_F d}\left(n - \frac{1}{4}\right);\ n = 1, 2, ... \tag{2.29}$$

The physical nature of the AMRO can be understood keeping in mind that the interlayer conductivity σ_{zz} is determined by the interlayer velocity v_z averaged over the

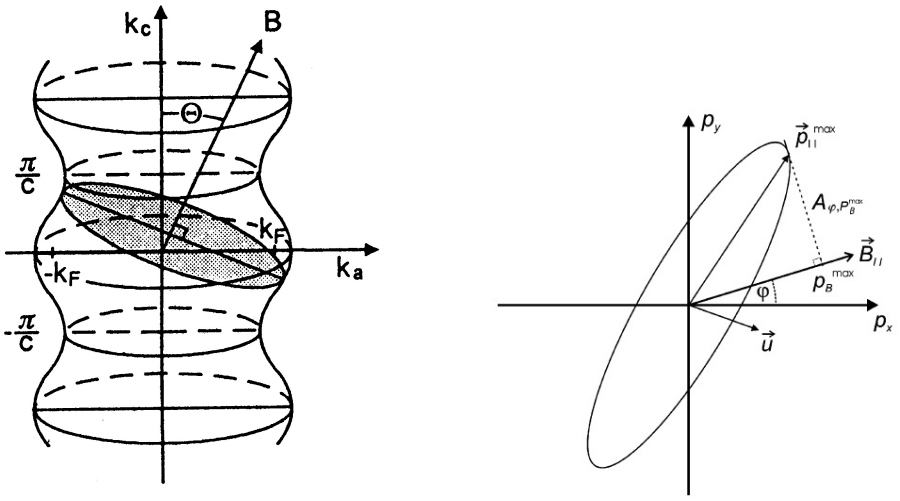

(a) (b)

Figure 2.3: (a) Sketch of a warped FS with a cross section for a tilted magnetic field (from [51]. (b) Sketch of a transverse cross section of a cylindrical FS (from [9]).

period of the electron motion on the closed orbit [66]. v_z depends on the dependence of the derivative of the orbit area on its position in **k**-space and can be written as:

$$\bar{v}_z = \frac{1}{\hbar}\overline{\frac{\partial E}{\partial k_z}} = -\frac{\frac{\partial S_{\mathrm{orb}}(K_z)}{\partial K_z}}{\hbar\frac{\partial S_{\mathrm{orb}}}{\partial E}} = \frac{\hbar\frac{\partial S_{\mathrm{orb}}}{\partial K_z}}{2\pi m_c}, \tag{2.30}$$

where K_z is the point at which the plane of the orbit intersects the k_z-axis. The cyclotron mass increases proportional to $1/\cos\theta$ in the q2D case. Generally the derivative $\partial S(K_z)/\partial K_z$ is finite and the conductivity σ_{zz}, therefore, saturates at a finite value with increasing field. However, at the Yamaji's angles $\partial S(K_z)/\partial K_z \approx 0$, leading to a vanishing average velocity $\overline{v}_z$ and, therefore, a vanishing σ_{zz}. For Yamaji's angles it was proven [67, 68] that the resistivity grows with $\rho_{zz} \propto B^2$ as long as $1 \ll \omega_c\tau \ll E_F/t_\perp$.

Equation (2.29) can be generalised for a more realistic dispersion relation:

$$E(\mathbf{k}) = E(k_x, k_y) - 2t_\perp \cos[(k_z d + k_x u_x + k_y u_y)], \tag{2.31}$$

where $E(k_x, k_y)$ is an even function of $k_{x,y}$, which corresponds to a convex cross section of the Fermi surface, and $u_{x,y}$ are the in-plane components of the direction vector $\mathbf{h} = (u_x, u_y, d)$ of the interlayer hopping. Equation (2.29) then is modified to [66]

$$|\tan\theta_n| = \frac{\pi\left(n - \frac{1}{4}\right) \pm \left(\mathbf{k}_{||}^{max} \cdot \mathbf{u}\right)}{k_B^{max} d},\ n = 1, 2, \ldots . \tag{2.32}$$

$\mathbf{k}_{||}^{max}$ is the in-plane Fermi momentum and k_B^{max} is its projection on the field rotation plane determined by φ as illustrated in Fig. 2.3(b) and the sign of the $\pm$ is equal to that of $\tan\theta$. For an elliptical FS cross section, k_B^{max} can be written as [69, 70]:

$$k_B^{max}(\varphi) = \left[(k_1\cos\varphi)^2 + (k_2\sin\varphi)^2\right]^{\frac{1}{2}}, \tag{2.33}$$

where φ characterises the inplane direction of the magnetic field.

Coherence peak

For a magnetic field close to parallel orientation a peak feature appears in $R(\theta)$ for some materials and some azimuthal angles φ. Experiments showed that the width of this peak is independent of the magnetic field strength suggesting a geometrical origin for the feature [71]. This increase of resistance can be explained by looking at the warping of the cylindrical FS. For all tilt angles higher than the critical angle θ_c additional closed orbits appear on the very side of the warped FS. The relevant point here is that at the same angle also self-touching orbits start to appear [72] as schematically shown in Fig. 2.4. For a weakly warped cylinder, that is if $t_\perp \ll E_F$, the Fermi velocity v_F of the electrons in the vicinity of the touching point A is almost parallel to the magnetic field, resulting in negligible Lorentz force acting on the electrons. This conserves their velocity and, therefore, they contribute most to the interlayer conductivity. For electrons far away from the self-touching orbits the situation is different. They experience a large

Lorentz force resulting in a strong oscillation of their interlayer velocity v_z averaging to zero over the scattering time. This leads to a local minimum of the interlayer resistance at $\theta = \theta_c$. When θ gets even closer to 90°, v_z^A decreases and becomes exactly zero at $\theta = 90°$. The result is a sharp peak in the magnetoresistance for $\theta_c < \theta < 180° - \theta_c$ [9]. Typical peak widths in organic metals vary between $\approx 1°$ and $\approx 3°$. The coherence peak width allows us to estimate the anisotropy ratio $2t_\perp/E_F$ from the experimental data [9]

$$\frac{2t_\perp}{E_F} \cong \frac{\pi - 2\theta_c}{k_F d}, \tag{2.34}$$

where d is the interlayer period.

The above mentioned feature was called a coherence peak because the effect only affects the coherent interlayer transport. This is because the incoherent interlayer transport, which is mainly caused by impurity scattering, is insensitive to magnetic fields parallel to the layers. Therefore, the existence of a coherence peak can be used as an evidence for coherent transport being the dominating component of the interlayer conductivity.

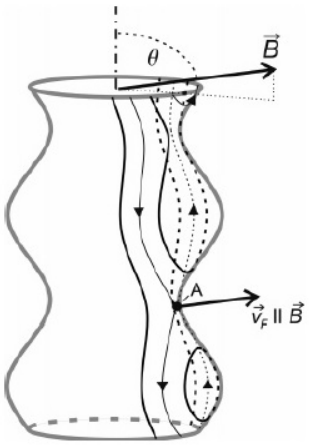

Figure 2.4: Schematic view of a warped cylindrical FS. The thin line on the cylinder indicates the self-touching orbit, while the other lines are single connected orbits.

2.3 Superconductivity

2.3.1 Basics of Superconductivity

Superconductivity is a widely studied topic since more than hundred years and a basic part of solid state physics and the basic theories of SC are generally known nowadays. For this reason we will present only the more specific parts of the theory of superconductivity that are relevant for this thesis. A full introduction about the topic of SC can be found in a number of textbooks e.g. [73–76]

Type I-II superconductors

In general two different kinds of superconductors are distinguished depending on their behaviour under an applied magnetic field. The two responsible properties for the different behaviour are the London penetration depth

$$\lambda_{\mathrm{L}} = \sqrt{\frac{m_s}{\mu_0 n_s q_s^2}}, \tag{2.35}$$

where m_s, n_s and q_s are the mass, the density and the charge of the superconducting charge carriers, respectively, and the Ginzburg-Landau coherence length

$$\xi_{\mathrm{GL}} = \sqrt{\frac{\hbar^2}{2m_s|\alpha|}}, \tag{2.36}$$

where α is a material dependent factor. According to the BCS theory the coherence length can be estimated from the critical temperature:

$$\xi_0 = 0.18 \frac{v_F \hbar}{k_B T_c}. \tag{2.37}$$

The penetration depth characterises how fast the magnetic field exponentially decays inside the superconductor according to

$$B(x) = B(0) e^{-\frac{x}{\lambda_L}}, \tag{2.38}$$

where $B(0)$ is the magnetic flux density outside of the superconductor and x is the distance to the surface inside the superconductor. ξ_{GL} represents the size of the Cooper pairs and, therefore, characterises the length scale on which the order parameter can change. The value of λ_L and ξ_{GL} depends on the material and their ratio is called the GL parameter

$$\kappa = \frac{\lambda_L}{\xi_{GL}}. \tag{2.39}$$

The size of κ determines whether a given superconductor is type I or type II:

- For $\kappa < 1/\sqrt{2}$ the material is a type I superconductor.
- For $\kappa > 1/\sqrt{2}$ the material is a type II superconductor.

In a type I superconductor the surface energy between normal- and superconducting domains is positive meaning that the superconductor tries to avoid having any such boundaries within the bulk volume. Therefore, disregarding demagnetization factors, magnetic field is completely expelled from a type I superconductor via shielding currents (Fig. 2.5(a)) and penetrates the SC volume only at the surface in the range of λ_L. The magnetization of the superconductor thereby is equal to the external field with

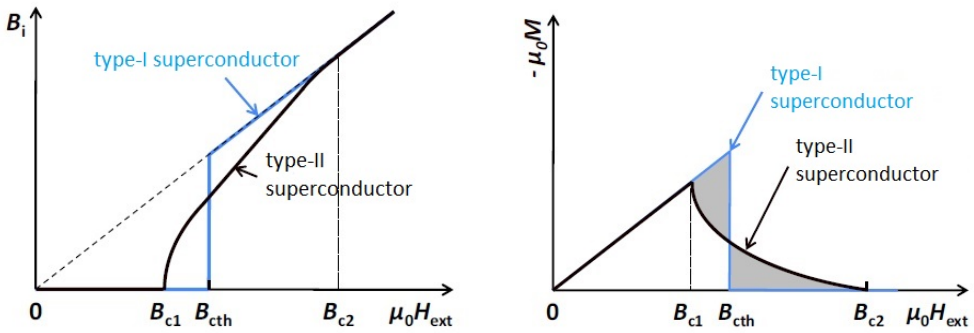

(a) (b)

Figure 2.5: Schematic representation of (a) the effective internal magnetic field and (b) of the magnetization as a function of the external field for a type-I superconductor (blue) and a type-II superconductor (black) (from [73]).

opposite sign as shown in Fig. 2.5(b): The superconductor acts as a perfect diamagnet and is in the so-called Meißner-phase. When the critical field $B_{c,th}$ is exceeded the SC state is broken and the magnetic field fully penetrates the superconductor. In case of a sufficiently high demagnetization factor a type I superconductor can enter an intermediate state, where some magnetic flux lines rearrange to pass through the superconductor destroying the superconducting state in the respective volume. This normal conducting domains arrange in a way to have minimum surface, whilst keeping the magnetic flux density at every surface of the superconductor just below the critical field $B_{c,th}$.

In a type II superconductor the surface energy is negative. Therefore, it becomes favourable for the superconductor to have as many phase boundaries inside the sample volume as possible, when a sufficiently high external field is applied. Starting from the lower critical field B_{c1} the magnetic field starts penetrating the SC volume forming vortices, where each vortex contains exactly one magnetic flux quantum $\Phi_0 = \frac{hc}{2e}$. This is called the Shubnikov or mixed phase. Each flux vortex contains a normal conducting core with a radius approximately equal to the coherence length ξ_{GL} surrounded by shielding currents. When the magnetic field further increases, the density of flux vortices increases until the normal conducting cores start to overlap. At this field the upper critical field

$$B_{c2} = \frac{\hbar}{q_s \xi_{\mathrm{GL}}^2} \tag{2.40}$$

is reached and the SC state is completely destroyed. This is called the orbital pair-breaking effect of superconductivity.

In a type I superconductor for a temperature much smaller than the critical temperature $T \ll T_c$ the transition from SC to normal state in increasing B is a 1st order phase transition, while in a type II superconductor it is of 2nd order. In the case of a first order phase transition we expect some kind of hysteretic behaviour that may be resolved in measurements of the SC to normal state transition and may allow to distinguish it from the second order phase transition of a type II superconductor.

Parameters influencing superconductivity

The properties of a SC state are influenced by a number of parameters. The influence of temperature and magnetic field can be generally understood by energetical arguments and are not presented here. We rather want to focus on the parameters, which are associated with the sample quality.

According to Andersons's thereom [77] non-magnetic impurities and crystal imperfections have almost no effect on BCS superconductors, that is in superconductors in which the Cooper pairs are phonon mediated and which are isotropic s-wave superconductors. Anderson shows that the BCS theory even is best valid in the dirty limit because of more constant interactions and, therefore, a more constant energy gap in dirty systems. On the other hand superconductivity can be destroyed very fast by adding magnetic impurities [78]. In many unconventional superconductors, where the SC energy gap $\Delta(\mathbf{k})$ has nodes, however, it can be shown experimentally that Anderson's theorem is

not valid and even non-magnetic impurities have a strong influence on superconductivity [79]. Several organic charge transfer salt superconductors show a strong sample dependence of the SC state and, therefore, are candidates for nodal superconductivity (as discussed in Secs. 5.1.2 and 6.2.3).

2.3.2 Superconductivity in layered compounds

Many of the unconventional superconductors like cuprates, pnictides and organics are layered materials. The low dimensionality of the electron systems changes some properties of the SC state. Therefore we list here, what changes from the conventional SC theories have to be considered for describing layered superconductors.

Highly anisotropic superconductors

Highly anisotropic superconductors are considered to have a high anisotropy in transfer integrals and, therefore, a reduced interlayer transport. However, the coupling between the conducting planes is still finite and the interlayer coherence length may be longer than the interlayer distance d. In such superconductors the critical field is strongly dependent on the polar angle θ, which is the angle of the magnetic field in respect to the normal of the conducting planes, because the shielding currents are strongly suppressed perpendicular to the layers, while being strong within the layers. Therefore, for parallel fields B_{c1} is lower, as the flux vortices can more easily enter the superconductor. But because of the much smaller $\xi_\perp$, the vortices can be more densely packed resulting in a higher critical field B_{c2}. According to Werthammer, Helfand and Hohenberg (WHH) [80, 81] the temperature dependence $B_{c2}(T)$ is linear until quite low temperatures as long as the pair breaking is orbital (see Sec. 2.3.1).

The first theory of anisotropic superconductors was the effective mass model formulated by Lawrence and Doniach [82] describing the layered compounds as stacks of Josephson coupled SC layers. Taking the GL theory and introducing an anisotropic effective mass of charge carriers (therefore, it is also called anisotropic Ginzburg-Landau (AGL) model), they described the parallel and perpendicular critical fields as

$$B_{c2,\perp} = \frac{\Phi_0}{2\pi\xi_\parallel^2}, \tag{2.41}$$

$$B_{c2,\parallel} = \frac{\Phi_0}{2\pi\xi_\parallel\xi_\perp}. \tag{2.42}$$

From that we extract the following equalities [75]

$$\frac{B_{c2,\parallel}}{B_{c2,\perp}} = \frac{\xi_\parallel}{\xi_\perp} = \frac{\lambda_\perp}{\lambda_\parallel} = \left(\frac{m_\perp}{m_\parallel}\right)^{\frac{1}{2}} \equiv \gamma \tag{2.43}$$

introducing a conventional dimensionless anisotropy parameter γ. $\lambda_{\perp,\parallel}$ and $\xi_{\perp,\parallel}$ stand for the parallel or perpendicular component of the penetration depth and the coherence

length, respectively. The angular dependence of the critical field is given by

$$B_{c2}(\theta, T) = \frac{\Phi_0}{2\pi\xi_{\parallel}^2(T)\sqrt{\gamma^2 \sin^2\theta + \cos^2\theta}}. \tag{2.44}$$

In the case where the interlayer coherence length becomes smaller than the interlayer distance the SC coupling between the layers vanishes. In this case the $B_{c2,\parallel}$ from the LD model diverges. Klemm, Luther and Beasly have developed a microscopic theory for the case of Josephson-coupled layers in the dirty limit of a superconductor ($\ell \ll \xi_0$, ℓ is the mean free path of an electron) [83] while Bulaevskiĭ developed one for the clean limit ($l \gg \xi_0$) [84, 85].

Superconducting thin films

Tinkham [75] studied the critical fields for superconducting thin films and for the purely 2D case

$$s \ll \xi_{\perp} \ll d, \tag{2.45}$$

where s is the layer thickness. Under these conditions there is no coupling between the layers any more. The dependence of the critical field on θ now follows the relation

$$\left|\frac{B_c(\theta)\sin\theta}{B_{c\perp}}\right| + \left(\frac{B_c(\theta)\cos\theta}{B_{c\parallel}}\right)^2 = 1, \tag{2.46}$$

with $B_{c2,\parallel}$ and $B_{c2,\perp}$ being the critical field in parallel and perpendicular direction to the conducting layers, respectively.

$B_{c\perp}$ is given by Tinkham [75] as

$$B_{c2,\parallel} = \frac{2\sqrt{6}B_{cth}\lambda}{s}. \tag{2.47}$$

Eq. (2.47) can also be written in the form

$$B_{c2,\parallel} = \frac{\sqrt{3}\Phi_0}{\pi s \xi_{\parallel}(0)}\sqrt{1 - \frac{T}{T_c}}. \tag{2.48}$$

This formula was already used to fit data obtained from experiments with q2D layered compounds [86].

Paramagnetic effect on superconductivity

All the formulas mentioned above describe the SC critical field for the orbital pair breaking effect. In strongly anisotropic superconductors, however, also the so-called Pauli-paramagnetic limit of superconductivity can become relevant. This is the case, where for parallel field the orbital critical field is so strongly enhanced that it exceeds the paramagnetic critical field. In a strong magnetic field the Zeeman splitting causes an energy difference for spin-up and spin-down electrons. For sufficiently high fields this favours a completely parallel alignment of the electron spins. In a spin-singlet

superconductor (s-wave and d-wave), however, the Cooper pairs have antiparallel spins. Therefore at the moment, when the energy gain of the paramagnetic spin alignment exceeds the SC energy gap Δ_0 the SC state is broken. For spin-triplet superconductors there exists no paramagnetic limit. The paramagnetic critical field was first calculated by B.S. Chandrasekhar [87] and A.M. Clogston [88]:

$$B_p = \frac{\Delta_0}{\mu_0 \mu_B \sqrt{2}}, \tag{2.49}$$

with μ_B being the Bohr magneton and μ_0 the vacuum permeability. After inserting $\Delta_0 = 1.76\, k_B T_c$ from the BCS theory we get

$$B_p = 1.84 \left[\frac{\mathrm{T}}{\mathrm{K}}\right] T_c, \tag{2.50}$$

which is called the "Chandrasekhar-Clogston paramagnetic limit" (CC-limit).

According to a theory proposed by P. Fulde and R. A. Ferrell [89] and simultaneously by A. I. Larkin and Y. N. Ovchinnikov [90], superconductivity can survive to even higher magnetic fields under certain conditions. This so-called FFLO-state is an inhomogeneous superconducting state, where the Cooper pairs have a finite center of mass momentum ($\boldsymbol{k}\uparrow, -\boldsymbol{k}\downarrow + \boldsymbol{q}\downarrow$). In this state the superconductor has a lower condensation energy than the BCS state, but as the Zeeman energy is reduced in the FFLO state, it is stable at sufficiently high fields. Thereby the spatial distribution of the energy gap $\Delta(\mathbf{r})$ is modulated meaning that some space of the superconductor is "sacrificed" and becomes normal metallic making it possible for the superconductivity to survive in other parts of the superconductor. For the FFLO state to show up, the compounds must have a Maki parameter $\alpha = \sqrt{2} B_{c2}^{\mathrm{orb}} / B_{c2}^{\mathrm{P}}$ [91] (ratio of orbital and paramagnetic critical field at $T = 0\,\mathrm{K}$) higher than 1.8 and it must be in the clean limit ($l \gg \xi_0$).

Since the FFLO state can only be observed in paramagnetically limited superconductors, it is expected to be largest in 1D superconductors (they show the strongest suppression of screening currents). In 2D superconductors it should be smaller but still visible, while in 3D superconductors a paramagnetic limiting usually is never observed [92]. No clear proof of the existence of the FFLO state has been found for many years, but recently there has been some evidence for the existence of a FFLO state in q2D organic superconductors [93–95].

2.4 Antiferromagnetism

2.4.1 Basics of Antiferromagnetism

All materials existing show some kind of interaction with an applied magnetic field. An overview of the different kinds of magnetism can, for example, be found in Refs. [73, 96, 97]. For most kinds of magnetic interaction, however, the existence of magnetic moments in the material is necessary. In the case where the moments interact only weakly with each other, the system shows a paramagnetic behaviour: At zero field the moments are not ordered and the net magnetization is zero. When a magnetic field is

applied the moments are aligned with the field depending on the field strength. This is until the saturation field is reached, at which all moments are fully aligned with the external field and the magnetization becomes saturated.

In materials with a sufficiently high interaction between the moments also a spontaneous ordering becomes possible below a certain ordering temperature. It can be shown that dipol-dipol interactions are much too weak to sustain the magnetic ordering. Heisenberg showed that the exchange interaction is responsible for the large molecular fields because it involves the large Coulomb energies. The exact nature of the ordering is then determined by the alignment and nature of the moments and the sign of the exchange interaction J. In the case of a negative J and only one type of localised magnetic moments the material makes a transition into an antiferomagnetic (AFM) state below the so called Néel temperature T_N. Most of the time an AFM system can be interpreted by two sublattices, where one contains all spin "up" moments (+) and the other all spin "down" (−) moments. The molecular field of each sublattice is then given by

$$B_{\pm} = -|\lambda| M_{\pm}, \tag{2.51}$$

where $|M_+| = |M_-| = M$ is the magnetisation of the respective sublattices and λ is the molecular field constant, which parametrises the strength of the molecular field as a function of the magnetization. The magnetization M of each sublattice follows

$$M = M_s B_j \left(\frac{g_j \mu_B j |\lambda| M}{k_B T} \right), \tag{2.52}$$

with j being the total angular momentum quantum number, B_J the Brillouin function and $M_s = ng\mu_B j$ the saturation magnetization. The net magnetization of the material $M_+ + M_- = 0$. The system becomes ordered below

$$T_N = \frac{g_j \mu_B (j+1) |\lambda| M_S}{3 k_B}. \tag{2.53}$$

The temperature dependence of the magnetic susceptibility of an antiferromagnet follows the Curie-Weiss law for $T > T_N$ and is shown in Fig. 2.6.

2.4.2 Antiferromagnetism in magnetic fields

When applying field to an antiferromagnet the field direction is important because the reaction is strongly dependent on whether the field is applied parallel or perpendicular to the direction of the staggered magnetization. The staggered magnetisation aligns in the direction, which is energetically favoured by the spins and is therefore conventionally called the easy axis of the magnetization. Any direction perpendicular to the easy axis is usually referred to as a hard axis. (There are also systems with two easy axes, but they will not be referred to here.) For the rest of this section we will assume that $T = 0$, meaning the $|M_+|$ amd $|M_-|$ both are equal to M_s.

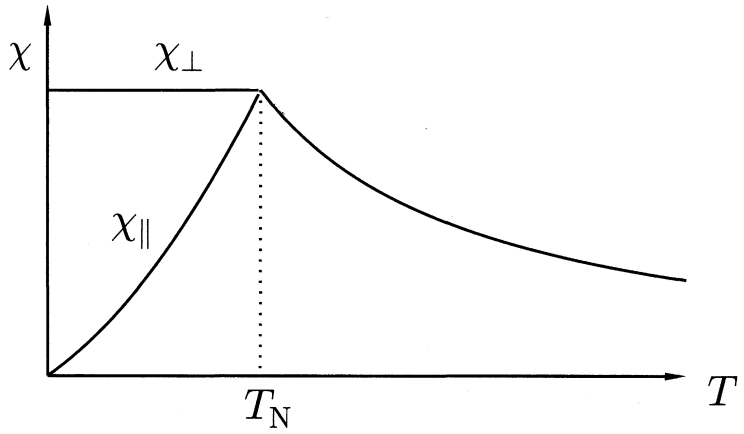

Figure 2.6: The antiferromagnetic susceptibility as a function of T (from [96]).

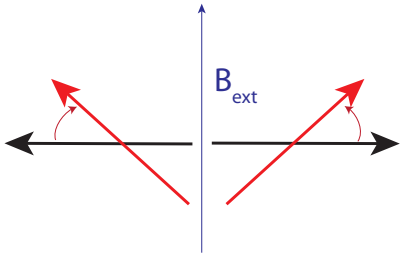

Figure 2.7: Schematic drawing of the canting of the spins in an AFM system at zero field (black) and with an applied magnetic field along the hard axis (red).

Magnetic field applied parallel to the hard axis

A magnetic field perpendicular to the staggered magnetization direction causes the magnetic moments to become canted as shown in Fig. 2.7. The state is then called a canted AFM state. This way the material obtains a finite magnetization component without breaking the AFM state meaning that $\chi_\perp \neq 0$. The net magnetization thereby is directed perpendicular to the easy axis. When the external field is increased the canting becomes stronger, increasing the net magnetization until the spins are fully aligned with the external field. At that moment the AFM state becomes broken and the material makes a transition into a saturated paramagnetic state.

Magnetic field applied parallel to the easy axis

For magnetic field applied parallel to the staggered magnetization direction the situation is more complicated. The field is then parallel to one of the sublattices and, hence, antiparallel to the other sublattice. As both sublattices are saturated in this direction the magnetic field has no effect on the spin orientation and the net magnetization re-

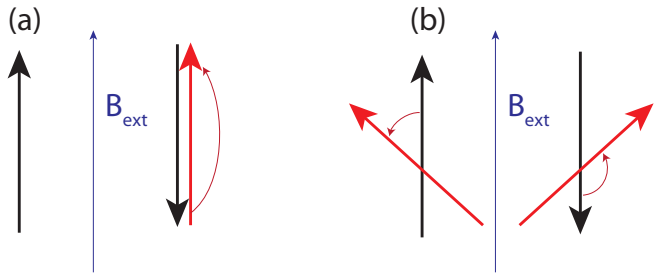

Figure 2.8: Schematic drawing of the spin orientation in an AFM system for zero external field (black) and for a high external field applied parallel to the easy axis (red). (a) Behaviour of the spins in the case of a spin-flip transition. (b) Behaviour of the spins in the case of a spin-flop transition.

mains zero as seen in Fig. 2.8(a). Therefore, $\chi_{\parallel} = 0$. For higher fields this configuration is, of course, energetically unfavourable. The reaction of the system to a higher field is determined by the magnetic anisotropy of the system. For a very anisotropic system (i.e. the energy difference for spin alignment parallel to the easy and hard axes is very big) the spins of the antiparallel sublattice turn by 180° producing a transition into the fully aligned paramagnetic state, which is called a spin-flip. The magnetization directly jumps from zero to the saturation value resulting in a first order nature of the phase transition.

In the case of a lower anisotropy a different behaviour is observed: Here at a sufficiently high field (which is lower than the spin-flip field for a similar T_N) the staggered magnetization direction changes by 90°, then going along the energetically favourable of the two hard axes (the intermediate axis) as shown in Fig. 2.8(b). Such a transition is called a spin-flop and also is a first order phase transition. This causes the staggered magnetization direction to be perpendicular to the field and allows a canting of the spins and a finite net magnetization like described for the hard axis above. When a field value is reached, where the spins become fully canted a second transition into the saturated paramagnetic state is observed. The fields where the system finally enters the fully aligned paramagnetic state are always lower for the field parallel to the easy axis than for field parallel to the hard axis.

A finite temperature allows the net magnetization and, therefore, the susceptibility $\chi_{\parallel}$ to become finite even below the respective spin-flip or spin-flop transition due to thermal disorder of the spins.

2.4.3 Influence of the exchange field on the conduction electrons

As explained above, the spontaneous ordering of the spins even at zero field is a result of the exchange interaction producing an effective field between the ordered magnetic moments. While this exchange field is not a real magnetic field it still has an effect on the spins of the respective electrons. In the organic metals, we are mainly interested in the influence of localised magnetic moments on the conduction electrons. The effective

field caused by this interaction we define as the exchange field B_e and, in an organic metal with localised magnetic moments, is described as [98]

$$B_e = \frac{J_{\pi d} S_d}{g\mu_B}, \tag{2.54}$$

where $J_{\pi d}$ is the exchange interaction of localised d spins S_d on the conducting π-electrons, which is called the π-d interaction.

Change of spin-splitting factor in Lifshitz-Kosevich theory

One effect of the exchange field B_e on the conduction electrons can be seen in the magnetic quantum oscillation. The presence of the exchange field alters the effect of the different spins on the oscillation amplitude resulting in a different formulation of the spin-splitting reduction factor [46, 99]. The reason for this is that in the normal metallic state the exchange field acts on the conduction electron spins in antiparallel direction of the external field leading to an effective field on the spins of $B_{\text{eff}} = B - B_e$. The exchange field, however, has no influence on the formation of the Landau tubes, which, therefore, are still proportional to B. When we introduce this effective field into the formula of the spin splitting factor (Eq. (2.16)) we get:

$$R_s = \cos\left[2\pi \frac{S_0}{4\cos\theta}\left(\frac{B_e}{B} - 1\right)\right], \tag{2.55}$$

with $S_0 = g^* m^*$. This means R_S becomes field dependent, i.e. the oscillation amplitude varies with the field, causing nodes in the field dependence of the oscillations, because the spin-up and spin-down components of the quantum oscillations obtain slightly different frequencies F_1 and F_2. The resulting frequency difference $\Delta F = F_2 - F_1$ is directly dependent on the exchange field

$$\Delta F = \frac{S_0 B_e}{2\cos\theta}. \tag{2.56}$$

From Eq. (2.56) the exchange field can be directly determined by taking the frequency difference from a fast-Fourier-transformation (FFT) spectrum of the oscillations, where the respective peak becomes split. However, this method is not very accurate since ΔF usually is small compared to F. In addition for many measurements only one clear node can be resolved making the splitting in the FFT spectrum imprecise. Another possible method is to use the θ-dependence of Eq. (2.55) and track the positions of the nodes in B for different θ.

Field-induced superconductivity (Jaccarino-Peter effect)

The above-mentioned compensation effect also has an influence on superconductivity. Jaccarino and Peter [100] were the first who showed theoretically that an internal exchange field can effectively cancel out the effect of the external field on the spins leading to a SC state in much higher fields than otherwise possible. It has to be noted that

this so called Jaccarino-Peter effect only affects the paramagnetic pair breaking effect of superconductivity (see Sec. 2.3.2). In the case of orbitally limited superconductivity the Jaccarino-Peter effect plays no role, because the exchange field only affects the electron spins. However, for paramagnetically limited superconductors a superconducting state will form in the field region $|B - B_e| \leq B_{c2,0}$, where $B_{c2,0}$ is the critical field without the influence of the exchange field. Such a high-field SC state has already been found in a number of systems including inorganic compounds like $Eu_xSn_{1-x}Mo_6S_8$ [101] but also organic metals like λ-FeCl [18] and κ-FeBr [22] as described in Sec. 3.2.6.

Exchange interaction and different ground states

A present exchange interaction notably influences the ground states of a systems. On one hand the exchange interaction can lead to the formation of unconventional superconductivity. Here the attractive interaction within the Cooper pairs is mediated by AFM fluctuations. On the other hand it is also possible that the exchange interaction drives the conduction electron system into an AFM insulating state. The latter is possible in case of a very strong π-d interaction and is manifested in λ-FeCl [17].

3 Organic Metals

In this thesis two different families of organic charge transfer salts have been investigated. Both of them will be introduced in this chapter.

3.1 The family of α-(BEDT-TTF)$_2$MHg(SCN)$_4$ (M = K, Tl, Rb, NH$_4$)

3.1.1 Synthesis

Crystals of α-(BEDT-TTF)$_2$MHg(SCN)$_4$ (M = K, Tl) (BEDT-TTF stands for bis(ethylenedithio)-tetrathiafulvalene, also often abbreviated as ET) are grown by electrochemical methods [7, 102, 103]. The molecules BEDT-TTF, KSCN and Hg(SCN)$_2$ are dissolved in a mixture of (1,1,2)trichloroethane and methanol. By applying a constant current using two Pt-electrodes the BEDT-TTF molecules are electrochemically oxidized. Thereby the solved salts serve as electrolytes. The electrochemical cell is left for a few weeks at a constant temperature of 20°C and a very low current density of 1-2 mA/cm^2 until small plate-like samples with a typical size of 0.5*0.5*0.1 mm^3 grow on the Pt-anode. The α-(BEDT-TTF)$_2$KHg(SCN)$_4$ (α-KHg) samples studied during this thesis were provided by H. Müller[1] and N. Kushch[2]. The used α-(BEDT-TTF)$_2$TlHg(SCN)$_4$ (α-TlHg) crystals were all grown by N. Kushch.

3.1.2 Crystal structure

The crystals of α-(BEDT-TTF)$_2$MHg(SCN)$_4$ (M = K, Tl) grow in the form of alternating layers of the organic BEDT-TTF$^+$ radical cations and inorganic MHg(SCN)$_4$ anions, where the layers lie in the *ac*-plane. The crystal structure of the Tl-salt is shown in Fig. 3.1, the data are from [104]. The structure of the K-salt is almost identical and, therefore, not shown [102]. The layered nature of the compound is seen in Fig. 3.1(a), where the view is along the *a*-axis and Fig 3.1(d), where the view is along the *c*-axis. The BEDT-TTF molecules are nearly flat due to their extended π-orbitals, which leads to a strong overlap of these orbitals and, hence, a high conductivity within the BEDT-TTF layers. The layers of the inorganic anions are insulating resulting in a high electronic anisotropy in the compound. When forming a crystal, every two BEDT-TTF molecules donate one electron to MHg(SCN)$_4$. Therefore, such compounds are called charge transfer salts.

[1] European Synchrotron Radiation Facility, 38043 Grenoble, France
[2] Institute of Problems of Chemical Physics, 142432 Chernogolovka, Russian Federation

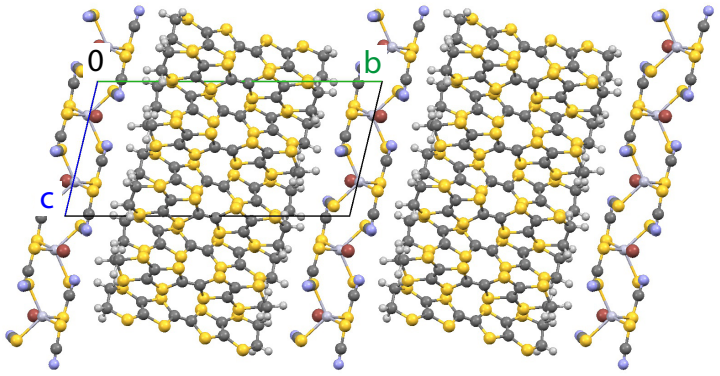

(a)

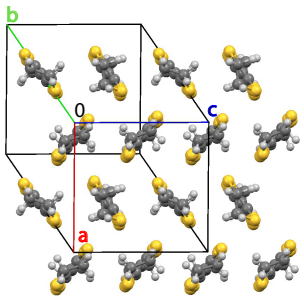

(b)

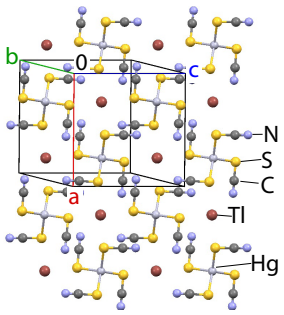

(c)

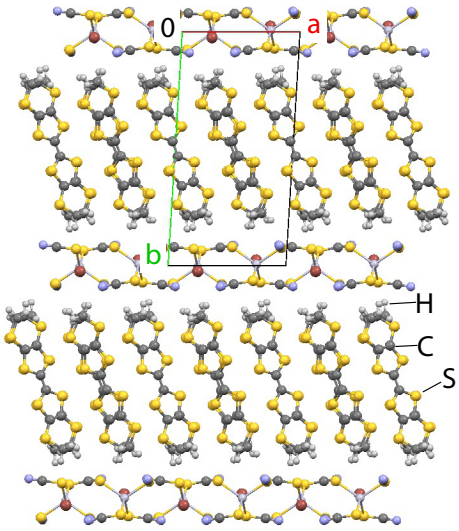

(d)

Figure 3.1: The crystal structure of α-(BEDT-TTF)$_2$TlHg(SCN)$_4$ viewed along the (a) a-axis, (b) the direction of the long axis of the (BEDT-TTF) (c) b^*-axis and (d) c-axis. In (b) we see the "fishbone" pattern typical of the α-phase and (c) shows the polymeric network of the anion layers. The crystallographic data are from [104].

The BEDT-TTF molecules are aligned with their long axis almost perpendicular to the layers. The short axes of the molecules are arranged in the so called "fishbone-pattern" which is characteristic for the α-structure as shown in Fig 3.1(b). The relatively thick anion layers form a polymeric network because the K^+ and the Hg^{2+} ions form bridges [102] (Fig. 3.1(c)). The crystal structure is triclinic. The lattice constants at $T = 300\,\mathrm{K}$ are $a = 1.0082\,\mathrm{nm}$, $b = 2.0565\,\mathrm{nm}$, $c = 0.9973\,\mathrm{nm}$ and the angles $\alpha = 103.7°$, $\beta = 90.91°$, $\gamma = 93.06°$, resulting in a total volume of $1.997\,\mathrm{nm}^3$ for the unit cell [102] for the K-salt and $a = 1.0051\,\mathrm{nm}$, $b = 2.0549\,\mathrm{nm}$, $c = 0.9934\,\mathrm{nm}$, $\alpha = 103.63°$, $\beta = 90.48°$, $\gamma = 93.27°$ and a cell volume of $1.990\,\mathrm{nm}^3$ for the Tl-salt [102]. (As β is almost 90° and a and c differ by only 1% the structure is close to monoclinic.) As we can see in these crystal structure parameters the distances are almost identical in the two salts. This is in agreement with almost identical sizes of the Tl^+ ions and the K^+ ions and should result in almost no change in chemical pressure.

3.1.3 Electronic band structure

The strong orbital overlap of the π-electron systems of the BEDT-TTF molecules gives rise to the formation of bands within the crystal. There are four BEDT-TTF molecules per unit cell resulting in four HOMO (highest occupied molecular orbital)-levels. As two electrons per unit cell are transferred to the anion layers, six electrons remain to fill the HOMO bands. Since the upper two bands overlap, each of them is partially filled resulting in the metallic character of the compounds. The band structure for α-KHg has been calculated by Mori *et al.* with the extended Hückel tight-binding method [105] and is shown in Fig. 3.2(a). A more recent determination of this band structure by a numerical atomic orbitals DFT approach [106] and the band structure of α-TlHg [102] are very similar and, therefore, not shown here.

The orbitals of molecules in neighbouring layers overlap only slightly, resulting in

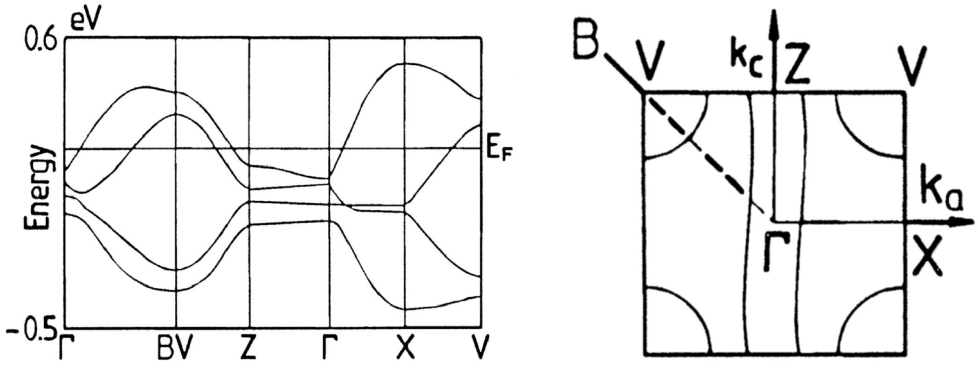

(a) (b)

Figure 3.2: (a) Band structure of α-(BEDT-TTF)$_2$KHg(SCN)$_4$ obtained from extended Hückel tight-binding theory at $T = 100\,\mathrm{K}$. (b) The resulting Fermi surface. Both taken from [105].

small but finite conductivity in the interlayer direction. The ratio between the intralayer and the interlayer transfer integral of about 500 [107] is among the highest in the known organic superconductors.

Figure 3.2(b) shows the 2D Fermi surface (FS) derived from the band structure for α-KHg. Again, the FS for α-TlHg is not shown because of high similarity. Due to the very small interlayer coupling the FS can be considered as quasi-2D and is only slightly warped in interlayer direction. The FS consists of electron-like open sheets, which are responsible for the 1D properties of the system and the hole-like cylinder responsible for the 2D properties. At zero pressure the open sheets can be nested on each other, giving rise to the CDW formation. The cylinders account for the existence of magnetic quantum oscillations, which have been used to determine the cylinder size as 16% of the first Brillouin zone area [108, 109].

3.1.4 Ambient pressure properties: charge-density wave (CDW) and filamentary superconductivity

Among the compounds of the family α-(BEDT-TTF)$_2$MHg(SCN)$_4$, where (M = K, Tl, Rb, NH_4), two different kinds of ground states are observed. The NH_4 compound becomes superconducting with $T_c = 2\,\mathrm{K}$ [110], while the other three salts enter a charge density wave (CDW) state with transition temperatures of $T_{\mathrm{CDW}} = 8\,\mathrm{K}$ (for M = K), $T_{\mathrm{CDW}} = 10\,\mathrm{K}$ (for M = Tl) and $T_{\mathrm{CDW}} = 12\,\mathrm{K}$ (for M = Rb) [28, 31, 36, 109, 111, 112]. This CDW results from a Peierls-type transition, which is caused by nesting of the q1D part of the FS. Thereby the charges in the crystal are redistributed with alternating density. The CDW transition causes a reconstruction of the FS with new closed orbits and new open sheets running in the direction of the nesting vector **Q** as depicted in Fig. 3.3. **Q** is tilted with respect to the c-axis by $\approx 20°$ for α-KHg according to [37, 63] and by $\approx 24°$ for α-TlHg [113].

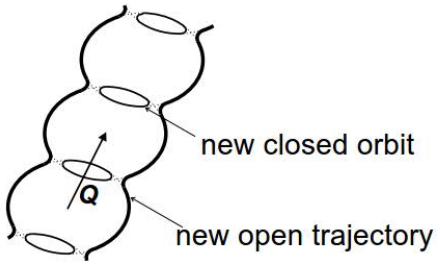

Figure 3.3: The reconstructed FS α-MHg in the CDW state (taken from [36]).

For the CDW compounds below a certain temperature of $T \approx 300\,\mathrm{mK}$ for α-KHg [27], $T \approx 100\,\mathrm{mK}$ (for α-TlHg) [40] and $T \approx 500\,\mathrm{mK}$ (for Rb-SCN) [40] an onset of a SC phase appears. However, the resistance does not go to zero. This is, because the formation of the CDW state does not allow the formation of bulk SC. Instead a SC state is realised only in small pockets within the charge ordered region, probably at domain boundaries. This spatially inhomogeneous filamentary SC state is seen in a reduction of the interlayer resistance, but since the SC does not occupy the whole volume, the resistance does not decrease to zero.

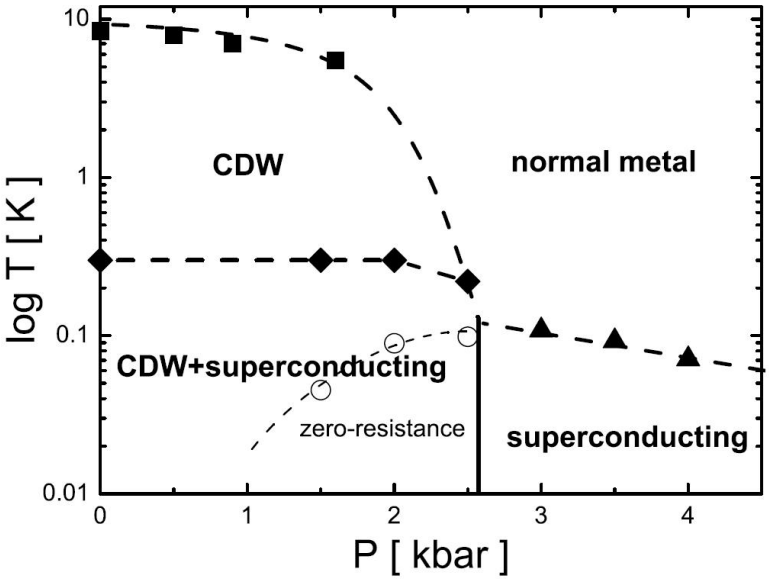

Figure 3.4: The T-p phase diagram of α-(BEDT-TTF)$_2$KHg(SCN)$_4$ (from [36]).

3.1.5 Influence of pressure on the CDW and SC state

In general organic charge transfer salts have a strong dependence on hydrostatic pressure because of their high compressibility [7]. The suppression of the CDW state under pressure is a result of the change in warping of the 1D part of the FS causing a worsening of the nesting conditions. Figure 3.4 shows the T-p phase diagram of α-(BEDT-TTF)$_2$KHg(SCN)$_4$. As we can see the CDW state is gradually weakened by applying pressure. Above a critical pressure of $p_c \approx 2.6\,\mathrm{kbar}$ the CDW state becomes fully suppressed giving rise to a homogeneous bulk SC state with a sharp transition with a maximum $T_c = 110\,\mathrm{mK}$. Already below p_c a zero resistance state is established, when coming close to p_c.

The pressure dependence of the critical magnetic field applied perpendicular to the layers of α-(BEDT-TTF)$_2$KHg(SCN)$_4$ was studied by Andres *et al.* [27] and is shown in Fig. 3.5. For $p > p_c$ the slope $\mathrm{d}B_\perp/\mathrm{d}T$ is linear, as would be expected for a purely orbital pair breaking mechanism (see Sec. 2.3.2). For undercritical pressures an upturn of the slope was observed, caused by the inhomogeneous nature of the superconductivity within the CDW state. Above the critical pressure T_c linearly decreases with increasing pressure with a slope of about $30\,\mathrm{mK/kbar}$. This decrease of T_c can be explained by the strong compressibility of the crystal lattice especially in the interlayer direction [6].

S. Jakob [38] investigated the critical field anisotropy of α-(BEDT-TTF)$_2$KHg(SCN)$_4$ at $p = 2.8\,\mathrm{kbar}$, which is slightly above p_c. An extremely high critical field anisotropy for fields applied perpendicular and parallel to the conducting layers was found. For a parallel orientation of the magnetic field the superconductivity clearly becomes limited by the Pauli-paramagnetic pair breaking effect. Also a considerable azimuthal anisotropy of the critical field was found. As this φ anisotropy does not fit any distinct direction on the FS its origin is unknown to date.

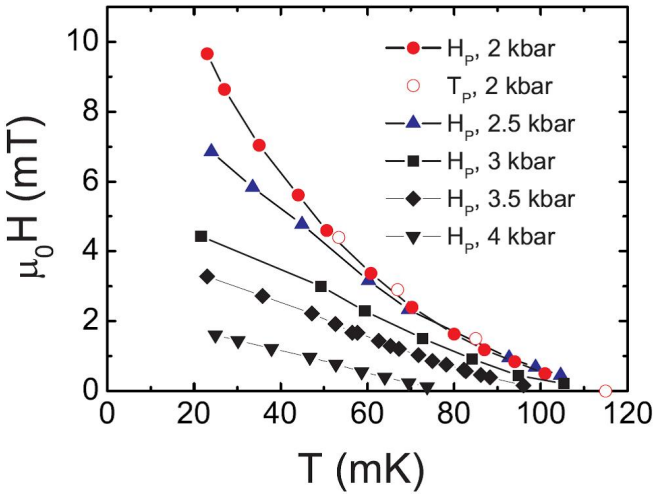

Figure 3.5: The perpendicular critical field of the SC state of α-(BEDT-TTF)$_2$KHg(SCN)$_4$ as a function of temperature for different pressures (from [27]).

The pressure dependence of the critical field anisotropy in α-(BEDT-TTF)$_2$KHg(SCN)$_4$ is still an open question. Therefore, the critical field anisotropy in α-KHg was studied at several higher pressures during this PhD thesis. The anisotropy of the SC state above and below the critical pressure have been compared. Further, this compound has a very high inplane coherence length $\xi_{\|} \approx 200\,\mathrm{nm}$ for $p = 3\,\mathrm{kbar}$, as compared to other organic superconductors. The London penetration depth λ_L is assumed to be of similar value as in other compounds. Therefore, we observe a Ginzuburg-Landau parameter κ close to 1. Since at very high pressures $\xi_{\|}$ is expected to increase even further, a crossover in the SC behaviour from type II to type I is expected. Therefore, measurements dedicated to the detection of such a crossover were performed.

For α-TlHg the T-p phase diagram has been studied by Schegolev *et al.* [39] up to $p = 3.5\,\mathrm{kbar}$ in the temperature range down to 1.3 K. However, properties like the critical pressure of α-TlHg or the existence of a SC state under pressure are still unknown. Therefore, the high pressure behaviour of the CDW and SC state of α-TlHg has been jointly investigated together with L. Höhlein in the frame of her master's thesis [41]. A comparison of the results should provide valuable information on the effect of chemical substitution on the material properties. Since the K^+ ions and the Tl^+ ions are almost identical in size, we do not expect an effect of chemical pressure. As α-TlHg is known to have a higher transition temperature into the CDW state [103] than α-KHg for zero pressure, maybe also a higher T_c of the bulk SC state above the critical pressure can be expected. If this is the case a broader part of the SC B-T phase diagram could be studied than for α-KHg. This would allow us to study a wider range of the SC region, which would be an advantage in the search of a Fulde-Ferell-Larkin-Ovchinnikov (FFLO) state, which is expected to appear in compounds with such a high anisotropy.

3.2 The family of κ-$(BETS)_2FeX_4$ (X = Cl, Br)

3.2.1 Synthesis

Single crystals of κ-$(BETS)_2FeX_4$ (X = Cl, Br) (where BETS stands for bis(ethylenedithio)-tetraselenavulvalene, also abbreviated as BEDT-TSF) are grown by similar electrochemical methods as mentioned above (see Sec. 3.1.1). Details can be found in Refs. [15, 20, 114]. The BETS molecules and tetraethylammonium iron(III) tetrabromide are dissolved in a 10% ethanol-chlorobenzene solution. A constant current of $0.7\,\mu A/mm^3$ was applied via Pt-electrodes and the solution was kept under a nitrogen atmosphere at ambient temperature or 40°C for 2-4 weeks. The typical sample sizes obtained on the Pt-anode are $0.5 \times 0.4 \times 0.03\,mm^3$.

3.2.2 Crystal structure

Similar to the α-family explained above, κ-$(BETS)_2FeX_4$ (X = Cl, Br) has a layered structure, where the organic BETS layers are conducting and the inorganic FeX_4 layers are insulating. The layers are arranged in the crystallographic *ac*-plane. The crystal structure of κ-$(BETS)_2FeBr_4$ (κ-FeBr) can be seen in Fig. 3.6 viewed along the different crystallographic axes. The crystal structure of κ-FeCl is almost identical and, therefore, not shown separately. The crystal structure is orthorhombic with the space group *Pnma*. The lattice constants at $T = 300\,K$ are $a = 1.1787\,nm, b = 3.6607\,nm$ and $c = 0.8504\,nm$ for κ-FeBr [114] and $a = 1.1693\,nm, b = 3.5945\,nm$ and $c = 0.84914\,nm$ for κ-FeCl [20]. The smaller lattice constants in the Cl-salt are caused by the Cl^- ions being smaller than the Br^- ions and should result in a higher chemical pressure in κ-FeCl.

In these compounds the organic molecules are stacked in the so-called κ-structure. In this structure the dimerisation of the BETS molecules is especially strong. The dimers are packed in a parquet-like pattern. Like in the α-phases the BETS molecules are tilted with respect to the perpendicular direction. In two adjacent layers they are tilted in opposite direction. Therefore, the lattice constant b is two times the interlayer distance $d = b/2$.

3.2.3 Band Structure and Fermi surface

The band structures of κ-FeCl [20] (shown in Fig. 3.7(a)) and κ-FeBr [114] have been calculated by the extended Hückel approximation and are very similar in overall shape. The resulting overlap integrals, mid-gap energies, and the bandwidth of the upper band of each compound are shown in Table 3.1. As we can see for both compounds the intradimer transfer integral p (shown in Fig. 3.6(b)) is by far the largest, reflecting the strongly dimerised structure of the κ-phase. As there are four donor molecules per unit cell, the bandstrucuture consists of four bands (similar to the α-phases). Also here every two BETS molecules donate one electron to the anion layers resulting in two effectively half-filled bands. Unlike the α-phases there is a large mid-gap due to the strong dimerisation. Generally the overlap integrals are stronger in the Br-salt,

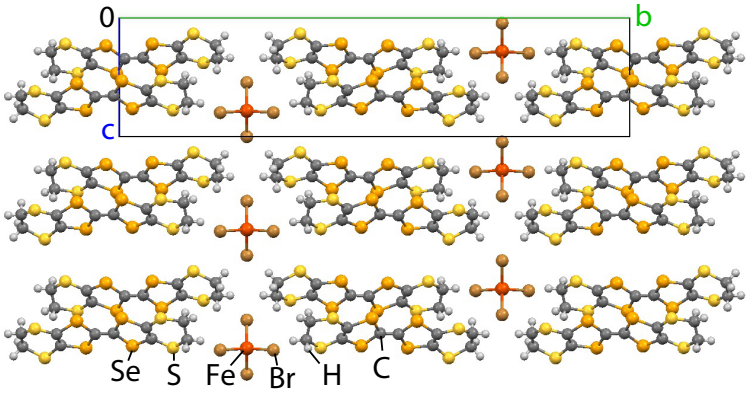

(a)

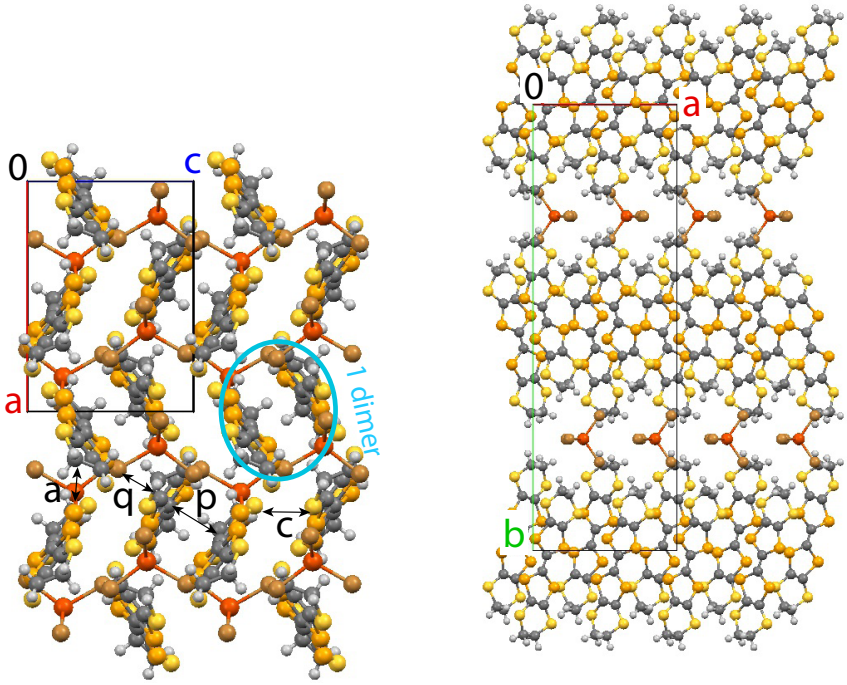

(b) (c)

Figure 3.6: The crystal structure of κ-$(BETS)_2FeBr_4$ viewed along the (a) a-axis, (b) b-axis and (c) c-axis (from [114]). The letters in (b) refer to the transfer integrals in the different directions given in Table 3.1

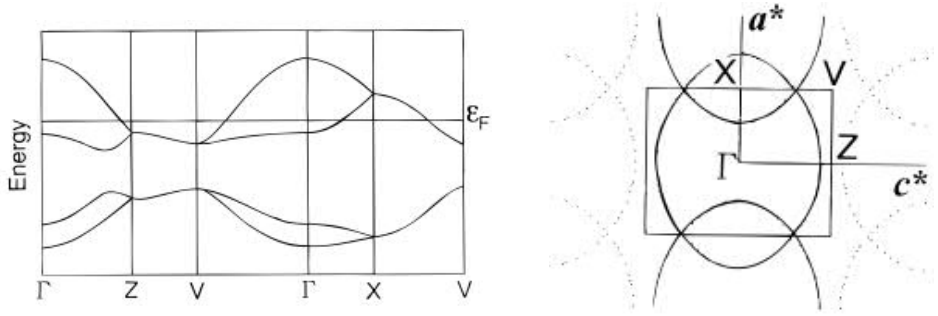

(a) (b)

Figure 3.7: (a) Calculated band structure of κ-FeCl for $T = 100\,\mathrm{K}$. (b) Resulting FS of κ-FeCl for $T = 100\,\mathrm{K}$. Both taken from [20].

which also has a much higher mid-gap energy. This is likely a sign of stronger electron correlations in κ-FeBr [115].

values in [eV]	a	p	q	c	E mid-gap	bandwidth
κ-(BETS)$_2$FeCl$_4$	-16.93	64.37	9.08	32.76	0.48	1.28
κ-(BETS)$_2$FeBr$_4$	-22.41	77.33	8.11	35.14	0.68	1.44

Table 3.1: The overlap integrals, mid-gap energies, and the bandwidth of the upper band of both κ-(BETS)$_2$FeX$_4$ (X = Cl, Br) (from [114]). All values are given in [eV].

The Fermi surface of κ-FeCl and κ-FeBr is typical for the κ phases. It is a closed, cylindrical FS with an area of ∼ 100% of the first Brillouin zone (FBZ) area. The folding of the FS into the FBZ splits this cylinder into a smaller cylindrical part around the X point of the FBZ and two open sheets running along the k_c-direction. The FS for κ-FeCl is shown in Fig. 3.7(b). The band structure calculations [20, 114] do not predict a gap between the two surfaces, however, measurements of magnetic quantum oscillations show that such a gap must exist [116–118]. In SdH oscillations on both compounds several frequencies were observed. An example of SdH oscillations in κ-FeBr is shown in Fig. 3.8(a). The main frequency, which corresponds to the orbit denoted as α, is $F_{\alpha,\mathrm{Br}} = 850\,\mathrm{T}$ ($F_{\alpha,\mathrm{Cl}} = 860\,\mathrm{T}$), which corresponds to ∼ 20% of the FBZ and is in good agreement with the expected size of the small cylindrical part. Without a gap, this frequency should not be observable. The frequency $F_{\beta,\mathrm{Br}} = 4280\,\mathrm{T}$ ($F_{\beta,\mathrm{Cl}} = 4295\,\mathrm{T}$) corresponding to ∼ 100% of the FBZ area must then be a magnetic-breakdown orbit. Also a slow frequency, $F_\gamma = 96\,\mathrm{T}$, corresponding to 2.4% of the FBZ area was observed [117, 118], but could not be explained yet. For κ-FeBr the FS topology has been confirmed from AMRO studies [23].

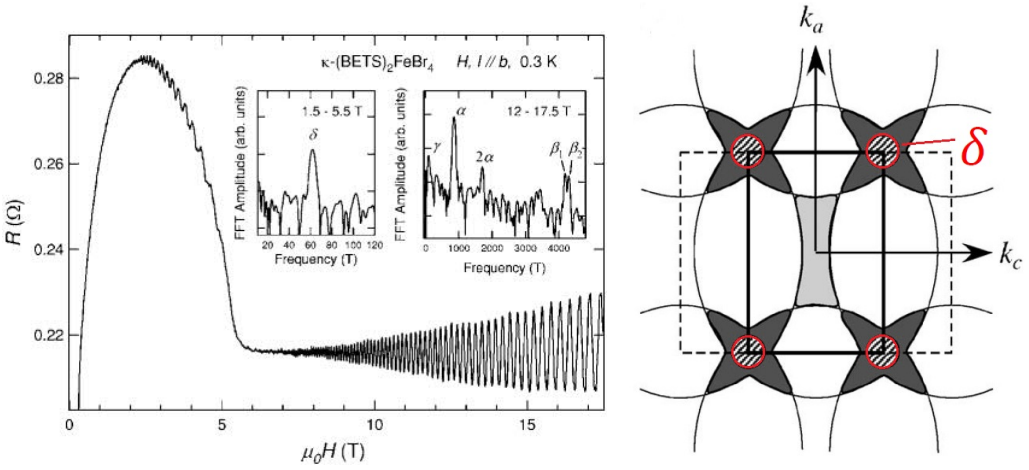

(a) (b)

Figure 3.8: (a) SdH oscillations in κ-FeBr at $T = 0.3\,\mathrm{K}$. For $B < 5\,\mathrm{T}$ the system is in the AFM state. Above 5 T the system is in the normal metallic state. The insets show FFT spectra above and below the AFM transition. (b) Reconstructed FS in the AFM phase. The solid rectangle shows the FBZ in the AFM state and the dashed line the original FBZ. The red circles indicate the orbit associated with F_δ. (Both from [23].)

3.2.4 Properties of the AFM state

κ-FeCl and κ-FeBr both undergo a transition into an antiferromagnetic (AFM) state below a Néel temperature of $T_N = 2.5\,\mathrm{K}$ for the Br-salt [114] and $T_N = 0.45\,\mathrm{K}$ for the Cl-salt [21]. In this AFM state the localised Fe^{3+} spins, which are in the spin 5/2 state, order antiferromagnetically. Unlike the differently structured λ-$(BETS)_2FeCl_4$ (λ-FeCl), where also the π-electrons order antiferromagnetically, resulting in an insulating state, the κ-phases remain metallic below the AFM transition (there is no magnetic ordering of the conduction electrons) [21, 114]. In resistance the AFM transition is reflected by a distinct step, where the resistance decreases by about 5%, which is likely due to spin-dependent scattering [21]. This step can be seen in the inset of Fig. 3.9. For both compounds the easy axis of the AFM ordering is parallel to the crystallographic a-axis as shown by susceptibility measurements [21, 114]. However it has been shown that for certain mixed compositions of Cl and Br, κ-$(BETS)_2FeCl_xBr_{4-x}$, the easy axis

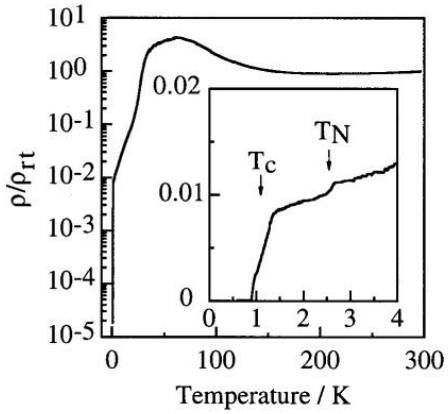

Figure 3.9: Temerature dependence of resistance of κ-FeBr. The inset shows the low temperature part with the AFM and SC transition (from [114]).

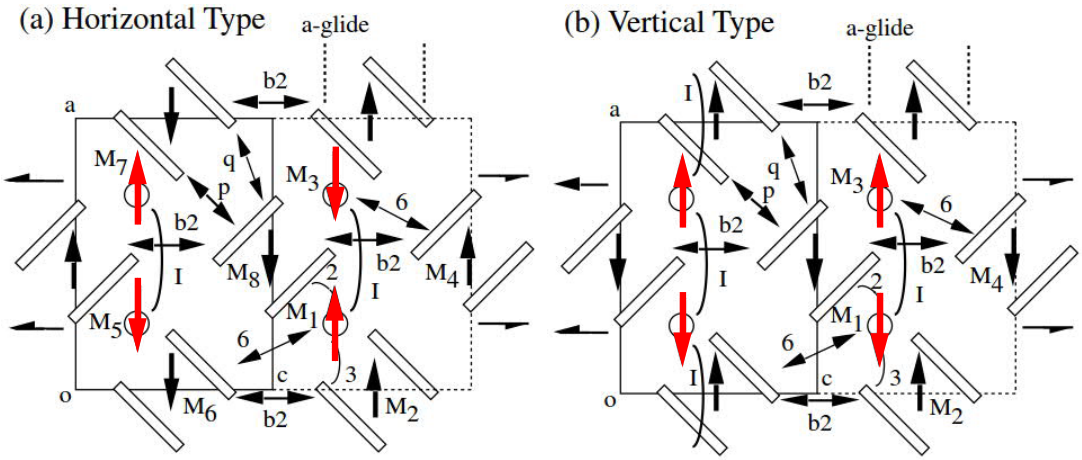

Figure 3.10: Stable magnetic structures for the localised iron spins (red) and the conduction electron spins (black) calculated for (a) the horizontal and (b) the vertical type of ordering by [98].

rotates in the *ab*-plane [119]. The difference in Néel temperature between the two compounds is likely a result of the stronger exchange interaction because of the larger Br atoms. Both comounds remain metallic below the Néel temperature.

λ-FeCl on the other hand becomes insulating for $T < 8\,\mathrm{K}$ [20]. This is because in this compound the conduction electrons are also being driven into an antiferromagnetic ordering due to the interaction with the localised moments [17]. However, the exact nature of the ground state is still under discussion [19, 120–123].

The different magnetic interactions in κ-FeBr and κ-FeCl were calculated by Mori and Katsuhara [98] based on the extended-Hückel molecular orbital method. The interactions are called d-d for the interaction in between the localised moments and π-d for the interaction between the localised moments and the conduction electrons. The magnetic structure was estimated to be of a horizontal type with the magnetic unit cell being (a, b, $2c$), where the spins order as shown in Fig. 3.10(a). The vertical type shown in Fig. 3.10(b) also is possible but not energetically favoured. Konoike *et al.* [23, 124, 125] found that within the AFM state a new SdH frequency named δ can be observed as shown in Fig. 3.8(a). Thereby $F_\delta = 60\,\mathrm{T}$, which corresponds to 1.5% of the FBZ area and $m^*_\delta = 1.1$. This strongly suggests a FS reconstruction in the AFM state. Because of the predictions by Mori [98] the authors suggested a folding of the FBZ in c direction (because a doubling of the lattice constant causes a halving of the respective reciprocal lattice constant). The reconstructed FS is shown in Fig. 3.8(b). The small circular orbital at the corners of the FBZ marked in red fit to the observed frequency. A second frequency was also found by Konoike *et al.* [125] and named F_ε. However, the authors did not give the mass of this second frequency. The SdH oscillations associated with the other closed orbits in the suggested reconstructed FS have not been found yet.

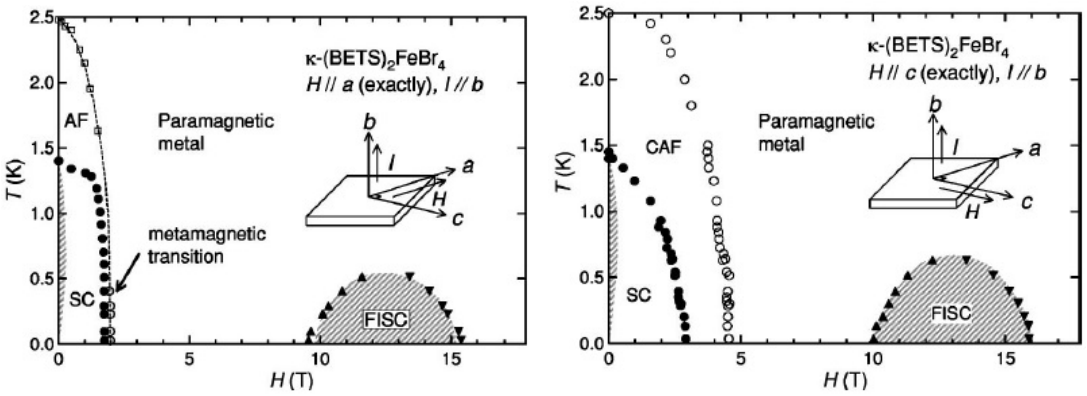

(a) (b)

Figure 3.11: B-T phase diagram of κ-FeBr for (a) $\mathbf{B}||a$ axis and (b) $\mathbf{B}||c$ axis (both from [22]). The hollow circles and squares represent the transition into the antiferromagnetic (AF) state, the filled circles indicate the transition into the superconducting (SC) state and the triangles show the boundaries of the field induced SC (FISC) state.

3.2.5 Magnetic phase diagram

The AFM state can be suppressed by a sufficiently high magnetic field. The exact critical field value strongly depends on the field direction. Figure 3.11 shows the B-T phase diagram of κ-FeBr for (a) $\mathbf{B}\|a$-axis (easy axis) and (b) $\mathbf{B}\|c$-axis obtained from resistive measurements [22]. For $\mathbf{B}\|b$-axis no detailed phase diagram has been reported yet. However, from Fig. 3.8(a) we can see that for $T = 0.3\,\mathrm{K}$ the AFM transition takes place at $B \approx 5.5\,\mathrm{T}$. When comparing the different field directions it becomes clear that the AFM state is most rapidly suppressed by a field parallel to the easy axis of the magnetisation as should be expected. For $\mathbf{B}\|a$ we would expect either a spin-flip or spin-flop transition, depending on the anisotropy of the system. For κ-FeBr a double feature at $B = 1.7\,\mathrm{T}$ and $B = 1.9\,\mathrm{T}$ in torque measurements hints to a possible spin-flop transition and a consecutive transition to the saturated paramagnetic state [126]. However no further prove for the existence of a spin-flop transition in κ-FeBr have been found. In κ-FeCl no studies on the influence of a magnetic field on the AFM state have been performed yet.

3.2.6 Superconductivity

As mentioned above κ-FeBr and κ-FeCl were the first two organic AFM superconductors. In the Cl-salt the SC state was found at a critical temperature $0.1\,\mathrm{K} < T_c < 0.2\,\mathrm{K}$ by measurements of AC-susceptibility [21]. However, the diamagnetic signal was weak and the authors did not see any sign of superconductivity in their resistive and specific heat measurements. Pratt *et al.* [24] associated a feature in muon-spin-rotation (μSR) measurements at $T = 0.17\,\mathrm{K}$ with the SC transition. There are no further reports on the SC state in κ-FeCl.

κ-FeBr becomes superconducting below $T_c = 1.4\,\mathrm{K}$ [22]. Also in resistive measurements the transition is clearly visible and the resistance drops to zero. The behaviour of the SC state under a magnetic field applied parallel to the layers can be seen in Fig. 3.11. We can see that it is important in which inplane direction the field is applied. For $\mathbf{B}\|c$ the SC state is suppressed at a critical field $B_{c2} = 3\,\mathrm{T}$ while the system still remains antiferromagnetic. For $\mathbf{B}\|a$ the SC and AFM state are broken at $B = 1.7\,\mathrm{T}$ at sufficiently low temperature. The reason for this can probably be found in the exchange field B_e. The π-d interaction between the localised iron spins and the conduction electrons produces an effective field on the conduction electron spins. This usually destabilises superconductivity. In the AFM state however this exchange field is compensated because of the antiparallel alignment of the neighbouring Fe spins. When the AFM state becomes broken due to the external field the full exchange field suddenly takes effect on the spins of the conduction electrons and destroys the superconductivity due to the Paul-paramagnetic meachanism (see Sec. 2.3.2).

Due to this exchange field, however, the compound also shows a field-induced SC (FISC) state. This happens because in the presence of an AFM exchange interaction the exchange field applies in opposite direction to the external field. When the external field reaches the value of the exchange field, the field affecting the conduction electron spins is effectively cancelled and the compound undergoes a reentrant transition into a SC state. A FISC state in organic compounds was observed for the first time in λ-FeCl. As already mentioned λ-FeCl becomes insulating at $T < 8\,\mathrm{K}$. By applying a magnetic field parallel to the layers, however, this insulating state is broken at $B \approx 10\,\mathrm{T}$ and at $B \approx 18\,\mathrm{T}$ the system undergoes a transition into a SC state [18]. High field measurements showed that the SC state is only broken again for fields higher than $B \approx 46\,\mathrm{T}$ [127, 128]. The exchange field of λ-FeCl was determined as $H_e = 33\,\mathrm{T}$. For κ-FeBr the exchange field is reported to be $H_e \approx 12.6\,\mathrm{T}$ from the center of the FISC dome and $H_e \approx 12.7\,\mathrm{T}$ the splitting of the β-SdH oscillations [22]. Therefore, a field induced SC state can be seen for $10\,\mathrm{T} < B < 15\,\mathrm{T}$ as shown in Fig. 3.11 [22].

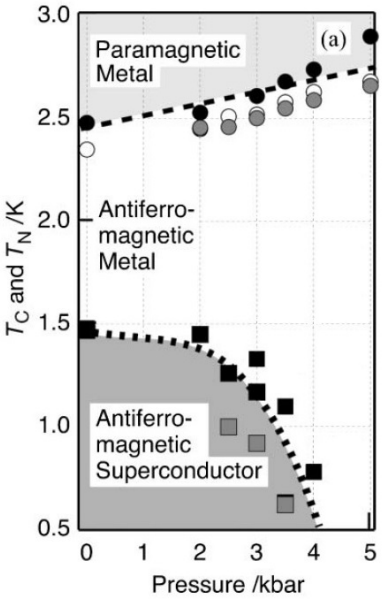

Figure 3.12: The T-p phase diagram of κ-FeBr.

3.2.7 Effect of pressure

As already mentioned above concerning α-KHg, pressure strongly affects the organic charge transfer salts. In κ-FeBr the SC state is suppressed by applying pressure, vanishing completely at a pressure of about 4 kbar [129]. However, the AFM state in κ-FeBr is enhanced by pressure: T_N increases to 2.7 K at $p = 5\,\mathrm{kbar}$. Both effects are visible in

the T-p phase diagram of κ-FeBr shown in Fig. 3.12.

Probably the most important effect of halogen substitution in the anion layer of organic charge transfer salts is the application of chemical pressure because of different atom sizes. This can, for example, be seen in the family of κ-(BEDT-TTF)Cu[N(CN)$_2$]X, where X = Cl, Br. In κ-(BETS)$_2$FeX$_4$ the substitution of Br by Cl, which corresponds to an increase of chemical pressure, reduces T_N. But since T_N increases by real pressure, the effect of chemical pressure cannot be responsible for the dependence of the magnetic properties on the halogen substitution. More probably it is connected with the much stronger d-d interaction in the Br-salt as calculated by Mori and Katsuhara [98].

Open questions

While the properties of the AFM and SC states of κ-FeBr under an applied magnetic field are already relatively well studied some interesting points remain. One of these is to measure the angular dependence of the SdH oscillations in the normal metallic state of κ-FeBr. This way the effect of the exchange field on the Zeeman-splitting can be better understood. Further it is interesting, to study the same dependence in κ-FeCl since there is no experimental result on the exchange field yet, which is supposed to be smaller (from theoretical predictions [98]). A comparison of the studies on the two compounds should yield deeper insight into the effect of the exchange field. SdH oscillations within the AFM state were measured in order to gain further information about the FS reconstruction and the change of the Spin-splitting in the ordered state. In κ-FeCl the normal state properties were further investigated by mapping the FS with the use of AMRO.

Another important topic during this PhD-thesis was the study of the AFM and SC state of κ-FeCl, on which there exists almost no data yet. This is probably due to the very low temperatures required. The main focus thereby was on the angular anisotropy of AFM and SC states in magnetic field. Therefore, the magnetic phase diagram of κ-FeCl for magnetic field applied along each of the three principal crystal axes was determined. This way more information about the effect of the weaker magnetic interaction in the Cl-salt could be gathered. Additionally signs of a similar FS reconstruction as proposed in κ-FeBr were found in form of SdH oscillations within the AFM state.

Further the B-T phase diagrams of κ-FeBr along the different crystal axes were determined for different hydrostatic pressures to further study the effect of hydrostatic pressure on the behaviour of the AFM state. The measurements on κ-FeBr were mainly performed jointly with L. Schaidhammer in the framework of his master's thesis [25] and F. Kollmansberger in the course of his bachelor's thesis [26].

4 Experimental setup

4.1 Measuring sample properties

4.1.1 Definition of angles

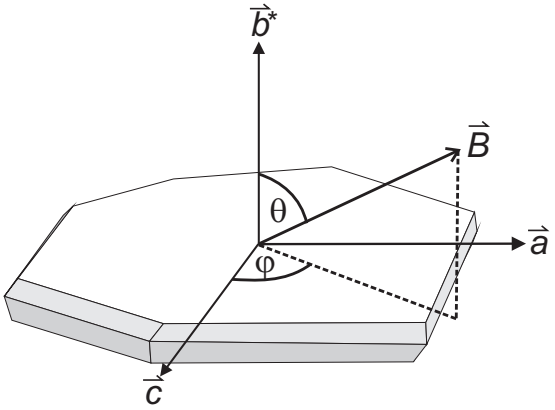

Figure 4.1: Definition of the angles describing the direction of the magnetic field with respect to the crystal axes.

The properties of organic charge transfer salts in a magnetic field strongly depend on their orientation with respect to the field direction. Therefore, most setups used in our experiments allowed in-situ rotation of the sample with respect to the magnetic field. To keep track of the field direction we from now on define the angles as sketched in Fig. 4.1: The polar angle θ determines the angle between the magnetic field direction and the normal to the plane of the conducting layers in the sample (ac-plane in Fig. 4.1). The azimuthal angle φ is the angle between the projection of the magnetic field direction on the conducting layers and the crystal axis c. Precise alignment of the samples on the sample holders was necessary for correct angular studies. In the manual orientation of the samples on the sample holders, usually misorientations smaller than 5° could be achieved. In most systems this misorientations could be compensated by in-situ rotation of sample and field, with the final precisions depending on the setup as explained below.

4.1.2 Resistance

The sample resistance was measured with the conventional 4-probe technique by the use of low-frequency lock-in amplifiers. To this end four annealed Pt wires were glued to the sample using conducting graphite paste. Depending on the sample size and the material

either 10 µm or 20 µm wires were used. Most of the time the wires were glued on top and bottom of the sample in order to measure the interlayer resistance as depicted in Fig. 4.2. The reasons for that are a much higher interlayer resistance due to the high anisotropy of the compounds and the fact that several of the measured features are much stronger or, in some cases, exclusively seen in the interlayer resistance. For some exceptional purposes also an inplane geometry was used. In that case all four wires were glued on the same side of the sample. In that case the sample was chosen as thin and long as possible in order to have a sufficient sample resistance.

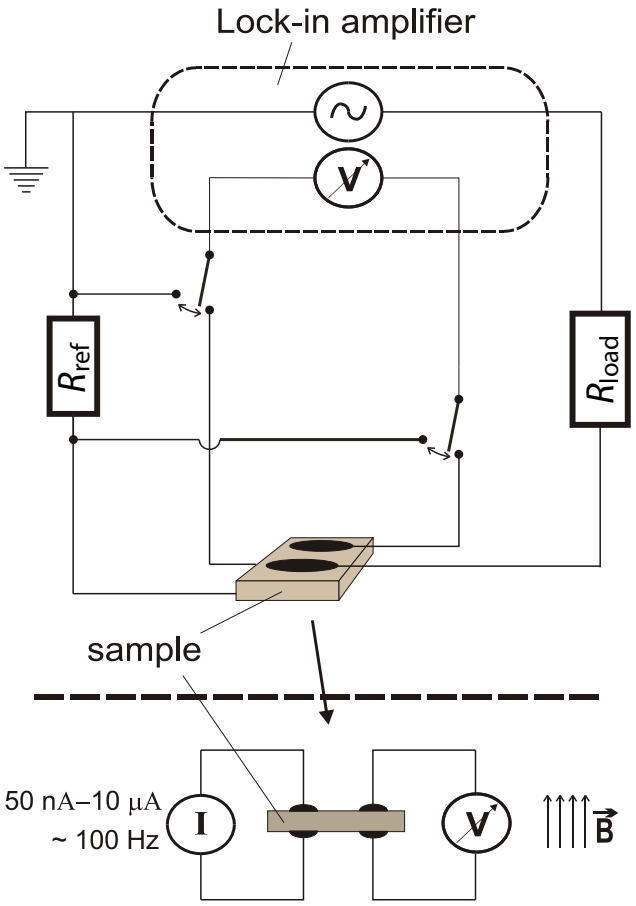

Figure 4.2: Circuit of the four point resistance measurement (taken from [36]).

In order to obtain the sample resistance a current was applied to one pair of the sample contacts, while the voltage drop on the other pair was measured. The current was provided by the lock-in amplifier's oscillator output. The exact circuit diagram is shown in Fig. 4.2. A big resistor R_{load} is coupled in series with the sample in order to set a constant current. The oscillator was usually set to 1 V, therefore for R_{load} typical values of 10 kΩ-10 MΩ were used, in order to achieve measurement currents in the range of 100 nA-100 µA. For fine tuning of the current a second resistor $R_{\mathrm{ref}} = 10$ or 100 Ω

was inserted into the current circuit. The current was then set as $I_{\mathrm{meas}} = \frac{U_{\mathrm{ref}}}{R_{\mathrm{ref}}}$. Because R_{load} is much bigger, the other resistances can be neglected and the measurement current I_{meas} is then given by

$$I_{\mathrm{meas}} = \frac{U_{\mathrm{osc}}}{R_{\mathrm{sample}} + R_{\mathrm{ref}} + R_{\mathrm{load}}} \approx \frac{U_{\mathrm{osc}}}{R_{\mathrm{load}}}, \tag{4.1}$$

providing a sufficient stability of the current in spite of the changes in resistances of samples, contacts and leads. To adjust the current the differential inputs of the lock-in can then be connected to the known reference resistor and U_{osc} is changed until the measured voltage yields a correct value of I_{meas}. Afterward the sample is connected to the differential input of the lock-in amplifier. The sample resistance is then determined by

$$R_{\mathrm{sample}} = \frac{U_{\mathrm{sample}}}{I_{\mathrm{meas}}}. \tag{4.2}$$

4.1.3 Magnetic torque

For measurements of the magnetic torque, the sample was glued to a silicon piezoresistive microcantilevers from Seiko Instruments Inc. originally designed for atomic force microscopy. In these cantilevers the deflection is detected by a piezoresistive current path implanted in the two legs of the cantilever. Next to the real cantilever a reference lever is mounted on the same platform. By the use of a Wheatstone bridge a precise measurement of the resistance change in the cantilever is possible, yielding a qualitative information about the torque on the sample.

4.2 The high-pressure clamp-cell

Several experiments in the scope of this thesis were conducted under high quasi hydrostatic pressure. The pressures were thereby achieved by placing the sample inside a clamp pressure cell as depicted in Fig. 4.3. The cell body is made of hardened Cu-Be alloy which is both very tough to withstand the high pressures and non-magnetic, which is important when working in high magnetic fields. The sample contacts are led into the cell via a feedthrough, which consists of a Cu-Be body with a small channel in the middle that contains copper wires embedded in Stycast 2850 epoxy. On top of the feedthrough the samples were connected by Pt-wires as mentioned above.

A Teflon cup, filled with a liquid pressure medium, was placed on top of the feedthrough and introduced into the cell. As pressure medium the silicon oil “GKZh” was used most of the time. The Teflon cup is sealed on both sides by two washers, made of soft Cu-Be, in order to prevent the Teflon from flowing through the gaps under high pressure.

For pressurising, a mechanical press is used to apply a force of several kN to the “mushroom” made of hardened steel. This force is transferred to the Teflon cup via a plate made of Cu-Be and a piston made of tungsten carbide (WC). When the desired pressure inside the cell is reached the nut is tightened and then the external force can be released.

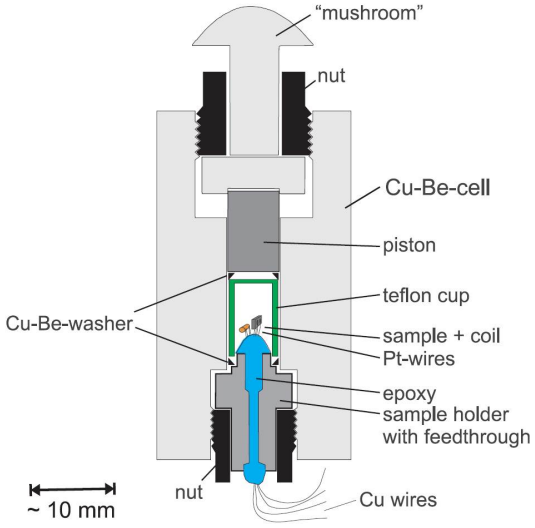

Figure 4.3: Schematic picture of a clamp pressure cell (taken from [36]).

For measurements in the dilution refrigerator all the parts (including the piston) were made of specially purified Be-Cu, with minimised paramagnetic impurities.

The pressure inside the cell is measured with a manganin coil. Manganin is suitable as a pressure gauge, because its resistance changes linearly with pressure. However, the dependence of 0.252%/kbar is not very high, resulting in a considerable pressure errror bar of about ± 150 bar. Additionally the manganin coil resistance tended to jump from time to time (especially at low temperatures). Therefore, the pressure was always checked by using sample properties if possible.

4.3 Equipment used for high field studies

For a number of experiments in this thesis high magnetic fields up to 15 T were necessary. This section introduces the available magnets and the compatible inserts and cooling systems.

4.3.1 Superconducting magnets

Two ^{4}He cooled superconducting magnet systems were available, which are able to apply a magnetic field of up to 14 T and 15 T respectively. The magnets also allow maximum fields of 16 T and 17 T, respectively, when the magnet coils are cooled to 2 K. This is achieved by reducing the pressure of the ^{4}He bath in the cryostats. However, due to the high helium consumption this option was rarely used. Apart from the difference in maximum field the magnets are constructed similar: They consist of two concentric coils. The outer one is made of NbTi and the inner one of Nb_3Sn. Additionally the magnets are equipped with a superconducting shunt. While sweeping the field this shunt is heated in order to become normal conducting so that the current is applied to the magnet coil. At

a constant field this shunt can be cooled to SC state to short circuit the magnet. Then the external current can be removed and the field becomes frozen inside the magnet, allowing experiments at constant field while having low helium consumption and a stable field. The external current was applied by different superconducting magnet power supplies. Most frequently used were the "Oxford IPS 120-10" and the "MercuryIPS" both produced by Oxford Instruments.

4.3.2 Cooling systems and temperature control

Control of temperature always is an important issue when performing measurements in a cryogenic environment. The lowest reachable temperature, the cooling power and the ability to control temperature are important. Depending on the temperature requirements of the respective experiments, one of the following cooling systems was chosen.

Thermometers and Heaters

In order to measure the temperature, mainly resistive Cernox and RuOx thermometers were used. The resistance of the thermometers was measured by a LakeShore Model 340 temperature controller or by AVS45/46 resistance bridges from Picowatt. Each of the used inserts was equipped with one or more heaters. Intelligent temperature control by the use of heaters was possible by using either the LakeShore 340 or directly from the computer using a self-written LabView program.

^{4}He-flow cryostat (variable temperature insert)

For temperatures down to 1.4 K a ^{4}He-flow cryostat, also called variable temperature insert (VTI) was used as sketched in Fig.4.4(a). The VTI consists of two coaxial tubes with some space between them that can be either evacuated or filled with exchange gas in order to optimize the thermal coupling of the sample space with the ^{4}He bath in the cryostat. On the bottom of the VTI a capillary with a very high impedance connects the sample space and the bath. When the inner space of the VTI is pumped, a small constant flow of helium enters the VTI through the capillary and cools the sample space. Between 1.4 and 4.2 K the temperature can be controlled by filling the sample space with liquid He and regulating the vapour pressure inside the VTI with a manostat. For temperatures above 4.2 K a regulated heater must be used to achieve a constant temperature.

^{3}He-evaporation cryostat

When temperatures lower than 1.4 K were required, a ^{3}He evaporation cryostat was used. A schematic drawing of the ^{3}He-system is shown in Fig. 4.4(b). With this system temperatures down to 0.4 K are possible. The ^{3}He-system consists of three concentric tubes. The space between the outer and the middle tube is the vacuum space. For operation of the ^{3}He-system it has to be well evacuated, otherwise the coupling to the ^{4}He bath at 4.2 K would cause too much heating in the sample space when going to

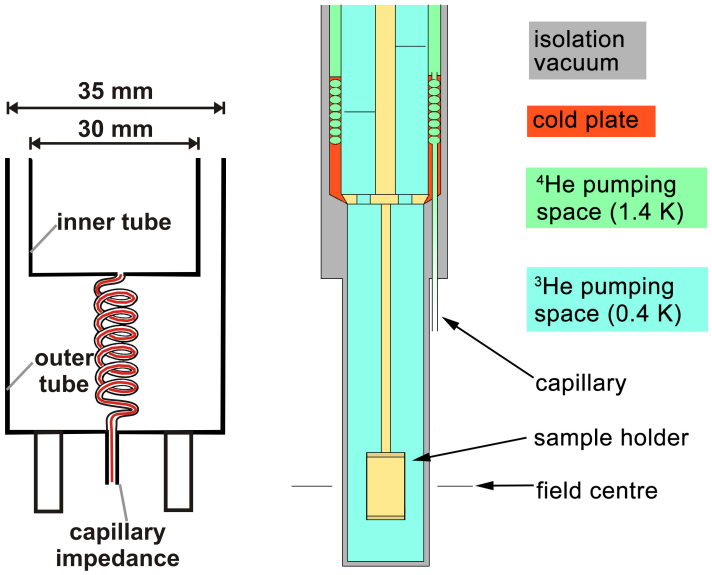

(a) (b)

Figure 4.4: (a) Schematic drawing of the lower part of the VTI with the impedance (taken from [130]). (b) Schematic drawing of the ^{3}He cryostat (taken from [131]).

lowest temperatures. The space between the middle and the inner tube is the ^{4}He-space. It is continuously pumped and is connected to the bath via a capillary that works the same way as the VTI described above. This space ends about 30 cm above the bottom of the sample space at a cold plate consisting of copper, which has a conical surface at the wall of the sample space. A fitting copper cone is mounted on each insert for the ^{3}He-system, coupling the ^{4}He-stage to the copper cold plate. At this place the ^{3}He condenses. This copper piece also works as a radiation shield and all the wires going down to the sample stage are thermally anchored there.

When now ^{3}He is introduced in the sample stage it is cooled down to 1.4 K. Therefore ^{3}He condenses until the corresponding gas pressure of about 50 mbar is reached. Afterward the ^{3}He is pumped out again cooling the environment down to 0.4 K at best. Constant temperatures in the range $0.4\,\mathrm{K} \leq T \leq 1.0\,\mathrm{K}$ can be achieved by regulating the valve at the entrance of the ^{3}He pump.

4.3.3 Two-axis rotator

As already mentioned, several measured effects are strongly dependent on the angle of the magnetic field. The above described magnets, however, are fixed solenoids, allowing only one field direction. In order to perform angle-dependent measurements a two-axis rotator built by D. Andres [36] was used. This insert allows changes of both θ and φ angles, as shown in the photograph in Fig.4.5. The platform of the rotator is turned by two worm-gear units. φ has to be rotated manually by introducing a screwdriver

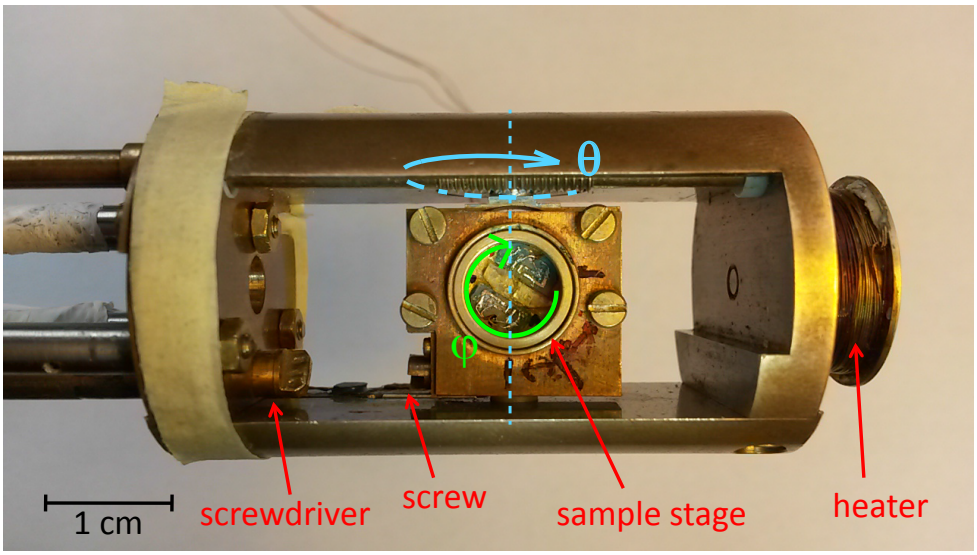

Figure 4.5: Photograph of the sample stage of the two-axis rotator (taken from [41]).

into the screw at the sample platform, at a fixed θ corresponding to the screw of the platform matching the screwdriver position. φ can be set to an accuracy of about $\pm 0.2°$. After setting φ the screwdriver has to be decoupled again. For a continuous θ rotation a piezomotor is utilized. The θ value can be calculated from the resistance of a 20 turn potentiometer coupled to the rotating rod at the top of the insert. The available θ-range is 240° and the angle accuracy of the rotator is $\pm 0.01°$ while rotating and drops to $\pm 0.4°$ while standing because of some relaxation in the mechanical gears. The sweep rate can be chosen between 0.1°/min and 50°/min.

4.4 Setup for very low temperatures

Many of the experiments performed in this thesis needed temperatures below 0.4 K (the lowest possible temperature for the ^{3}He insert). To this end a dilution refrigerator unit in combination with a 2D vector magnet was utilized. Both main components were not compatible with any of the above mentioned magnet and cooling systems.

4.4.1 Dilution refrigerator unit

The dilution refrigerator unit was originally built at the WMI by K. Neumaier. The insert containing the dilution refrigerator was built and wired by S. Jakob [38]. The gas-handling system containing the tanks, valves and the pump needed to run the dilution refrigerator was assembled by J. Geißmann. A schematic drawing of the dilution refrigerator insert is shown in Fig. 4.6(a).

In the steady state the dilution refrigerator works as follows: During its way through the dilution refrigerator unit the ^{3}He passes a spiral shaped heat exchanger (1) coupled with the ^{4}He bath, a Joule-Thomson heat exchanger (2) thermally coupled with the

main pumping line, a heat exchanger coupled with the distillation chamber (3) and a counterflow heat exchanger (4), where concentrated ^{3}He flowing to the mixing chamber and the diluted ^{3}He flowing from the mixing chamber to the distillation chamber are thermally coupled. The impedances at (A) and (B) are needed to enable Joule-Thomson cooling. The tubes connecting the chambers (in order to make the insert stable) are made of Degussit[1] (C), which has a low heat conductivity.

The mixing chamber itself is filled with a labyrinth of sintered copper (D) at the bottom to increase thermal coupling between the mixture and the bottom of the mixing chamber. In the mixing chamber the barrier layer between concentrated and diluted phases of ^{3}He is located. When the diluted phase is pumped in the distillation chamber mainly ^{3}He evaporates because it has a higher vapour pressure than ^{4}He. That decreases the amount of ^{3}He in the distillation chamber, resulting in a flow of ^{3}He from the mixing chamber into the distillation chamber. Now the diluted phase in the mixture lacks ^{3}He, which is replaced by ^{3}He from the concentrated phase. This dilution of ^{3}He costs energy and therefore the mixture as well as the mixing chamber is cooled down. At a constant temperature of 100 mK the dilution refrigerator provided a cooling power of about 5 μW.

4.4.2 Temperature control

For a reliable determination of temperature the dilution refrigerator is equipped with several thermometers. At mK temperatures mainly three RuOx thermometers were important. One was mounted on the mixing chamber. The other two were mounted on the ring, where the sample holder/pressure cell was screwed, and on the sample holder/pressure cell itself, respectively. With such a distribution of thermometers it was not only possible to determine the temperature in the sample space, but also to collect information about the thermal coupling between the different parts of the systems. This proved important because the coupling several times worsened considerably, either due to oxidisation of the copper parts or due to a slight loosening of the screws. In case of the former it was necessary to completely disassemble the parts below the mixing chamber and to deoxidise them with chemicals. In case of the latter only a re-tightening of the screws was needed. The thermometer resistances were generally measured with AVS 45/46 resistance bridges. These bridges can be set to very low measurement currents, which is necessary to prevent a self heating of the thermometers in a dilution refrigerator.

In addition, the mK stage of the dilution refrigerator was equipped with two heaters in order to control the temperature. One sitting on the ring and one on the bottom of the mixing chamber. The choice of which heater to use was made depending on the requirements of the given measurement. However, most of the time the mixing chamber heater proved to be the better choice due to the higher heat capacity of the mixing chamber and, therefore, a better controllable temperature. The current to the heaters was applied by a Keithley 220 Current Source. The regulation of the temperature by using thermometers and heaters was done by a LabView program originally built by S. Jakob [38] and further developed during this thesis.

[1] Degussit: sintered Al_2O_3 from Friatec AG, Mannheim

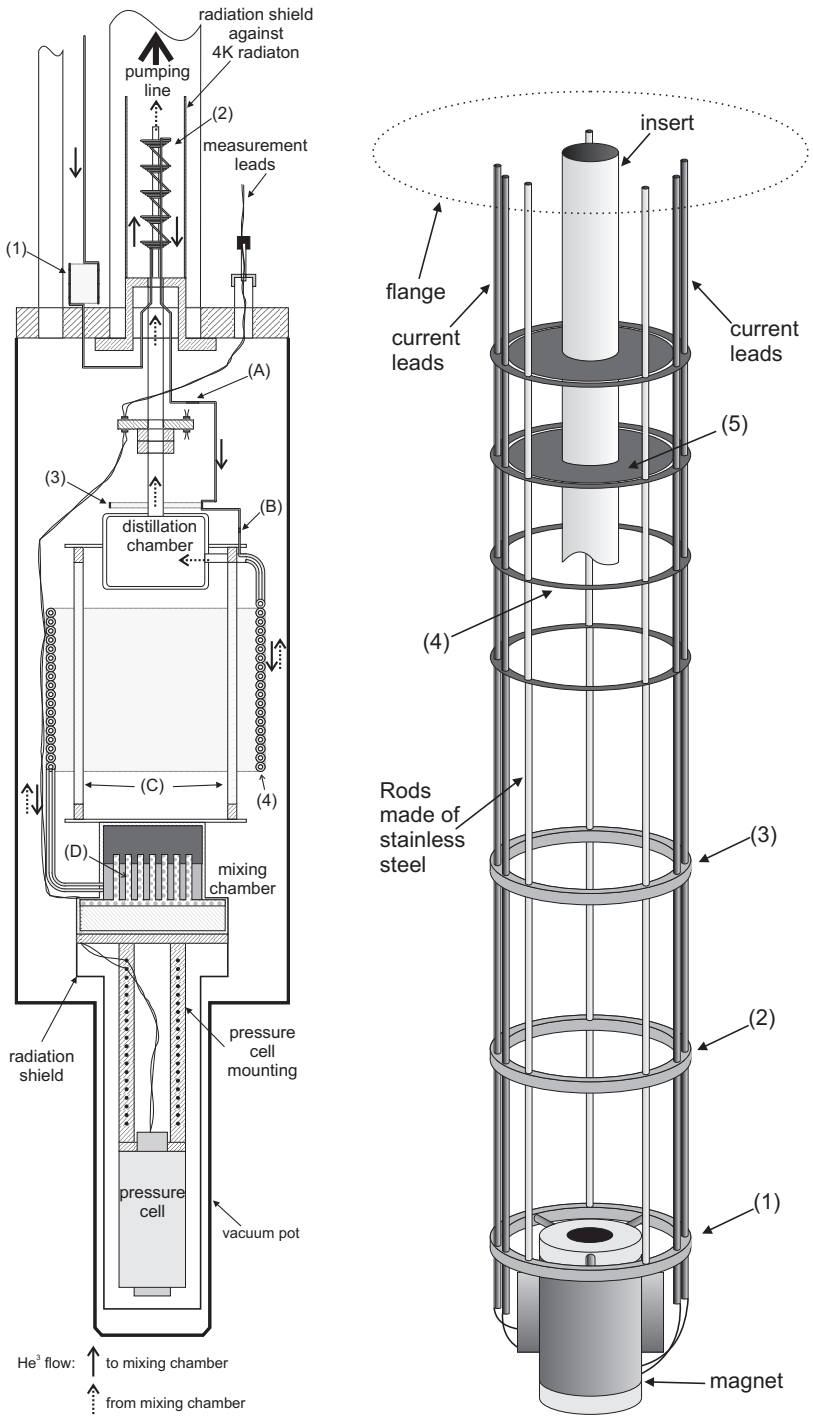

Figure 4.6: (a) Schematic drawing of the dilution refrigerator. Details are explained in the text. (b) Schematic drawing of the vector magnet insert. (both taken from [38])

4.4.3 2D vector magnet

Also in the dilution refrigerator setup, magnetic field orientation was a major topic. However, mechanical rotation in a dilution refrigerator is very difficult due to the low cooling power of the system. Therefore a superconducting 2D vector magnet was utilised. The magnet itself was built by G. Eska at the WMI, the insert containing the magnet was designed by S. Jakob [38]. A schematic picture of the magnet insert is shown in Fig. 4.6(b). The vector magnet consists of a main coil, which is a solenoid that is aligned vertically and has two correction coils on both ends, and a split pair arranged in horizontal direction. The vertical coil has an inner diameter of 38.5 mm and a field constant of 23.7 mT/A and can be used for fields up to 2 T. The horizontal coil has a field constant of 5.05 mT/A and can be used up to 0.44 T. The field constants were checked with a hall sensor during this thesis.

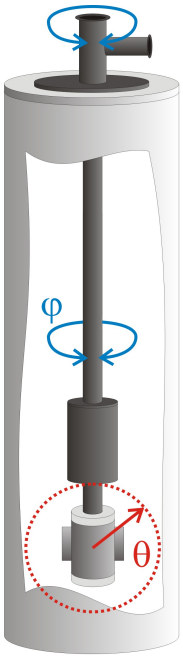

Figure 4.7: Schematic drawing of the cryostat with the vector magnet system. The red lines indicate the field rotation in a vertical plane using the 2D vector magnet. The blue arrows demonstrate the manual rotation of the dilution refrigerator insert inside the vector magnet, thus enabling a field rotation in all three dimensions.

These two coils can now be driven individually by two different magnet power supplies. The total field in the center of the magnet is then determined by vector addition of the two components. The angle of the magnetic field is determined by

$$\theta = \arctan\left(\frac{B_{\text{vertical}}}{B_{\text{horizontal}}}\right) \tag{4.3}$$

and the total field strength by

$$B_{\text{total}} = \sqrt{B^2_{\text{vertical}} + B^2_{\text{horizontal}}}. \tag{4.4}$$

Thereby, an angular resolution of up to 0.001° can be reached, depending on the resolution of the used magnet power supply. Conventionally the samples were placed in the cryostat with the conducting plane perpendicular to the vertical coil axis. In that case it was possible to make measurements at different φ angles, since the insert containing the vector magnet can be rotated with respect to the insert containing the dilution refrigerator. The principle is graphically explained in Fig. 4.7. This alters the direction of the horizontal field with respect to the sample.

A problem when using superconducting coils is remanent fields that can be frozen into the superconductor and stay there even when the applied magnet current is reduced to zero. Especially during the measurements of the α-MHg family this was a major issue due to the extremely low perpendicular critical fields, less than 1 mT in the most extremal case. Therefore, only tiny changes of the field angle caused by remanent fields were influencing the measurements.

To this end the remanent field was measured by perpendicular field sweeps after every few field or angle sweeps and compensated accordingly. The value of the remanent field was strongly dependent on the highest field applied in perpendicular direction in the preceding runs. As long as only low field experiments ($B_{\mathrm{vertical}} \leq 20\,\mathrm{mT}$) were performed, the remanent field usually was lower than 0.2 mT. After a sweep up to 1.8 T a remanent field of about 3 mT could be detected. With a freshly cooled magnet usually the earth magnetic field was detected. The remanent field in the horizontal direction was much less critical due to the much higher horizontal critical fields of the samples. For the measurements on the κ-(BETS)FeX_4 family the remanent field did not play a noticeable role.

Part II

Results and discussions

5 Highly anisotropic superconductivity in pressurised α-(BEDT-TTF)$_2$MHg(SCN)$_4$ (M = K, Tl)

Many of the properties studied within this thesis are strongly dependent on the quality of the measured samples. One sample of α-(BEDT-TTF)$_2$KHg(SCN)$_4$ (α-KHg), which is of extraordinary quality, had already been found. It is well characterised and was already used in a number of earlier works [36, 38, 132] and will be referred to as sample #1. In [132] another uncharacterised sample, from now on referred to as sample #2, was studied in dilution refrigerator but proved to be not of sufficient quality. Therefore, it was of great interest to make characterisation measurements on a number of samples in order to find the samples with the best quality. For α-MHg (M = K, Tl) it was also necessary to determine the orientation of the crystal axes.

For this reason an extensive characterisation of a large number of samples of both α-KHg and α-TlHg was performed. The results of the characterisation of the K-salt are presented in Appendix A.1. From the characterisation measurements only the sample labelled #8 was cooled down in the dilution refrigerator. The characterisation of the Tl-salt was executed jointly with L. Höhlein and can be found in [41].

5.1 Critical field anisotropy of α-(BEDT-TTF)$_2$KHg(SCN)$_4$ far above the critical pressure

Up to now the critical field anisotropy in α-KHg has only been studied slightly above the critical pressure of $p_c \approx 2.6\,\mathrm{kbar}$ [38, 133]. Some effect of pressure on the behaviour of the SC state could already be seen in the authors diploma thesis [132], where a pressure of $p = 3.4\,\mathrm{kbar}$ was applied and which we will include in the following presentation of the results. Results on the phase diagram for magnetic fields in out-of-plane and inplane direction have been reported in [133]. However, as both applied pressures of $p = 2.8\,\mathrm{kbar}$ and $3.4\,\mathrm{kbar}$ are rather close to the critical pressure, it remained an interesting point, how the system would behave far away from the critical pressure. To this end, a similar set of measurements was executed at a pressure of $p = 4.7\,\mathrm{kbar}$. This pressure was chosen, because it is the highest pressure, where the full SC transition in temperature was still accessible above the base temperature of our dilution refrigerator.

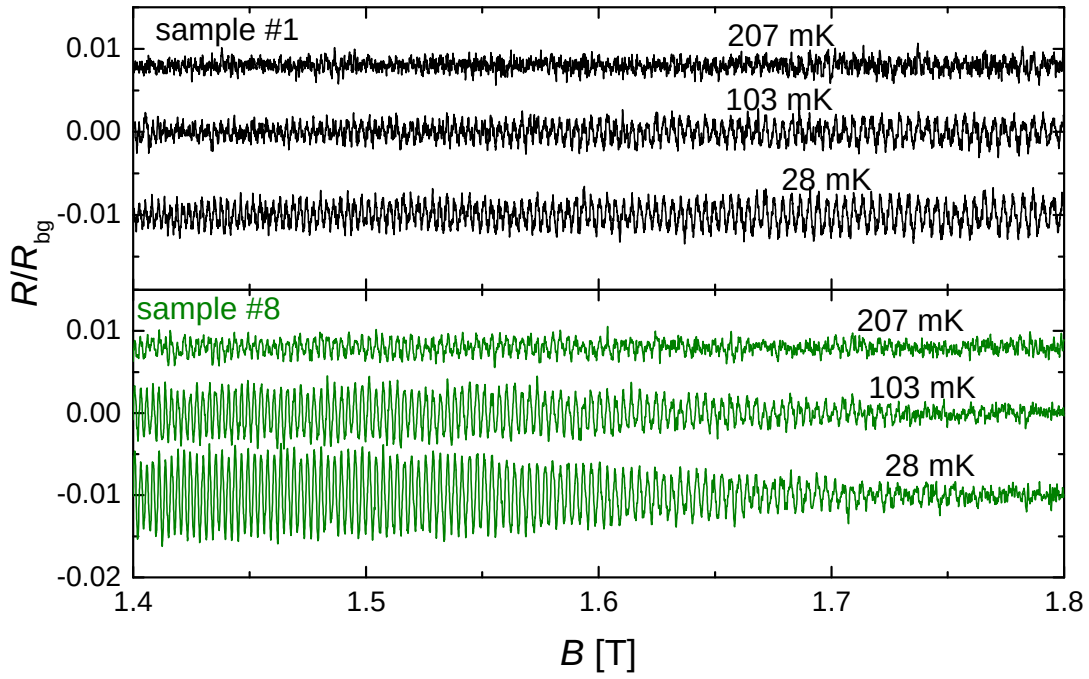

Figure 5.1: Oscillatory part of the resistance (normalised to the background resistance R_{bg}) as a function of the magnetic field at different temperatures. The curves are vertically offset for better visibility.

5.1.1 Evaluation of pressure from Shubnikov-de Haas (SdH) oscillations

During the measurement in the dilution refrigerator the SdH oscillations in the samples where studied. This was especially important, since the manganin coil used as pressure sensor during this experiment did not show a reasonable resistance value at low temperatures. Fortunately the pressure can be reliably determined from the frequency and cyclotron mass of the SdH oscillations. To this end field sweeps with magnetic field perpendicular to the conducting layers were performed at different temperatures in a field range between 1.2 T and 1.8 T. Some examples of such measurements are shown in Fig. 5.1 for both samples. In sample #8 the oscillations are somewhat stronger than in sample #1. Also it seems that sample #8 shows a node in the oscillations at, or slightly above $B = 1.8\,\mathrm{T}$. The appearance of such nodes in the presented compound have been reported before [134, 135].

The SdH frequencies were determined as $F = (750 \pm 2)\,\mathrm{T}$ for sample #1 and $F = (751 \pm 2)\,\mathrm{T}$ for #8. Because the SdH frequency changes linearly with pressure in the present compound [36, 132] we can estimate the pressure from the frequency to a value of $p = (4.7 \pm 0.1)\,\mathrm{kbar}$. The cyclotron mass was estimated from the temperature dependence of the SdH amplitude in the field range of $1.2\,\mathrm{T} < B < 1.8\,\mathrm{T}$ by fitting with the formula for the temperature damping factor Eq. (2.11). The exact procedure is thoroughly described for κ-FeCl in Sec. 6.1.2. We obtain a value of $m_c = (1.77 \pm 0.1)\,m_e$ for sample #1 and $m_c = (1.79 \pm 0.1)\,m_e$ for #8. When looking at the former data

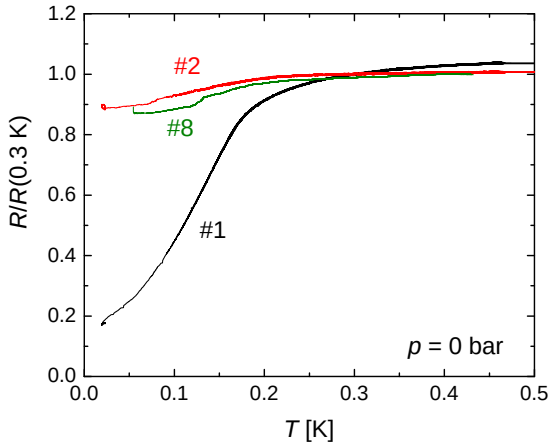

Figure 5.2: Low temperature resistance behaviour of several samples of α-KHg. The resistances have been normalised to the respective values at $T = 300\,\mathrm{mK}$.

[132], this suggests a pressure in the range between 4.5 kbar and 5 kbar and is, therefore, consistent with the value estimated from the frequency. This pressure estimate is also consistent with the ambient temperature pressure and the T_c.

5.1.2 Superconducting transition

Even though the methods described above are used to select high quality samples, still a strong sample dependence of the SC state of α-KHg is observed, both in the inhomogeneous SC state at ambient pressure and under high pressure, where the CDW state is already suppressed. Therefore, let us first look at some SC transitions of different samples at different pressures: A sample dependence of the 0 bar SC state in this compound was already reported by Andres *et al.* [27]. Figure 5.2 shows the low temperature resistance behaviour of three different samples of α-KHg. The resistances have been normalised to the resistance values at $T = 0.3\,\mathrm{K}$. We can see that the SC state is clearly most pronounced in sample #1. Samples #2 and #8 are very similar to each other. This strong sample dependence is a result of the inhomogeneous superconductivity in the CDW state, where impurities and defects have a very big effect [27].

The strong sample dependence of the SC state, however, is also observed at pressures above the critical value of $p_c \approx 2.6\,\mathrm{kbar}$. In Fig. 5.3 we see the SC transition of the same three samples under pressure. Samples #2 and #8 were never measured at the same pressure. Therefore, two graphs with different pressures are shown. Sample #1 was present in both measurement runs and its transition shows roughly the same shape for both pressures. Both other samples have a lower T_c respectively compared to sample #1. Sample #2 has a much broader transition, mainly due to the fact that the transition consists of two different slopes. On sample #8 the transition starts very sharp, but has a second step at a resistance of about 40% of the normal state resistance.

At this pressure the sample difference can no longer be explained by the influence of the CDW state as it is already fully suppressed. One possible explanation is an

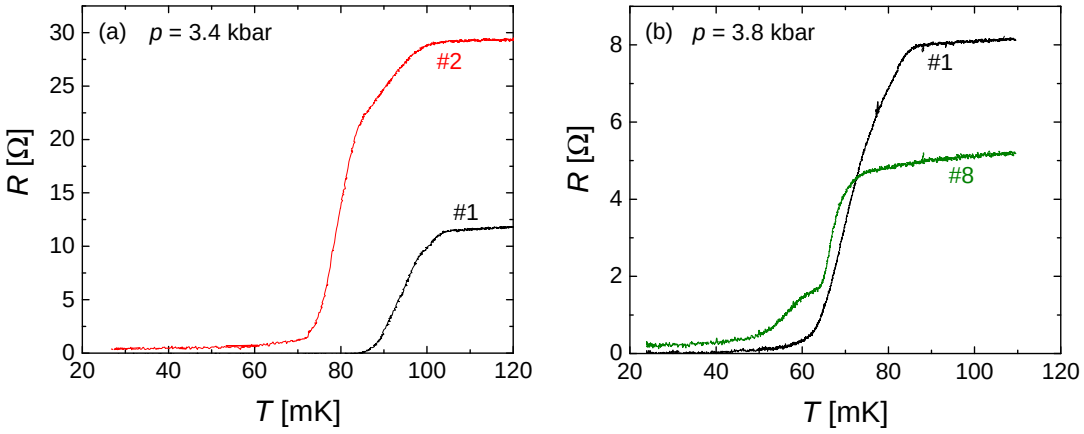

Figure 5.3: Comparison of the shape of the SC transition of different samples under pressure of (a) $p = 3.4\,\mathrm{kbar}$ and (b) $p = 3.8\,\mathrm{kbar}$.

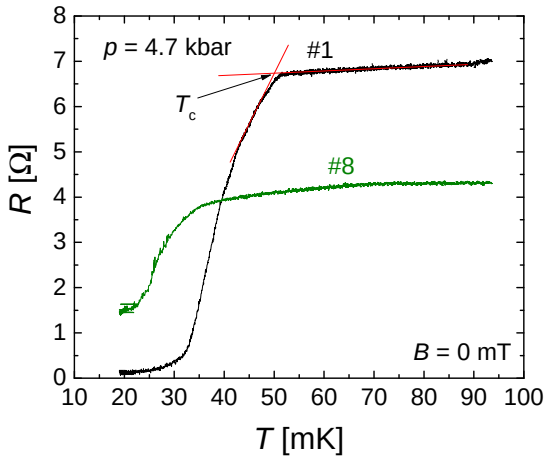

Figure 5.4: The low temperature part of the $R(T)$ of α-KHg at $p = 4.7\,\mathrm{kbar}$ featuring the SC transition. The red lines show the construction used to determine the value of T_c.

unconventional kind of superconductivity with nodes in the energy gap, where Anderson's theorem [77] is not valid and also non-magnetic impurities have a big impact on the SC state [79]. Another possible explanation is that internal strains are responsible for the strong differences in the superconducting transition: We know that hydrostatic pressure reduces T_c with $\sim 30\,\mathrm{mK/kbar}$. Additionally, depending on the direction, uniaxial strain may have an even bigger effect. Further, the idea of internal strain being responsible for the reduced T_cs in samples #2 and #8 also offers a possible explanation for the double feature observed in the transition of sample #8, in the case that the strain is not constant over whole sample volume. A similar strong sample dependence was also observed in the SC state of κ-FeBr and will be discussed in Sec. 6.2.3.

At $p = 4.7\,\mathrm{kbar}$ the SC transition starts at a temperature of about 50 mK as can be

seen in Fig. 5.4 for sample #1. We immediately see that the T_c for sample #8 is at an even lower temperature. In addition, the resistance in sample #8 does not even drop completely to zero (probably the second step, seen in Fig. 5.3(b) at 3.8 kbar is lower than our lowest temperature). As discussed above this can be either a result of lower purity or internal strains. The low T_c and incomplete transition make a determination of the critical field anisotropy for this sample unreliable. For this reason we will only refer to sample #1 in the following.

The red lines in Fig. 5.4 indicate the construction used to determine the value of the critical temperature T_c. This criterion, which we will refer to as the upper construction, was used for most of the determinations of T_c and B_{c2} in the following. The transition width defined as the temperature range, where the sample resistance is between 10% and 90% of the normal state resistance, for sample #1 was determined as $\Delta T_c = 14\,\mathrm{mK}$, which is slightly higher than in earlier measurements at lower pressure [38, 132].

In general, a determination of T_c from resistance measurements is not always fully straightforward. This is due to the fact that the measured resistance may already become finite within the SC state because of the existence of vortex motion and fluctuations. However, in the present compound the T_c is so low that the influence of flux motion and fluctuations should be weak. Additionally, some of the dependencies were verified by using the transition midpoint. For sweeps, where a zero resistance is still observed, a good consistency was found. We, therefore, assume that we can reliably determine T_c and B_{c2} this way. However, for sweeps without a zero resistance (field sweeps at temperatures close to T_c and temperature sweeps close to B_{c2}) the transition midpoint could not be reliably used any more. Therefore, for the rest of this thesis we will use the transition points determined by the "upper construction".

We can now compare $T_c(p = 4.7\,\mathrm{kbar})$ with the T_c values at lower pressures. In

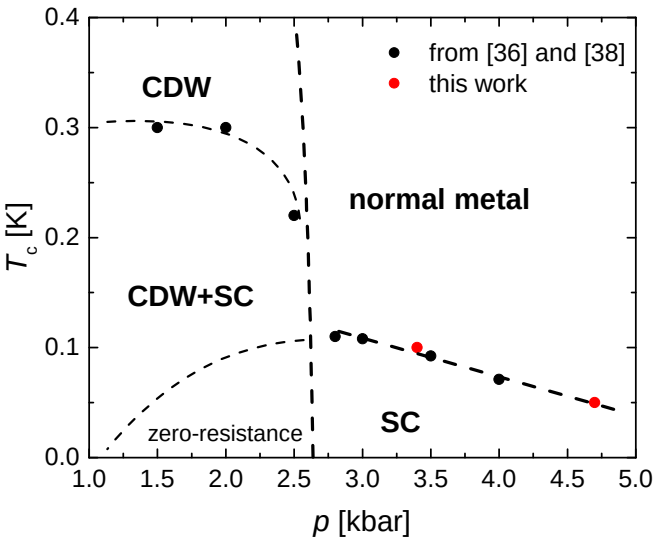

Figure 5.5: The T-p phase diagram of α-KHg from [36] and [38] (black symbols) and the present studies (red symbols).

Fig. 5.5 the phase diagram obtained by D. Andres [36] and S. Jakob [38] (black dots) is plotted including the points from the the present experiment represented by red dots. As we can see, for the new pressures the estimated T_c fits perfectly into the extrapolated dependence of $T_c(p)$, also at $p = 4.7\,\mathrm{kbar}$. This means we can confirm that $T_c(p)$ drops linearly with $\mathrm{d}T_c/\mathrm{d}p = -30\,\mathrm{mK}$ as reported by Andres *et al.* [27].

5.1.3 Critical field perpendicular to the conducting layers

First the B-T phase diagram for fields applied perpendicular to the conducting layers was determined. To this end a number of temperature sweeps at different constant fields and field sweeps at different constant temperatures were executed. Some examples can be seen in Fig. 5.6. Because of the extremely low critical fields in this direction the field was swept in both negative and positive directions to eliminate any influence of additional fields from outside or from remanent fields in the magnet (see Sec. 4.4.3). In Fig. 5.6(a) we can see that the minimum of the resistance is slightly shifted to the negative side by $\Delta B = 0.05\,\mathrm{mT}$. Since the magnet was freshly cooled right before executing these sweeps and since the value and direction are approximately correct, we associate this shift to the earth magnetic field, which is maybe slightly enhanced by the steel reinforcements in the floor. When recording the temperature sweeps in Fig. 5.6(b) the earth magnetic field was compensated by applying an antiparallel field in the magnet.

Figure 5.7 shows the field and temperature behaviour of the SC state. The empty and filled symbols were obtained by field and temperature sweeps, respectively. In general the phase line mainly shows a roughly linear behaviour. This is expected, since for this field direction only the orbital pair breaking mechanism plays a role [80, 81] and this linear behaviour was already observed at lower pressures [36, 38].

When we extrapolate the $B_{c2}(T)$ dependence to $T = 0\,\mathrm{K}$, we can calculate the

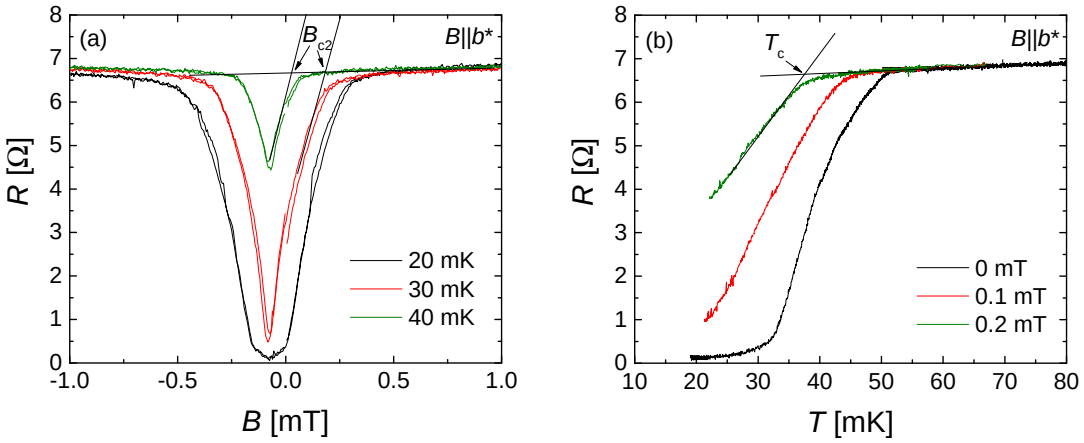

Figure 5.6: (a) Field sweeps at different temperatures and (b) temperature sweeps at different fields for $B \| b^*$. The lines show the construction used in order to determine the critical field and temperature.

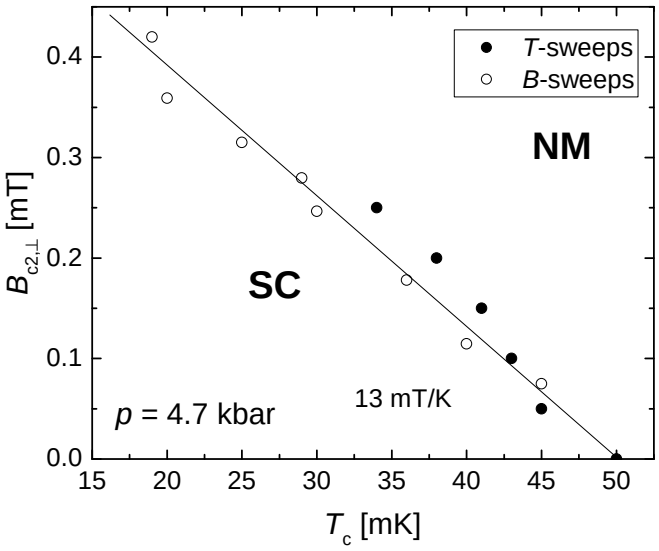

Figure 5.7: B-T phase diagram for $B\|b^*$. The empty and filled symbols indicate points obtained from field and temperature sweeps respectively.

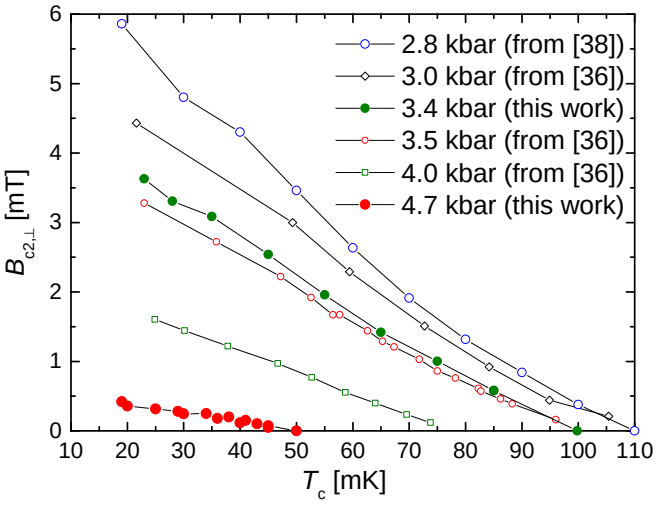

Figure 5.8: SC phase diagram for $B\|b^*$ for several different pressures. The phase diagrams at other pressures were measured in [36, 38].

Ginzburg-Landau coherence length parallel to the layers. A linear extrapolation of the phase boundary line yields a value of 0.65 mT at 0 K. Using the GL formula Eq. (2.41) we get

$$\xi_{\|,0}(avg) = \sqrt{\frac{\Phi_0}{2\pi B_{c2,\perp}(0)}} \approx 710\,\text{nm}. \tag{5.1}$$

Note that this value is an average over all directions φ within the conducting layers. But since there is a φ-dependence of $\xi_{\|,0}$, we also have to look at $B\|ac$-plane to calculate a

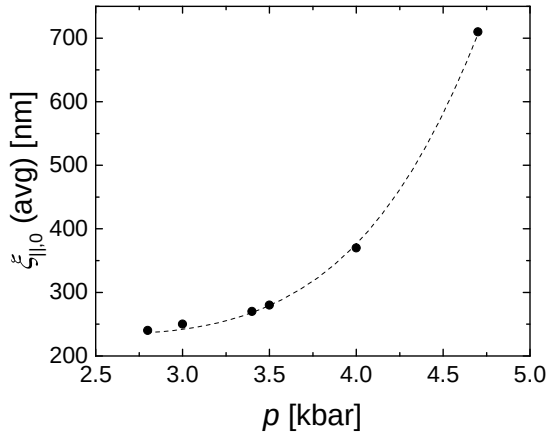

Figure 5.9: The average inplane coherence length as a function of pressure. The points were taken from the dependencies in Fig. 5.8.

distinct $\xi_{\parallel,0}(\varphi)$. If we compare this value of the coherence length with the BCS value, which is only depending on T_c as expressed in Eq. (2.37), yielding $\xi_0 = 2740\,\mathrm{nm}$, we see that $\xi_\parallel$ is significantly smaller. This means that $B_{c2,\perp}(0)$ is higher than we would expect from T_c according to the BCS theory. Perpendicular critical fields, which are higher than predicted from BCS theory have also been observed in many other organic superconductors [6]. However, it is by far the highest in the present compound, which is probably a sign of high electron correlation effects.

To get a better idea about the meaning of this values let us compare these results with lower pressures: Figure 5.8 shows the phase diagram for $B\|b^*$ at $p = 4.7\,\mathrm{kbar}$ in comparison to several lower pressures. As expected not only T_c but also the slope $\mathrm{d}B_{c2,\perp}/\mathrm{d}T$ decreases with increasing pressure. In Fig. 5.9 a pressure dependence of the inplane coherence length is plotted. As we can see, the coherence length grows with increasing pressure with what looks almost like an exponential dependence. A comparison of $\xi_\parallel$ with T_c instead of p still yields a more than linear dependence. Therefore, the difference of $\xi_\parallel$ and the BCS ξ_0 becomes smaller with increasing pressure. Perhaps, this indicates that the behaviour of SC state becomes more conventional at higher pressure, which can be a result of reduced correlation effects.

5.1.4 φ-dependence of the inplane critical field

When applying fields parallel to the conducting layers, we can observe that α-KHg shows a significant inplane anisotropy. Our earlier measurements [132] already showed that this anisotropy is different, when comparing ambient and overcritical pressure. The most recent experiment now yields information about the behaviour far above the critical pressure.

For the determination of the φ anisotropy a number of θ-sweeps in a small angular range around the inplane field orientation at different φ were performed. Due to the very strong polar anisotropy the critical field is much higher for fields parallel to the conducting layers, resulting in resistance dips for fields around the parallel orientation.

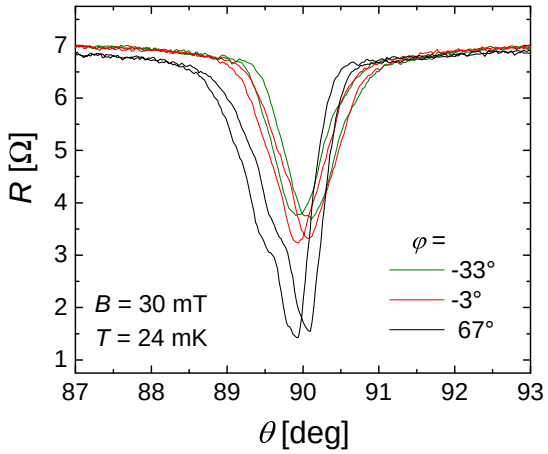

Figure 5.10: (a) Angular sweeps at different azimuthal orientaions of φ at $B = 30\,\mathrm{mT}$ and $T = 24\,\mathrm{mK}$.

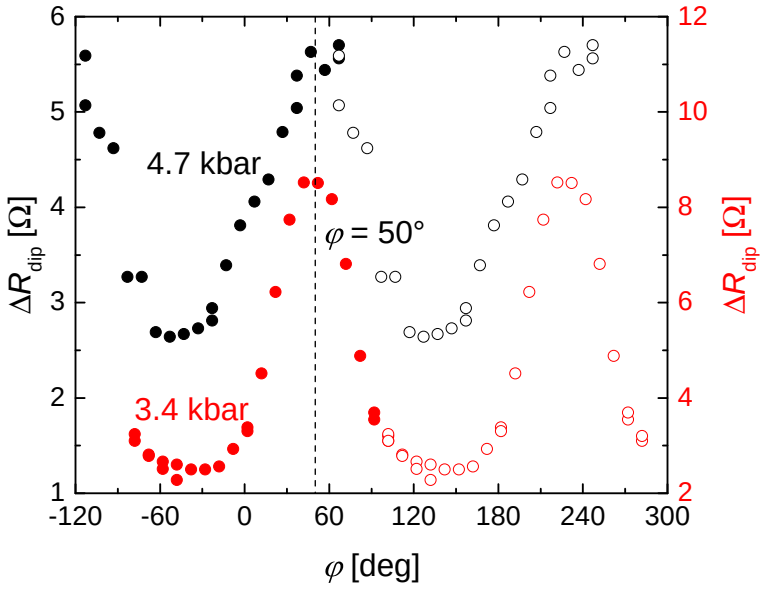

Figure 5.11: φ-dependence of the depth of the resistance dip at $B\|ac$-plane. The depth of the dips has been calculated as $\Delta R_{\mathrm{dip}} = R(\theta = 93°) - R(\theta = 90°)$. The 3.4 kbar data was alredy presented in [132]. The empty symbols are the same data as the filled symbols translated by 180° for better visibility.

The field and temperature were chosen in a way that these resistance dips at parallel orientation have a minimum resistance value of $\sim 20\%$ of the normal state resistance for the φ with the strongest superconductivity. This way the difference in the depth of the dip between the different φ becomes maximum. Some examples of such angular sweeps are shown in Fig. 5.10. From these angular sweeps we can now determine the depth of the dip ΔR_{dip} by subtracting the resistance value at the bottom of the dip from the

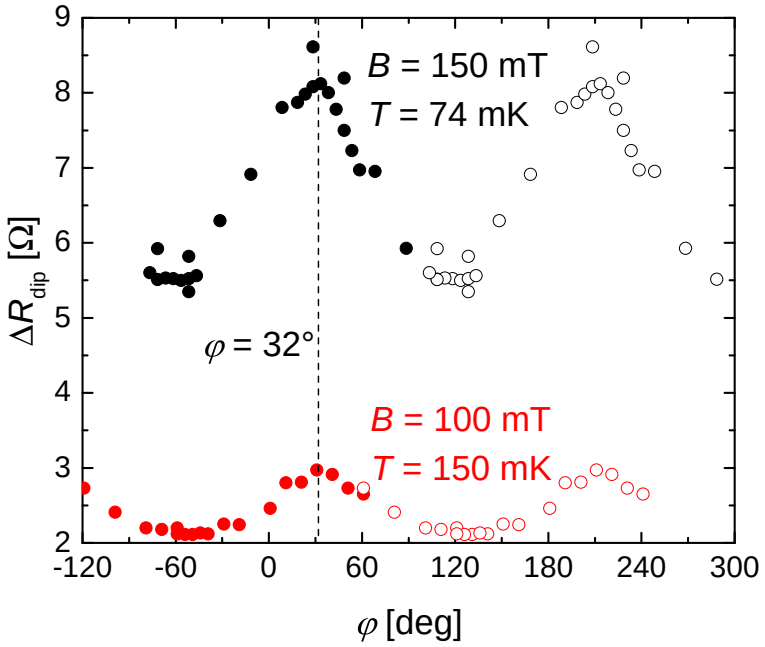

Figure 5.12: The depth of the SC dips at $B \| ac$ at $p = 0\,\text{kbar}$ calculated as $\Delta R_{\text{dip}} = R(\theta = 93°) - R(\theta = 90°)$. The black data was already shown in [132]. The empty symbols are the same data as the filled symbols translated by 180° for better visibility.

normal state resistance. For the normal state resistance we used the resistance value with $\theta = 93°$. The resulting $\Delta R_{\text{dip}} = R(\theta = 93°) - R(\theta = 90°)$ is plotted in Fig. 5.11 (black dots). The red dots show a similar set of data at 3.4 kbar.

Of course, the dependence in Fig. 5.11 is not exactly a φ-dependence of the critical field. However, the comparison of ΔR_{dip} with the real $B_{c2,\|}(\varphi)$ in [132] shows that we get a correct estimation of the qualitative change of $B_{c2,\|}(\varphi)$ this way. The symmetry of the φ-dependence is twofold like at the lower pressures. Since we would generally expect a four-fold symmetry for a d-wave superconductor, we cannot give a clear answer about the electrons system responsible for the formation of the SC state.

When we compare the two different pressures in Fig. 5.11 both qualitatively show a similar dependence. For $p = 3.4\,\text{kbar}$ we estimate the maximum SC at $\varphi = 50° \pm 5°$, while for $p = 4.7\,\text{kbar}$ the maximum is not so clear. The strongest SC was measured at $\varphi = 67° \pm 10°$ but the curve still looks more symmetric to $\varphi = 50°$. Since there also is some scattering of the points, we can not clearly say whether there is a φ-shift of the strongest SC between the different pressures. (The measurements at $p = 2.8\,\text{kbar}$ from [38] are not shown, because they yielded the same qualitative $B_{\text{c2},\|}(\varphi)$ dependence as at $p = 3.4\,\text{kbar}$.)

We can now compare the high pressure data with ambient pressure, where we only have the inhomogeneous filamentary SC state inside the CDW state. A similar φ-dependence of the depth of the SC dip for ambient pressure is shown in Fig. 5.12 for two different values of temperature and magnetic field. This was done in order to check,

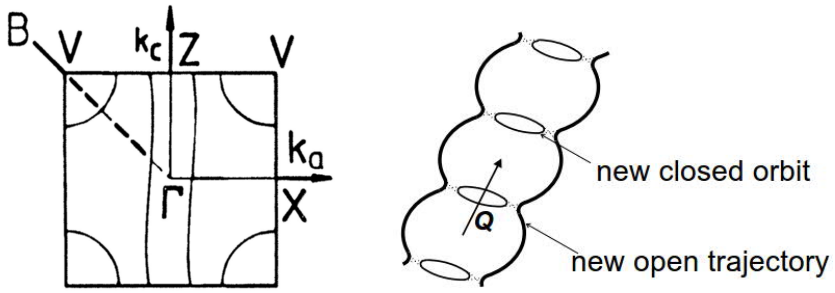

(a) (b)

Figure 5.13: (a) The basic (from [105]) and (b) the reconstructed (from [36]) FS of α-KHg.

whether there are in fact different SC subsystems with different parameters contributing to the reduction in resistance. (This is something one could think of in such an inhomogeneous state, where the SC is only formed spatially separated because of the CDW state.) The comparison of the black and the red curve shows us that the φ of the strongest SC is not dependent on the value of temperature and magnetic field. Therefore, it seems unlikely that there are different separated SC subsystems with different parameters. The position of the highest SC at this pressure is at $\varphi = 32° \pm 5°$. This φ is significantly different from what we observe at higher pressures. This suggests that due to the FS reconstruction different electron systems are responsible for the formation of the SC state within the CDW state as compared to the normal metallic state.

We can now compare these φ-dependencies with the FS shape, which is plotted in Fig. 5.13. For the q1D electron system we would naively expect a highest critical field for B applied parallel to the direction of the high conductivity, since for that direction the shielding currents should be most strongly suppressed. In our case this would be along c for the high pressure case and along $\mathbf{Q}$ for the ambient pressure case. Obviously, this condition is met for neither of the cases. For the elliptical part of the FS the direction of strongest superconductivity could probably be expected for a field parallel to the long semiaxis of the ellipse, since for this direction the electron momentum along the field direction is highest. But the direction of the long semiaxes lies at $\varphi \approx 80°$ and, therefore, also does not fit the observed anisotropy.

While the observed anisotropy in both the ambient and high pressure states does not seem to aligned along any distinct axis of the electrons system, we note that the φ value of the strongest SC changes by $\approx 20°$, upon the transition of the CDW to the NM state. This is about the same margin as the change of the direction of the q1D FS sheets, suggesting that there is some connection of these open FS sheets and the formation of the SC state. Maybe a more clear answer on that question can be obtained by further studies of the azimuthal anisotropy at pressures slightly below the critical pressure.

5.1.5 SC phase diagram for magnetic fields in inplane direction

Because of the extremely low perpendicular critical field and, therefore, very high sensitivity of the SC state to the exact field orientation close to parallel, an exact determination of the misorientation of the sample is necessary. This can be done with the use of similar angular sweeps around parallel orientation like the ones presented in the previous section. Figure 5.14 explains the method how the parallel orientation was determined from such angular sweeps: We estimate the center of the dip for up- and down-sweep, respectively. The average of these two values was taken as parallel orientation.

For parallel orientation the SC phase diagram was determined at two different azimuthal angles: Once at $\varphi = 67°$, where we saw the highest $B_{c2,\parallel}$, and once at $\varphi = -35°$ with a relatively low $B_{c2,\parallel}$ (as can be seen in Fig. 5.11). In Fig. 5.15 some examples of field and temperature sweeps at different temperatures and fields for the two φ values

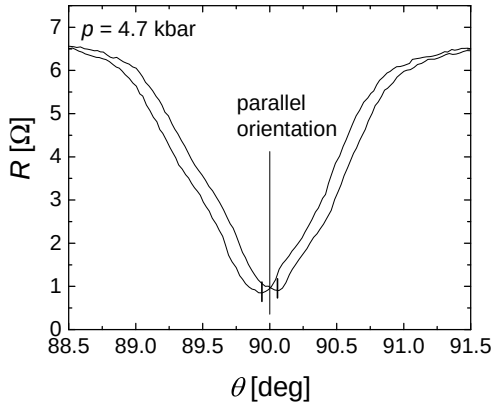

Figure 5.14: Construction used to determine the exact orientation of the magnetic field parallel to the layers. Due the sweep direction induced shift of the curves the average value of up- and down-sweeps is taken.

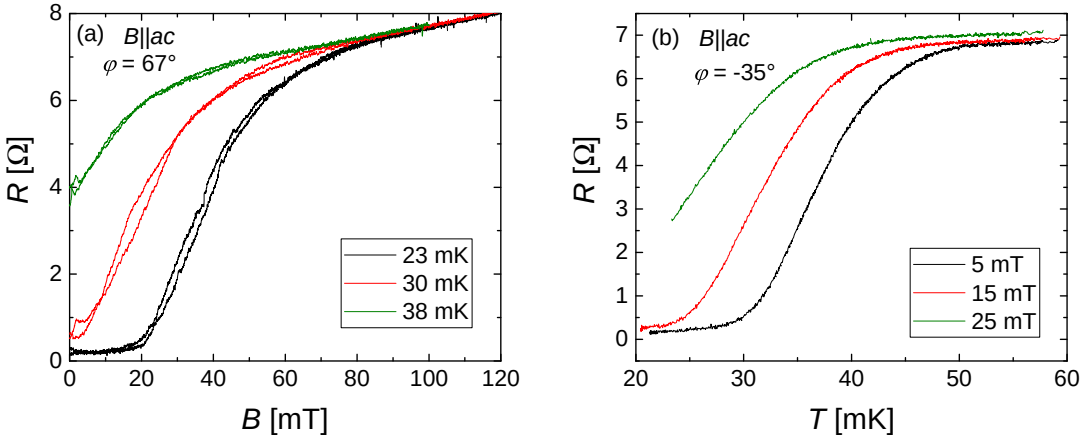

Figure 5.15: (a) Field sweeps at different temperatures and (b) temperature sweeps at different fields for $B \| ac$. The sets were taken at different azimuthal angles φ.

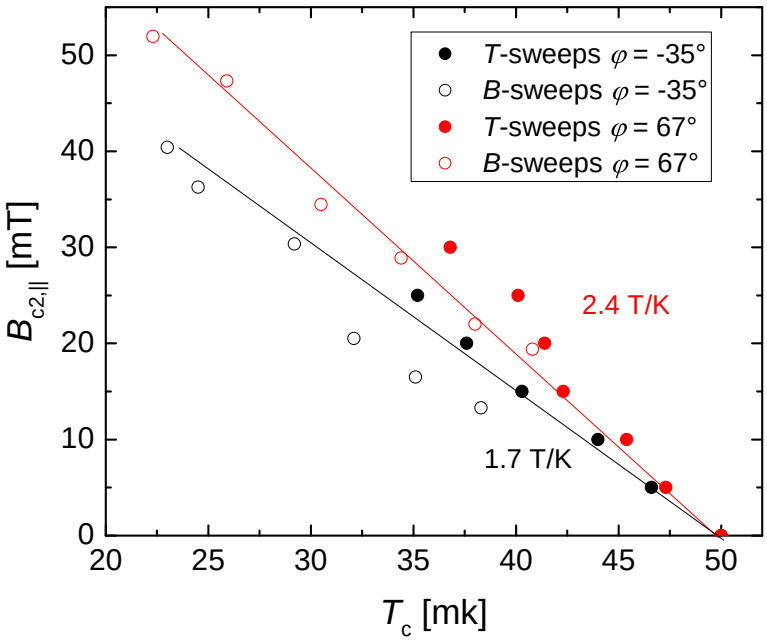

Figure 5.16: SC phase diagram for $B\|ac$-plane at two different values of φ. The filled and empty symbols indicate data from temperature and field sweeps, respectively.

are shown. In the field sweeps in Fig. 5.15(a) it immediately becomes obvious that the critical fields are significantly higher than for perpendicular orientation. We can also see some irregular hysteresis in the curves (especially in the red curve), which is a result of magnet current and sweep direction dependent overheating caused by the magnet power supply used for the horizontal coil. The temperature sweeps shown in Fig. 5.15(b) look more smooth, because the problem with the power supply only exists while the field is sweeping.

Figure 5.16 shows the SC phase diagram for magnetic field parallel to the layers, for the two described φ orientations. For both φ we see that there is no very good consistency between the field and temperature sweep data, which is probably caused the relatively broad transition curves for $B\|ac$ and by the overheating mentioned above.

The temperature dependences of the critical field for both φ in Fig. 5.16 within our accuracy look linear in the whole studied temperature range. This suggests that at this pressure the SC state is only orbitally limited down to the lowest accessible temperature even for the φ with the higher SC. From the slopes near T_c we can calculate the perpendicular coherence length using Eq. (2.42) obtaining

$$\xi_{\perp,0} = \frac{\Phi_0}{2\pi\xi_{\parallel,0}(dB_{c2,\parallel}/dT)T_c(0)} \approx 3.9\,\mathrm{nm} \tag{5.2}$$

for $\varphi = 67°$ and

$$\xi_{\perp,0} \approx 5.4\,\mathrm{nm} \tag{5.3}$$

for $\varphi = -35°$. In fact there can only be one unique value of $\xi_{\perp,0}$. The reason for the two different values lies in the φ-dependeince of $\xi_{\parallel,0}$. The true value of $\xi_{\perp,0}$ most likely

is the average of the above values:

$$\xi_{\perp,0} \approx 4.7\,\mathrm{nm}. \tag{5.4}$$

This allows us to recalculate the φ-dependent values of $\xi_{\parallel,0}$, which should follow the relation:

$$\frac{\xi_{\parallel,0}(\varphi = 67°)}{\xi_{\parallel,0}(\varphi = -35°)} = \frac{\xi^*_{\perp,0}(\varphi = 67°)}{\xi^*_{\perp,0}(\varphi = -35°)}, \tag{5.5}$$

since the φ-dependence of $\xi_{\parallel,0}$ must be linearly reflected in the apparent φ-dependence of $\xi_{\parallel,0}$. The resulting φ-dependent values of $\xi_{\parallel,0}$ then are

$$\xi_{\parallel,0}(\varphi = 67°) \approx 595\,\mathrm{nm} \tag{5.6}$$

and

$$\xi_{\parallel,0}(\varphi = -35°) \approx 824\,\mathrm{nm}. \tag{5.7}$$

The value of $\xi_{\perp,0} \approx 3.1\,\mathrm{nm}$ is about $1.5 \cdot d$, meaning that the SC state is already rather in the 3D limit.

Knowing the coherence lengths along the different directions we can now calculate the anisotropy parameter

$$\gamma = \frac{\xi_{\parallel,0}(-35°)}{\xi_{\perp,0}} = 127 \tag{5.8}$$

and

$$\gamma = \frac{\xi_{\parallel,0}(67°)}{\xi_{\perp,0}} = 177. \tag{5.9}$$

yielding rather similar values than for the lower pressures, where for $p = 3.4\,\mathrm{kbar}$ $\gamma(-28°) = 111$ is even slightly lower and $\gamma(52°) = 200$ is somewhat higher than at 4.7 kbar. This is a bit surprising, since we would expect a higher three-dimensionality at such high pressures due to the stronger interlayer overlap, revealing itself in a decrease of the anisotropy. But obviously the increase of the coherence length in intralayer direction almost equals the one in interlayer direction. Another idea might be that for the lower pressures already close to T_c some contribution of the paramagnetic pair-breaking is observed, reducing the apparent anisotropy.

We can now again compare the results with those obtained at lower pressures. Figure 5.17(a) shows the parallel phase diagram at the φ with the strongest superconductivity for the three different pressures studied so far. Here it becomes especially clear how strongly the SC state is already suppressed at $p = 4.7\,\mathrm{kbar}$. For a better comparison of the curves, we have normalised the data to the respective values of the critical temperature and the Chandrasekhar-Clogston (CC) limit (calculated using Eq. (2.50)). The results are shown in Fig. 5.17(b). Here we can clearly see that the slope of the transition line close to T_c monotonically decreases with increasing pressure. From this normalisation it also becomes apparent, why we hardly see any influence of the paramagnetic pair breaking at 4.7 kbar, since the critical field at lowest temperature still stays significantly below the CC-limit.

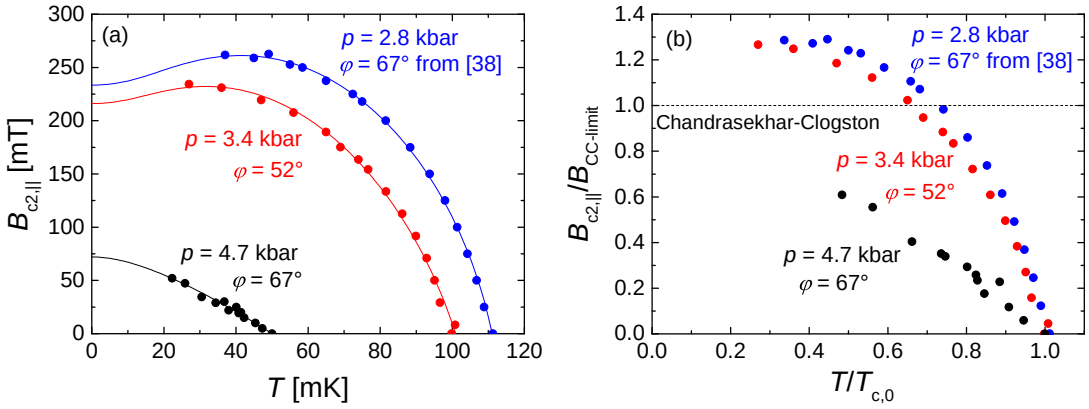

Figure 5.17: (a) The SC phase diagram for $\varphi = 67°$ (the φ with the strongest superconductivity) for the three different overcritical pressures studied so far (the 2.8 kbar data is from [38]). The lines are fits to the dependence in order to determine the Maki-parameter α. (b) The same data as in (a) normalised to the respective values of T_c and the Chandrasekhar-Clogston limit.

The lines in Fig. 5.17(a) are fits to the phase diagrams in order to determine the Maki-parameter α by the following formula [136]:

$$\ln\left(\frac{T_c}{T}\right) = \mathrm{Re}\left[\Psi\left(\frac{1}{2} + \frac{1}{7.12}\frac{T_c}{T}\frac{H_{c2}}{H_{c2}^{\mathrm{orb}}(0)}(1 + i\alpha)\right) - \Psi\left(\frac{1}{2}\right)\right], \qquad (5.10)$$

where Ψ is the digamma function and i is the complex number. The results for the three pressures are summarised in Table 5.1. From the pressure dependence of α it becomes

p [kbar]	$\frac{\mathrm{d}B_{c2,\parallel}(T)}{\mathrm{d}T}\vert_{T_c}$ [T/K]	T_c [mK]	$H_{c2}^{\mathrm{orb}}(0)$ [mT]	α
2.8	10.2	111 ± 0.4	1260 ± 70	5.2 ± 0.4
3.4	8.0	101 ± 0.5	740 ± 40	3.3 ± 0.3
4.7	2.4	50 ± 1	74 ± 9	0.2 ± 1.2

Table 5.1: The slope close to T_c and the fitted values of the critical temperature T_c, the orbital critical field H_{c2}^{orb} and the Maki-parameter α from the fits in Fig. 5.17(a) with Eq. (5.10) for the different pressures.

clear that the influence of the paramagnetic pair-breaking becomes reduced strongly under increasing pressure: already at 3.4 kbar α is reduced by almost a factor of 2. At 4.7 kbar α is almost zero verifying that indeed there is no longer any influence from the paramagnetic pair-breaking observed at this pressure.

For 2.8 kbar and 3.4 kbar the Maki-parameter is sufficiently high to satisfy the conditions for the observation of a Fulde-Ferrel-Larkin-Ovchinnikov (FFLO) state [89, 90] as described in Sec 2.3.2. However, no indication for a FFLO state was detected in our data. One possible reason for this is that our system is not in a sufficiently clean limit of the superconducting state, as we will discuss in Sec. 5.2. Another possible option is that

our lowest accessible temperatures during the parallel field measurements of $\sim 0.3\,T_c$ were not sufficiently low for the FFLO state to appear. But we also have to take into account that it is difficult to detect a FFLO state in resistive measurements.

5.1.6 θ-sweeps near parallel orientation

When looking at the θ-sweeps used for the determination of the azimuthal anisotropy of superconductivity (Fig. 5.10), we can see that some of them are very symmetric while others contain additional features on one side of the minimum. In order to obtain more information about this asymmetry, angular sweeps at different magnetic fields were performed for both the most symmetric and the most asymmetric φ as shown

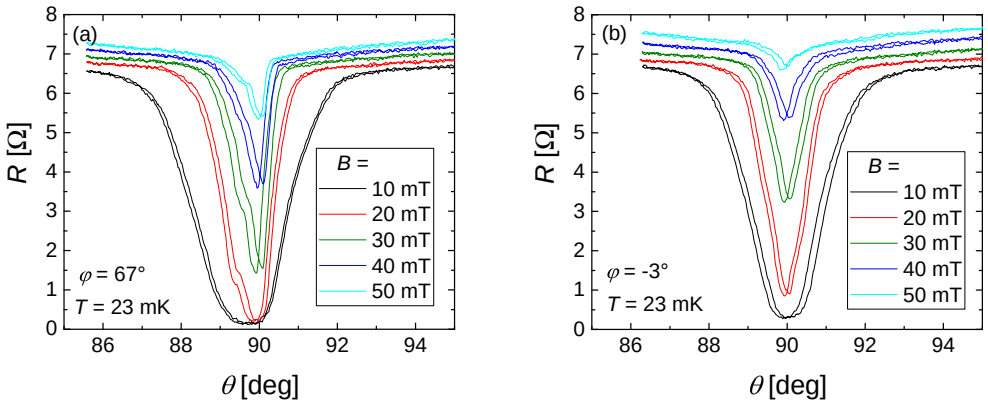

Figure 5.18: Angular sweeps with different values of the magnetic field for (a) $\varphi = 67°$ and (b) $\varphi = -3°$ at $T = 23\,\mathrm{mK}$.

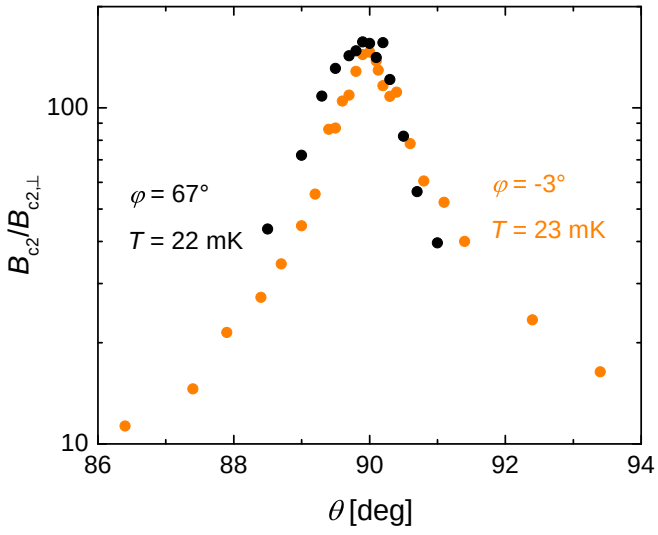

Figure 5.19: θ-dependence of the critical field normalised to the perpendicular critical field for $\varphi = 67°$ (strongest SC, most asymmetric) and $\varphi = -3°$ (most symmetric).

in Fig. 5.18. In Fig. 5.18(a) we can clearly see that the asymmetry indeed shows a noticeable field dependence. For high fields we observe an asymmetric dip with a very sharp minimum. The right hand slope of the dip is very steep while on the left hand slope an additional feature is observed. For lower fields this additional feature seems to shift to lower θ while the main minimum stays at the same position. For the lowest applied field of $B = 10\,\mathrm{mT}$ we already observe some angular range with zero resistance. The whole dependence then looks like a broad rather symmetric dip (even though the slopes of the dip still are notably different). However, the centre of the dip is recognisably shifted in respect to what we would define as the parallel position from the angular sweeps at higher fields. For $\varphi = -3°$ shown in Fig. 5.18(b) the dip looks rather symmetric for all studied values of B. The only exception is that for the lowest field the slope slightly decreases at $\theta > 91°$.

This asymmetric behaviour is also reflected in the θ-dependence of the critical field: In Fig. 5.19 we see a comparison of the θ-dependence of B_{c2} at $\varphi = 67°$ (black) with the one at $\varphi = -3°$ (orange) (both at lowest possible temperature). The first one shows the most asymmetric behaviour and the latter one the most symmetric behaviour. When comparing the two curves, we clearly see that the hump on the left hand side of the maximum in the black curve causes a clear deviation from the expected behaviour for these values of θ. On the other side of the maximum the slopes of the two curves are in reasonable agreement close to parallel orientation. However, we can see that also the orange curve has a somewhat asymmetric behaviour for $\theta > 91°$, which we already saw in the θ-sweep with the lowest field.

Possible reasons for this asymmetry could be crystal defects, like a small crystallite, with slightly tilted planes. Or maybe it is just a result of the low symmetry triclinic crystal structure of the compound. The field dependence of the θ position of the second feature at $\varphi = 67°$, however, is an argument against the asymmetry being caused by a second crystallite: In the case of a bicrystal we would expect the minimum for both crystallites to be field independent. It is much more likely that the reason for this asymmetry is found in the vortex dynamics. One possibility is the existence of very good pinning conditions for a certain direction, reducing the flux motion and, therefore, the resistance for magnetic fields in this direction. Similar features in the interlayer resistance for magnetic fields rotated in an angular range around parallel to the conducting layers have also been reported in other anisotropic superconductors including high-T_c cuprates and organics [137–140].

5.1.7 θ-dependence of critical field

The critical field studies at $p = 4.7\,\mathrm{kbar}$ will be concluded with a study of the θ-dependence of the critical field. Again, a similar study was already done at lower pressures in [38, 132]. However, for those two pressures the $B_{c2}(\theta)$ was only studied for the φ with the highest $B_{c2,\parallel}$. For $p = 4.7\,\mathrm{kbar}$ the θ-dependence was studied for several values of φ.

To this end a number of field sweeps at different values of θ were executed. This was done at two different temperatures each and at three different φ. Some examples of field sweeps at different θ at $T = 23\,\mathrm{mK}$ and $\varphi = -35°$ (the lowest $B_{c2,\parallel}$) are shown in

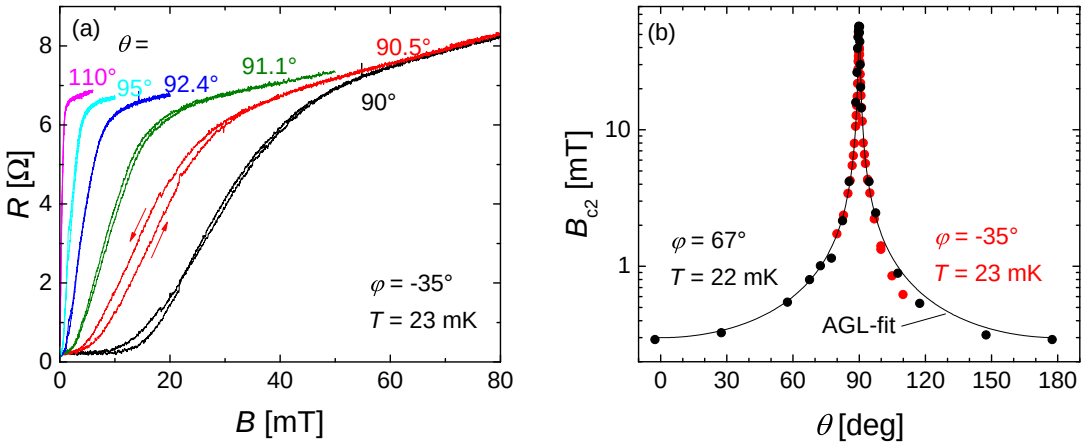

Figure 5.20: (a) A collection of field sweeps at different polar angles θ at $T = 23\,\mathrm{mK}$ and $\varphi = -35°$. (b) The θ dependence of the critical field at the same temperature for two different values of φ. The line is a fit to the dependence with the AGL model.

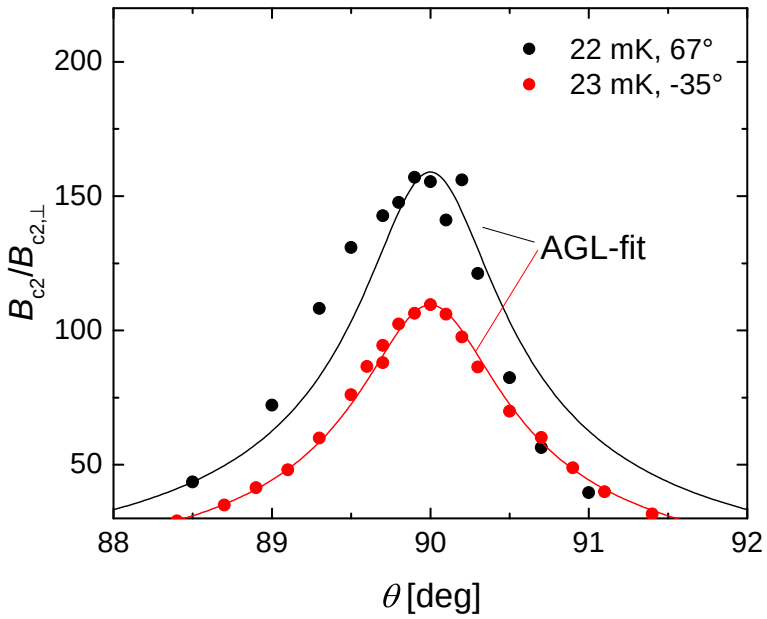

Figure 5.21: θ-dependence of the critical field normalised to the perpendicular critical field for the respective temperature in a small window around parallel orientation for two different temperatures and two different φ. The fits were made to the low temperature curves by the AGL model (Eq. (2.44)).

Fig. 5.20(a). Already when looking at the sweeps it becomes obvious that the critical field depends strongly on θ for field orientations close to parallel.

In Fig. 5.20(b) the critical field is plotted as a function of θ at the lowest possible temperature for the φ angles with the strongest and the weakest superconductivity, respectively. From this graph one can immediately see the extremely high anisotropy.

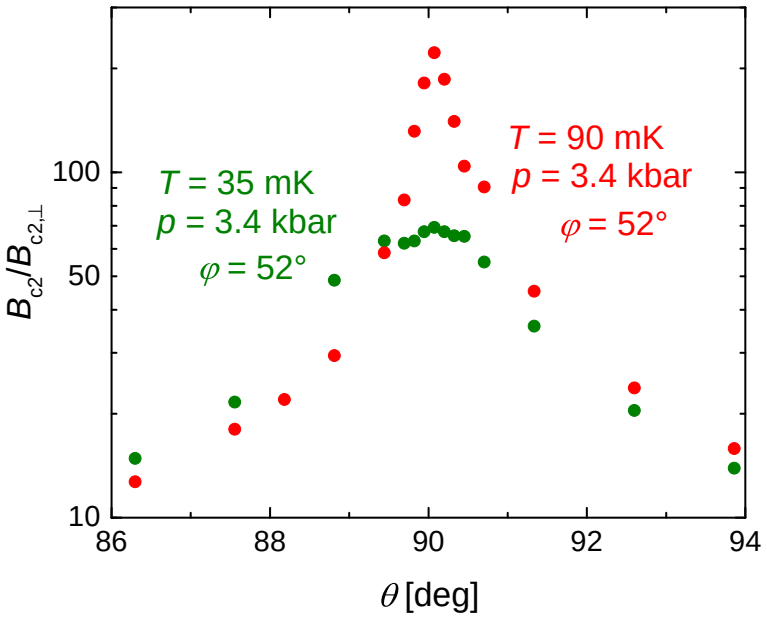

Figure 5.22: $B_{c2}(\theta)$ normalised to the respective $B_{c2,\perp}$ for the lowest and highest temperatures studied at $p = 3.4\,\mathrm{kbar}$, at the respective φ with the strongest SC.

Note that the critical field is plotted in logarithmic scale, since otherwise the dependence would not be resolvable by eye. Figure 5.21 shows the θ-dependence of the critical field, normalised to the perpendicular critical field, in a small angular range around the parallel orientation. No plateau (like it was observed at lower pressures in [38, 132]) is observed at this pressure, indicating no significant impact from the paramagnetic pair breaking effect. The anisotropy values obtained from the θ-dependence are:

$$\frac{B_{c2,\parallel}}{B_{c2,\perp}} \approx 175 \text{ for } T = 22\,\mathrm{mK},$$

while for $\varphi = -35°$ we get

$$\frac{B_{c2,\parallel}}{B_{c2,\perp}} \approx 138 \text{ for } T = 23\,\mathrm{mK}.$$

For both angles of φ, the $B_{c2}(\theta)$ was also studied at a higher temperature. In both cases no notable differenc in the dependence was observed. This is in contrast to the observations from lower pressures, where always a higher anisotropy was found at the higher temperature as shown in the $p = 3.4\,\mathrm{kbar}$ curve in Fig. 5.22. The reason for the low pressure behaviour lies in the paramagnetic pair-breaking effect. There it becomes dominant for fields parallel to the conducting layers for sufficiently low temperatures resulting in the plateau observed in the 35 mK curve in Fig. 5.22. Only at temperatures close to T_c, where even for the field parallel to the layers the orbital effect is still dominant, the full anisotropy is observed (90 mK curve in Fig. 5.22).

At $p = 4.7\,\mathrm{kbar}$ we seemingly do not observe any significant influence from the paramagnetic effect according to the phase diagram for $B \| ac$-plane, so we might expect

a temperature independent behaviour of the anisotropy, which is indeed observed. A strange feature at $\varphi = 67°$ is that the peak still looks slightly flattened on the top. However, this likely is only an artifact of the asymmetry of the curve, as discussed in the last section.

For both φ values the low-temperature data in Fig. 5.21 was fitted with the anisotropic Ginzburg-Landau (AGL) model (Eq. (2.44)). While the fit to the $\varphi = -35°$ data is in very good agreement with the measurements, the fit to the $\varphi = 67°$ data fits only poorly in the shown angular range. The reason for this is the discussed asymmetry of the peak in the $B_{c2}(\theta)$ dependence for this φ. In the φ range further away from the parallel orientation both dependencies are fitted well, as can be seen in Fig. 5.20(b). This indicates that we are clearly in the regime of anisotropic 3D superconductivity for this pressure, which is in agreement with the relatively large $\xi_{\perp,0}$. The Tinkham formula (Eq. (2.46)) also fits most of the dependence well but significantly overestimates the critical field exactly parallel to the layers proofing that the 2D model is not valid.

5.2 Possible type I/type II crossover in α-(BEDT-TTF)$_2$KHg(SCN)$_4$ at $p = 4.7$ kbar

Among the notable properties of α-KHg are the extremely low critical fields and temperatures as already shown above. From the BCS theory it is immediately obvious that such a low critical temperature results in a high coherence length ξ_0 (c.f. Eq. (2.37)). While we already showed above, that the critical field is enhanced compared to what we would expect from BSC-theory we still have an interlayer coherence length close to 1 µm. This is a much higher value then commonly observed for other organic superconductors, where the coherence lengths usually are more than an order of magnitude smaller due to the higher T_c [6]. On the other hand, the normal state properties, which are responsible for the London penetration depth λ_L are similar to other organics, where λ_L also has typical sizes of a little bit below 1 µm.

For an exact comparison we evaluate the λ_L for the present compound. In general the penetration depth can be calculated by [73]

$$\lambda_L = \sqrt{\frac{m_s}{\mu_0 n_s q_s^2}}, \tag{5.11}$$

where m_s is the mass, q_s the charge and n_s the densitiy of the SC charge carriers. For this estimation we assumed that m_s is given by the cyclotron mass at the respective pressure $m_s = 2m_c$, where $m_c(p = 4.7\,\text{kbar}) = 1.8\,m_e$ (see Sec. 5.1.1). n_s was determined from the size of the FS sheets. As described in Sec. 3.1.3 the cylinder size was determined by magnetic quantum oscillations as 16% of the FBZ [108, 109]. In compensated metals the size of the hole and electron like orbits must be equal. For our system this implies that the area of the open sheets must be similar to the cylinders meaning that in total we have a filling of 32% of the FBZ. Since FS with the same size as the FBZ contains two electrons, we have a filling of 0.64 carriers per unit cell. The size of the unit cell for zero pressure is $\sim 2\,\text{nm}^3$. Since we are lacking crystallographic data under pressure we

used this value. With $q_s = 2e$ we get

$$\lambda_L \approx 390\text{nm}. \tag{5.12}$$

This value of λ_L is indeed smaller than the value of the $\xi_{\parallel,0}(\text{avg}) = 710\,\text{nm}$ determined in Eq. (5.1) above. From that we can now calculate the Ginzburg-Landau (GL) parameter [75]

$$\kappa = 0.96\frac{\lambda_L}{\xi_{\parallel,0}} = 0.42 < \frac{1}{\sqrt{2}}. \tag{5.13}$$

For this value of κ we indeed should be in the type I regime of superconductivity. However, we also have to take into account the inplane mean free path ℓ of the electrons in our sample since for superconductors in the dirty limit the GL-parameter is determined by $\kappa = 0.715\frac{\lambda_L}{\ell}$ [75]. In order to estimate ℓ we need the Fermi-velocity v_F of α-KHg and the scattering rate τ of the specific sample. v_F of α-KHg was determined from field-induced CDW effects by Andres *et al.* [35, 135] and with the use of angle-dependent periodic orbit resonance measurements performed by Kovalev *et al.* [141] both yielding a result of $v_F \approx 10^5\frac{m}{s}$.

The scattering time τ of this sample also was estimated by two different methods: The estimation of the Dingle temperature from high-field SdH oscillations yields a relatively low scattering time of $\tau = 1.3\,\text{ps}$ [132] resulting in a rather small mean free path of $\ell = v_F\tau = 110\,\text{nm}$. This is due to the fact that with the Dingle temperature method only a lower boundary is estimated [46] as explained in Sec. 2.1.2. The usual transport relaxation time may be up to one order of magnitude higher [142]. Another estimation was done by Kartsovnik *et al.* [107] using AMRO yielding a value of $\tau = 15\,\text{ps}$ and, hence, $\ell = 1250\,\text{nm}$. However, the second method is only of approximate nature, since the relevant properties of AMRO can only be determined with a rather low accuracy and, therefore, has to be considered as not very precise. Still the second estimation probably is more relevant for the SC state, and if we believe that the Dingle scattering time indeed is one order of magnitude lower than the transport scattering time, we end up with a mean free path of

$$\ell \approx (1 \pm 0.5)\,\mu\text{m}. \tag{5.14}$$

When comparing this to the estimated $\xi_{\parallel,0} \approx 710\,\text{nm}$, our systems is just on the border of the clean limit if we are in the higher part of the error range. However, if we assume a mean free path at the lower end of the error range $\ell = 500\,\text{nm}$ the GL-parameter would become $\kappa = 0.715\frac{\lambda_L}{\ell} \approx 1.3 > \frac{1}{\sqrt{2}}$, which would mean that our system still is a type II superconductor. In any case we have to consider that our system is not in the far clean limit of $\ell \gg \xi_{\parallel,0}$.

We also have to consider that for rather similar values of $\xi_{\parallel,0}$ and λ_L we may not be fully inside the type I or type II regime: Luk'yanchuk [143] and Mohamed *et al.* [144] estimated that for superconductors with $\kappa \approx 1/\sqrt{2}$ the system can be in some intermediate regime, where a direct transition from a normal metallic to SC state in the Meißner-phase is only observed for temperatures close to T_c. At lower temperatures the system tends to form a vortex state lying in between, meaning that the transition resembles that of a type II superconductor as shown in Fig. 5.23. The exact shape of

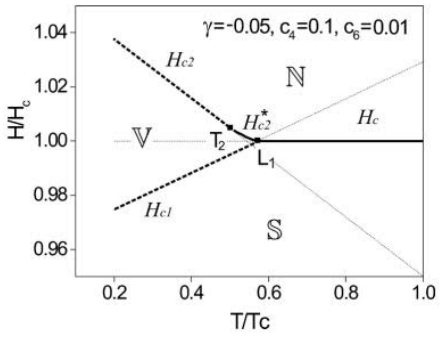

Figure 5.23: Possible B-T (H-T) phase diagram of a superconductor with $\kappa \approx 1/\sqrt{2}$. It includes normal metallic (N), vortex (V) and Meißner superconducting (S) states. Solid and dashed lines correspond to the discontinuous (first order) and continuous (second order) transitions, and dotted lines present the auxiliary critical fields. (from [143])

the phase diagram is thereby determined by the difference in the coefficients in the perturbation functional theory.

After looking at all the relevant parameters we can answer the question, whether α-KHg can really be a type I superconductor. Of course, for magnetic fields parallel to the conducting layers, the interlayer coherence length $\xi_{\perp,0}$ becomes relevant. And since $\xi_{\perp,0} \approx 4.7\,\mathrm{nm} \ll \lambda_L$ at the current pressure, we can savely assume that our system is in the strongly type II regime of superconductivity for magnetic fields in inplane direction.

For fields perpendicular to the conducting layers, where only the inplane coherence length is relevant, the relevant lengths, while being close, allow the possiblity of observing superconductivity in the type I regime. Therefore, this compound might give us the interesting possibility to observe a field-direction dependent crossover from the type II to the type I regime. This leads us to the question, how we are able to judge whether our system is in the type I regime or not: One possibility might be a hysteretic nature of the transition in the type I regime, where the transition upon reaching the critical field value $B_{c,th}$ is of first order (while in a type II superconductor at B_{c2} we always have a second order phase transition). Another possibility might be to find a hint in the angular dependence of the critical field $B_c(\theta)$, since the crossover from one regime to the other must take place at a certain θ. From the most simple assumptions we might expect an angle independent critical field in the type I regime. This is because in the Meißner phase all magnetic field is supposed to be expelled from the SC volume. However, if we take into account the demagnetisation, we very likely end up in an intermediate state, where still some angular dependence is observed, especially since the demagnetisation factor changes with the angle. Yet there is still some hope that the angular dependence in the type I regime may show some difference to that in the type II regime.

After these thoughts let us now look at the results of the measurements: First we will display the behaviour for magnetic field perpendicular to the layers and afterwards analyse the θ-dependence for signs of a type I/type II crossover.

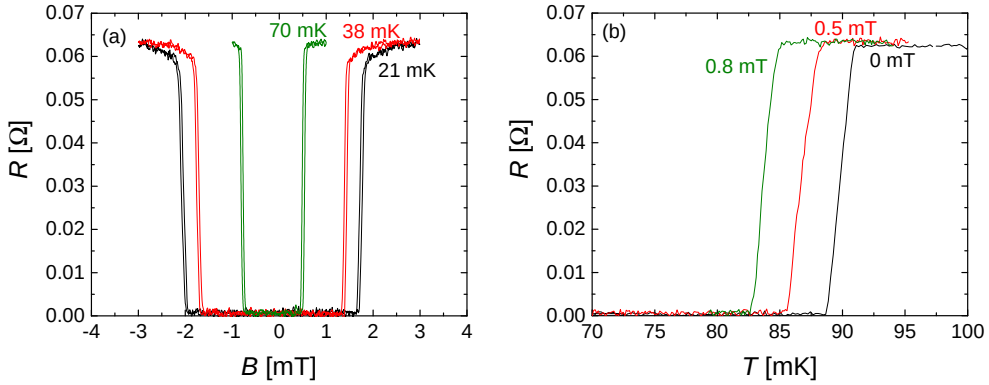

Figure 5.24: (a) Resistance of an iridium wire as a function of magnetic field for different temperatures. (b) Resistance of the same iridium wire as a function of temperature at different values of the magnetic field.

5.2.1 Behaviour in perpendicular magnetic field

If the present compound indeed undergoes a crossover into the type I superconductivity regime, it should be best observed for magnetic field perpendicular to the conducting layers. In Sec. 5.1.2 we already presented temperature- and field-sweeps for fields in this direction (Fig. 5.6) at $p = 4.7$ kbar. When taking a closer look at the field sweeps in Fig. 5.6(b) we do not see any direct evidence for type I superconductivity: The transitions look similar to those at lower pressures, where the system certainly is in the type II regime because of the lower $\xi_{\parallel,0}$. The calculated value of κ of course is in general valid only for $T = 0$ K. And we also have to take into account that we are maybe in an intermediate regime, where a vortex state may be formed between the norml metallic and the Meißner phase in some part of the phase diagram [143], as discussed above. However, as seen in Fig. 5.23, the highest chance to observe a direct transition from metallic to Meißner state is close to T_c. But also for the highest temperatures no anomalous behaviour of the SC transition is visible.

But we also cannot exclude the possibility that there is no visible manifestation of the difference between the phase transition in type I and type II superconductors in resistance. For comparison we take a look at the resistive SC transition of an iridium wire with a zero field critical temperature $T_{c,0} = 90$ mK, since it is generally known to be a type I superconductor. Some collection of field and temperature sweeps are shown in Fig. 5.24. The SC transition of iridium is, of course, much sharper than in α-KHg as could be expected since iridium is a pure metal. However, as we can see in Fig. 5.24(a) apart from the smaller transition width the transitions in field look very similar to those of α-KHg and no sign of any hysteretic behaviour is observed. The Ir wire used for this study was found to contain approximately 2% of Fe impurities according to EDX, which is in agreement with the reduction of the critical temperature as compared to the literature value of $T_c = 112.5$ K.

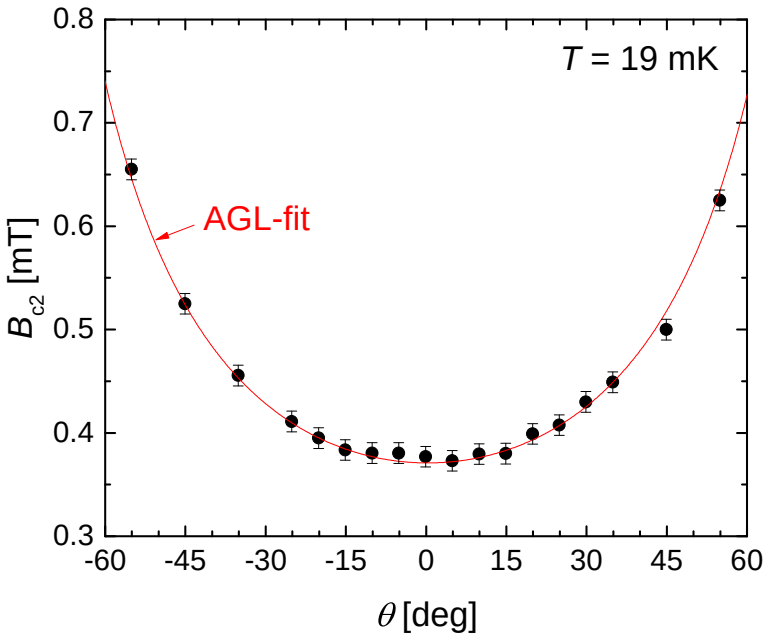

Figure 5.25: $B_{c2}(\theta)$ around perpendicular orientation for $T = 19\,\mathrm{mK}$. The red curve is a fit with the AGL model.

5.2.2 θ-dependence of critical field near perpendicular field orientation

Since the field and temperature sweeps for $B \| b^*$ did not give us any direct evidence for the crossover into the type I SC regime, we investigated the θ-dependence of B_{c2} around perpendicular orientation in search of some manifestation of the type I/ type II crossover. Since $\xi_\perp$ still is very small, even at this pressure, the SC state is in the strongly type II regime for magnetic fields parallel to the conducting layers. This means the crossover should take place at some distinct θ. To this end a number of field sweeps at different polar angles θ were performed in a wide range around perpendicular orientation as shown in Fig. 5.25. The data has been fitted with the AGL model (like in Fig. 5.20(b)), which reproduces the dependence very well within error range.

Figure. 5.25 clearly shows us that there is no θ-region, where B_c is θ-independant. However, as discussed above this scenario was highly unlikely. The good coincidence with the AGL model further shows us that there is no notable change of the θ-dependence of B_c, giving us no hint for a type I/type II crossover.

In the further search for manifestations of the type I/ type II crossover a number of θ-sweeps at different values of the magnetic field over the full angular range were performed as shown in Fig. 5.26. As we can see, again no distinct feature is visible, which could be used as an indicator for a type I/ type II crossover. To further clarify, whether there exist any hysteretic effects caused by the first order nature of a transition into a type I SC state, additionally angular sweeps in different directions and with different starting points were executed (not shown). However, in all cases the behaviour of the presented sweeps was fully reversible. For a number of sweeps in Fig. 5.26, there

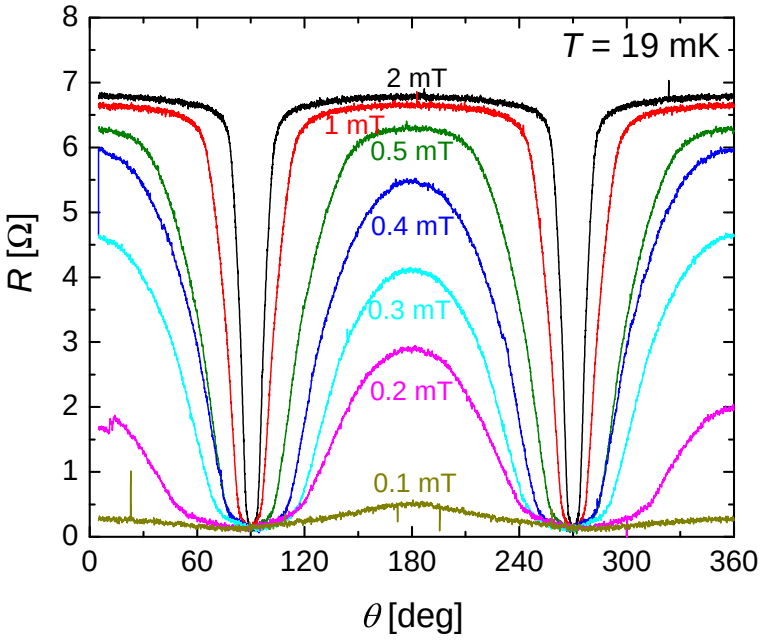

Figure 5.26: θ-sweeps for different low magnetic fields at $T = 19\,\mathrm{mK}$.

exists some asymmetry between 0° and 180°. But this asymmetry is most likely a result of slight changes of the remanent field between the sweeps.

This means we have to conclude that we could not find any experimental evidence for a type I/ type II superconductivity crossover in α-KHg, even though our estimations of ξ_{GL} and λ_{L}, if sufficiently correct, suggest such a crossover. However, it must be noted that the task may be indeed difficult. First, as already mentioned, we cannot be sure that a type I/ type II crossover will show any manifestation in resistive measurements. Second, we are still very close to $\kappa = 1/\sqrt{2}$ and may be in some intermediate regime, where the transition in field is not yet of first order for some part of the temperature range, as proposed by theory [143, 144]. According to the authors in such conditions a more complex study of the vortex dynamics has to be undertaken in order to figure out, whether the superconductor behaves as a type I or a type II superconductor in the given situation. And third, according to our estimations of the mean free path ℓ of our sample, we are very close to the border between the clean and dirty limit of superconductivity. Since our ℓ is not very well determined, it is possible that our system is in the dirty regime and, hence, still in the type II regime of superconductivity.

5.3 The T-p phase diagram of α-(BEDT-TTF)$_2$TlHg(SCN)$_4$

α-TlHg has a slightly higher CDW transition temperature at ambient pressure than its sister compound α-KHg. Apart from that much less is known about this compound's low-temperature properties at high pressure. For this reason α-TlHg was studied under

high pressures at low temperatures jointly with L. Höhlein in the frame of her master thesis [41].

In α-TlHg the value of the critical pressure, where the CDW state becomes suppressed was to date unknown. Moreover, no information about the existence and nature of a possible bulk SC state at and above critical pressure was available. For this reason a series of measurements under different hydrostatic pressures close to the expected critical value was performed in order to map the T-p phase diagram.

5.3.1 Pressure dependence of $R(T)$ and the CDW transition

When we look at the interlayer resistance in the temperature range below $T = 20\,\mathrm{K}$ as shown in Fig. 5.27 we can see the effect of pressure on the CDW state: The anomaly at the CDW transition temperature shifts downwards with increasing pressure and becomes less pronounced. At ambient pressure we observe the CDW transition to be at $T_{\mathrm{CDW}} \approx 10\,\mathrm{K}$, while for $p = 3.1\,\mathrm{kbar}$ it shifts down to approximately 2 K. At higher pressures no further transition feature could be detected, however, for reasons explained below we assume that the CDW state is not completely suppressed until significantly higher pressure.

5.3.2 Superconducting state under pressure

Figure 5.28(a) shows $R(T)$ of α-TlHg for $T < 1\,\mathrm{K}$. All but the ambient pressure curve undergo a clear SC transition below 100 mK. The SC transition region is shown in

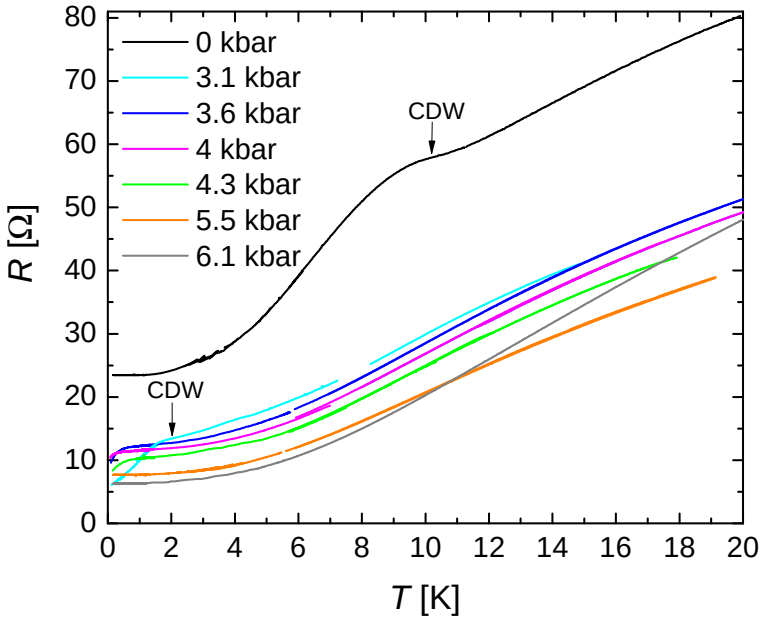

Figure 5.27: $R(T)$ of α-TlHg for temperatures below $T = 20\,\mathrm{K}$ at different pressures (from [41]).

Fig. 5.28(b). Here we can see that the maximum T_c was observed for $p = 4.0\,\text{kbar}$ and 4.3 kbar, which had a similar value of $T_c = 70\,\text{mK}$. The transition width for these pressures is about 24 mK, which is significantly broader than the value observed for α-KHg. At higher and lower pressures T_c goes down, indicating that the critical pressure must be somewhat close to 4.3 kbar.

At 3.6 kbar the sample resistance does not yet go down to zero. Comparing to α-KHg this is a clear evidence that the CDW state is not yet suppressed at this pressure even though no CDW transition anomaly was observed in the $R(T)$. For the higher pressures we cannot directly judge from the SC transition whether the system still undergoes a transition into the CDW state. However, if we have a closer look at Fig. 5.28(a) we see that we still observe a clear SC precursor starting from $T_{\text{onset}} \approx 0.6\,\text{K}$ for all pressures up to 4.3 kbar. At 4.0 kbar the precursor also sets on at 0.5. K, although the magnitude of the effect is lower than for the other presssures. For $p = 5.5\,\text{kbar}$ and above the $R(T)$ is completely flat until the main SC transition is starting at $\sim 60\,\text{mK}$. This is an indication that the CDW state is only fully suppressed for $p > 4.3\,\text{kbar}$.

Starting from $p = 5.5\,\text{kbar}$ T_c decreases again, with $T_c(5.5\,\text{kbar}) = 57\,\text{mK}$ and $T_c(6.1\,\text{kbar}) = 40\,\text{mK}$. From that we obtain a slope of $\mathrm{d}T_c/\mathrm{d}p \approx 20\,\text{mK/kbar}$. This slope is a little bit lower than the one observed in α-KHg [27], but follows the trend that SC is suppressed by pressure in organic superconductors under increasing pressure.

5.3.3 Precursor of superconductivity

A characteristic feature in this family of compounds is an inhomogeneous SC state, which is formed in small volume fractions inside the CDW state. In α-KHg the onset temperature is much higher than the main SC transition observed under pressure. In α-TlHg a similar onset is observed at $\sim 0.6\,\text{K}$ as it was already shown in Fig. 5.28(a), which we attribute to a similar SC state and which is at a much higher temperature than the reported value of 0.1 K [40]. The behaviour of this state in α-TlHg was further investigated under the influence of a perpendicular magnetic field.

Figure 5.29(a) shows a number of field sweeps at different temperatures with the mag-

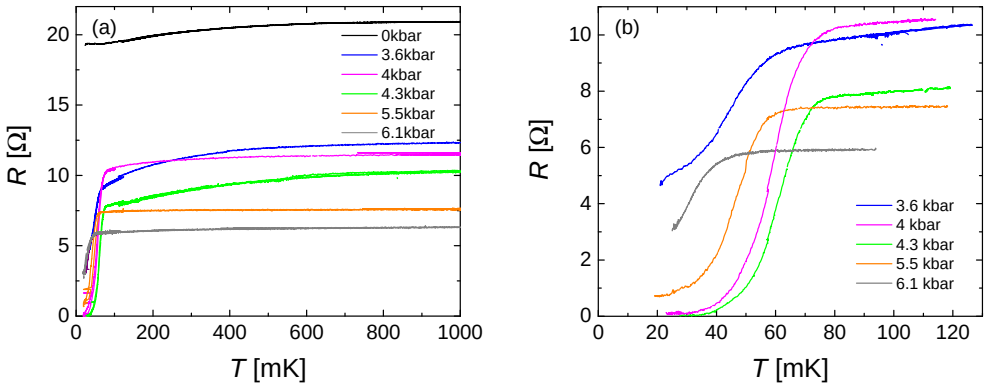

Figure 5.28: (a) $R(T)$ of α-TlHg for $T < 1\,\text{K}$. (b) The low temperature part of the same data set featuring the SC transition. (both from [41])

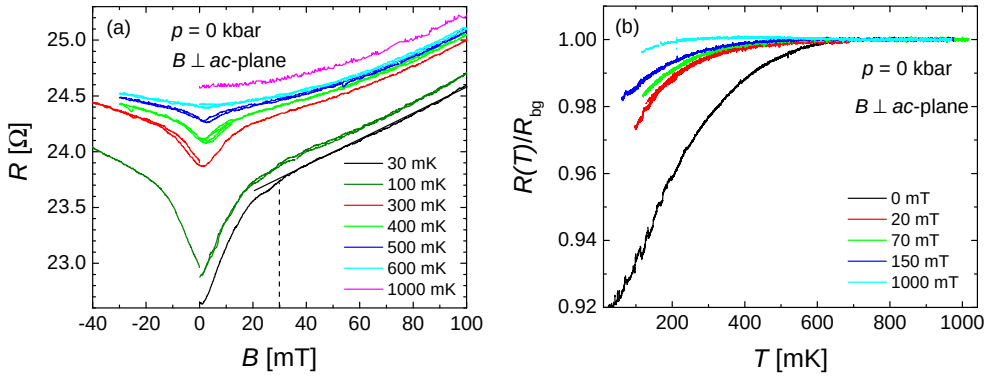

Figure 5.29: (a) $R(B)$ at different temperatures for $p = 0\,\mathrm{kbar}$. (b) Normalised temperature sweeps at different fields for $p = 0\,\mathrm{kbar}$. The background resistance R_{bg} is defined as a linear slope fitted to the curves in the temperature range between 0.7 K and 1 K. (both from [41])

netic field applied perpendicular to the conducting layers. As we can see the resistance significantly increases at low magnetic fields, as we would expect for a SC state for this field direction. Therefore, we assume that also in α-TlHg superconductivity is responsible for the reduction in resistance below 0.6 K. For the lowest temperature the onset of superconductivity (defined as the deviation of the resistance behaviour from the B^2-dependence as indicated by the dashed line in Fig. 5.29(a)) is observed at $B_\perp \approx 30\,\mathrm{mT}$. For temperatures above the SC onset temperature of approximately 600 mK no feature due to the SC state is observed any more.

In temperature sweeps, however, an unexpected behaviour was found, as we can see in Fig. 5.29(b). Here, a number of temperature sweeps for different values of the perpendicular magnetic field are plotted. Above the onset temperature the resistance is rather linear. Therefore, the resistance value was normalised to a straight line fitted to the respective resistance in the temperature range between 0.7 K and 1 K in order to make the curves better comparable. Here we can see that even at fields much higher than the estimated critical field of 30 mT still a downturn in resistance is clearly visible. Besides, a downturn, while being gradually suppressed by magnetic field, is still observed until a field as high as 1 T, suggesting that some additional effect to the filamentary SC state is reducing the resistance in the present compound. No such behaviour was observed in α-KHg.

Figure 5.30 shows a similar collection of normalised temperature sweeps for (a) $p = 3.6\,\mathrm{kbar}$ and (b) $p = 4.0\,\mathrm{kbar}$. When we compare these curves with the ambient pressure data, it becomes obvious that the discussed effect is weakened by hydrostatic pressure. While the resistance drop at zero fields is even stronger at 3.6 kbar than at ambient pressure, it is more rapidly suppressed by magnetic field. Here the reduction in resistance is already completely suppressed for field higher than 100 mT. At 4.0 kbar there is hardly any effect left at $B = 70\,\mathrm{mT}$. For pressures above the critical value the onset in this temperature range is completely suppressed. Therefore, we can conclude that the effect responsible for the decrease in resistance, which persist when the fila-

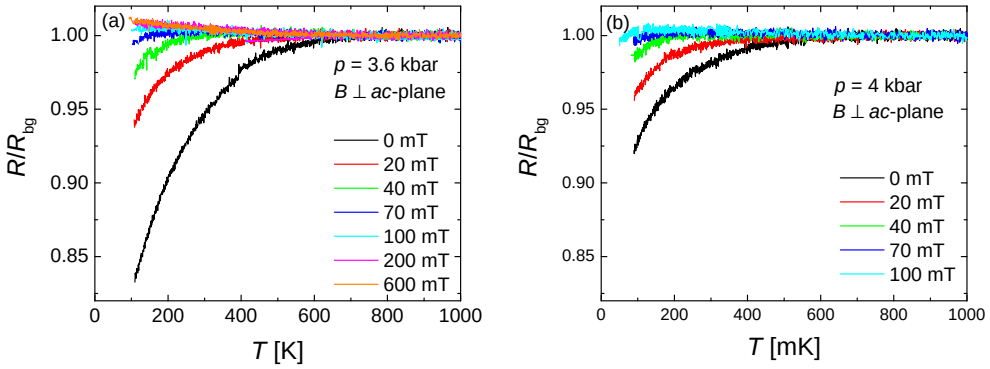

Figure 5.30: Temperature sweeps at different magnetic fields for (a) $p = 3.6\,\mathrm{kbar}$ and (b) $p = 4.0\,\mathrm{kbar}$ normalised to the background resistance R_{bg}. R_{bg} is defined as a linear slope fitted to the curves in the temperature range between 0.7 K and 1 K. (both from [41])

mentary SC state is suppressed by magnetic field, becomes completely suppressed by sufficiently high pressure. The higher magnitude of the feature at 3.6 kbar could possibly be caused by a superposition with the CDW transition feature. But since this feature is suppressed by magnetic fields, this is probably not the case. In the following we will discuss some possible effects that could be responsible for this additional decrease in resistance.

Of course, the most obvious idea is that there exists an SC state in a small volume fraction, which is much more robust in magnetic field, than the rest of the filamentary superconductivity, which is destroyed above $B = 30\,\mathrm{mT}$ at ambient pressure. This additional superconductivity could be caused by fluctuations, which might exist due to the low dimensional nature of the system. From this we would be able to understand the pressure dependence of the effect, since the higher pressure would cause a decrease of the fluctuations due to the higher 3-dimensionality. However, the main question in this explanation could be, why a similar behaviour is not observed in the sister compound α-KHg having similar strong anisotropies.

Another possible explanation might be the existence of weak anti-localisation (WAL), which was suggested by Brooks *et al.* [145] for a similar field and temperature dependence in the sister compound containing Rb (α-(BEDT-TTF)$_2$RbHg(SCN)$_4$). Weak localisation is an effect known from dirty 2D systems, which in general causes the resistance to increase logarithmically with temperature. It is caused by coherent interference of the electrons on self-crossing paths through the material after a number of elastic scattering processes. When this interference is constructive, the back-scattering probability is significantly increased: The electron becomes "localised" at the scattering center and the resistance increases [146]. The influence of strong spin-orbit coupling can cause this self-interference to become destructive, which then causes a decrease of the back-scattering and, therefore, the resistance [147].

According to Abrikosov and Gor'kov [148], the spin-orbit scattering rate τ_{SO}^{-1} is related to the transport scattering rate τ^{-1} by $\tau/\tau_{\mathrm{SO}} \propto Z^4$, with Z being the atomic number.

Our present compound indeed contains the very heavy atom Tl, which is not present in α-KHg and which could be responsible for a sufficiently strong spin-orbit coupling. Of, course we have to take into account that the Tl atoms are located in the insulating anion layers. But we are probing the interlayers resistance, which should be sensitive to the structural aspects of the anion layers. And indeed strong spin-orbit coupling was already found in organic charge transfer salts, as reported by Sugano *et al.* [149] in α-(BEDT-TTF)$_2$I$_3$ caused by the interaction of the triiodate with the BEDT-TTF molecules.

WAL also would be in agreement with the observed effect of magnetic field, since WAL is generally suppressed by sufficiently high magnetic fields, which often are in the range of 0.5-2 T, depending on the material. This can be explained by the fact that a magnetic field introduces a phase shift in the electron wave function and suppresses the interference after a time proportional to B^{-1} [150]. In our case a field of 1 T was not yet sufficient to completely suppress the effect at ambient pressure. The fact that the effect is weakened by increasing pressure can also be understood in terms of WAL: Generally the weak (anti-)localisation effect can only be observed in low-dimensional systems, since the probability for self-crossing paths is greatly reduced in three dimensions. Under higher pressure the electron system in our compound becomes less anisotropic and, hence, more three dimensional. For that reason a weakening of the WAL effect under pressure would be expected. Also the reduction of the magnetic field necessary to suppress the effect at higher pressures, as found in our measurements, would be in agreement to this. However, without further studies we cannot give a final answer as to which effect is responsible for the logarithmic decrease in resistance, which remains even when the filamentary SC state is suppressed by magnetic fields.

5.3.4 Summary of the T-p phase diagram

From the measurements shown above we were able to build the T-p phase diagram of α-TlHg, which is shown in Fig. 5.31. In the graph the squares mark the transition into the CDW state: with the filled boxes resulting from our measurements and the empty boxes from Shegolev *et al.* [39]. The data are in good agreement.

The diamonds show the onset of the filamentary SC state, as discussed above. The triangles mark the transition into the SC state according to the common construction as explained in Sec. 5.1.2, while the circles show the temperature, where the resistance reaches zero. The highest $T_c \approx 70$ mK was observed at $p = 4.0$ kbar and 4.3 kbar. Since still some SC precursor is observed at 4.3 kbar and since the zero resistance region has a positive slope until this pressure, we conclude that the critical pressure must be higher than 4.3 kbar. At the next higher studied pressure of 5.5 kbar T_c already significantly decreased again, indicating that we are significantly above the critical pressure, where the highest T_c is expected. From the slope between the points for 5.5 kbar and 6.1 kbar we conclude that the critical pressure lies in the range of $p_c = (4.7 \pm 0.3)$ kbar as indicated by the shaded area in Fig. 5.31.

When we compare this phase diagram with that of α-KHg (Fig. 5.5), we see that the critical pressure is significantly higher in α-TlHg as could be expected from the higher transition temperature. Since the sizes of the K^+ ion and the Tl^+ ion are almost

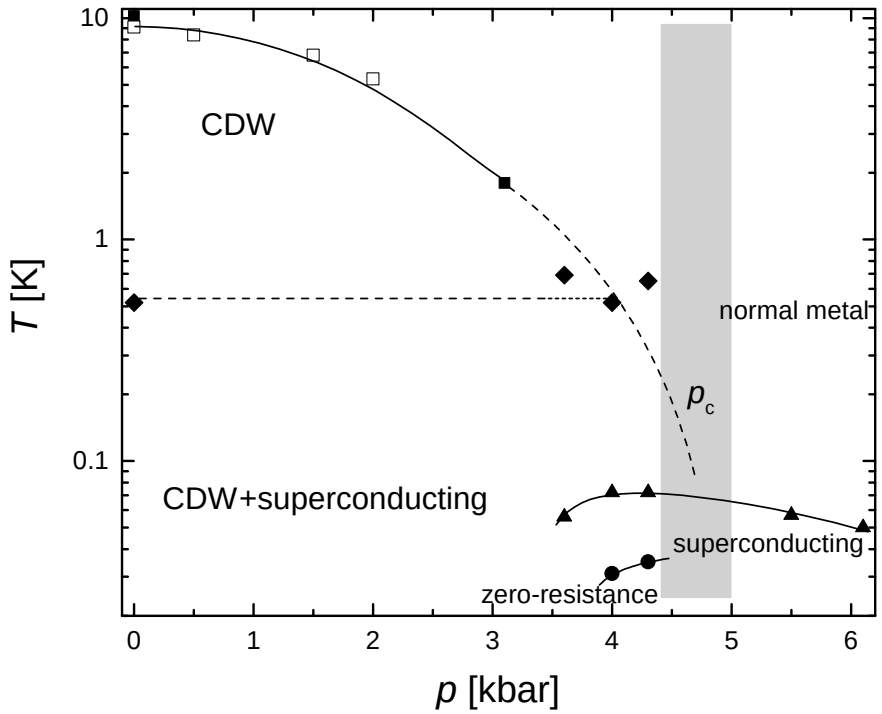

Figure 5.31: The T-p phase diagram of α-TlHg. The squares show the transition from the normal to the CDW state at $p = 0$ kbar and 3.1 kbar; the hollow symbols are taken from [39]. The diamonds mark the onset of the filamentary SC state within the CDW state. The triangles mark T_c determined at the main transition into the SC state, while the circles indicate, where the sample resistance has reached zero. The shaded area is the region in which we propose the critical pressure. The lines are guides to the eye. (from [41])

identical we cannot attribute this changes to chemical pressure. Therefore, other effects caused by the Tl^+ ions must be responsible for the change in critical pressure of α-TlHg. The onset temperature of superconductivity at ambient pressure of α-TlHg was also found to be a factor of 2 higher than in α-KHg. But while this SC onset temperature is higher, we found that the maximum T_c of the bulk SC state is significantly lower than in the K-salt. Further, it seems that the SC state in α-TlHg is more robust to pressure, since the slope of $\mathrm{d}T_c/\mathrm{d}p \approx 20$ mK/kbar is lower than in α-KHg, where the slope is ≈ 30 mK/kbar. For a more exact determination of the critical pressure, further measurements in the pressure range between 4.5 kbar and 5.0 kbar would be necessary.

5.4 Critical field anisotropy in α-(BEDT-TTF)$_2$TlHg(SCN)$_4$

For some of the set pressures also measurements of the critical field anisotropy were performed. The measurements were very similar to those carried out for α-KHg as described in Sec. 5.1. Therefore, we will present only the resulting B-T phase diagrams here and compare them to those of α-KHg. Also these studies were done in joint work with L. Höhlein [41].

5.4.1 Magnetic field perpendicular to the conducting layers

Figure 5.32 shows the B-T phase diagram of α-TlHg for fields applied perpendicular to the conducting layers at pressures of $p = 4.0$ kbar, 4.3 kbar and 5.5 kbar. The empty and filled symbols indicate points taken from field and temperature sweeps, respectively. The consistency between the two methods is not perfect, which we attribute to the relatively broad transition. As we can see in Fig. 5.32 the $B_{c2,\perp}(T)$-dependence for $p = 4.0$ kbar and 4.3 kbar behave almost identical. We observe a positive curvature for temperatures lower than 40 mK. Such a positive curvature of $B_{c2,\perp}(T)$ was already observed in α-KHg by D. Andres below p_c [27], see Fig. 5.8. This is a result of the CDW state and was explained by the existence of SC islands rather than bulk superconductivity [75]: When the size of the SC regions becomes smaller than the coherence length, the resistive transition maybe largely determined by the coupling of the SC islands or filaments rather than the B_{c2} within the islands, causing an enhancement of the measured B_{c2}.

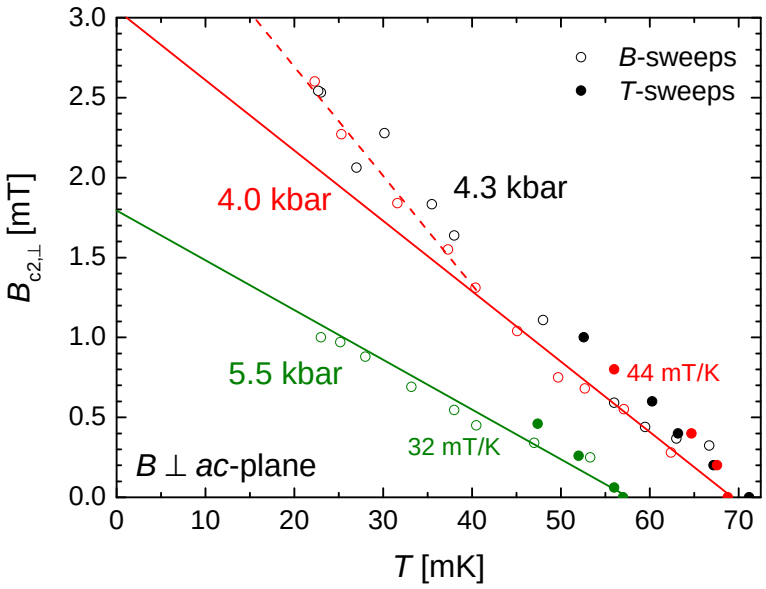

Figure 5.32: B-T phase diagram of α-TlHg for $B \| b^*$ at three different pressures. The empty and filled circles indicate points obtained from field and temperature sweeps respectively. (from [41])

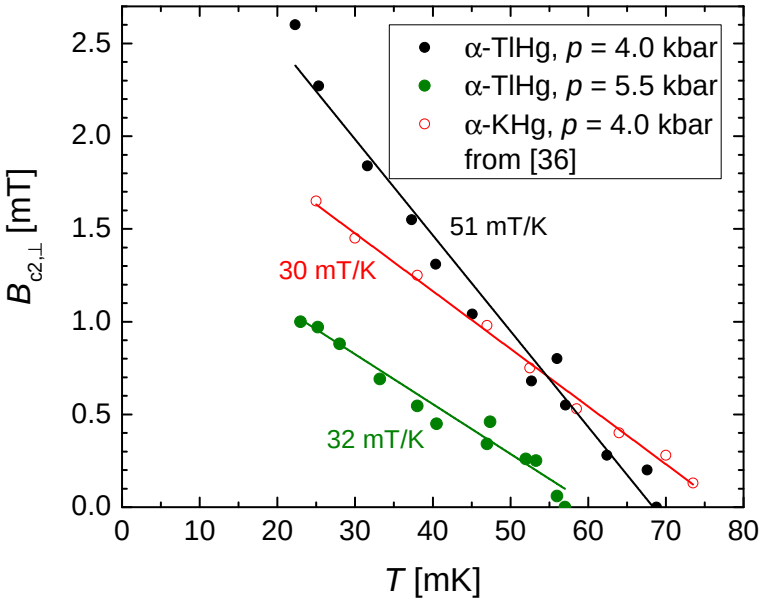

Figure 5.33: Comparison of the B-T phase diagram of α-TlHg (filled symbols) at two different pressures with α-KHg (empty symbols) at $p = 4.0\,\mathrm{kbar}$ from [36].

Similar effects were for example observed in $TMTSF_2PF_6$ [151–153].

In Fig. 5.33 we compare the $B_{c2,\perp}(T)$-dependence of α-TlHg at two pressures with the $p = 4.0\,\mathrm{kbar}$ curve of α-KHg. We can see a significant difference in the slope. When looking at the same pressure of $p = 4.0\,\mathrm{kbar}$ the slope of α-TlHg is about 40% higher even with a slightly lower T_c. However, this might be expected since the system in the Tl-salt is still in the CDW state. But even when looking at $p = 5.5\,\mathrm{kbar}$ the slope of α-Tl is still slightly higher than the slope of α-KHg at 4.0 kbar. We remind that the T_c of the K-salt is 25% higher at the same pressure. This shows us that the SC state in α-TlHg is more robust to an applied magnetic field perpendicular to the layers. Since the electronic parameters like the Fermi velocity v_F should be very similar in the sister compounds, the reason for the higher slope remains an open question.

The coherence lengths of α-TlHg for the different pressures were calculated the same way as in α-KHg and are summarised in table 5.2.

p	T_c	$B_{c2,\perp}(0\,\mathrm{mK})$	$\xi_{\parallel,0}(\mathrm{avg})$
4.0 kbar	69 mK	3.5 mT	320 nm
5.5 kbar	54 mK	1.8 mT	430 nm

Table 5.2: Critical temperature, perpendicular critical field for $T = 0$ (linear extrapolation) and the resulting inplane coherence length of α-TlHg for different pressures.

5.4.2 Azimuthal anisotropy of superconductivity for inplane magnetic fields

Figure 5.34 illustrates the azimuthal anisotropy of the SC state of α-TlHg for two different pressures. The points were determined by the same method as the points in Fig. 5.10(b). For $p = 4.0\,\mathrm{kbar}$ we observe a clear φ-dependence of the SC dip magnitude, with the strongest superconductivity being observed at $\varphi = 50° \pm 5°$. For 5.5 kbar the field orientation corresponding to the strongest superconductivity seems to be the same. However, the scattering of the points is almost as big as the observed dependence, allowing us no definite conclusion, whether the anisotropy is really the same. This is caused by the fact that the angular sweeps were performed at too high field and temperature for this pressure.

When we compare this φ-dependence of the SC state with α-KHg, we come to the conclusion that the φ angle, at which we see the strongest superconductivity, within error range is the same for $p = 4.0\,\mathrm{kbar}$ (and maybe also 5.5 kbar) in α-TlHg and for overcritical pressure in α-KHg. This is an interesting result, since we know that in the K-salt at ambient pressure we have a shifted anisotropy as discussed above. Therefore, this seems to contradict the observations in α-KHg, where the anisotropy changes between overcritical and undercritical pressure. However, we have to keep in

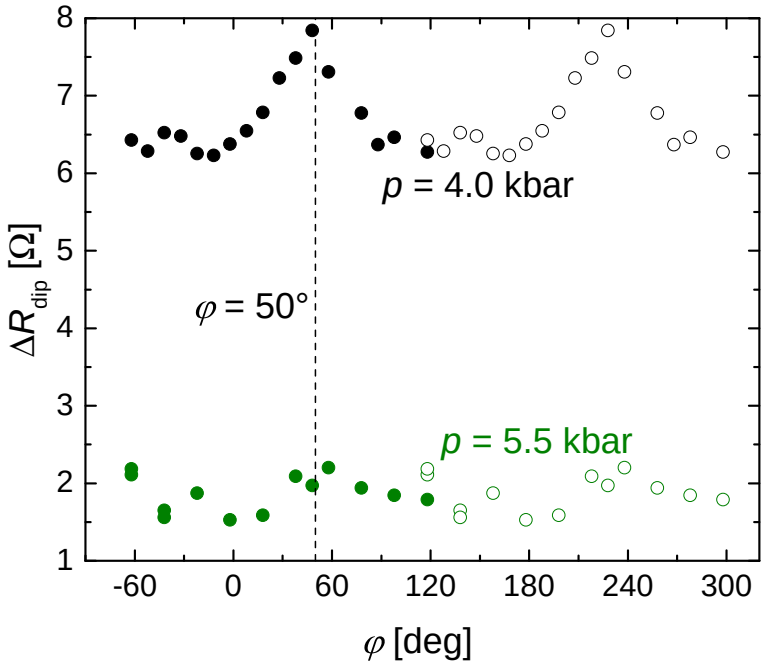

Figure 5.34: The depth of the dips caused by the SC state as seen in angular sweeps around parallel orientation calculated by $\Delta R_{\mathrm{dip}} = R(\theta = 93°) - R(\theta = 90°)$ for two different pressures. The angular sweeps were performed at $B = 50\,\mathrm{mT}$ and $T = 40\,\mathrm{mK}$. The empty symbols are the same data as the filled symbols translated by 180° for better visibility. (from [41])

mind that the anisotropy, which we observe in α-TlHg at 4.0 kbar is that of the sharp SC transition and not the one of the precursor, which is seen at higher temperatures. On the other hand the ambient pressure measurements in α-KHg only analysed the behaviour of this precursor, since there is no sharp transition at ambient pressure. So we could suggest that the SC state responsible for the precursor is different from the one responsible for the main transition, meaning we have a coexistence of the two states at this pressure. However, the electrons responsible for the SC state associated with the main transition seem to be the same above and below the critical pressure. To get further proof for this suggestion both studies of the SC precursor in α-TlHg at ambient pressure and of the bulk SC state (and maybe separately the precursor, if possible) in α-KHg at slightly undercritical pressure would be required.

Another notable difference is that the dependence looks less sinusoidal than in α-KHg, with a sharper peak at the strongest SC. We do not have a clear explanation for this behaviour yet, but maybe it can be attributed to the presence of the CDW state.

5.4.3 Phase diagram for inplane magnetic field

In Fig. 5.35(a) the B-T phase diagram for the magnetic field parallel to the layers is shown for $p = 4.0$ kbar. Like with α-KHg this dependence was studied for both the inplane direction with the strongest superconductivity $\varphi = 48°$ and the direction with the weakest superconductivity $\varphi = 138°$. The starting slopes for the respective φ orientations are similar to the ones observed in α-KHg at $p = 2.8$ kbar [38]. At this pressure also in α-TlHg a clear influence of the paramagnetic pair breaking effect is seen, since the curves flatten already significantly in the observed temperature range. This flattening is especially pronounce at $\varphi = 48°$, where the strongest SC was observed (see previous section). This is also reflected in the high Maki-parameter, which for this curve was determined as $\alpha = 4.5 \pm 0.8$.

In Fig. 5.35(b) we compare the phase diagram for inplane magnetic field for two differ-

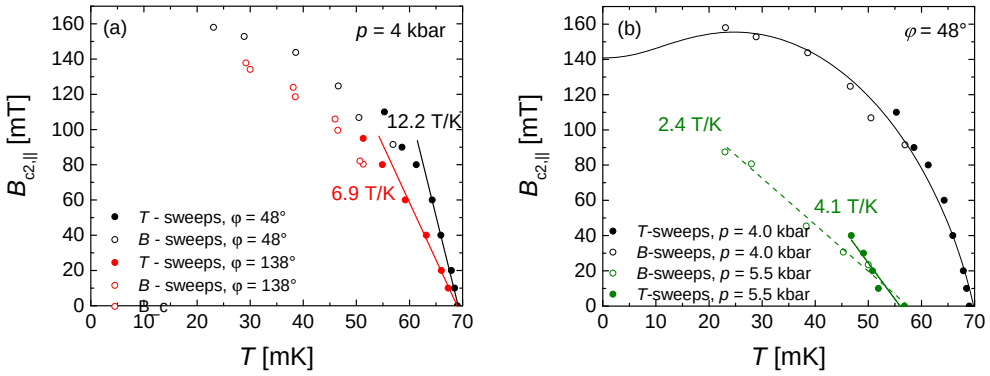

Figure 5.35: (a) The B-T phase diagram for $B \| ac$-plane for two different φ at $p = 4.0$ kbar. (b) The B-T phase diagram for $B \| ac$-plane for two different pressures at $\varphi = 48°$. The black line is a fit with Eq. (5.10) in order to obtain the Maki-parameter (both from [41])

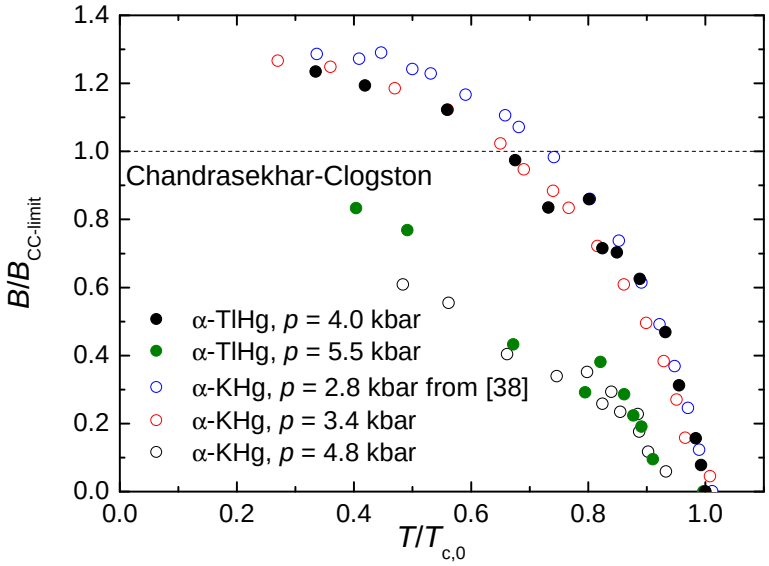

Figure 5.36: B-T phase diagram of α-TlHg (filled symbols) and α-KHg (empty symbols) for several different pressures at the respective φ with the highest SC. The temperature has been normalised to the respective T_c and the field has been normalised to the respective $B_{\mathrm{CC-limit}}$. The data for α-KHg are the same as shown in Fig. 5.17.

ent pressures of 4.0 kbar and 5.5 kbar, where $B_{c2,\parallel}(T)$ is shown for $\varphi = 48°$. For 5.5 kbar the consistency of field and temperature sweeps is worsened dramatically, allowing us only the use of temperature sweeps close to T_c and field sweeps at low temperatures. When comparing the slopes, even the higher slope determined from the temperature sweeps is notably lower than what we observed for 4.0 kbar. This indicates that the system is becoming more 3-dimensional and the orbital pair-breaking effect becomes dominant for most of the field range. Since the temperature dependence of the critical field is linear until the lowest temperature (which is $\sim 0.4\,T_c$), we would assume that no paramagnetic effect is observed any more for this pressure. This is also reflected in the perpendicular coherence lengths, which are presented in table 5.3.

p	φ	T_c	$\mathrm{d}B_{c2,\parallel}(0\,\mathrm{mK})/\mathrm{d}T$	$B_{c2,\parallel}(0)$	$\xi_{\perp,0}$	$\xi_{\perp,0}(avg)$
4.0 kbar	48°	69 mK	12.2 T/K	840 mT	1.3 nm	1.8 nm
	138°		6.9 T/K	480 mT	2.2 nm	
5.5 kbar	48°	54 mK	3.6 T/K	205	3.7 nm	-

Table 5.3: Critical temperature, the slope of $B_{c2\,\parallel}(T)$ close to T_c, the orbital parallel critical field (from extrapolation of the slope) and the resulting perpendicular coherence length of α-TlHg for different pressures.

These results we again compare to the results on α-KHg. Therefore, in Fig. 5.36 we have normalised the data for $p = 4.0$ kbar and 5.5 kbar to the respective T_c and the

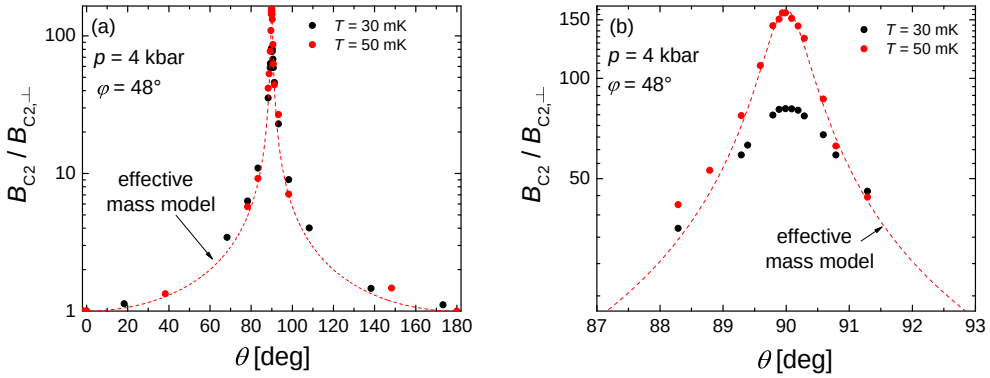

Figure 5.37: (a) θ-dependence of the critical field at $p = 4.0\,\text{kbar}$ and $\varphi = 48°$ for two different temperatures. The data has been fitted by the AGL model. (b) The same data as in (a) zoomed to a small θ range around parallel orientation. (both from [41])

respective Chandrasekhar-Clogston limit $B_{\text{CC-limit}}$. The data on α-TlHg are given by the filled symbols. For α-KHg we take the same data as shown in Fig. 5.17(b), which are now shown by the empty symbols. As we can see, the behaviour of α-TlHg at $p = 4.0\,\text{kbar}$ very much resembles its sister compound at 3.4 kbar. This means that the two compounds react almost identical to field applied parallel to the conducting layers. The $p = 5.5\,\text{kbar}$ curve of α-TlHg is somewhat similar to α-KHg at 4.7 kbar. The comparison of this dependencies shows us that at pressures close to p_c, the influence of the paramagnetic pair-breaking effect is similarly big in both of the compounds.

5.4.4 θ-dependence of the critical field

Finally, in α-TlHg also the θ-dependence of the critical field was studied for two different pressures. In Fig. 5.37 the critical field normalised to the respective $B_{c2,\perp}$ is shown versus θ at $p = 4.0\,\text{kbar}$ for two different temperatures. As we can see, the dependence is similarly sharp as observed in α-KHg. In Fig. 5.37(b) we can observe that the peak for the $T = 30\,\text{mK}$ curve is flattened, which is another clear evidence for the existence of paramagnetic pair breaking under these conditions, as discussed in the previous section. For the same reason the anisotropy at 50 mK is significantly higher than at 30 mK, as can be seen in Table 5.4, because the paramagnetic effect becomes less relevant at higher temperatures. However, if we look at the B_{c2} anisotropy at 50 mK we still get a significantly lower value than calculated from the coherence lengths. This means that even at $T = 50\,\text{mK}$ there is still a notable contribution from the paramagnetic effect. Looking at the phase diagram in Fig. 5.35(a) this seems realistic. In spite of this, the dependence is in very good agreement with the AGL model as shown by the fit in Fig. 5.37. Measurements at an even higher temperature were not possible because of the broad transition width. [9]

A similar θ-dependence of the critical field was also determined at $p = 5.5\,\text{kbar}$. In Fig. 5.38 the 5.5 kbar data is shown together with the 50 mK curve at 4.0 kbar. As we can see in Table 5.4, the anisotropy is smaller at 5.5 kbar, which is in agreement with

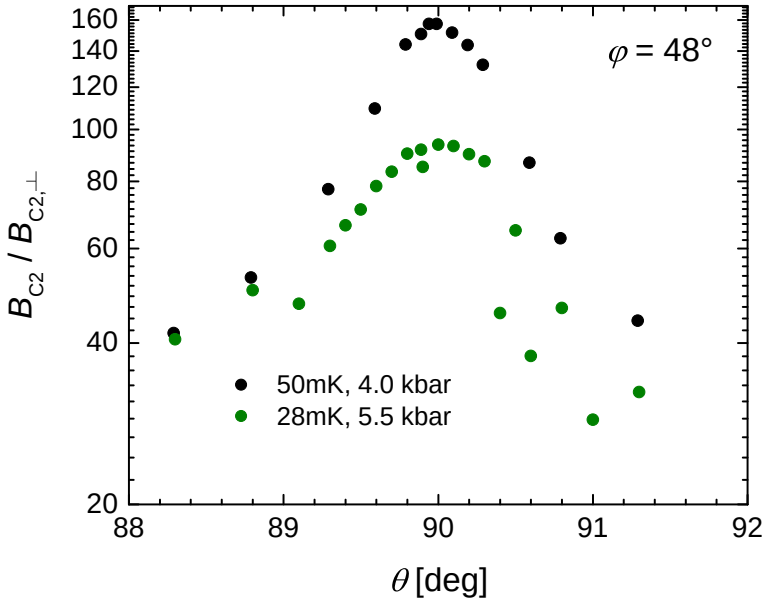

Figure 5.38: θ-dependence of the critical field normalised to $B_{c2,\perp}$ at different temperatures and different pressures for $\varphi = 48°$.

p [kbar]	T [mK]	$B_{c2,\parallel}/B_{c2,\perp}$
4.0	30	81
	50	160
5.5	28	94
	38	83

Table 5.4: The anisotropy parameters from the ration of the inplane and perpendicular critical fields for the different studied temperatures and pressures.

our expectations of the system becoming more 3-dimensional at higher pressure. In addition we do not observe a temperature-dependence of the critical field anisotropy at 5.5 kbar. This is in agreement with our observations that there is no longer an influence of the paramagnetic pair-breaking effect at this pressure. Overall the θ-dependence of B_{c2} in α-TlHg is very similar to that in α-KHg, yielding the same interpretations.

5.5 Conclusion: The anisotropic SC state in α-(BEDT-TTF)$_2$MHg(SCN)$_4$

The bulk SC state in α-KHg at overcritcal pressure is characterised by a very strong dependence of the critical field on the field direction in respect to the conducting layers. The critical field further shows a significant dependence on the azimuthal angle. The anisotropy of the coherence length $\xi_{\mathrm{GL}}(\theta)$ was found to decrease only slowly with increas-

ing pressure. The inplane coherence length changes only by a somewhat smaller factor as the out-of-plane coherence length resulting in only a small change of the anisotropy parameter. For slightly overcritical pressures a clear influence of the paramagnetic pair-breaking mechanism was detected for fields applied in the inplane direction. The Maki parameter was determined as $\alpha = 3.3$ at 3.4 kbar. In spite of a sufficiently high Maki parameter no sign for an FFLO state was found. At 4.7 kbar as expected no obvious influence of the paramagnetic pair-breaking mechanism was observed any more, clearly indicating that the system is becoming more three-dimensional.

Even though α-KHg exhibits a very high inplane coherence length compared to other organic charge-transfer salt superconductors, no crossover of the SC behaviour into the type I regime of superconductivity was found even for the highest measured pressure of $p = 4.7$ kbar. Estimations of $\xi_{\parallel}$ and λ_L for this pressure yield a GL-parameter κ of slightly bigger than $1/\sqrt{2}$, which would suggest our system to be in type I regime for fields perpendicular to the layers. However, our estimations of the mean free path ℓ raise questions, whether our system is in the clean limit of SC, which, in our case, would be necessary for the crossover into the type I regime. Since $\xi_{\parallel}$, λ_L and ℓ are of the same order of magnitude our system probably is in some intermediate regime concerning both cleanness and the type of superconductivity resulting in no clear hints for the crossover. However, we also have to take into account that a crossover into the type I regime of superconductivity is maybe hard to detect in the behaviour of the interlayer resistance.

A bulk superconducting state in α-TlHg was found under pressure for the first time. The critical pressure, where the CDW state in this compound becomes fully suppressed was determined as $p_c = (4.7 \pm 0.3)$ kbar, which is considerably higher than in the K-salt, and a large part of the p-T phase diagram could be established. For a more exact determination additional measurements in this pressure region would be necessary. The critical field anisotropy of the bulk SC state was found to be about a factor of 2 lower than in the K-compound. Still a clear influence of the paramagnetic pair-breaking was visible at pressures close to the critical pressure.

In both compounds the inplane anisotropy of SC was studied, yielding about the same φ-direction of the strongest superconductivity for both compounds in the bulk SC state. No clear four-fold symmetry was found, which would have been a strong evidence for a d-wave pairing. The direction of the strongest superconductivity is in neither of the directions, where one would naively expect the highest B_{c2} for either the q1D or the q2D FS sheets. However, comparison with the SC anisotropy of the K-salt in the SC/CDW state coexistence region reveal a shift in the φ angle of strongest SC of $20° \pm 5°$ which is about the same margin as the change of the direction of the q1D FS sheets between the CDW and the NM state. While the reason for the φ direction of the strongest SC is not yet clear, this suggests that the q1D FS sheets play an important role in the formation of the SC state.

6 Organic metals with magnetic ions: κ-$(BETS)_2FeX_4$ (X = Cl, Br)

In this chapter we will present the results on the organic antiferromagnetic superconductors κ-$(BETS)_2FeCl_4$ (κ-FeCl) and κ-$(BETS)_2FeBr_4$ (κ-FeBr). The focus was in the investigation of the interaction between localised magnetic moments and the conduction electrons. To that end magnetoresistive effects like SdH oscillations and AMRO were studied in both the AFM and PM state and the influence of magnetic field on the AFM state along different crystal axes was examined. The results on the low temperature resistive behaviour, the SdH oscillations in the AFM state and the magnetic phase diagram on κ-FeCl are reported in [154]. The results on the SdH oscillations in the normal and AFM state in κ-FeBr (Secs. 6.2.1 and 6.2.2) were jointly obtained with F. Kollmannsberger in the course of his bachelor thesis [26] and the results on the SC state and the studies of κ-FeBr under pressure (Secs. 6.2.3 and 6.2.4) were jointly obtained with L. Schaidhammer in the course of his master thesis [25].

6.1 κ-$(BETS)_2FeCl_4$

6.1.1 Low temperature resistance behaviour and superconductivity

Figure 6.1 shows the behaviour of the interlayer resistance of κ-FeCl between ambient and low temperature. The black and red curves are related to the same sample with the difference that the sample was recontacted between the two measurement runs and part of it broke off. The latter point is the reason for the higher ambient temperature resistance. Unlike for many other organic charge transfers salts, including the sister compound κ-FeBr, there is no pronounced maximum of the resistance during cooling. At around 150 K there is only a slight indication of a peak. In the range $5\,\mathrm{K} < T < 110\,\mathrm{K}$ the resistance shows a quadratic behaviour. A notable property of κ-FeCl is the huge resistance ratio (RR). For the measured samples the RR between 300 K and 0.5 K (where $T = 0.5\,\mathrm{K}$ was chosen as the lower temperature because it is just above the AFM transition) showed values of $\frac{R(300\,\mathrm{K})}{R(0.5\,\mathrm{K})} \cong 5000 - 15000$. These values, while being among the highest known RR values even when compared to usual clean metals, are typical for κ-FeCl [20, 21]. While the RR, as will be discussed in Appendix. A.1.1, is not always a very reliable indicator for the sample quality, such a high value is bound to indicate a very low rate of impurity scattering.

In Fig. 6.2 we see the low temperature part of the $R(T)$ of the same sample under the same conditions. A clear kinklike feature, where the resistance drops by about 5% is observed for all the curves indicating the transition to the AFM state [21]. From these

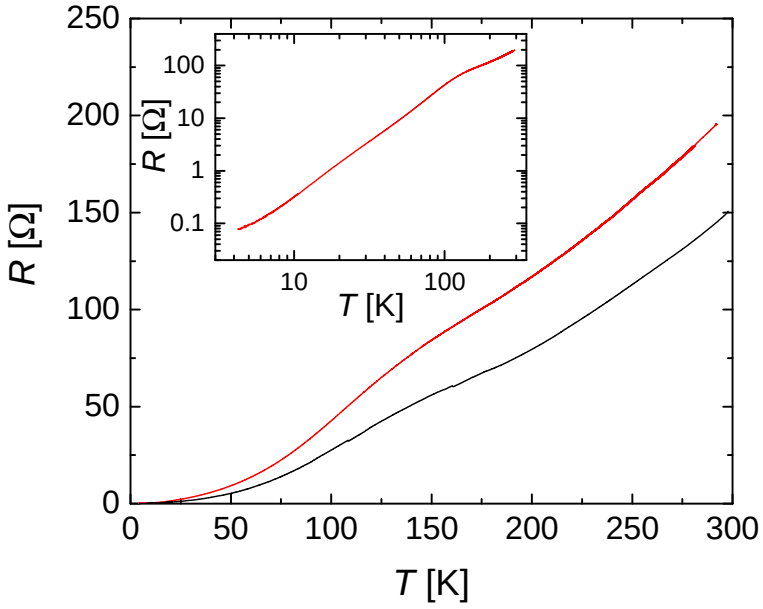

Figure 6.1: $R(T)$ of one sample of κ-FeCl in two different cooling runs between 300 K and 4 K. The sample was recontacted in between the measurements and part of the sample broke off. The inset shows the same data as the red curve in the main graph plotted in double logarithmic scale.

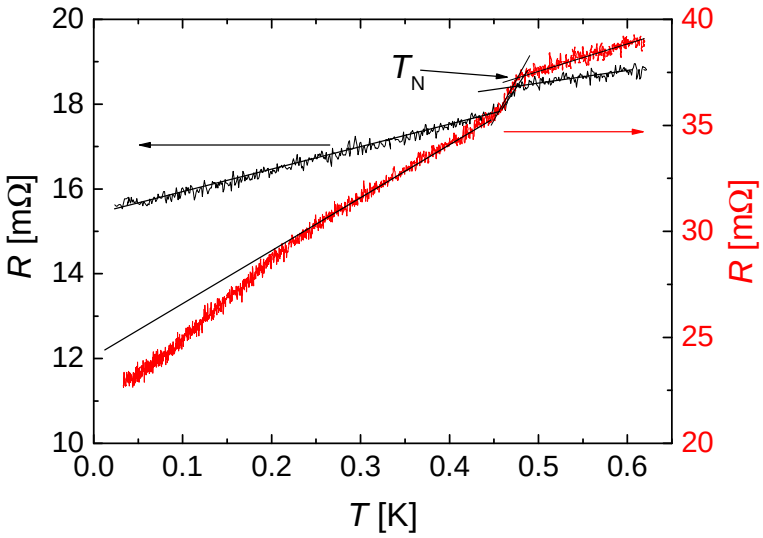

Figure 6.2: Interlayer resistance $R(T)$ of κ-(BETS)$_2$FeCl$_4$ below 0.6 K for one sample in two different cooling runs with a measurement current of $I_s = 1\,\mu$A. The black curve shows the initial sample, while the red curve shows the same sample after a part broke off. T_N was determined as shown by the crossing of linear fits to the transition and the resistance behaviour above.

sweeps the Néel temperature was determined to be $T_N = 473 \pm 2\,\mathrm{mK}$. The origin of this step in resistance is supposed to be a reduction of spin-dependent scattering, when the system performs the transition into the magnetically ordered state [21] and is a clear evidence of the π-d interaction between the conduction electrons and the localised magnetic moments.

There is still a considerable linear temperature dependence of the resistance below 1 K, $\frac{1}{R}\frac{\mathrm{d}R}{\mathrm{d}T} = 0.15\,\mathrm{K}^{-1}$, down to the AFM transition temperature for the black curve and even $0.37\,\mathrm{K}^{-1}$ for the red curve. Interestingly these slopes are doubled below the AFM transition. This linear dependence, seen until the lowest measured temperature, without showing any sign of saturation, has been considered as an indication of a possible non Fermi liquid behaviour for a number of materials [155–157]. This suggests that our system is close to a quantum critical point. It is, however, not clear, whether the transition from the AFM to the paramagnetic (PM) state is the reason for this behaviour. Indeed, the AFM state in κ-FeCl is an ordering of the localized Fe spins only and, therefore, is not expected to cause a linear $R(T)$ behaviour. However, it might be that also the conduction electron system is close to a magnetic ordering triggered or assisted by the ordered Fe spins similar to the ground state in the isomer λ-$(BETS)_2FeCl_4$ (λ-FeCl) [17, 120, 122]. But since the present compound has a strongly dimerised structure and, hence, a half-filled conduction band it is also possible that we are in the vicinity of a Mott state. From the BEDT-TTF salts it is known that a Mott state is typical for κ-phases [6, 11, 158]. It is, however, hard to judge, whether we have sufficient onsite repulsion in our compounds to cause an instability in the conducting electron system in κ-FeCl. The monotonic $R(T)$ when cooling from ambient temperature and the high resistance ratio rather suggest a good metallic character.

Despite the high crystal quality (according to the resistance ratio), a firm evidence of a SC state was not found in our measurements. While we cannot detect any sign of a SC

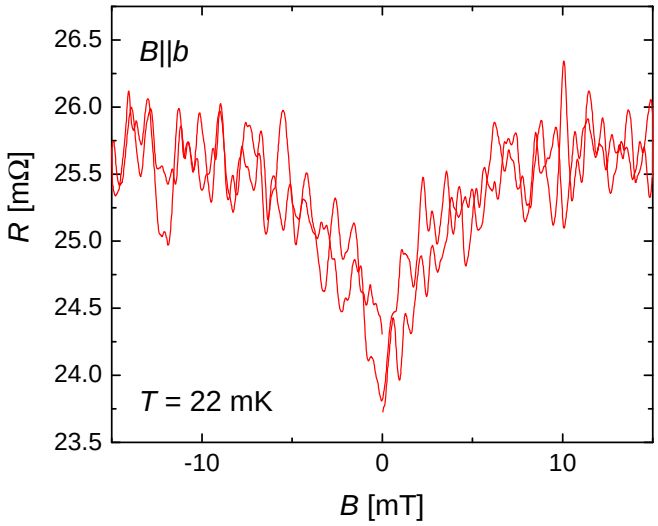

Figure 6.3: The interlayer resistance as a function of magnetic field applied perpendicular to the conducting layers.

state in the first run (black curve in Fig. 6.2), in the second run (red curve in Fig. 6.2) we see a small downturn from the linear extrapolation below 0.2 K (reproducible in two subsequent cooling runs). This downturn can be suppressed by the application of a small magnetic field of 10 mT applied perpendicular to the layers as we can see in Fig. 6.3. This figure shows a field sweep with magnetic field applied perpendicular to the conducting layers revealing a dip in the resistance around zero field. This might indicate an inhomogeneous, filamentary SC state, where the onset temperature of $T = 0.21$ K is in agreement with earlier reports on magnetisation measurements [21]. The data presented in Fig. 6.2 is, to the best of our knowledge, the first hint of a possible SC state by resistance measurements. For example Otsuka *et al.* [21] report $R(T)$ measurements down to 60 mK without any sign of a SC transition. In our studies this feature was only seen in one sample.

If the observed feature is indeed caused by superconductivity, then it is present only in a very small volume fraction of the sample. This is in agreement with the reports on AC-susceptibility where the detected SC signal also corresponded to a SC volume of less than 1% of the sample volume [21]. This could mean that the SC state in this compound only appears because of internal strain and, therefore, in our sample was only seen after breaking. In the AC-susceptibility measurements a polycrystalline sample was used [21], which could explain the appearance of internal strain in their sample.

6.1.2 Shubnikov-de Haas oscillations in the normal metallic state: Determination of the exchange field

We will start with discussing the normal state properties of the compound. Figure 6.4(a) shows the interlayer resistance of κ-FeCl as a function of magnetic field applied perpendicular to the conducting layers at a temperature $T = 0.46$ K. Above 1 T the sample shows hardly any magnetoresistance. Starting from $\mu_0 H = 6$ T Shubnikov-de Hass (SdH) oscillations with several frequencies become visible. The fast Fourier transformation (FFT) spectrum for $\theta = 0°$ is shown in Fig. 6.4(b). The dominant peak at a frequency of $F_\alpha = (873 \pm 3)$ T originates from the α-orbit on the Fermi surface ($\sim 20\%$ of 1st Brillouin zone area, see the inset in Fig. 6.4(a)). In addition, the β-oscillations originating from magnetic breakdown with $F_\beta = (4280 \pm 20)$ T ($\sim 100\%$ of first Brillouin zone area) are visible. The obtained FS areas follow the predictions from band structure calculations [20]. The three smaller peaks in between correspond to the frequencies of $2F_\alpha$, $F_\beta - 2F_\alpha$ and $F_\beta - F_\alpha$ and are a result of quantum interference and, possibly, the frequency mixing effect, often observed in highly 2D organics [9].

Such field sweeps were done at several different temperatures. The oscillatory component of the resistance normalised to the background resistance is shown in Fig. 6.5. While for the lowest temperature the oscillation amplitude is higher than 20% of the background resistance it decreases with increasing temperature as expected. By plotting the temperature dependence of the amplitude and fitting it with the temperature damping factor from LK-theory (Eq. (2.11)) the effective cyclotron mass can be determined. For the α-frequency the result was $m_c = 3.3\, m_e$ and for the β-frequency $m_c = 6.0\, m_e$. These values are in agreement with earlier measurements by Harrison *et al.* [116] and Pesotskii *et al.* [159]. Additionally, we also obtained slow oscillations

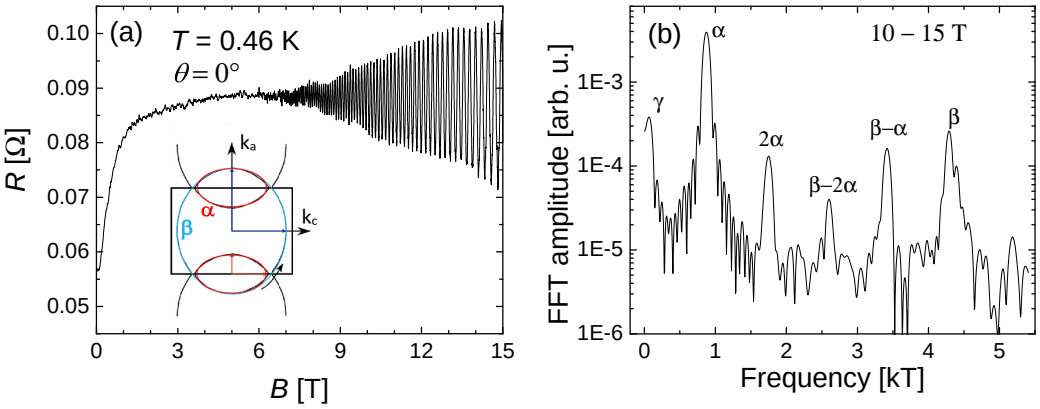

Figure 6.4: (a) Resistance of κ-FeCl as a function of magnetic field applied perpendicular to the conducting layers. The inset shows the FS, where the red ellipse is the α-orbit and blue the β-orbit. (b) The FFT spectrum of the curve between 10 and 15 T.

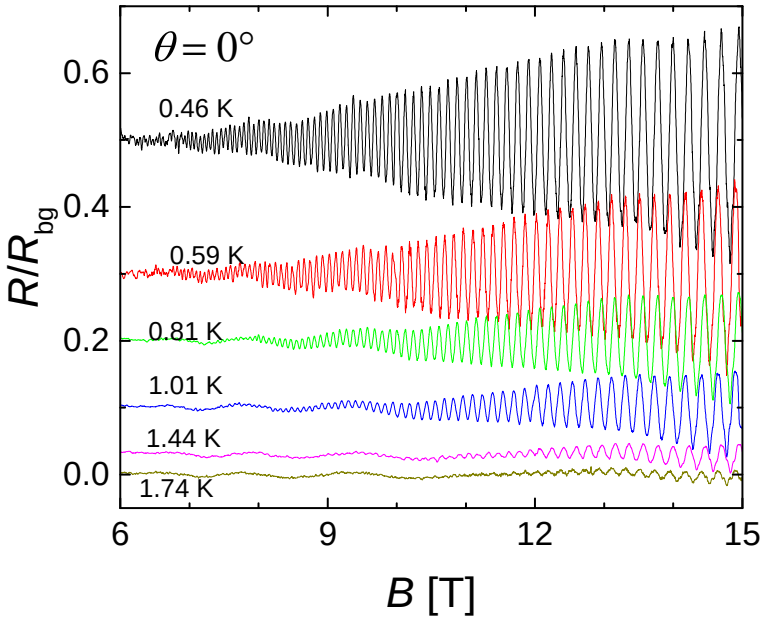

Figure 6.5: Oscillatory component of the signal after normalising to the background resistance R_{bg} at different temperatures. The curves are vertically offset for better visibility.

with a frequency of 48 T (corresponding to 1.1% of the FBZ area) labelled γ in the FFT spectrum (Fig. 6.4(b)). By eye these γ-oscillations are better visible at higher temperatures in Fig. 6.5. These γ oscillations, however, only become well pronounced, when tilting the field away from the exact perpendicular orientation (see $\theta = 20°, 55°$ in Fig. 6.6). These frequencies are very similar to those obtained in the κ-FeBr salt

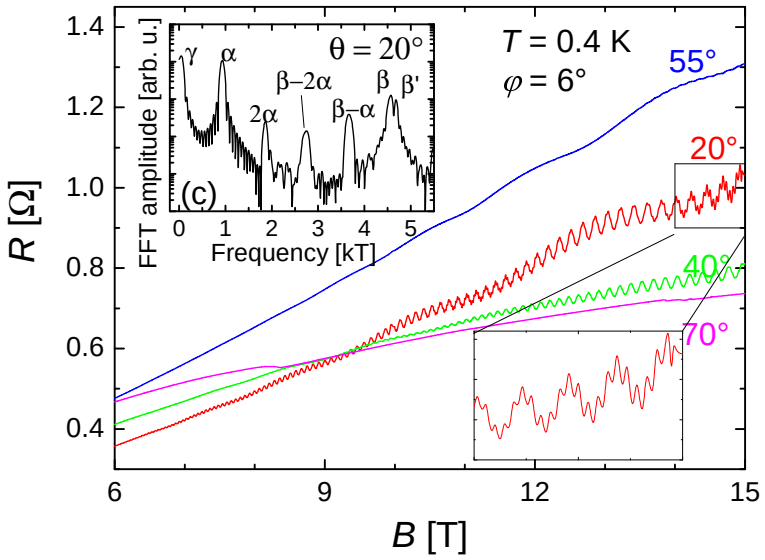

Figure 6.6: (a) High field magnetoresistance at different polar angles θ. The inset shows the FFT spectrum for $\theta = 20°$.

[23]. The slow oscillations are analogous to those seen in [117, 118] and could not be explained yet. The cyclotron masses of both α and β orbits are smaller than in κ-FeBr, where $m_{c,\alpha} = 5.2\,m_e$ and $m_{c,\beta} = 7.9\,m_e$ [117, 118], which is a sign of a weaker electron correlation. The oscillation frequency for tilted field follows a $1/\cos\theta$-dependence as expected for cylindrical FSs.

In order to obtain more information about the interactions in the system, the θ dependence of the SdH oscillations was studied. Figure 6.6 shows sample curves with SdH oscillations in the field range $6\,\mathrm{T} < \mu_0 H < 15\,\mathrm{T}$ for different tilt angles θ within the *bc*-plane. The magnetoresistance is much higher than for perpendicular field, but it strongly depends on the angle due to strong AMRO (as visible in Fig. 6.9). We can see that the relative amplitude of the different frequencies varies with θ. For example it can be directly seen in the raw curve at $\theta = 20°$ for fields bigger than 13 T that the β frequency is sufficiently stronger than it is at 0° (shown in the bottom right of Fig. 6.6). For $\theta = 20°$ and 55° the γ frequency is especially strong, while for $\theta = 40°$ and 70° it is hardly visible. Of course, at high angles all frequencies become difficult to detect.

On the $\theta = 20°$ curve in Fig. 6.6 one can see by eye that the β oscillations show a beating behaviour with a local minimum in amplitude at about $B = 13\,\mathrm{T}$. This beating is reflected in a splitting of the β peak in the FFT spectrum for $\theta = 20°$ shown in the inset of Fig. 6.6. This splitting is in accordance with data from Pesotskii *et al.*[159] and has also been observed in κ-FeBr [117, 118] and λ-FeCl [160]. It was interpreted by Cépas *et al.* [99] as a result of the exchange field B_e as described in Sec. 2.4.3. By measuring the beat frequency F_{beat} one immediately gets access to the exchange field [99]. However, in our case F_{beat} of the β-oscillations is too small to be determined reliably from a single field sweep because we could not resolve more than one node.

In order to obtain a more exact evaluation of the the exchange field, we carried out a

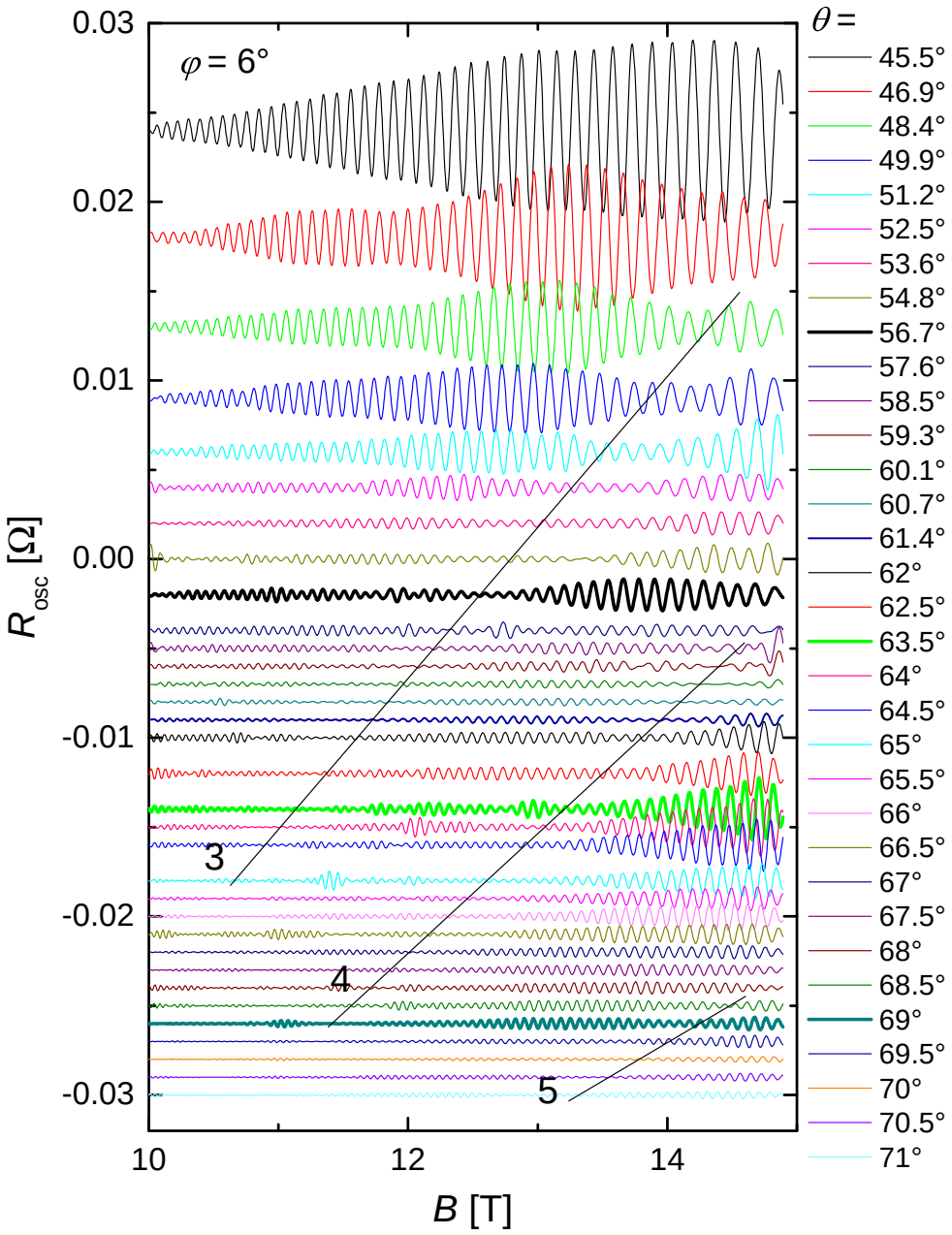

Figure 6.7: α-component of high field SdH oscillations obtained by inverse FFT with subtracted background at different polar angles θ. The azimuthal angle of the field rotation plane was $\varphi = 6°$ (close to the bc-plane). The curves are vertically shifted. The lines are guides to the eye connecting approximate positions of oscillation nodes, indicating that the nodes move to lower field for higher angles. The lines are numbered 3, 4 and 5 in respect to the order of the nodes. The thicker lines indicate the curves, which were taken at AMRO maxima.

series of field sweeps at different angles of θ. Fig. 6.7 shows the α component of the high field SdH oscillations at different polar angles θ, where the field was rotated close to the bc-plane ($\varphi = 84°$). The curves shown are obtained by subtracting background and filtering out higher and lower SdH frequencies with an inverse Fourier transformation. Starting from $\theta \approx 45°$ clear modulations in the oscillation amplitude appear. Most curves do not show a full node. In our data the amplitude rather has a minimum and the phase shifts gradually with field. The absence of perfect nodes could be due to the fact that the bands for spin-up and spin-down give different contributions to the conduction and/or scattering processes. Since we are measuring the interlayer resistance, the electrons have to tunnel through the layers containing the localised magnetic moments. Some spin-dependence of this tunnelling process cannot be excluded. This would result in non equal amplitudes for spin-up and spin-down electrons, respectively [46].

One has, of course, to distinguish the nodes caused by the field dependent spin-splitting factor of Eq. (2.55) from those caused by a weak warping of the Fermi surface cylinder along k_z [9, 51] and by twinning. Fortunately this can be done by inspecting the evolution of beats with changing the field orientation. In case the beats originate from the Fermi surface warping the behaviour of the modulations should be linked to the AMRO (angular magnetoresistance oscillations). In this case the frequency of the beats and, therefore, the posistions would be oscillating. In particular they must vanish at the positions of the AMRO maxima [65, 161], which for the present case are observed for $\theta = 55.8°$; $63.5°$ and $68.7°$ (as visible in Fig. 6.9). In Fig. 6.7 the fields sweeps at θ-positions close to the AMRO maxima are bold. However, in our case the nodes shift monotonously over the full covered θ-range, with no notable change at the AMRO peaks. So FS warping as reason for the nodes can be ruled out.

If we have one or more crystallites with slightly different orientations, the areas of the Fermi surface cross section perpendicular to the field are slightly different. This causes beats in the SdH oscillations where the beat positions shift to higher fields with increasing θ. Instead in Fig. 6.7 we see these beat minima shift to lower fields with increasing angle θ (the black straight lines approximately point out the "node" positions). So we can conclude that twinning is also not the reason for the beats. Taking into account that a shifting of the beat positions to lower fields with increasing θ is a rather unusual behaviour for q2D metals, it seems unlikely that there are other possible explanations for the beats apart from them being caused by the influence of the exchange field.

In Fig. 6.8 we plot the positions of the nodes in B vs. θ. Their positions can be fitted by taking them as zeros of the spin-splitting factor in the presence of an exchange field ($R_s(H) = 0$) given in Eq. (2.55). For that Eq. (2.55) was solved to B yielding

$$B = \frac{B_e}{\cos(\theta)\left(\frac{1}{2} - n\right)\frac{2}{g\,m^*} + 1}, \tag{6.1}$$

where $n = 1, 2, ...$ is the order of the node counting from the exchange field, $m^* = m_c/m_e = 3.3$ for the α-oscillations and $g = 2$ the Landé factor. During the fitting procedure it became clear that the first appearing node in fact corresponds to $n = 3$.

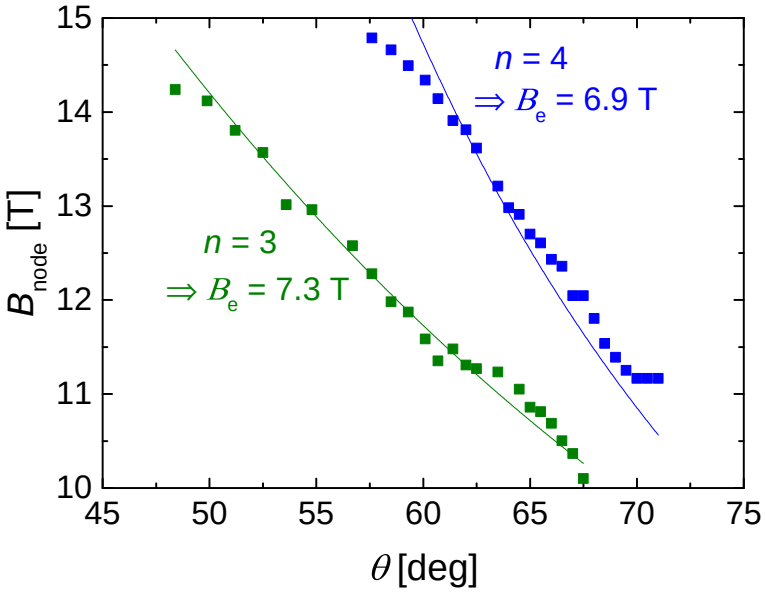

Figure 6.8: The field dependence of the node positions fitted with Eq. (6.1) for the first appearing node (green) and the second appearing node (blue).

We obtained $B_e = (7.3 \pm 0.2)$ T for $n = 3$ and $B_e = (6.9 \pm 0.5)$ T for $n = 4$. The third node was only observed in a very narrow range of $69° < \theta < 71°$ and did not provide a reliable result.

The obtained value of $B_e \approx 7$ T is about 20% higher than theoretically predicted by Mori and Katsuhara, [98] $\mu_0 H_e = 5.8$ T. Taking into account the approximate character of the theoretical estimation, this can be considered as a good agreement. The value is considerably lower than for κ-$(BETS)_2FeBr_4$ (~ 12 T, estimated from the position of the center of the field-induced SC (FISC) dome [22]).

Interestingly, as mentioned above, the observed nodes correspond to $n = 3, 4$ as a result of the fit. The nodes corresponding to $n = 1$ and $n = 2$ remained completely invisible. For $\theta = 0°$ the node $n = 1$ in α would be expected for a field value of $B = 8.25$ T and moves to even smaller fields for increasing θ. At $\theta > 25°$ the node position is outside the field range where the oscillations are observed. For $\theta < 25°$ the SdH oscillations are observed down to sufficiently low fields. The $n = 2$ node should be even easier to observe, as it is expected to be at $B = 12.5$ T for $\theta = 0°$ and shifts to below 10 T only for $\theta > 50°$. We do not have an explanation for the absence of the nodes in this region to date. Note that in κ-FeBr also no nodes in the α oscillations at low θ were observed. The results of similar measurements on κ-FeBr are presented in Sec. 6.2.1 and will be further discussed there.

A similar analysis was performed for the β oscillations in κ-FeCl. However, in the angular range of $|\theta| < 20°$ an anomalous behaviour of the nodes was found. Further above $|\theta| > 30°$ the amplitude of the β oscillations becomes to weak for an accurate determination of the node positions. Therefore, it was not possible to determine a reliable value of the exchange field from β.

6.1.3 Construction of the Fermi surface from angular magnetoresistance oscillations (AMRO)

In order to gain more information about the FS we studied the angular magnetoresistance oscillations (AMRO). Figure 6.9 shows the interlayer resistance plotted against the polar angle θ at a magnetic field of $B = 15\,\mathrm{T}$ and a temperature of $T \approx 0.48\,\mathrm{K}$. The azimuthal angle was $\varphi = 6°$, which is the same φ as was used for the θ-dependent SdH oscillation study above. Strong oscillations in θ are observed, which are periodic in $\tan(\theta)$. In addition, for $\theta < 45°$ we also see SdH oscillations. At $\theta = \pm 90°$ a sharp peak feature appears with a height of almost 20% of the background resistance. This feature, which is associated with coherent interlayer transport and, therefore, often called a coherence peak (see Sec. 2.2.2), will be discussed more closely later.

In Fig. 6.10 we can see θ-sweeps at different magnetic fields at $T = 1.4\,\mathrm{K}$ for an azimuthal angle $\varphi = 96°$ (close to the ab-plane). Unlike for $T = 0.48\,\mathrm{K}$, no SdH oscillations are seen any more even for highest fields. At this φ for $\theta > 60°$ an influence of additional AMRO sets becomes visible. The position of the peaks remains constant when the field is reduced, demonstrating that the oscillations are related to the geometry of the FS. The amplitude of the dominating component at $B = 15\,\mathrm{T}$ reduces strongly with decreasing field. The other frequencies' amplitudes decrease by a smaller extent and, therefore, become better visible at lower fields. At $B = 2.2\,\mathrm{T}$ the component dominating at high field is completely suppressed and only slower oscillations remain, as indicated by the black arrows in Fig. 6.10. We can understand this behaviour as follows: The dominating frequency at high fields is a result of the magnetic breakdown orbit β (as described in Sec.6.1.2). At low enough field the electrons can no longer tunnel

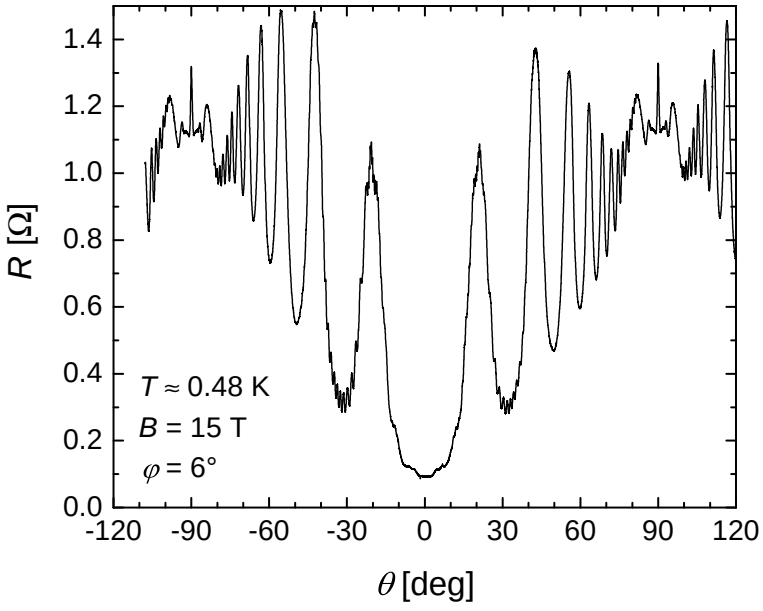

Figure 6.9: The interlayer resistance as a function of the polar angle θ at $T \approx 0.48\,\mathrm{K}$, $B = 15\,\mathrm{T}$ and $\varphi = 6°$ (close to bc-plane).

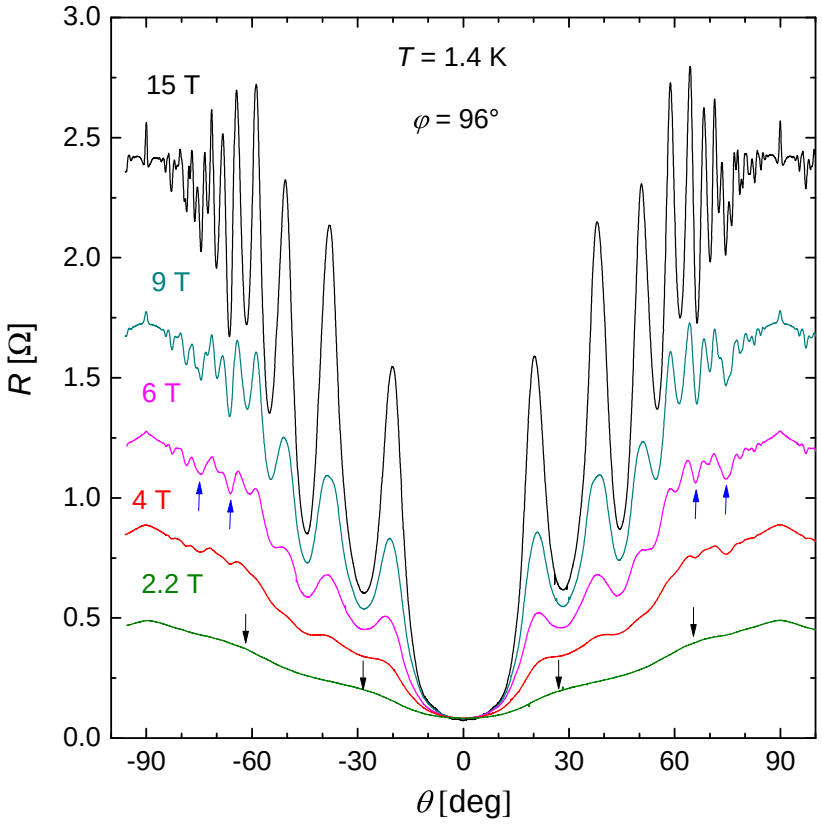

Figure 6.10: AMRO curves at different fields for $T = 1.4\,\mathrm{K}$ and $\varphi = 96°$ (close to ab-plane). The black arrows on the 2.2 T curve indicate the AMRO maxima for the slower frequency, which become visible when the higher frequency AMRO are suppressed. The blue arrows on the 6 T curve indicate a few characteristic LMA dips.

through the gap between different FSs and the contribution of the β-orbit vanishes. The remaining set of AMRO at low B can be associated with the classical α-orbit, which does not require magnetic breakdown.

The contribution from the α-frequency is, of course, difficult to analyse, because it is covered by the dominant β-frequency at high fields. It also gets rather weak at low fields making it impossible to see more than the first two maxima. Therefore, fast Fourier transformations were used to analyse the AMRO in a similar way like for the SdH oscillations. Since all AMRO effects are periodic in $\tan\theta$, we first transformed the x-axis into $\tan\theta$ and then performed a FFT in the range $\tan 25° < \tan\theta < \tan 85°$. Figure 6.11(a) shows an example of a FFT spectrum of the 15 T curve in Fig.6.10; the frequency is in units of $(\tan(\theta))^{-1}$. The two most prominent peaks can be associated with the AMRO from the 2D α- and β-orbits. But even a third peak was detected, which originates from the Lebed-Magic-angle (LMA) resonances caused by the 1D part of the FS. For some values of φ the characteristic dips of the LMA could also be seen directly in $R(\theta)$ curves as shown by the blue arrows in Fig. 6.10. The small peak at the

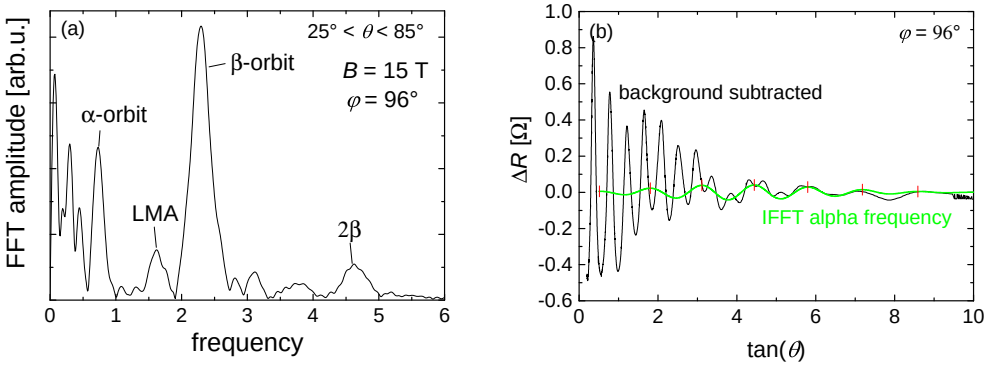

Figure 6.11: (a) Example of a FFT spectrum originating from a θ-sweep at $T = 1.4\,\mathrm{K}$, $B = 15\,\mathrm{T}$ and $\varphi = 96°$ in the angle range of $25° < \theta < 85°$. The frequency is in units of $(\tan\theta)^{-1}$. (b) The inverse FFT of α-peak of the FFT shown in (a) in comparison with the original curve, both plotted against $\tan\theta$.

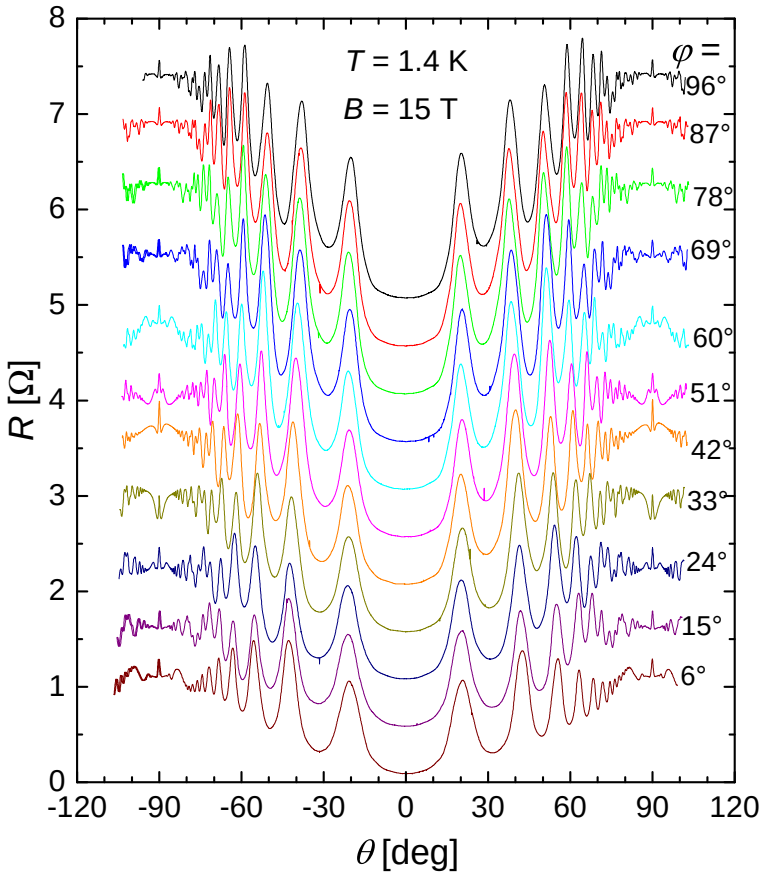

Figure 6.12: AMRO curves at different angles φ for $B = 15\,\mathrm{T}$ and $T = 1.4\,\mathrm{K}$. The curves are vertically shifted for better visibility.

frequency $f \approx 4.6$ probably corresponds to 2β and has to be expected for oscillations with such an anharmonic shape (sharp peak and rather broad dip). In order to get the exact positions of AMRO peaks from the α-orbit and the LMA dips, an inverse FFT was used as shown in Fig. 6.11(b).

The same three AMRO components could already be resolved in the sister compound κ-FeBr by Konoike *et al.* [23] and have been confirmed by our own measurements [25].

Figure 6.12 shows angular sweeps for different values of the azimuthal angle φ. The sweeps are shifted vertically for better visibility. We observe some shift in the AMRO peak positions for the dominating frequency as expected. The coherence peak at $\theta = \pm 90°$ is visible for all values of φ. By use of FFT analysis, as explained above, the φ-dependent frequencies of all 3 sets of AMROs could be determined. The results are shown in Fig. 6.13.

The frequency of the oscillations follows the relation $f = \frac{k_{\parallel}^{\max} d}{\pi}$, where $d = b/2$ is the interlayer distance. Assuming an elliptical shape of the FS cross sectional area, $k_{\parallel}^{\max}$ can fitted by

$$k_{\parallel}^{\max} = \left[(k_1 \cos\varphi)^2 + (k_2 \sin\varphi)^2 \right]^{\frac{1}{2}}, \tag{6.2}$$

with k_1, k_2 being the principal semiaxes of the ellipse. For the α-orbit we obtained $k_{1,\alpha} = 0.127\text{Å}^{-1}$ and $k_{2,\alpha} = 0.195\text{Å}^{-1}$ and for the β-orbit $k_{1,\beta} = 0.404\text{Å}^{-1}$ and $k_{2,\beta} = 0.324\text{Å}^{-1}$. The values are in reasonable agreement with the ones of the calculated FS at 10 K in [20], which are $k_{1,\alpha} = 0.127\text{Å}^{-1}$ and $k_{2,\alpha} = 0.217\text{Å}^{-1}$ for the α-orbit and

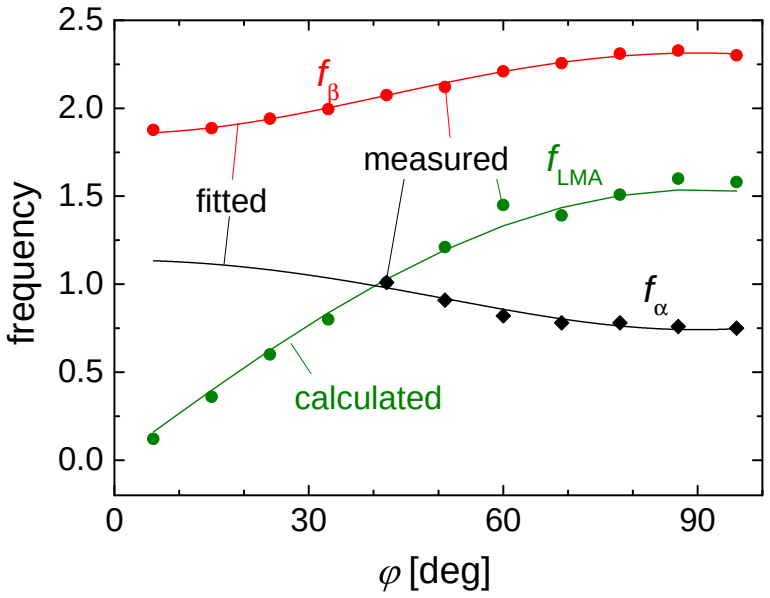

Figure 6.13: φ-dependence of the frequencies of the three AMRO components, f_α, f_β and f_{LMA}, found in the data shown in Fig. 6.12. The symbols indicate the measured frequencies. The red and black lines are fits to f_α and f_β. The green line is calculated from the LMA condition (Eq. (2.26)).

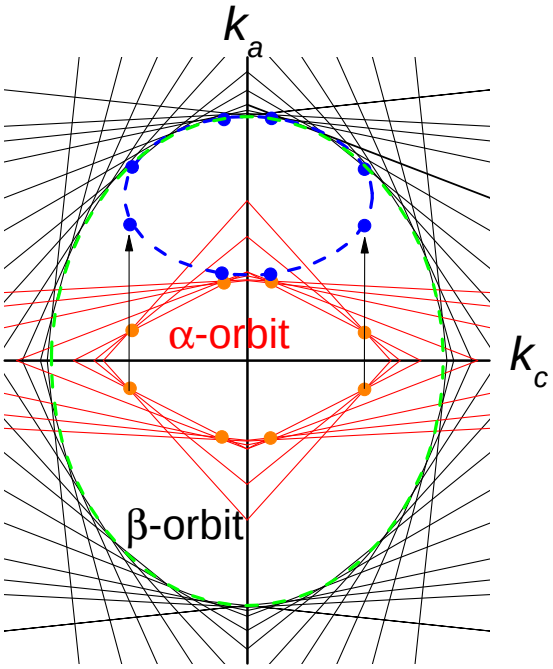

Figure 6.14: Construction of the Fermi surface from the AMRO frequencies. The black lines are tangentials to the β- and the red lines to the α-orbit, respectively. The blue points are from the α-orbit shifted in order to touch the β-orbit, with the blue ellipse inscribed to the points. The green ellipse is inscribed to the β-orbit.

$k_{1,\beta} = 0.396\text{Å}^{-1}$ and $k_{2,\beta} = 0.331\text{Å}^{-1}$ for the β-orbit.

The obtained periods for the α and β oscillations can be used for constructing the Fermi surface. The positions of the AMRO peaks follow the relation given in Eq. (2.32). $k_B^{\max}(\varphi)$ can be determined from the ARMO frequency $k_B^{\max}(\varphi) = \frac{\pi f(\varphi)}{d}$. For each φ we now can draw a line perpendicular to the direction of $\mathbf{B}_{\|}$ at the distance of $k_B^{\max}$ from the coordinate origin, which will be a tangential of the respective FS-orbit. If we do that for various φ the figure inscribed will be the FS cross section. This was done for both α- and β-frequencies. Due to the symmetry of the orthorhombic crystal structure the resulting lines could be translated to the other quadrants. The result is displayed in Fig. 6.14.

In Fig. 6.14 the black lines are tangents to the β-orbit and the red lines are tangents to the α-orbit. The construction very nicely reproduces the shape of the β-orbit. The FS area obtained from this construction is in good agreement with the one obtained from the SdH frequency. The semiaxes values from the ellipse in Fig. 6.14 of $k_1 = 0.40\,\text{Å}^{-1}$ and $k_2 = 0.33\,\text{Å}^{-1}$ are identical to the ones from the fit in Fig. 6.13 within our accuracy. When we compare the resulting area of the β-orbit to the value obtained from the SdH oscillations at low temperature, we also have a difference of less then 5% meaning that the elliptical form nicely describes the FS.

As the α frequency was much harder to resolve the values for $k_B^{\max}$ are somewhat less

accurate. In the range of $\varphi < 40°$ no contribution to the AMRO from the α-orbit was found. This is in agreement with the reported AMRO in κ-FeBr [23]. Also, of course, no tangentials for the α-orbit could be drawn for this φ-range. In the resulting construction in each quadrant most of the tangentials cross each other in one of two points marked orange in Fig. 6.14. We assumed that these crossing points must be points lying on the FS.

Note that AMRO do not determine the position of the FS in the FBZ. However, since we know that the β-orbit shares the FS sheet of the α-orbit in the upper and lower part, we should shift the points accordingly: Translating these points in k_a-direction and fitting them with an ellipse (blue points and blue dashed line in Fig. 6.14) shows that the curvature at the upper side is the same for the α- and for the β-orbit as necessary. We can, therefore, conclude that the consistency of the α-orbit is rather accurate. Also the obtained area is in good agreement with the SdH frequency and the values of the semiaxes of $k_1 = 0.13\,\text{Å}^{-1}$ and $k_2 = 0.21\,\text{Å}^{-1}$ are again only $\sim 5\%$ different from the theoretical values.

The frequencies of the LMA were calculated by

$$f_{\text{LMA}} = \frac{d}{a}\cos\varphi, \tag{6.3}$$

where $a = 11.787\,\text{Å}$ is a lattice constant. This follows from the LMA condition (Eq. (2.26)) after reducing it to the case, where we assume that the electrons can only cross one layer per hopping in b-direction, which is realistic for highly anisotropic materials.

While the frequency of the LMA resonances is well reproduced by the calculation, the exact positions of the resistance dips are not where one would routinely expect them to be. Usually the angles θ_n, for which we would expect the dips are given by [162]

$$|\tan\theta_n| = \frac{n}{\sin\varphi}\cdot\frac{a}{d},\ n = 0,\ 1,\ 2... \tag{6.4}$$

However, when we look at the experimentally observed dip positions, we see that they follow the condition

$$|\tan\theta_n| = \frac{n+1/2}{\sin\varphi}\cdot\frac{a}{d},\ n = 0,\ 1,\ 2... \tag{6.5}$$

We can maybe find an answer to this puzzle in the physical nature of the LMA resonance: We have a current through the sample applied in the direction perpendicular to the conducting layers ($B\|b$). An applied magnetic field causes a deflection of the conduction electrons in real space due to the Lorentz force. In the case, where the magnetic field is applied exactly parallel to a $(1, n)$-th component of the hopping integral in Eq. (2.22), i.e. along the vector $(na, b, 0)$ (assuming $\varphi = 0°$ for simplicity) the conduction electrons are not affected by the Lorentz force and the magnetoresistance is at a minimum. Usually this transport direction is along a translation vector of the crystal lattice and are indicated by the red lines in Fig. 6.15. In κ-FeCl, due to the parquet structure of the dimers in the κ-type packing of the $BETS^+$ radical cations, the next dimer in a direction lies at a distance of $a/2$. This might suggest that the condition for Lorentz-force free hopping is probably already fulfilled for all θ_n from Eq. (6.4) after

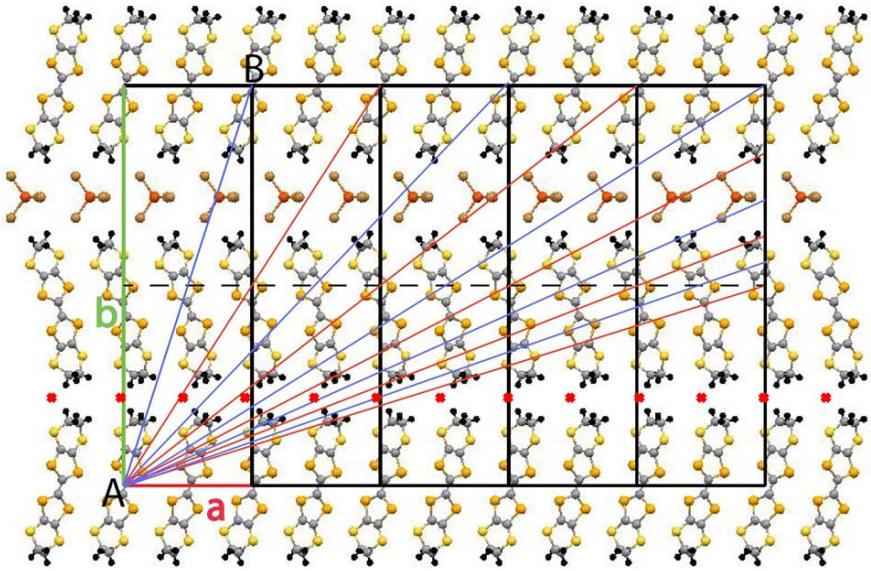

Figure 6.15: Directions of the interlayer charge transport as obtained from Eq (6.4) (red lines) and Eq. (6.5) (blue lines). Orthorhombic unit cells of the crystal lattice are indicated by black rectangulars. The red crosses indicate the positions of the Fe Atoms in the same layer, which are not shown. (from [25])

substituting a by $a/2$. However, this idea is also not in agreement with the observed condition given by Eq. (6.5).

A different idea is that the transport is influenced by the position of the $FeCl_4$ units in the anion layers. As we can see in Fig. 3.6 the $FeCl_4^-$ anions in neighbouring layers are shifted by half a period in both a and c direction. For this reason there are no visible $FeCl_4$ units in the lower anion layer in Fig. 6.15, where only half of the layer thickness in c direction is shown for better visiblity. Therefore, the positions of the Fe atoms in the ab-plane are indicated by the red crosses. When we now look at the directions of the blue lines in Fig. 6.15, the lines either pass directly through $FeCl_4$ units or, respectively, directly through the middle between two of them in the adjacent anion layers. The red lines on the other hand only slightly intersect the $FeCl_4^-$ ions. This brings us to the assumption that the half period shift of the LMA dips is connected to the shifts of the anions of half a lattice constant in adjacent anion layers.

In Fig. 6.16 θ-sweeps for $B = 15\,\mathrm{T}$ at different φ are shown for the magnetic field direction close to the parallel orientation ($80° < \theta < 100°$). The coherence peak looks very similar for all different φ.

The φ-dependence of the coherence peak width $2\theta_c$ is drawn in Fig. 6.17. The width of the peak varies between $\approx 0.75°$ and $\approx 1°$ yielding an anisotropy parameter $2t_\perp/E_F$ in the range of $\sim$ 0.006 to $\sim$ 0.009. From this we obtain a value of the interlayer transfer integral $t_\perp \approx 0.15\,\mathrm{meV}$, where E_F was estimated as 40 meV from the results of

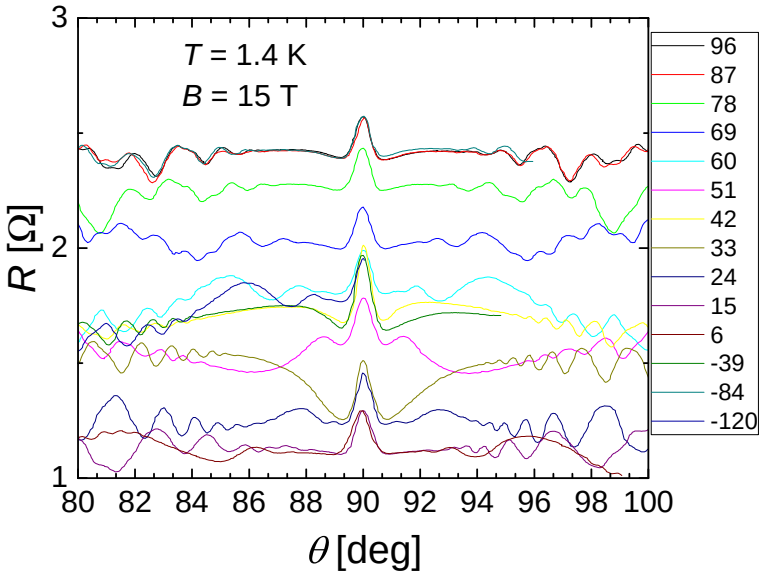

Figure 6.16: Coherence peak at different azimuthal angles φ.

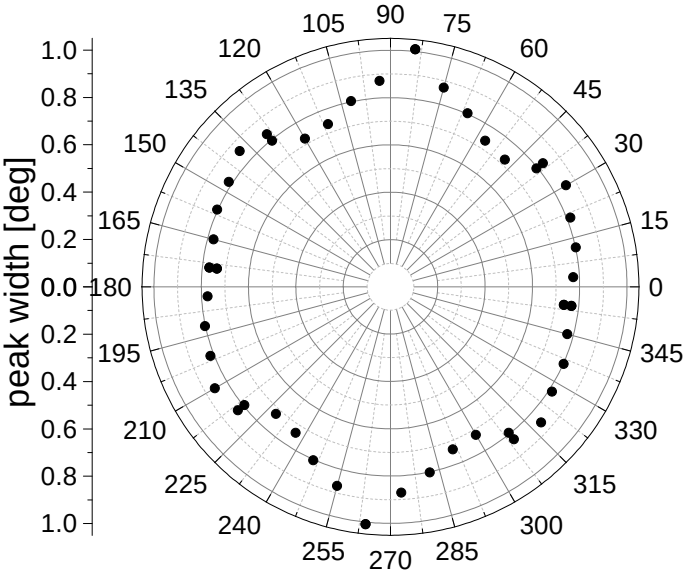

Figure 6.17: Angular dependence of the coherence peak width.

the SdH oscillations. This corresponds to a temperature of approximately 2 K. A sharp maximum of the coherence peak width is observed close to c-axis, while near a-axis we observe a broad minimum.

6.1.4 Magnetoresistance and SdH oscillations in the AFM state

Manifestations of the AFM state in magnetoresistance

In Fig. 6.18 the magnetic field dependence of the interlayer resistance for the field direction perpendicular to the layers is shown for $T = 0.18\,\mathrm{K}$. At $B = 1.3\,\mathrm{T}$ a resistance step similar to the kink feature in the temperature sweep (Fig. 6.2) is observed. Because of the similarity to the feature in $R(T)$, we suggest that this is the transition from the AFM to the paramagnetic (PM) state, caused by magnetic field. This guess is further confirmed by the fact that the SdH oscillations, which will be discussed in the next chapter, vanish at this feature like they do in κ-FeBr at the AFM–PM transition [23]. The field corresponding to this kink feature will be called B_k.

The low-field AFM state is characterised by a strong hysteresis of the magnetoresistance. The hysteresis loop is fully reproducible by sweeping the field up to B_k and back to 0 T. However, if the sweep direction is inverted at a field within the hysteresis range, the resistance shows a reversible behaviour, continuously changing in between the upper and lower branches of the hysteresis loops, see Fig. 6.19. The exact trace is thereby only determined by the value of the highest applied field. Since a similar hysteresis was also studied in κ-FeBr, which is presented in Sec. 6.2.2, we will discuss this hysteresis there.

SdH oscillations in AFM state

In Fig. 6.18 starting from $B = 0.8\,\mathrm{T}$ SdH oscillations with a frequency of 58 T appear (corresponding to 1.4% of the FBZ area). The FFT spectrum of the oscillations is shown in the inset of Fig. 6.18. The oscillations abruptly vanish at B_k. This means that these oscillations are inherent to the AFM state. They also show a clear dependence on the sweep direction and thermal history. As we can see in Fig. 6.18, the oscillation amplitude on the down-sweep is considerably lower than on the up-sweep. This would suggest a stronger scattering on the down-sweep. With increasing temperature the transition is shifted to lower fields, so the window for the observation of the SdH oscillations becomes smaller as we can see in Fig. 6.20(a). As a result, the determination of the effective cyclotron mass m_c from the temperature dependence of the oscillation amplitude is only possible in a very limited field and temperature range. Figure 6.20(b) shows the sweeps used for the determination of m_c. We determine $m_{c,\delta} = (0.82 \pm 0.1)m_e$ in the field window 0.8 T to 1.1 T and the temperature range between 0.18 K and 0.28 K using standard Lifshitz-Kosevich theory [46]. The fit of the temperature dependent amplitude with Eq. (2.11) is shown in Fig. 6.21(a). This mass is very high for such a small Fermi surface. It implies that many-body interactions and correlation effects are important in this system, which would be in agreement with the linear temperature dependence at low temperatures presented in the previous section.

According to the standard theory of SdH oscillations in a quasi-2D metal [9, 46, 163] it is possible to extract the quasipartical lifetime τ from the field dependence of the oscillation amplitude as described in Sec. 2.1.2. To this end the oscillation amplitude of the lowest temperature curve is shown in a so called Dingle-plot in Fig. 6.21(b). The dependence of the up-sweep has been fitted with the formula of the Dingle damping

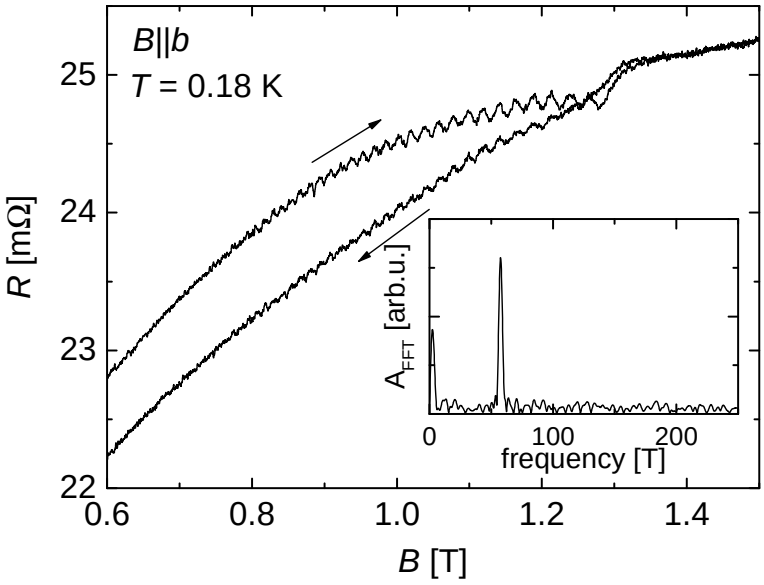

Figure 6.18: Field dependence of the interlayer resistance with magnetic field applied perpendicular to the conducting layers near the transition point. The inset shows the FFT spectrum of the upsweep.

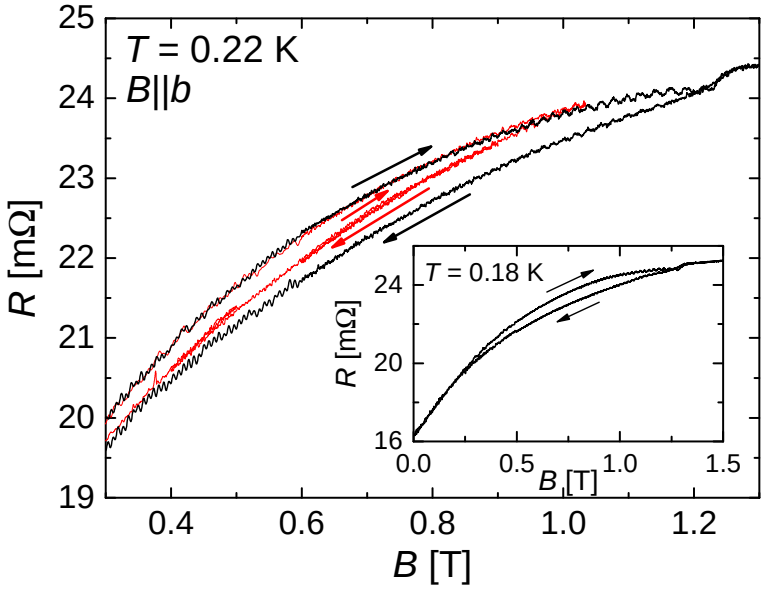

Figure 6.19: $R(B)$ in the full field range (black curve) and a sequence of up and downs sweeps at intermediate fields (red curve) to study the hysteretic behavior. For the red curve the following sequence was executed, starting from 0 T: $B \rightarrow 1.03\,\mathrm{T} \rightarrow 0.8\,\mathrm{T} \rightarrow 0.9\,\mathrm{T} \rightarrow 0.6\,\mathrm{T} \rightarrow 0.8\,\mathrm{T} \rightarrow 0.4\,\mathrm{T} \rightarrow 0.5\,\mathrm{T} \rightarrow 0\,\mathrm{T}$. The inset shows the full field range.

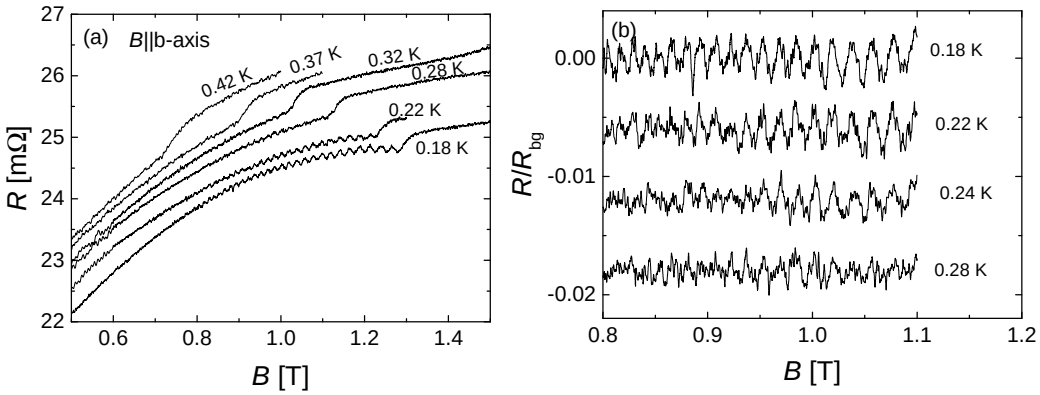

Figure 6.20: (a) $R(B)$ at different temperatures with magnetic field applied perpendicular to the conducting layers at increasing field. (b) The oscillatory component of the magnetoresistance normalized to the background resistance taken at different temperatures. The curves are vertically shifted.

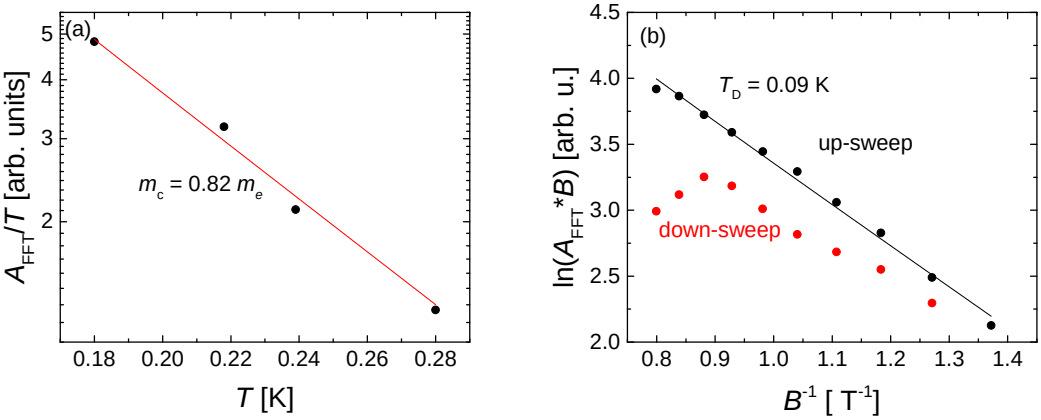

Figure 6.21: (a) Amplitude of the SdH oscillations plotted vs. temperature fitted by Eq. (2.11) to determine m_c. (a) Dingle plot of SdH oscillations for up- and down-sweep. The fit with Eq. (2.13) yields the Dingle temperature.

factor R_D, Eq. (2.13) in the 2D LKS formula (Eq. (2.9)). Inserting the cyclotron mass of $m_c = 0.82\,m_e$ a very low Dingle temperature of $T_D = 0.09\,\mathrm{K}$ was obtained, indicating a long scattering time of $\tau = 8.6\,\mathrm{ps}$, which is another evidence for the very high crystal quality.

On the down-sweep, the SdH amplitude is considerably lower and clearly violates the conventional behaviour. This enhanced damping of the oscillations in the down-sweep is obviously caused by the same additional, field-dependent scattering that causes the hysteresis of the non oscillating magnetoresistance presented above.

In κ-FeBr similar low frequency SdH oscillations were reported [23]. The authors suggest a FS reconstruction as the reason for the appearance of this new frequency. Since the two compounds are very similar, we suggest a similar FS reconstruction in

κ-FeCl. This topic will be discussed in more detail in Sec. 6.2.2, where our own results on the SdH oscillations in the AFM state of κ-FeBr are presented.

6.1.5 Influence of magnetic field on the AFM state: The *B*-*T* phase diagram

The pronounced step-like anomaly in the interlayer resistance at the AFM to PM transition (see Figs. 6.2 and 6.20) can be utilized for establishing the magnetic phase diagram. For each of the three crystal axes the transition was studied in isothermal magnetic field sweeps at different temperatures starting with the lowest temperature up to $0.9\,T_N$. In addition, the phase boundaries were studied by temperatures sweeps at different magnetic fields.

$B \parallel b$-axis

Fig. 6.20(a) shows a number of field sweeps at different temperatures for a magnetic field $B \| b$. To obtain the whole phase diagram also a number of temperature sweeps at different values of the magnetic field were executed. Those sweeps are presented in Fig. 6.22. As we can see the transition is clearly visible in all of the sweeps. From that the B-T phase diagram for $B \| b$, shown in Fig. 6.23, has been determined. There is an excellent consistency between the two methods.

According to susceptibility measurements [21], the out-of-plane b-axis is a hard magnetisation axis. For a magnetic field applied parallel to the hard axis we expect a

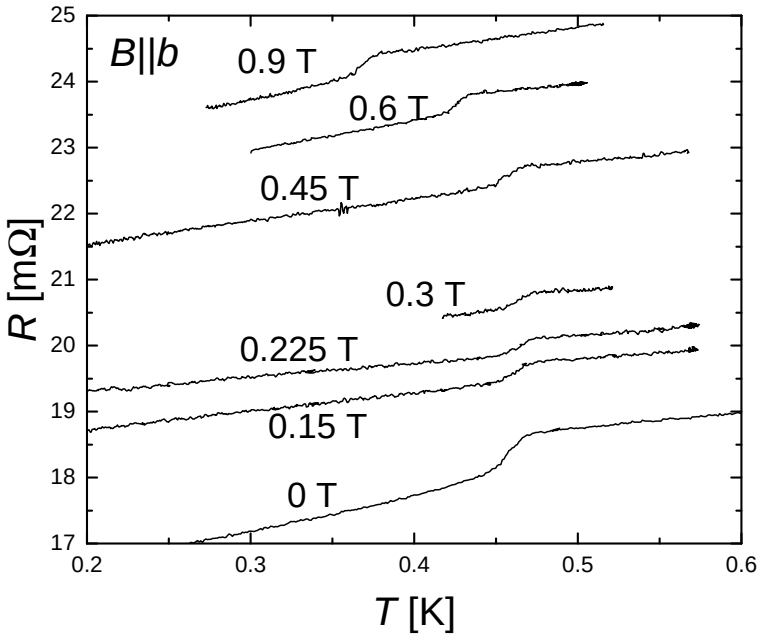

Figure 6.22: $R(T)$ for different magnetic fields applied perpendicular to the conducting layers.

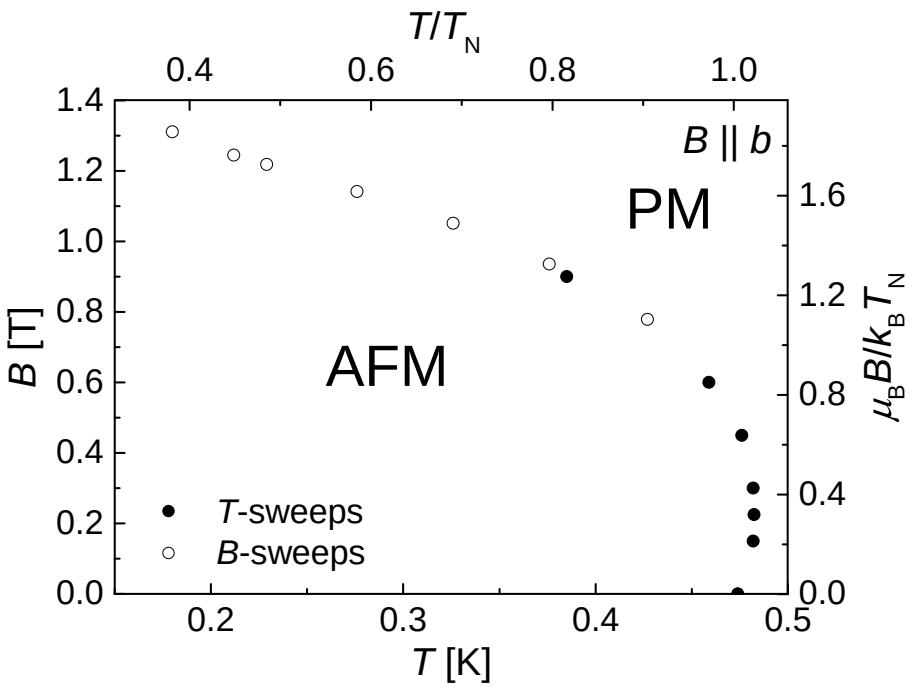

Figure 6.23: B-T phase diagram for magnetic field perpendicular to the conducting layers ($B \| b$-axis). Empty and filled symbols are determined from B- and T-sweeps, respectively. The right and top axes, respectively, show the transition field and temperature normalised to T_N.

canting of the antiparallel spins in the direction of the magnetic field. The canting grows stronger with increasing field until the spins become fully aligned and the AFM state completely broken at the transition field B_k. Besides canting, there obviously is some more complex mechanism at work, resulting in the hysteresis presented in the previous section. For higher temperatures the field where the AFM ordering is destroyed decreases, because now also the thermal fluctuations help to break the ordered state. Therefore, we can understand the general shape of the ordered state, which is conventional for many ordering phenomena.

The most interesting feature of this phase diagram is that for low magnetic fields T_N first slightly increases with increasing field. The highest transition temperature $T_N = 0.482\,\mathrm{K}$ is reached at $B \approx 0.2\,\mathrm{T}$ (compared to $T_N = 0.473\,\mathrm{K}$ at zero field). This increase is for sure bigger than the experimental error of the temperature determination. Only for $B > 0.3\,\mathrm{T}$ the phase boundary line shows the conventional negative slope. Similar effects are, for instance, reported for heavy fermion compounds [164] and quasi-two-dimensional (q2D) antiferromagnets [165]. In both cases the effect is explained by a suppression of phase fluctuations by a magnetic field. For a q2D antiferromagnet (almost no interlayer coupling of the magnetic moments) T_N is diminished compared to the value one would obtain from mean field calculations. The reason for this are phase fluctuations, which suppress long range ordering in the 2D case. These fluctuations are

reduced, when a magnetic field is applied and, therefore, T_N increases. At higher fields the effect of suppression of the AFM state due to the increasing Zeeman energy becomes dominant and T_N decreases [165].

In order to obtain a quantitative comparison between the transition field and temperature, we now introduce quantities normalized to the Néel temperature. For temperature we use $t = T/T_N$ and for magnetic field $b = \mu_B B \,/\, k_B T_N$. In the phase diagram (Fig. 6.23) the normalized values are given on the top and right hand side. As we see $b_k > 1$ for temperatures lower than $0.9\,t_N$. This is probably another hint that the Néel temperature is suppressed by fluctuations (thought the effect is pretty small). The normalised quantities will be used later in order to compare the transition fields and temperatures to the sister compound κ-FeBr in Sec. 6.2.4.

$B \parallel c$-axis

The crystallographic c-axis is the inplane hard axis of the system. The field direction parallel to the conducting planes is characterised by a much higher magnetoresistance than for perpendicular field, as we already saw in the AMRO curves (e.g. in Fig. 6.9). Two examples of field sweeps can be seen in Fig. 6.24(a). The $R(B)$ behaviour is quadratic up to the highest shown field, $B = 1\,\mathrm{T}$.

As we can see in Fig. 6.24(a) the resistance anomaly at the phase transition from AFM to PM state is hardly visible by bare eye: The sweeps at $T = 0.34\,\mathrm{K}$ show almost no difference to the one at $0.5\,\mathrm{K}$ (above T_N), where no transition feature is present. This is due to the high magnetoresistance and because the transition feature is much weaker for this field direction. However by subtracting the field sweep at $T = 0.5\,\mathrm{K}$ from the ones at lower temperature, a clear feature is revealed, which we associate with the AFM to PM transition. A few examples of such sweeps after subtraction are presented in Fig. 6.24(b). The arrows mark the points taken as the transition field. A collection of temperature sweeps at different fields is shown in Fig. 6.24(c). In the temperature sweeps

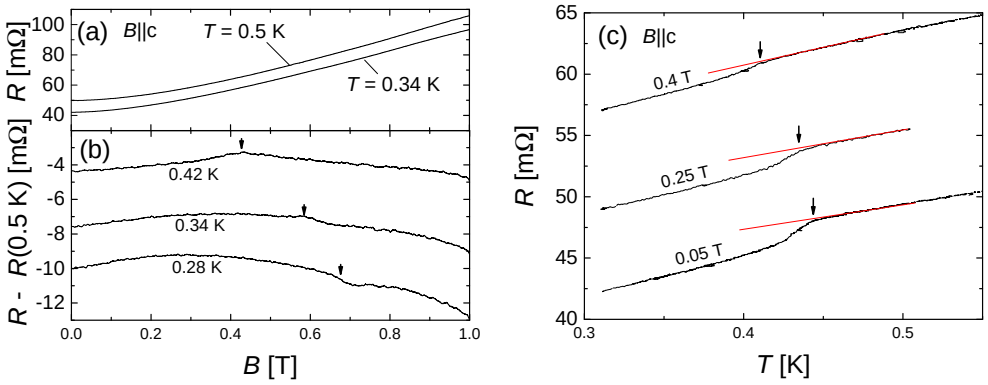

Figure 6.24: (a) Magnetic field sweep for $B \parallel c$ at $T = 0.34\,\mathrm{K}$ and $T = 0.5\,\mathrm{K}$. (b) Field sweeps at different temperatures after subtracting the data from the sweep at $T = 0.5\,\mathrm{K}$. (c) Examples of temperature sweeps at different values of the magnetic field for $B \parallel c$. The arrows mark the points taken as the transition.

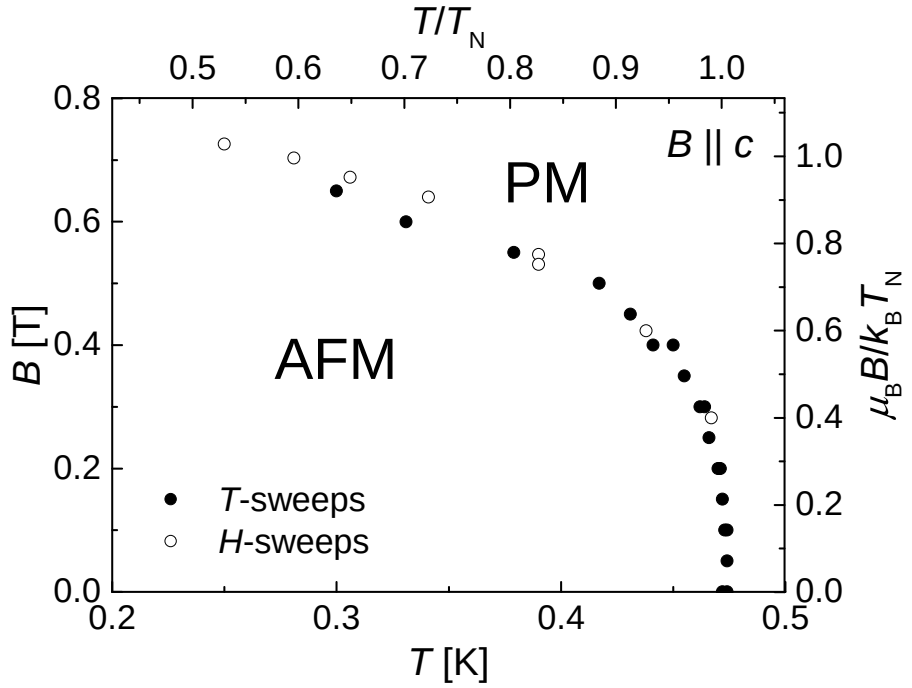

Figure 6.25: B-T phase diagram for magnetic field along the c-axis. Empty and filled symbols are determined from B- and T-sweeps, respectively. The right and top axes respectively show the transition field and temperature normalised to T_N.

the feature remained sufficiently strong to analyse it without subtracting a background even for higher fields. Here the arrows mark the transition temperature. Unlike for field along the b direction the sweeps did not show any hysteretic behaviour.

The resulting phase diagram for $B\|c$ is shown in Fig. 6.25. The points from field and temperature sweeps are again indicated by empty and filled symbols respectively. The shape of the phase diagram is very similar to the one for $B\|b$-axis. This could be expected since the crystallographic c-direction is also supposed to be a hard axis. We do not see a clear positive slope close to T_N within error range, but a slight enhancement of T_N at a field of $B \approx 50\,\mathrm{mT}$ cannot be completely ruled out. It is, however, noteworthy that the low temperature transition field is reduced by almost a factor of 2 compared to $B\|b$. This leads us to the conclusion that for the spin orientations the c-axis is "less hard" than the b-axis.

$B \parallel a$-axis

Last we come to magnetic field applied parallel to the a-axis, which is the easy axis of the AFM state. Here a more complex behaviour of the AFM phase is expected. That this is indeed the case is already visible in the field and temperature sweeps. Figure 6.26(a) shows a number of field sweeps containing the transition feature. The curves were obtained by subtraction of the data of a similar curve at $T = 0.5\,\mathrm{K}$, as

explained above. In Fig. 6.26(b) a number of temperature sweeps are presented. From the temperature sweeps we can see that the transition goes rapidly down in temperature, when we increase the field up to $B = 0.28\,\mathrm{T}$, but above this value it shifts again to higher temperatures. And we also observe that the size of the transition feature decreases with increasing field until it vanishes above 0.33 T (as seen in the 0.36 T curve in Fig. 6.26(b)). Starting from 0.45 T the feature reappears with inverted sign.

The magnetoresistance behaviour is similar to $B\|c$ with the only difference that the field-dependent increase of $R(B)$ is twice as high as for the c-direction. Also in the field sweeps a more complex behaviour of the AFM transition is visible. Close to T_N the transition is still indicated by a distinct step upwards as can be seen in the $T = 0.41\,\mathrm{K}$ curve in Fig. 6.26(a). At low temperatures we see a second significant step also marked by an arrow, e.g. at $B = 0.59\,\mathrm{T}$ in the curve measured at $T = 0.17\,\mathrm{K}$ in Fig. 6.26(a).

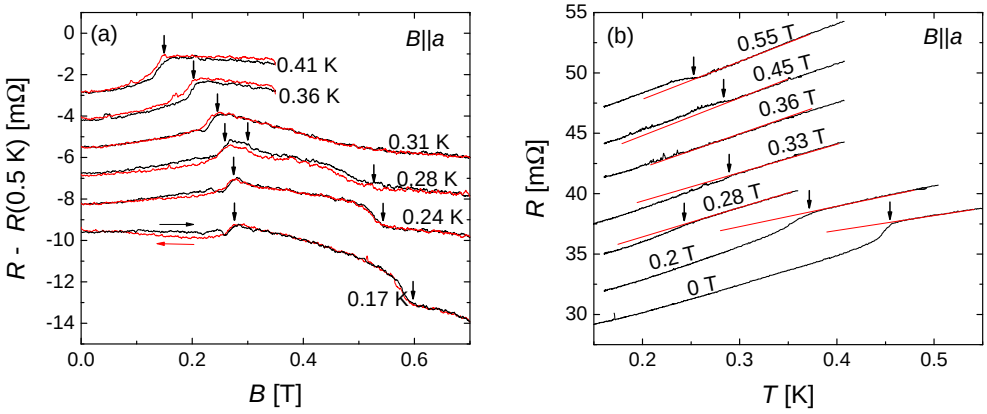

Figure 6.26: (a) Field sweeps at different temperatures after subtracting the data of a similar sweep at $T = 0.5\,\mathrm{K}$. (b) Examples of temperature sweeps at different values of the magnetic field for $B\|a$. The arrows mark the points taken as the transition.

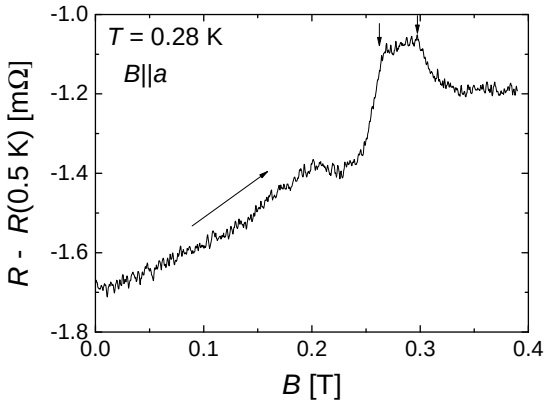

Figure 6.27: Magnetic field sweep at $B\|a$-axis with subtracted background for $T = 0.28\,\mathrm{K}$. There are two transitions in close vicinity indicated by the arrows. The second one is the reentrant transition into the spin-flopped AFM state.

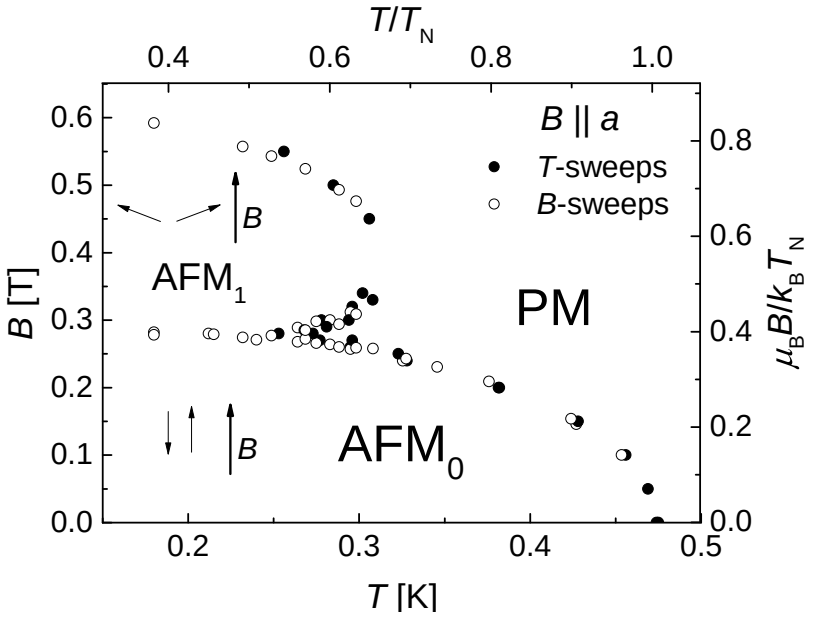

Figure 6.28: B-T phase diagram for magnetic field applied along a-axis. Empty and filled symbols are determined from B- and T-sweeps, respectively. The top and right axis show the transition field and temperature normalised to T_N.

Below 0.26 T there is a small but clear hysteresis between up and down sweeps lasting at least till 0.1 T. This hysteresis in the low-B state is reproducible and appears in all field sweeps for $T < 0.3$ K.

In the narrow temperature range $0.25\,\mathrm{K} \leq T < 0.31\,\mathrm{K}$ even a third feature can be resolved (see curve at $T = 0.28$ K in Fig. 6.26(a)). This additional feature is best seen in a field sweep at $T = 0.27$ K, which was done up to 0.4 K and is shown in Fig. 6.27. Here we see a step up at $B = 0.26$ T and a smaller step down at $B = 0.3$ T. The reason why the reentrant feature is less pronounced in the sweeps up to 0.7 T shown in Fig. 6.26(a) is likely a less exact orientation of the magnetic field.

The resulting phase diagram for $B\|a$-axis is shown in Fig. 6.28. We can clearly see two distinct phase lines. The AFM_1 state in the "high-field" region in the range $0.28\,\mathrm{T} < B < 0.6\,\mathrm{T}$ at low T is most likely a spin-flopped AFM state with the phase line at $B = 0.28$ T being the spin-flop transition with a bicritical point at $B = 0.28$ T and $T \approx 0.25$ K. Such an appearance of the phase diagram for magnetic field parallel to the easy axis is described in several textbooks and articles, see e.g. [96, 166–169]. At this transition the staggered magnetisation direction changes by 90° in a way that after the transition it is perpendicular to the external field. This allows the spins to become canted along the external field, as described for the hard axes above, resulting in a decrease in Zeeman energy. Since the transition field for $B\|c$ is much smaller than for $B\|b$ we suggest that the staggered magnetisation direction in the AFM_1 state is parallel to the c direction. This would mean that c is the intermediate axis of the crystal. We note that the low-temperature transition fields parallel to a and c-axis are very similar,

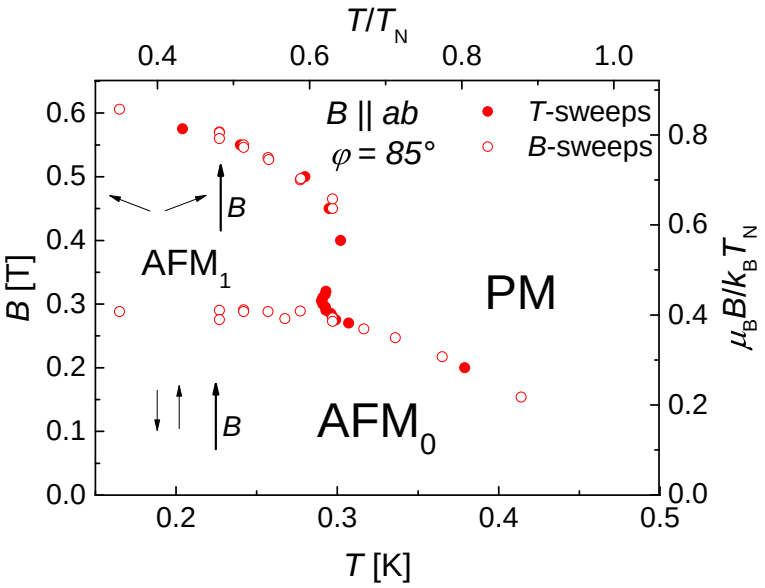

Figure 6.29: B-T phase diagram for magnetic field $B\|ac$-plane with $\varphi = 85°$. Empty and filled symbols are determined from B- and T-sweeps, respectively. The right and top axis show the transition field and temperature normalised to T_N.

which is likely favouring the spin-flop transition.

The narrow region of the PM phase between the AFM_0 and AFM_1 states above the bicritical point is probably caused by thermal fluctuations. In this field regime the energy difference between the regular and the spin-flopped AFM states is very small. So obviously only a weak thermal excitation is enough to scatter the system from one ordered state to the other resulting in a destruction of the long range order and, therefore, a paramagnetic state. At sufficiently higher or lower fields, the energy difference between the two ordered states is again high enough that long range order is realised. For $T \gtrsim 0.31\,\mathrm{K}$ the thermal fluctuations are strong enough to completely destroy the spin-flopped state. Below the bicritical point the thermal energy is so low that a direct transition from one ordered state to the other is observed.

The spin-flopped AFM_1 phase is suppressed in a second order phase transition at approximately two times the spin-flop field at the lowest temperatures. When going to higher temperatures, this upper transition moves to lower fields while the spin-flop field stays approximately constant until the bicritical point.

The guess that a small misorientation is the reason for the weakening of the reentrant transition feature in the sweeps to higher fields is supported by a set of measurements that was executed with magnetic field parallel to the conducting layers but with an azimuthal orientation of the field $\varphi = 85°$ (5° away from the a-axis). The phase diagram for this field orientation is shown in Fig.6.29. We observe that no sharp bicritical point can be determined any longer. The gap between the two ordered states has almost disappeared, resulting in no reentrant transition visible in any of the field sweeps.

Next we want to discuss the missing of transition features between 0.33 T and 0.45 T

and the reappearance with inverted sign. The resistance step at the transition to the AFM state at 0 T is likely due to reduced spin-dependent scattering. However, this mechanism does not work any more at high magnetic fields, as the spins of the conduction electrons are fully aligned already in the PM state. A possible explanation might be increased disorder or domain structure in the spin-flopped state leading to a higher resistance. This change in sign of the kink, however, is only seen for $B\|a$ and not for the other directions. It is even sensitive to a precise orientation of the magnetic field $B\|a$. In the series of temperature sweeps with an azimuthal tilt of the field of $\varphi = 85°$, the transition from the AFM to the PM state yields a step up in resistance for all fields and temperatures. For this field direction the transition can also be observed in the field range between $0.33\,\mathrm{T} < B < 0.45\,\mathrm{T}$, where no kink could be seen for a field alignment exact along a. Therefore, we believe that also for $B\|a$ in this field range the transition takes place at the expected temperature, but is not visible in the resistance. The reason for such a peculiar behaviour of the transition feature at the exact $B\|a$ orientation still remains unclear.

6.2 κ-$(BETS)_2FeBr_4$

As already mentioned in the beginning of Chapter 5, the quality of the used samples is always an important issue when measuring low-temperature properties. In the case of κ-$(BETS)_2FeBr_4$, this topic was specifically important: For the studies of the spin-splitting effect by use of SdH oscillations in both the AFM and PM state, it was necessary to still observe the oscillations even at higher tilt angles. Therefore, we were in need of exceptionally clean samples for this set of experiments. For this reason several different samples of κ-FeBr were investigated. The measurements were mainly executed on four different samples. Two of them were grown by N. Kushch in two different batches. The two others were from H. Fujiwara from one and the same batch. We will label them as follows: The Kushch's sample from the batch AD244 is sample #1 and the one from batch AD251 is sample #2. The two samples from Fujiwara are samples #3 and #4. An estimation of the sample quality from different criteria is given in Appendix A.2.

6.2.1 SdH oscillations in the normal metallic state

An example of a field sweep perpendicular to the conducting layers for sample #3 at $T = 0.4\,\mathrm{K}$ is given in Fig. 6.30(a). We observe SdH oscillations in the PM state down to below 6 T. The FFT spectrum, which is shown in Fig. 6.30(b) shows a number of different frequencies. The main frequencies are α, originating from the classical cylindrical orbit on the FS, and β, originating from the magnetic-breakdown orbit. The orbits are indicated by the red (α) and blue (β) ellipses in the inset of Fig. 6.30(a). They are very similar to κ-FeCl as presented in Sec. 6.1.2. The frequency of the main oscillations is $F_\alpha = 843 \pm 4\,\mathrm{T}$, which is in good agreement with earlier reports [117, 118]. Unlike in κ-FeCl the β peak is clearly split into two slightly different frequencies with the values $F_{\beta_1} = 4160\,\mathrm{T}$ and $F_{\beta_2} = 4265\,\mathrm{T}$. However, this splitting was not observed for all the samples measured. The intermediate peaks again are a result of the quantum

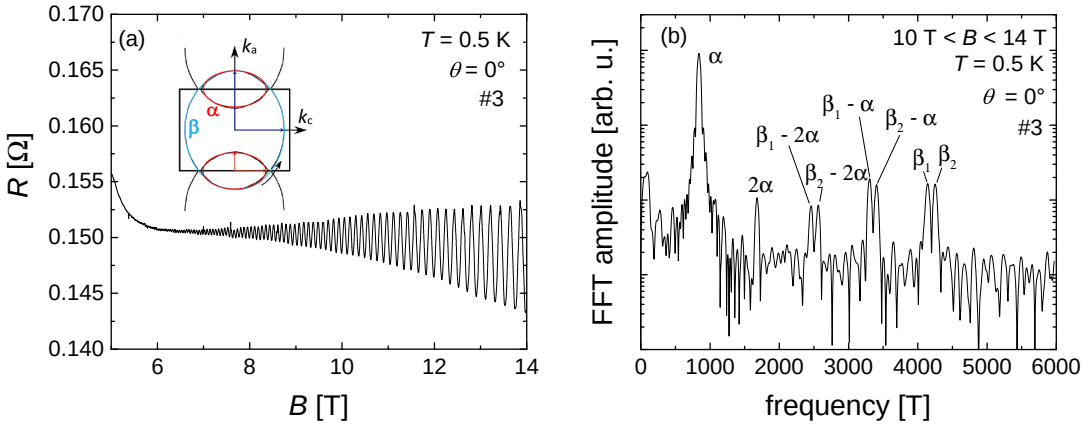

Figure 6.30: (a) High field SdH oscillations for field applied perpendicular to the conducting layers at $T = 0.5\,\mathrm{K}$. (b) FFT spectrum of the same field sweep in the field range $10 < B < 14\,\mathrm{T}$.

interference effect and possibly the frequency mixing effect [9, 46].

Determination of the exchange field

The splitting of the peaks is a result of the exchange field as already described in Sec. 6.1.2. Due to the clear splitting of the β frequency we can already try to determine the exchange field from the frequency difference: According to Eq. (2.56) we get

$$B_e = \frac{2\Delta F \cos\theta}{S_0} = (13.3 \pm 0.8)\,\mathrm{T}, \tag{6.6}$$

with $m^* = 7.9$ [118], $\theta = 0°$ and assuming $g = 2$. The obtained value is somewhat higher than the expected value obtained from the center of the FISC dome in the phase diagram (Fig. 3.11) of $B_e = 12.6\,\mathrm{T}$, but still within error range. So it seems that the splitting of β would give a reasonable value of B_e. But we have to take into account that this method of determining B_e is not very accurate since $\Delta F/F \ll 1$ and we only have a low number of nodes in the analysed field window. Additionally, we do not observe any nodes in the α oscillations like in κ-FeCl. Since $\Delta F_\alpha \approx 43\,\mathrm{T}$ from theory, the splitting, if present, should be resolvable. For this reason in the following we have studied the angle dependence of the nodes in both α and β oscillations in order to obtain information about the influence of the exchange field on the SdH oscillations jointly with F. Kollmannsberger in the course of his bachelor thesis [26].

Figure 6.31(a) shows the β component of the SdH oscillations for field sweeps at different angles θ. The oscillations clearly show nodes in the full investigated θ range. However, like in κ-FeCl, there seems to be an anomaly of the node behaviour around $\theta = 10°$, which cannot be explained yet. Above $\theta = 40°$ the β oscillations become hardly visible making a determination of the peak positions impossible. However, in most of the curves we are able to resolve more than two nodes. Thus, it became possible to fit node positions of several nodes on one specific θ with the spin splitting factor R_S.

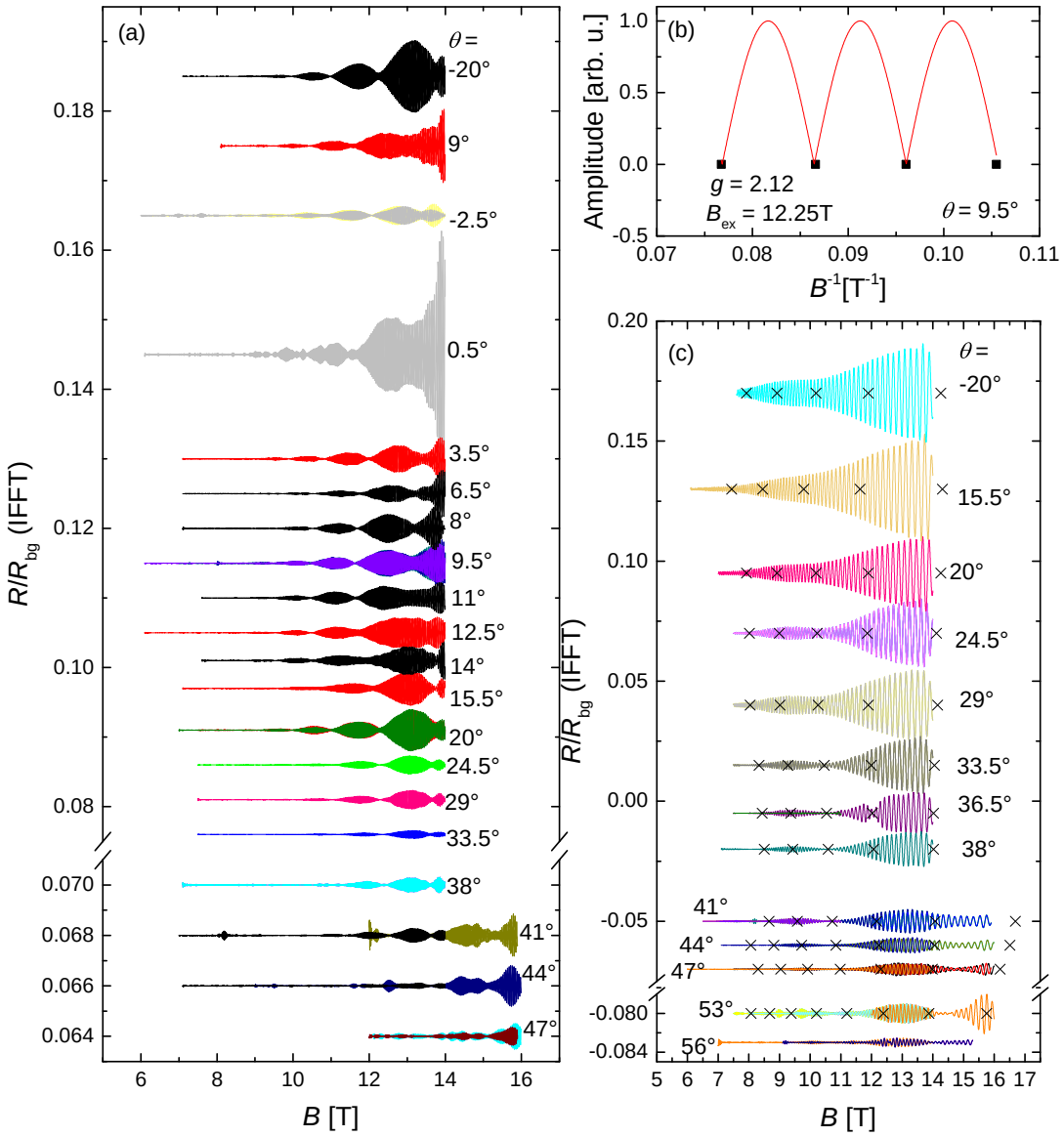

Figure 6.31: (a) The β component of the high field SdH oscillations obtained by inverse FFT normalised to the background resistance at different polar angles θ. The curves are arbitrarily shifted. (b) The fit used to obtained the values of B_e and g from the node positions of a single sweep. (c) The α component of the SdH oscillations after the same treatment as in (a). The crosses mark the points, where nodes would be expected according to the B_e and g value determined from the β. (all from [26])

At the same time, a fitting of the angular dependence of one specific order of a peak as done on κ-FeCl (Sec. 6.1.2) was not possible. However, since the first method should be more exact and additionally allows to trace the angular dependence of g, this should be rather an advantage. The exact fitting procedure is shown in Fig. 6.31(b): The node

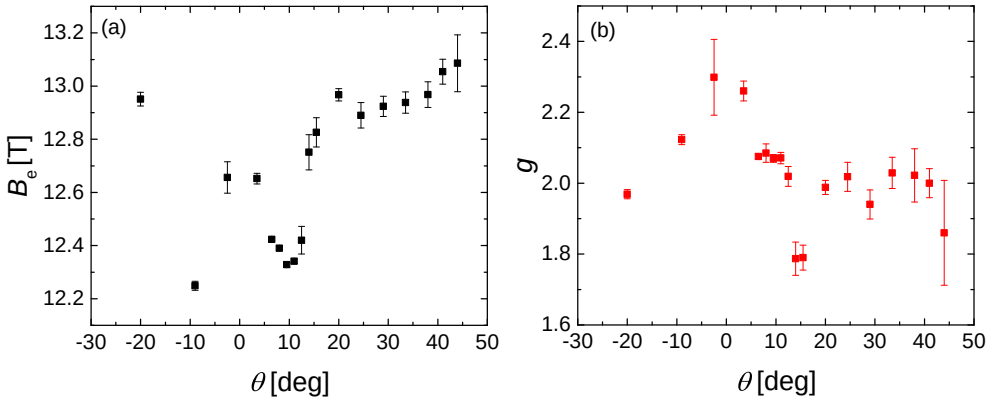

Figure 6.32: (a) The exchange field and (b) the Landé factor estimated from the node positions of the β oscillations as a function of θ. The error bars show the errors estimated by the fitting algorithm. (both from [26])

positions were plotted as points with zero amplitude at their respective positions in $1/B$. Then R_S (Eq. (2.55)) was fitted to those points, with the zeros of $R_S(B)$ matching the node positions. The resulting values of B_e and g as a function of θ are plotted in Fig. 6.32. As we can see, the estimated value of the exchange field is relatively stable at $B_e \approx (13.0 \pm 0.1)$ T for $\theta > 15°$. Only at around $\pm 10°$ the value of B_e is significantly lower. g is approximately 2.3 close to the perpendicular orientation and otherwise is close to 2.0.

In Fig. 6.31(c) the α component of the SdH oscillations is shown. Like in κ-FeCl there are no visible nodes for $|\theta| \leq 20°$. Above 20° some modulations in the amplitude start to appear, but only above 30° they become full nodes. These nodes, however, do not follow the expected behaviour. For $B < B_e$ it looks like only every second node is observed. For example, at all the positions where the third node would be expected, we see a maximum of the amplitude instead. For $B > B_e$, we were able to observe only one node at highest θ, due to the limit of the maximum field of the magnet. This node, however, is observed exactly between the positions of where we would expect to see the first and second order nodes. This behaviour is somewhat different than in κ-FeCl where we do not observe the nodes of first and second order, but third, fourth and fifth.

The values of B_e from the β oscillations are a little higher than the ones determined from the FISC state (see Sec. 6.2.3 below). The reason for this might be dependent on the fact that the FISC state is only observed for magnetic field parallel to the conducting layers while the SdH oscillations were mainly measured in the region close to perpendicular. So this deviation might be a result of an angle dependence of the g factor as suggested by Fig. 6.32, since B_e is g-dependent (see Eq. (2.54)) and we expect the exchange interaction to be angle independent. It is unclear at the moment if such an angular dependence of B_e and g is realistic in the present compound. To clarify this, additional studies of the angle dependence of the g factor would be required.

Effect of pressure on the Shubnikov-de Haas oscillations

We also studied the pressure dependence of the SdH oscillations. This was only done on sample #2 jointly with L. Schaidhammer [25]. To this end the sample was cooled down at pressures of $p = 1.9\,\text{kbar}$ and $4.5\,\text{kbar}$. At $1.9\,\text{kbar}$ the α oscillations were weakened but still visible, while the β frequency was absent. At $4.5\,\text{kbar}$ no oscillations at all were observed for $B \leq 15\,\text{T}$. This is in fact interesting because for most organic charge transfer salts the SdH oscillations rather become enhanced at higher pressure [131, 132, 134, 170]. We cannot explain this effect yet. More measurements on higher quality samples would be necessary to solve this issue.

At $p = 1.9\,\text{kbar}$ the frequency of the α oscillations was $F_\alpha(1.9\,\text{kbar}) = 835\,\text{T}$. This is $\sim 1\%$ smaller than at ambient pressure, which is highly unusual since, due to the compressibility of the crystals, the crystal parameters reduce with pressure leading to an increase of the FBZ and, therefore, the cylindrical FS parts, resulting in a higher frequency. The decrease of the α-pocket in the present case probably implies changes of the band structure under pressure. The cyclotron mass of the oscillations was estimated by the LK theory yielding a value of $m_c(1.9\,\text{kbar}) = 3.3\,m_e$, which is considerably lower than the one reported for ambient pressure of $m_c = 5.2\,m_e$ [117, 118]. This drop of the cyclotron mass is a sign of reduced electron correlations under pressure and is a typical result for organic metals.

6.2.2 SdH oscillations in the AFM state

Like seen in its sister compound κ-FeCl, κ-FeBr also shows oscillations in the AFM state. These oscillations have different frequencies from the ones seen in the PM state and indicated the same kind of FS reconstruction that was already discussed in Sec. 6.1.4. Figure 6.33 shows an example of a field sweep for $B \| b$ and $T = 0.42\,\text{K}$. Clear SdH oscillations are visible in the field range between 2 T and the AFM transition at 5.2 T. Between up- and down-sweeps a clear hysteresis similar to that in κ-FeCl (Sec. 6.1.4) is observed, which will be investigated in more detail later. The inset in Fig. 6.33 shows the FFT spectrum of the up-sweep. Next to the dominant frequency $F_\delta = (62 \pm 0.5)\,\text{T}$ as reported [23] a second frequency is observed, which is labeled ε. After we found this new frequency, we became aware of a publication [125], where the same frequency had been reported. The authors associated the ε oscillations with a breakdown orbit containing the δ orbit and two spikes of the star. The normal and reconstructed FS containing the suggested orbits for δ and ε are shown in Fig. 6.34.

The ε oscillations have a frequency of $F_\varepsilon = (178 \pm 2)\,\text{T}$. This is close to three times the frequency of δ, but as $3F_\delta = 186\,\text{T}$ and our accuracy is better than 2 T we can rule out that it is the third harmonic of δ. In addition it would be highly unlikely that we see the third harmonic of δ while the second harmonic is not visible.

The observation of these very low frequency oscillations is in agreement with the proposed reconstruction of the Fermi surface by a magnetic superstructure with the wave vector π/c, as proposed by theoretical calculations [98]. Since the frequency and effective mass determined in our measurements in κ-FeCl are very similar to these results on κ-FeBr the origin of the oscillations is obviously the same in both compounds. The

observation of these new frequencies in the AFM state is a strong argument in favour of the horizontal type of AFM arrangement (see Fig. 3.10) as proposed by Mori and Katsuhara [98], since for the vertical AFM arrangement no FS reconstruction should take place.

Cyclotron masses

The cyclotron masses of both δ and ε were determined by measuring the temperature dependence of the oscillation amplitude as explained above. For the δ oscillations we obtained $m_{c,\delta} = (1.1 \pm 0.1)\, m_e$ [25] for samples #1 and #2, which is the same value as reported by Konoike *et al.* [23]. For sample #3 the resulting cyclotron mass was $(1.3 \pm 0.3)\, m_e$ [26], but the difference can be understood from the fact that the cyclotron mass of sample #3 was determined in a much smaller temperature range than on the other samples. For sample #4 no reliable cyclotron mass could be determined.

For the ε orbit the mass was determined as $m_{c,\varepsilon} = (2.75 \pm 0.2)\, m_e$ [26]. This mass is much higher than expected, assuming a simple elliptical FS. In this case the mass usually scales with $\sqrt{S_{\mathrm{extr}}}$. As $F_\varepsilon \approx 3F_\delta$ a usual estimate would be $m_{c,\varepsilon} \sim \sqrt{3}\, m_{c,\delta}$. However, if we look at the origin of this frequency on the FS, we also come to the conclusion that the ε frequency is a result of a more complex orbit, e.g. the star-like FS orbit (or a part of it as suggested in [125]). Since the cyclotron mass is proportional to the circumference of the orbit, this would explain the high cyclotron mass, because a star has a much bigger circumference than an ellipse with the same area.

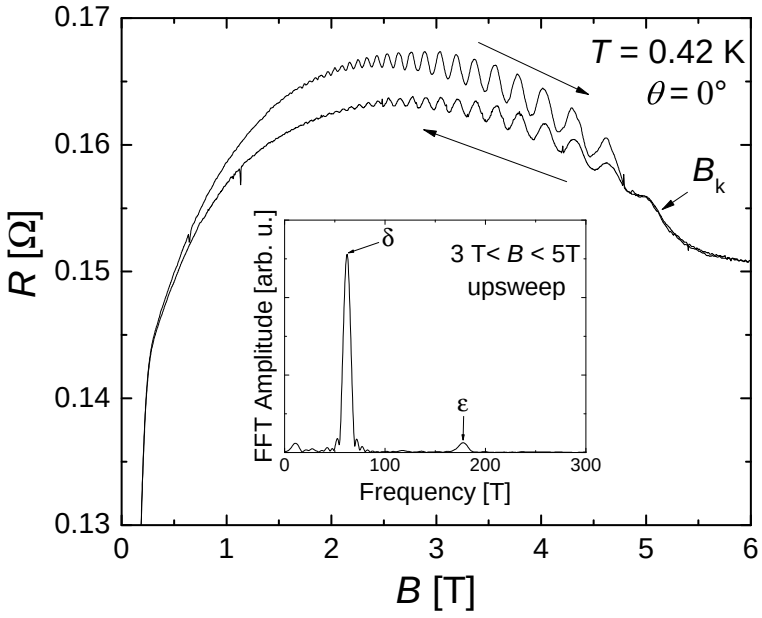

(a)

Figure 6.33: A field sweep featuring SdH oscillations in the AFM state with $B \| b$ and $T = 0.42\,\mathrm{K}$. The inset shows the FFT spectrum of the upsweep. (from [26])

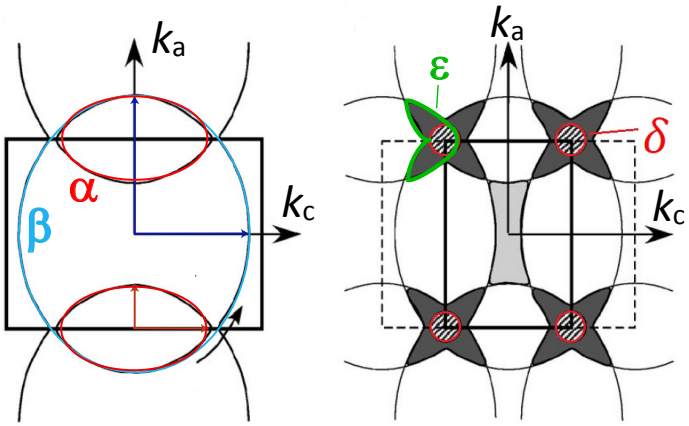

(a) (b)

Figure 6.34: (a) The FS of κ-FeBr in the PM state. (b) The proposed FS of κ-FeBr in the AFM state. The green lines sketch the orbit of the ε oscillations as proposed by [125]. (both from [23])

The δ oscillations have been studied under pressure at $p = 1.9\,\text{kbar}$ [25]. The measured frequency was 62 T, which is the same value as at ambient pressure. The determined cyclotron mass was $m_{c,\delta}(1.9\,\text{kbar}) = 0.83\,m_e$, which is about 75% of the ambient pressure value. $m_{c,\alpha}$ on the other hand, was reduced to about 63% of the ambient pressure value. From this we guess that the effect of pressure on the δ is smaller than on α. At $p = 4.5\,\text{kbar}$ also the δ oscillations could no longer be observed.

Hysteresis

Like in κ-FeCl (presented in Sec. 6.1.4), a clear hysteresis in the behaviour of background resistance and the oscillation amplitude is observed between up- and down-sweeps. However, there are some differences in the hysteretic behaviour in κ-FeBr. One of them is that in κ-FeBr the hysteresis also shows some kind of memory effect. This means that, when the sample is cooled below T_N and then the magnetic field is swept up and down several times, the second up-sweep (and all subsequent ones) shows a different behaviour than the first one. The initial up-sweep behaviour is again observed after heating the sample above T_N and cooling at zero field. The hysteresis is also strongly sample dependent, as we can see in Fig. 6.35, where the hysteretic behaviour for all the four studied samples is shown. The up-sweeps are shown by solid lines, while the down-sweeps are dashed lines. Always the first up- and the first down-sweep are given the same colour while the second up- and the second down-sweep have another colour. The numbers indicate the chronological order in which the sweeps were performed.

When looking at all the different samples, we see that the hysteresis of the background behaviour is very strongly sample-dependent (only samples #1 and #4 have a somewhat similar behaviour). This is even true for the samples #3 and #4, which originate from

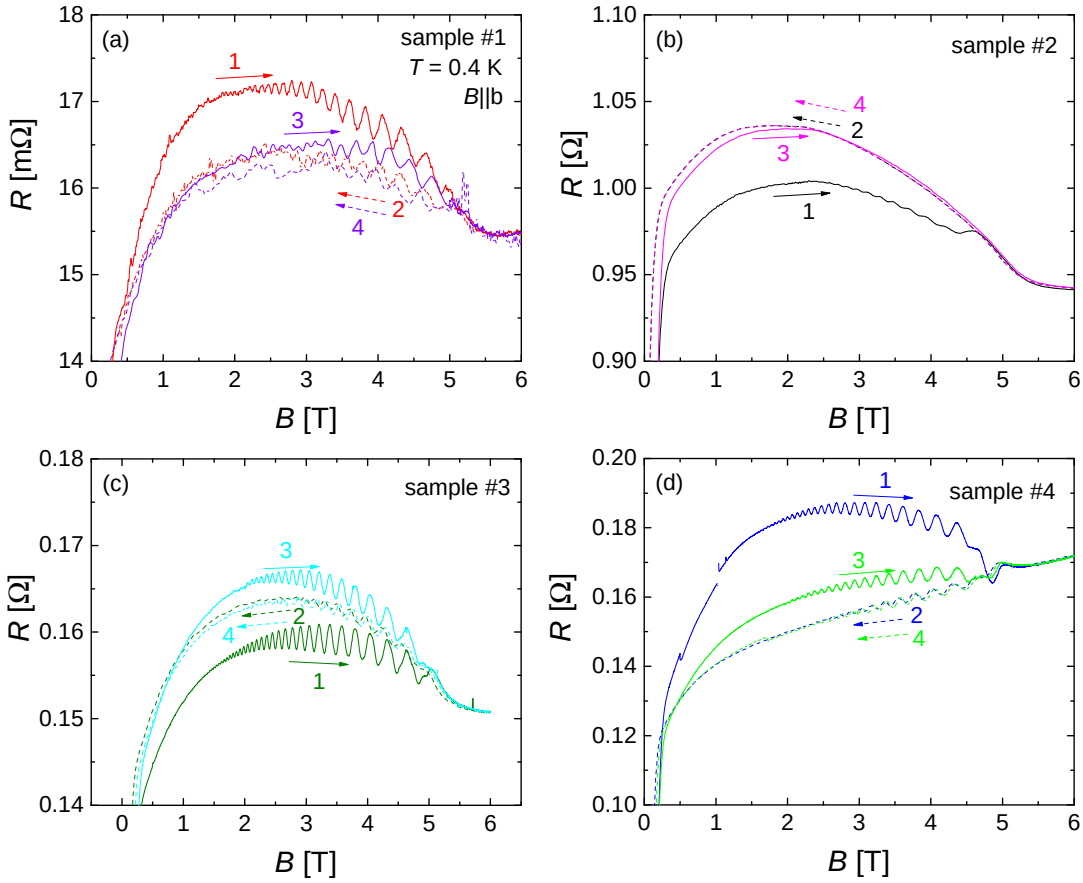

Figure 6.35: The hysteretic behaviour of the four studied samples for $B\|b$ and $T = 0.4\,\mathrm{K}$. The straight and dashed lines are up- and down-sweeps, respectively. The first up- and down-sweep always share a colour while the second up- and downsweep share a different colour. The numbers indicate the historical order of the sweeps.

the same batch. In contrast behaviour of the SdH amplitude is rather similar for all the samples: The highest amplitude is always observed in the initial up-sweep. The amplitude of the second up-sweep is slightly (or strongly in case of #2) smaller than on the first one. The down-sweep shows significantly smaller amplitude for all the samples (in #2 the oscillations vanish completely), which is similar to the observations on κ-FeCl presented in sec. 6.1.4.

A similar kind of hysteresis in κ-FeBr was also observed by Konoike *et al.* [125]. The authors explain the hysteresis by a field induced disorder after the first up-sweep: In the zero-field cooled state a long range order of the Fe spins exists in both intra- and interlayer directions. When the system comes back to the AFM state after applying magnetic field the AFM order is restored in each of the anion layers but without long range order in the interlayer direction due to the weak interlayer coupling, resulting in a formation of domains. This reduced order results in a higher scattering at the domain boundaries and, therefore, a reduced SdH amplitude.

From increased scattering we would, of course, expect a higher resistance on the down-sweep. In fact, we observe the opposite, contradicting the proposed mechanism. On the other hand, we should take into account the very high anisotropy in the present compounds giving rise to the possibility that the resistance is reduced by incoherent interlayer scattering [171]. The fact that the hysteresis in the background resistance is so strongly sample dependent enforces the explanation that this hysteresis behaviour is strongly influenced by the relative contributions of the coherent and incoherent channels.

However, in general there is no stable AFM order in 2D systems, which might be an argument against the formation of domains due to very weak interlayer coupling. Therefore, one possible idea is that fluctations are an explanation for the hysteretic behaviour rather than domains. And indeed, our measurements indicate that the hysteresis is already established before the field reaches B_k as is for example shown in Fig. 6.19 in Sec. 6.1.4. In this curve it becomes apparent that the value of the background resistance and, therefore, the magnitude of the hysteresis is determined by the field value, where the sweep direction is inverted. We also found a similar behaviour in κ-FeBr.

We further note that, at least in κ-FeBr, the behaviour of the background resistance on the down-sweep inside the AFM state always seems to follow the behaviour of the background resistance right above the transition field. This suggests that inside the hysteretic region not the whole sample volume is antiferromagnetically ordered, but rather there exist some paramagnetic volume fractions where the normal FS is established, reducing the SdH amplitude from the reconstructed FS. If this explanation is true, F_α should still be observable inside the AFM state on the down-sweep. For an unambiguous answer to this question, a measurement of sample #3 at lower temperature (i.e. in a dilution refrigerator) would be necessary.

Spin-splitting in the AFM state

In the normal metallic state the spin-zero effect in SdH oscillations shows a clear influence from the exchange field and, therefore, allows a determination of the exchange field value. In the AFM state the exchange field should be compensated due to the two sublattices with inverse spins. Therefore, one could naivly expect the conventional form of the spin factor R_S (Eq. (2.16)) to be restored. However, there is a theory suggesting the absence of spin zeros within an AFM ordered system [172–176]. Studies of underdoped YBCO yielded contradicting results as to the validity of this theory. However, according to the authors this theory only covers specific systems of doped antiferromagnets. Therefore it is not clear, whether we would expect angle-dependent spin-zeros in accordance with the usual spin-splitting factor (Eq. (2.16)) in κ-FeBr or whether they are completely absent as predicted by theory for doped AFM systems.

To that end field sweeps at different polar angles θ were performed at $T = 0.4\,\mathrm{K}$. The field was rotated in the bc-plane in order to have a highest possible field window for the analysis of the oscillations. (When the field is rotated towards the a-axis the transition field B_k decreases rapidly with increasing θ.) From these sweeps the θ-dependence of the δ-oscillations was extracted. The first try to obtain the angular dependence of the oscillation amplitude was undertaken in the master's thesis of L. Schaidhammer [25]

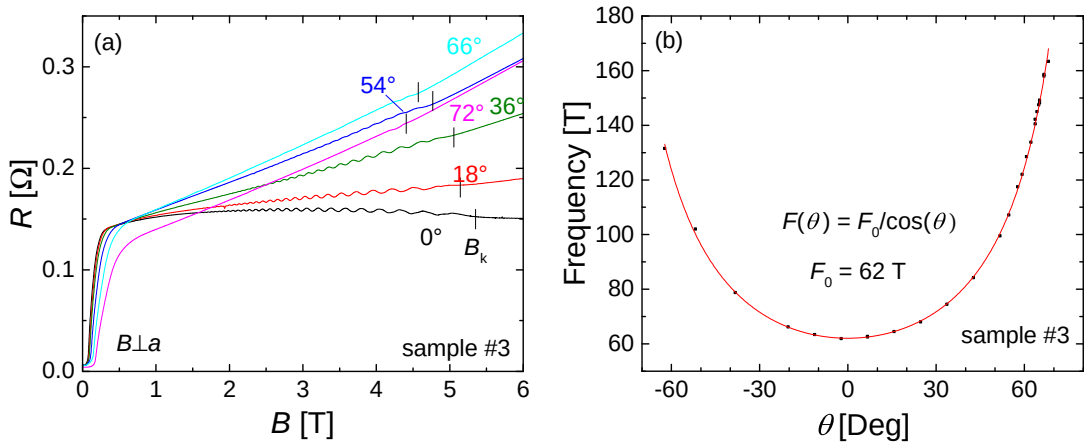

Figure 6.36: (a) Field sweeps in the AFM region at different polar angles θ. The short black lines mark the transition field B_k. (b) Oscillation frequency as a function of θ fitted with a $1/\cos\theta$ dependence. (both from [26])

using samples #1 and #2. However, the SdH oscillations in those samples were too weak and, therefore, became unresolvable at a value of $\theta \gtrsim 50°$. Therefore, no definite conclusion could be drawn yet, since this dependence would be in agreement with all values of $g \leq 1.5$. The experiment was repeated during the bachelor's thesis of F. Kollmannsberger [26] using samples #3 and #4.

Figure. 6.36(a) shows some examples of fields sweeps at different angles θ for the best sample #3. The θ-dependence of the oscillation frequency is plotted in Fig. 6.36(b). The curve clearly follows the expected $1/\cos\theta$-dependence.

The θ-dependence of the amplitude of the δ-oscillations for sample #3 is shown in Fig. 6.37. The amplitude plotted in this graph was determined by the height of the peak in the FFT spectrum for a field window of 3-4.2 T. The graph contains several fits by the θ-dependent Lifshitz-Kosevich (LK) formula:

$$|A_{osc}(\theta)| = a \cdot \frac{Km^*T\left[1-\exp\left(-\frac{B_{\mathrm{MB}}}{B_\perp}\right)\right]^2 \exp\left(-\frac{Km^*T_D}{B_\perp}\right)}{B\cos\theta\sinh\left(\frac{Km^*T}{B_\perp}\right)} \cdot \left|\cos\left(\frac{\pi m^* g}{2\cos\theta}\right)\right|, \qquad (6.7)$$

where $B_\perp = B\cos\theta$ is the field component perpendicular to the layers, $B_{\mathrm{MB}} = 20\,\mathrm{T}$ is the breakdown field and a a fitting parameter, for different values of g. For the cyclotron mass the value $m^*(\theta = 0°) = 1.1$ was used. The red fitting curve was done without considering the spin-splitting damping factor (which is equvalent to $g = 0$ in Eq. (6.7)). The Dingle temperature was used as a fitting parameter and yielded values of $T_D = (0.4 \pm 0.1)\,\mathrm{T}$, which is a realistic value for the present sample. As we can see, for all the fits with a finite g-value some spin-zero must be observed in the studied angular range. This obviously contradicts the experimental result. On the other hand the formula without the spin-splitting term fits the observed dependence extremely well. A closer analysis shows that for fitting the measured dependence reasonably well it is required that $|g| < 0.3$. Since this value is unrealistically low, we can assume that

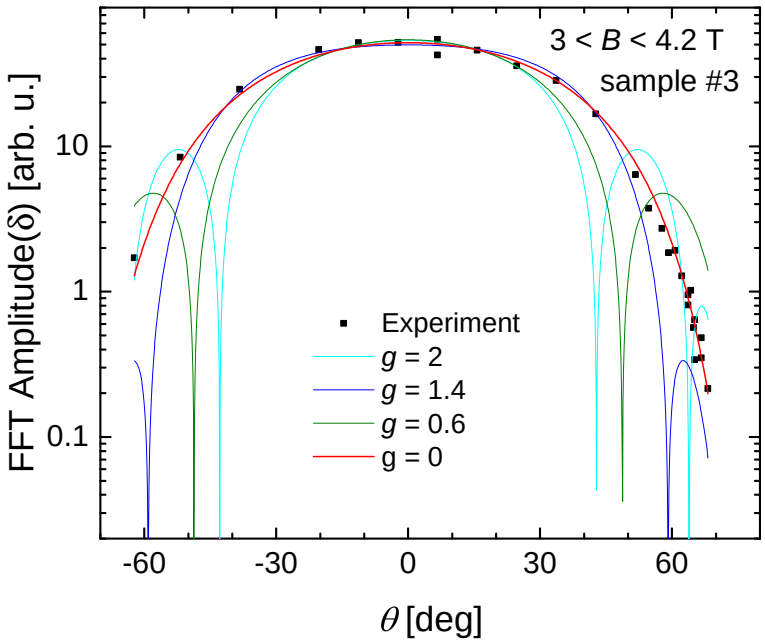

Figure 6.37: SdH amplitude as a function of θ. The amplitude was determined by the peak height in the FFT spectrum in a field range of 3-4.2 T. The fits were performed with the θ-dependence of the LK formula (Eq. (6.7) for different values of g. (from [26])

indeed there seems to be no spin splitting effect on the SdH oscillations in the AFM state in κ-FeBr. A similar behaviour of missing spin-zeros was also observed in NCCO [130], which also is an antiferromagnetic system.

This all leads to the conclusion that the absence of the spin-splitting in AFM systems as predicted by theory [172–176] is indeed observed. However, we note that the predictions were made only for FS pockets at the boundaries of the AFM Brillouin zone. Since the δ oscillations in our system originate from an orbit, which is also at the border of the PM FBZ according to the suggested reconstruction, some adjustment to the reconstructed FS or the theory are necessary for a better agreement. This is a difference to the observations in NCCO since there all the FS pockets are located at the magnetic Brioullin zone boundaries.

6.2.3 SC state

Unlike in κ-FeCl (see Sec. 6.1), a clear SC transition is observed in κ-FeBr. A number of temperature sweeps showing a SC transition is shown in Fig. 6.38. The AFM transition temperature seems to be not strongly dependent on the sample quality: Samples #3 and #1 show an identical transition temperature; in sample #2 it is only 30 mK lower. However, in the SC transition a strong sample dependence is observed. Sample #3 is the best with a critical temperature $T_{c,u} = 1.43$ K, according to the upper construction, as explained in Fig. 6.38. It also has the smallest transition width $\Delta T_c = 0.4$ K (that

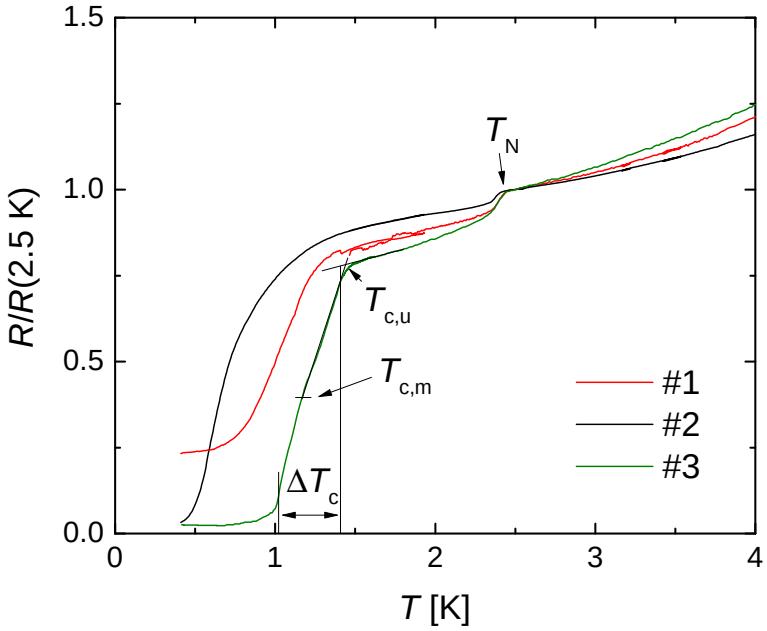

Figure 6.38: (a) The AFM and SC transition of samples #1,#2 and #3.

is the temperature range where the value of the resistance is between 10% and 90% of the normal state resistance). For sample #1 $T_{c,u} = 1.26\,\mathrm{K}$ and $\Delta T_c = 0.47\,\mathrm{K}$, making this sample clearly the second best in this category and for #2 $T_{c,u} = 0.87\,\mathrm{K}$ and $\Delta T_c = 0.64\,\mathrm{K}$. In sample #2 the SC onset is also much less sharp than for the other samples making a construction of $T_{c,u}$ less precise. Therefore, the critical temperatures were also checked with transition midpoint method $T_{c,m}$. There all values are 0.22 K lower, respectively, than obtained by the upper construction. The absolute differences between the $T_{c,m}$ values were identical. The reason why the resistance of sample #1 does not drop to zero most likely is a rather high contact resistance as the sample was extremely tiny and good contacts were no longer possible.

Like in α-MHg the behaviour of the SC state is especially sensitive to the specific samples. As we discussed in Sec. 5.1.2 the reason for this can either be an unconventional nodal type of superconductivity in the compounds or the result of internal strain. However, the most interesting points associated with the SC state in the present compound are the FISC state and the exact nature of the transition from the SC and AFM state to the NM and PM state in a field $B\|a$. To that end an analysis of the SC state in κ-FeBr was done during L. Schaidhammers master thesis [25] using sample #1.

Figure 6.39 shows a field sweep for $B\|a$ at $T = 0.5\,\mathrm{K}$. The low field part was also measured at various other temperatures and is enlarged in the inset of Fig. 6.39. In all the sweeps only one transition is observed, which for low temperatures is much sharper than usual for organic superonductors. This leads to the conclusion that SC and the AFM state are broken simultaneously. The transition field of $B_c = 1.8\,\mathrm{T}$ for the lowest temperature is notably lower than the critical field parallel to the inplane c-axis, which was reported as 3.1 T [22].

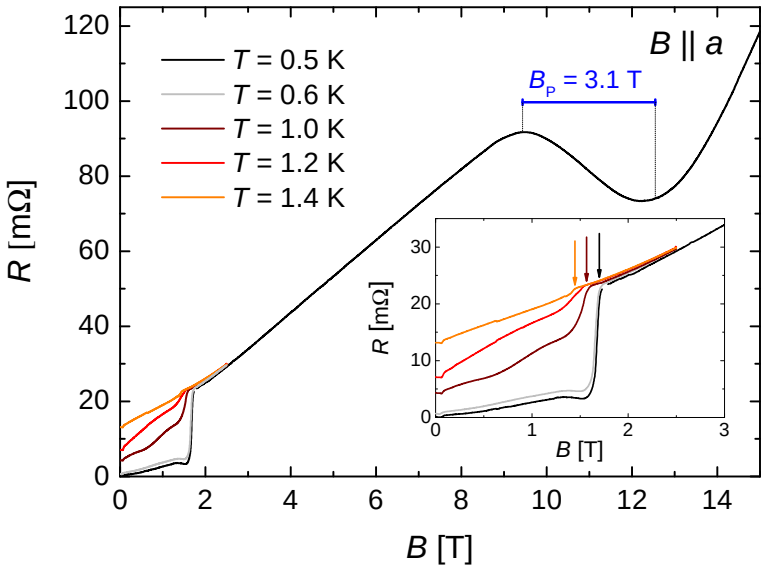

Figure 6.39: Resistance as a function of magnetic field for $B\|a$. The low field part was measured at various temperatures and is enlarged in the inset. The arrows mark the transition field. (from [25])

The reason for this rapid breaking of the SC state for $B\|a$ can be found in the AFM ordering: Like in κ-FeCl the a-axis is the easy axis of the system. This means for fields applied parallel to this direction we expect either a spin-flip or a spin-flop transition to happen at a certain field value, depending on the anisotropy of the system. Since there is no further transition observed above the SC transition at 1.8 T, we suggest that there the AFM state becomes broken by the field. Because of this, the exchange field is no longer compensated, resulting in a rapid breaking of the SC state. The fact that we see only one transition suggests that a spin-flip transition is taking place at 1.8 T. However, we cannot exclude that a spin-flop transition like it was seen in κ-FeCl, takes place at a lower field but is not observed in $R(T)$, since it is shunted by the SC state. But it is not clear whether a spin-flop transition would destroy the SC state. A similar behaviour for $B\|a$ has been reported by Konoike *et al.* [22]. However, there are also reports about a second transition feature: In torque measurements [126, 177] two features were observed at respective field values of 1.7 T and 1.9 T and were suggested to be a result of a spin-flop transition and the subsequent transition into the PM state. This point will be further discussed in the next section.

The FISC state is clearly visible in the high-field part of Fig. 6.39. The resistance does not drop to zero at this temperature of $T = 0.5$ K, which is in agreement with the temperature dependence reported in [22]. After subtracting the linear background, the value of the exchange field B_e can be determined as the center of the FISC dip: $B_e = 12.6$ T. This value is somewhat lower than the value estimated from the SdH oscillations as discussed in Sec. 6.2.1. The half width of the FISC dome is 3.1 T. Since the FISC state appears in the region $B_P = |B - B_e|$, we can conclude that $B_P = 3.1$ T is the paramagnetic critcal field for this compound. This is also in agreement with [22]

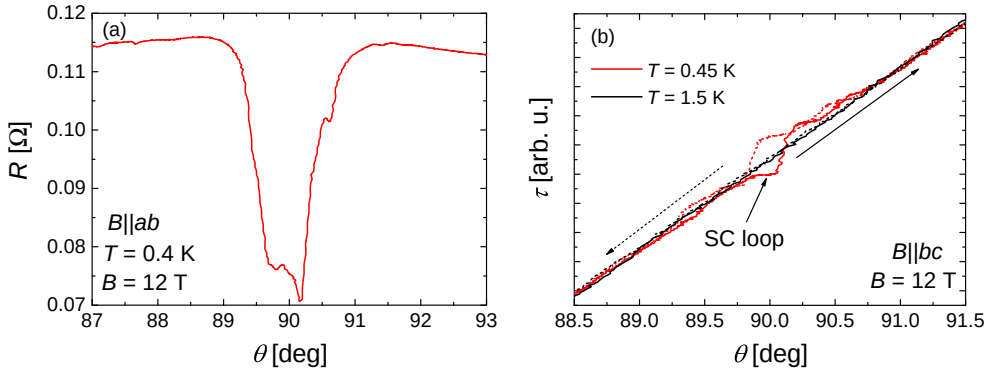

Figure 6.40: (a) Resistance as a function of θ at $B = 12\,\mathrm{T}$ and $T = 0.45\,\mathrm{K}$. (b) Magnetic torque as a function of θ at $B = 12\,\mathrm{T}$. The red curve was recorded at $T = 0.45\,\mathrm{K}$ and the black curve at $T = 1.5\,\mathrm{K}$. (both from [25])

and with the low-field data for $B\|c$ in [22].

We also investigated the FISC state in angular sweeps: Figure 6.40(a) shows $R(\theta)$ at $B = 12\,\mathrm{T}$ and $T = 0.45\,\mathrm{K}$. A clear dip at around $\theta = 90°$ indicates the field induced superconductivity. The small dip width of about 2° shows the strong sensitivity of the FISC state on the field orientation. The reason for this is that for fields perpendicular to the conducting layers the orbital critical field is very low. And, as mentioned in Sec. 2.4.3, the orbital critical field is not influenced by the exchange field. Therefore, only a small out-of-plane component of the field is sufficient to destroy the FISC state. In the center of the dip some kind of double feature is observed. In λ-$(BETS)_2GaCl_4$ also a small peak in the center of the SC dip in the angle dependence was found and associated with Josephson-vortex dynamics [178]: For the field exactly parallel to the layers, the vortices go through the insulating layers. When the field becomes tilted, the vortices are forced to go through the SC layers and become pinned, resulting in a decrease in vortex motion and, therefore, a decrease in resistance [138, 139].

An angular sweep at the same field and temperature was performed while measuring magnetic torque and is shown in Fig. 6.40(b). Here the sweeps were performed at two different temperatures. At $T = 1.5\,\mathrm{K}$ (the black curve in Fig. 6.40(b)) a monotonic θ-dependence of the torque is observed which follows a $\sin 2\theta$-dependence. At $T = 0.45\,\mathrm{K}$, however, a hysteretic loop around $\theta = 90°$ is found, which is most likely caused by the FISC transition. This is, to our knowledge, the first indication of a FISC state in a magnetisation measurement in κ-FeBr. For verification a similar angular sweep was performed at $T = 0.45\,\mathrm{K}$ and $B = 1\,\mathrm{T}$, which showed a similar feature, which we associate with the low-field SC state. The angular range of $\theta = 90° \pm 0.2°$ in which the FISC state is observed in torque is much smaller than in resistance.

6.2.4 Effect of pressure on the B-T phase diagram

For ambient pressure the magnetic phase diagrams of the present compound were already published [22, 114] as shown in Fig. 3.11. Here we will present the phase diagrams

again and discuss similarities and differences to the sister compound κ-FeCl, where the phase diagrams at ambient pressure were shown in Sec. 6.1.5. Otsuka *et al.* [129] observed that the Néel temperature of the compound is increased by applying hydrostatic pressure. However, the impact of pressure on the exact shape of the magnetic field-temperature phase diagram was not reported yet.

In order to fill this gap of knowledge, sample #2 was studied under two different hydrostatic pressures, $p = 1.9\,\text{kbar}$ and $p = 4.5\,\text{kbar}$ at low temperatures during the master's thesis of L. Schaidhammer [25]. In agreement with [129] T_N was found to be increasing by increasing pressure. We determined $T_N(1.9\,\text{kbar}) = 2.6\,\text{K}$ and $T_N(4.5\,\text{kbar}) = 3.0\,\text{K}$. The value for 4.5 kbar is significantly higher than reported in [129]. We suggest that this is a result of an overestimation of pressure in the cited paper.

In general, the behaviour of an enhancement of the AFM state by pressure is uncommon for this class of organic charge transfer salts. For example in both λ-FeCl and in κ-(BEDT-TTF)$_2$Cu[N(CN)$_2$]Cl (κ-ETCl) the AFM ground state becomes suppressed under sufficiently high hydrostatic pressure. We guess that the reason for this lies in the influence of the conducting system on the AFM ordering. In both λ-FeCl and κ-ETCl also the conduction systems are antiferromagnetically ordered. Since in organic charge transfer salts pressure generally drives the conduction system into a more metallic state the tendency of the conduction electrons to order decreases and the ordered state becomes weakened. In κ-FeBr and κ-FeCl the AFM ordering is rather independent from the conduction electrons, since the coupling of the of the magnetic moments with the conduction electrons via the π-*d* interaction is weak, while the direct *d*-*d* interaction between the magnetic moments is dominant [98]. We suggest that the shorter distances of the Fe atoms, due to the compression of the crystal under pressure, lead to stronger *d*-*d* interactions and, therefore, an increase in T_N.

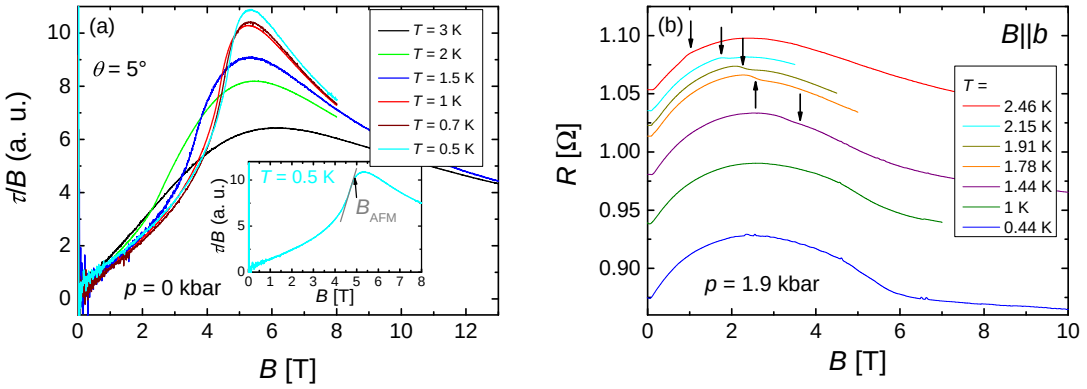

Figure 6.41: (a) Magnetic torque as a function of magnetic field for different temperatures at $\theta = 5°$ and $p = 0\,\text{kbar}$. (b) Interlayer resistance as a function of magnetic field for different temperatures at $B \| b$ and $p = 1.9\,\text{kbar}$. (both from [25])

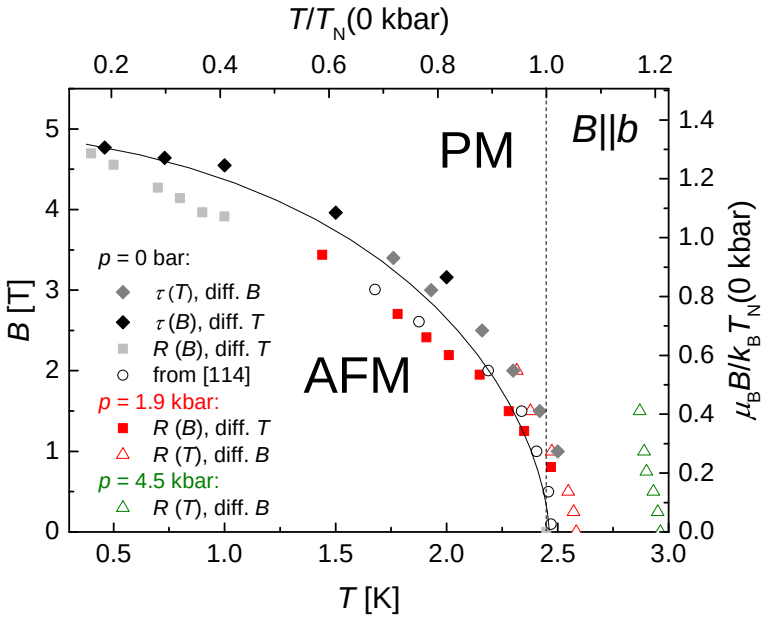

Figure 6.42: The phase diagram of κ-FeBr for $B\|b$ at different pressures. The empty symbols at ambient pressure are from [114]. The line is a guide to the eye for the ambient pressure phase diagram. The right and top axis show the transition field and temperature normalised to the zero pressure T_N. (from [25])

$B \parallel b$-axis

Figure 6.41 shows examples of sweeps used to determine the phase diagram for $B\|b$ at ambient pressure and 1.9 kbar. At zero pressure mainly measurements of magnetic torque have been performed. Under pressure the transitions were only determined by measurements of the interlayer resistance.

Figure 6.42 shows the phase diagram for $B\|b$-axis. Here it seems that the phase line starts with a very steep, almost infinite, negative slope even for $p = 0$ kbar [114]. However, a slight positive slope for low B cannot be completely excluded. The points from torque measurements suggest the existence of such a positive slope, but due to the different experimental methods showing different kinds of features, an exact comparison is not possible. The data from [114] (indicated by the empty symbols), do not indicate a positive slope. If an enhancement of the transition temperature is indeed observed, it certainly would be weaker than for the Cl-salt. This is some indication of a higher interlayer coupling of the spins in κ-FeBr: The smaller reduction of T_N by phase fluctuations is a sign for higher three-dimensionality.

To compare the field and temperature values of the two sister compounds we now look at the quantities normalized to the compounds' respective Néel temperature at zero pressure. For temperature we defined $t = T/T_N(0\,\text{kbar})$ and for magnetic field $b = \mu_B B \,/\, k_B T_N(0\,\text{kbar})$ with t_N being the normalised transition temperature and b_k the normalised transition field. In the phase diagram (Fig. 6.42) the normalized values are given on the top and right hand side. At $t = 0.5$ for κ-FeBr $b_k = 1.13$, while for

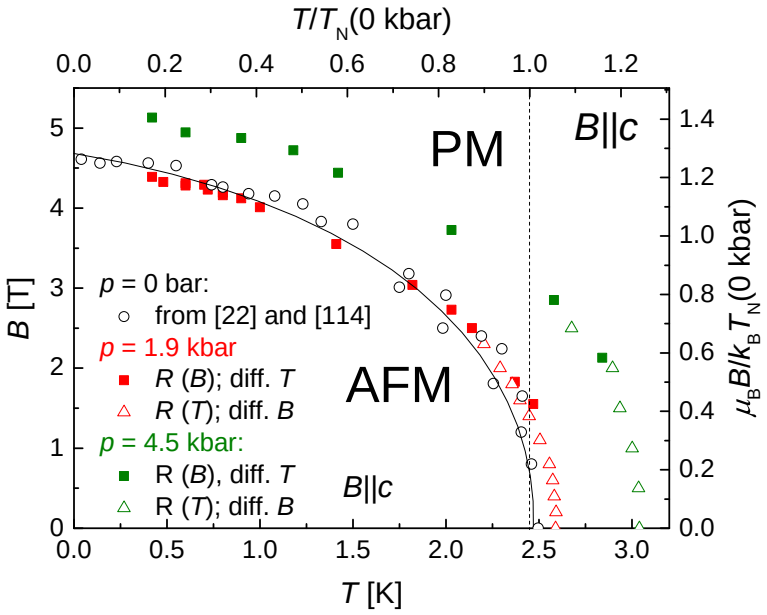

Figure 6.43: The phase diagram of κ-FeBr for $B \| b$ at different pressures. The data at 0 kbar is from [22] and [114]. The line is a guide to the eye for the ambient pressure phase diagram. The right and top axis show the transition field and temperature normalised to the zero pressure T_N. (from [25])

κ-FeCl $b_k = 1.7$ as visible in Fig. 6.23. This means that the AFM state in κ-FeCl is considerably more robust to magnetic field applied perpendicular to the layers than in κ-FeBr. Maybe this is another indication for a weaker magnetic interlayer coupling in κ-FeCl as was already speculated [21, 115]. However, calculations reveal [98] that the π-d interactions, which should be responsible for the interlayer coupling, are not significantly different between the two compounds. The main difference in the exchange interaction of the two compounds is in the d-d coupling, which only acts within the FeX_4 layers.

An interpretation of the phase diagram under pressure for this field direction is difficult. The features at the transition in resistance became extremely weak under pressure. At $p = 1.9$ kbar there is still a clear steplike feature observed in both temperature and field sweeps for low fields and high temperatures. For low temperatures and high fields no transition feature at all was observed in both methods as can be seen in Figure 6.41(b) where field sweeps at different temperatures for this pressure and field direction are shown. At $p = 4.5$ kbar the transition was only observed in temperature sweeps at low fields. Therefore, apart from the starting slope, no phase line could be drawn for this pressure.

$B \parallel c$-axis

The phase diagram for $B \| c$ is shown in Fig. 6.43. The curve at zero pressure, reported by [22] and [114], looks very similar to the zero pressure curve for $B \| b$ (Fig. 6.42).

From this it seems that in κ-FeBr the difference between the inplane hard axis (c-axis) and the out-of-plane hard axis (b-axis) is very small. This is a major difference to the sister compound κ-FeCl, where the transition fields at low T differ by almost a factor of two between those two directions, as can be seen in Fig. 6.25. The comparison of the normalised transition field yields that with $b_k = 1.05$ for κ-FeCl and $b_k = 1.07$ for κ-FeBr [22] at $t = 0.5$ the two compounds are almost identical for $B\|c$.

For $B\|c$ a complete phase diagram under pressure could be drawn. For this field direction a clear transition feature is detected for both field- and temperature sweeps (filled and empty symbols in Fig. 6.43) even at $p = 4.5\,\text{kbar}$ and there is a good consistency of the two methods. Here we can see that, while having a slightly higher Néel temperature the phase lines of $p = 0\,\text{kbar}$ and $1.9\,\text{kbar}$ lie on each other within the error range. For $p = 4.5\,\text{kbar}$, however, the whole phase line is clearly shifted to higher fields and higher temperatures. This means that the AFM state at higher pressures becomes more robust to both thermal excitations and magnetic fields.

$B \parallel a$-axis

In Fig. 6.44 we present the phase diagram for $B\|a$-axis. At zero pressure we again show data from [22] in addition to our own data. The black line is a guide to the eye for the data from [22]. Our own measurements were only perfomed between 0.4 K and 1.5 K. It seems that there is a constant shift between the two data sets. Maybe this is because of slightly different criteria for the points taken as the transition or different quality crystals. Turning to comparison between κ-FeBr and κ-FeCl for this field direction, the phase diagrams look significantly different. For κ-FeBr no unambiguous evidence for a spin-flopped AFM state has been found yet. In resistance measurements usually only one transition is visible where SC and AFM state are broken at the same field as we presented in Sec. 6.2.3. It is possible that a spin-flop transition takes place but is not observed in resistance because of the SC state. Konoike *et al.* [22] observed a second feature in resistance just above the SC transition in resistance. However, it is not fully clear if this is a distinct individual transition and the authors do not comment on the second feature. A hint towards a spin-flop state in κ-FeBr was reported by the same authors in torque measurements [126] where two distinct features at $B = 1.7\,\text{T}$ and $1.9\,\text{T}$ at $T = 30\,\text{mK}$ could be resolved. Similar features were also seen in torque measurements by Pesotskii *et al.* [177]. If the state between 1.7 and 1.9 T is indeed a spin-flopped state, it is much more narrow than for κ-FeCl: The normalised transition values for κ-FeCl are $b_{\text{sf}} = 0.4$ and $b_k = 0.8$ comparing to $b_k = 0.5$ in κ-FeBr (and no observable spin-flop transition) for $t = 0.5$. If there indeed also exists a spin-flop state in κ-FeBr it exists only at much lower temperatures.

A comparison of the normalised transition values for $B\|a$ and $B\|c$ of the two compounds yields another interesting point: At $t = 0.5$ we have $b_k = 1.07$ for $B\|c$ and 0.5 for $B\|a$ in κ-FeBr. In κ-FeCl the respective values are $b_k = 1.05$ for $B\|c$ and 0.8 for $B\|a$. This means that the transition fields along the two inplane axes are much more similar in the Cl-salt. Probably this higher similarity of the transition fields favours the appearance of a spin-flop phase.

All this hints to a smaller inplane anisotropy for the spin alignment in κ-FeCl: The

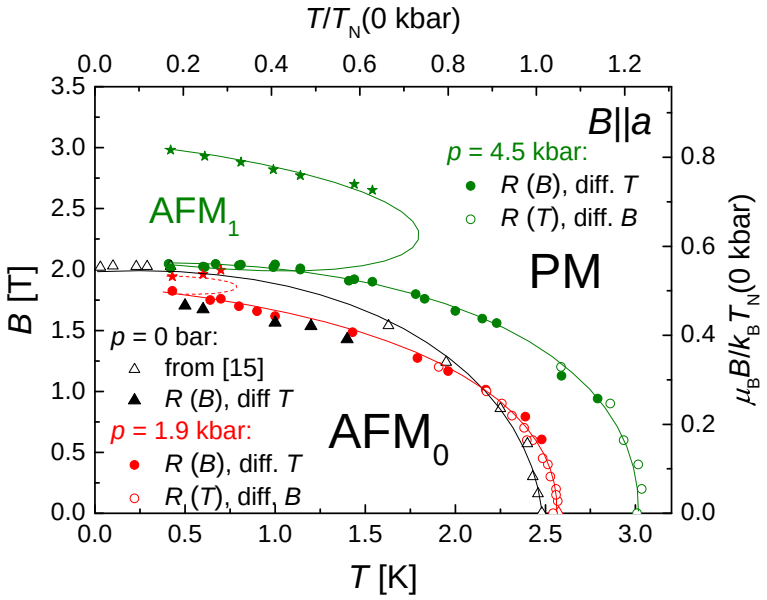

Figure 6.44: The phase diagram of κ-FeBr for $B\|a$ at different pressures. A part of the data at 0 kbar is from [22]. The right and top axis show the transition field and temperature normalised to the zero pressure T_N. (from [25])

existence of a spin-flopped state is strongly dependent on the energy-loss of the system, when changing the staggered magnetisation direction. If the energy-loss is small (the intermediate axis has not very much higher energy than the easy axis) a spin-flopped state is developed at a relatively low field. When the energy difference to the easy axis is higher the spin-flop transition field increases. In the case of a very anisotropic system no spin-flop state is observed anymore because the system remains in the zero field AFM state until at a certain field a spin-flip transition is observed, where half of the spins, which are antiparallel to the external field, turns by 180° and the AFM state is broken completely in one transition.

When we now look at the higher pressures in Fig. 6.44, wee see that for $p = 1.9$ kbar the phase line stays underneath the one reported by [22]. However, it is slightly above the points from our zero pressure measurements for this field direction, which can be extracted from the sweeps shown in Fig. 6.39. This indicates that the transition field does not change significantly at 1.9 kbar for this field direction. For the field sweeps at lowest temperatures a second transition feature becomes visible as shown by the arrows in Fig. 6.45(a). In the phase diagram this second feature is given by the red stars in Fig. 6.44. This raises the question, whether this indicates the appearance of a spin-flop phase at this pressure. However, the transition seems to move to higher field for higher temperatures. Furthermore the shape of the transition being a drop in resistance rather than an increase is expected for the AFM to PM transition. Therefore, it would rather suggest that this is a reentrant transition into the AFM phase like observed in κ-FeCl in Fig. 6.27. However, no further transition was found for higher fields.

For $p = 4.5$ kbar the phase-line starts at a higher temperature but becomes flatter

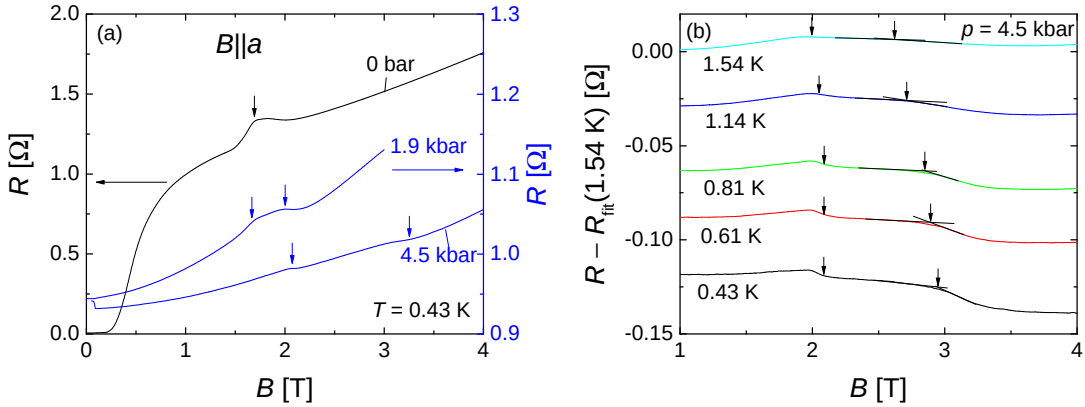

Figure 6.45: (a) Field-sweeps with $B\|a$ for different pressures at $T \approx 0.4\,\mathrm{K}$. The left axis gives the resistance of the 0 kbar curve and the right axis for the high pressure data. (b) Field-sweeps at different temperatures at $p = 4.5\,\mathrm{kbar}$ after subtracting a third order polynomial fit to the curve at $T = 1.54\,\mathrm{K}$. In both graphs arrows mark the points taken as the transition field.

compared to literature data for ambient pressure [22] showing almost the same transition field at $T \to 0\,\mathrm{K}$. Also here a second feature was observed in field sweeps at low temperatures (indicated by the arrows in the 4.5 kbar curve in Fig. 6.45(a)) and is represented by the green stars in Fig. 6.44. This transition feature shifted to lower fields at higher temperatures and was observed up to $T = 1.5\,\mathrm{K}$. For higher temperatures the feature became difficult to observe. Therefore, a third order polynomial fit to a curve at 1.54 K was subtracted. The curves with this subtracted "background" are shown in Fig. 6.45(b).

This behaviour together with the strong flattening of the transition line of the lower transition might be a stronger indicator for a spin-flop phase that covers a significant field range. No hint for the existence of this "high-field" phase was found in temperature sweeps. This may be caused by the very flat slope of $B(T)$ for most of the phase line. At the maximum temperature of the spin-flop phase (probably at $\sim 1.6\,\mathrm{K}$ and $\sim 2.3\,\mathrm{T}$ for κ-FeBr) a similar "white spot" was found in κ-FeCl, because of the inversion of the kink feature. However, since this second feature is very weak, there is no unambiguous evidence for the existence of a spin-flop phase at this pressure. For clarification measurements with higher quality samples would be necessary.

6.3 Conclusion: Interplay of magnetic and conducting subsystems in κ-$(BETS)_2FeX_4$

In both compounds κ-FeCl and κ-FeBr a clear influence of the magnetic subsystem on the conduction electrons was found in the normal state SdH-oscillations. The appearance of nodes in the contributions from both the α and the β orbits could mainly be attributed to the exchange interaction. From the behaviour of these nodes a determi-

nation of the exchange field became possible. For κ-FeBr it yielded $B_e = (12.8 \pm 0.3)\,\mathrm{T}$, which is in reasonable agreement with the value obtained from the FISC state. For κ-FeCl the exchange field could be determined for the first time, using this method, yielding $B_e = (7.1 \pm 0.3)\,\mathrm{T}$. However, for both compounds the nodes in the α oscillations were found only for tilt angles of $\theta > 20°$. And also at the higher tilt angles we found discrepancies to the theoretical model.

The FS shape of κ-FeCl was mapped by the use of AMRO. Three different AMRO components have been resolved. Two of them are q2D AMRO and could be attributed to the 2D classical orbit α and the breakdown orbit β, respectively. The elliptical FSs obtained from the 2D AMRO are in very good agreement, with the properties obtained from the SdH oscillations.

The third component is a LMA resonance and results from the q1D open FS sheets. For the LMA the θ positions of the dips were found to be shifted by half a period as compared to the standard LMA condition. An explanation in terms of the stacking pattern of the BETS molecules is proposed.

SdH oscillations in the AFM state indicate a FS reconstruction below the transition for both compounds, which is a clear sign of the impact of the magnetic ordering on the conduction electrons. In κ-FeBr the angular dependence of this δ oscillations revealed no influence of the Zeeman splitting on the oscillations within the AFM state. In general the absence of the spin-splitting effect in an AFM state has been predicted by theory [172–176], however, either some adjustment of the FS reconstruction or the theory are necessary in order to be in full agreement.

A determination of the magnetic phase diagram of κ-FeCl at magnetic field along the easy axis a revealed the existence of a spin-flop state. For the other two crystallographic axes only one phase line was observed, as was expected for those directions. A small enhancement of the transition temperature at small fields for $B \| b$ was observed, which could be a result of phase fluctuations and is predicted for q2D antiferromagnets. This may be an indication for a very weak interlayer coupling in the present compound, which would be in agreement with calculations of the exchange interaction [98]. A comparison with the magnetic phase diagram of κ-FeBr suggests a stronger out-of-plane anisotropy for the Cl-compound but a stronger inplane anisotropy in the Br-compound.

Under pressure the AFM state of κ-FeBr becomes enhanced, resulting in a higher Néel temperature and transition field as revealed by the magnetic phase diagrams for fields applied along all three principle axes. For $B \| a$ (easy axis) our measurements suggest the existence of a spin-flop phase at a pressure of $p = 4.5\,\mathrm{kbar}$, which was not unambiguously established in this compound at ambient pressure.

7 Summary

In this Ph.D. thesis compounds from two different families were investigated, mainly by measurements of interlayer resistance. In α-(BEDT-TTF)$_2$MHg(SCN)$_4$ (M = K, Tl) (α-KHg and α-TlHg) the SC state was thoroughly examined with magnetic field applied along different directions, under different hydrostatic pressures. In κ-(BETS)$_2$FeX$_4$ (X = Cl, Br) (κ-FeCl and κ-FeBr) the interplay between localised magnetic and conducting subsystems was studied using magnetoresistive phenomena.

One major topic was the analysis of the critical field anisotropy in the compounds α-KHg and α-TlHg above and below the critical pressure for the CDW state. An important step in this topic was the first discovery of a bulk SC state under high hydrostatic pressure in α-TlHg. A large part of the p-T phase diagram in the pressure range above 3.5 kbar has been determined for the first time. The critical pressure was found to be $p_c = (4.7 \pm 0.3)$ kbar. For both compounds the anisotropy parameter $B_{c2,\parallel}/B_{c2,\perp}$ was found to change only weakly with pressure, which is in contrast to expectations of a higher 3-dimensionality of the compounds under pressure. This is because the out-of-plane critical field also decreases strongly with pressure. In comparison, the SC state of α-TlHg is more robust with respect to fields applied perpendicular to the conducting layers, which results in a factor of 2 lower anisotropy as compared to the K-compound.

Close to the critical pressure both compounds clearly exhibit a strong influence of the paramagnetic pair-breaking effect for magnetic fields applied parallel to the conducting layers. This is manifested both in the temperature-dependence of the inplane critical field and in the evolution of the polar angle-dependence with temperature. Maki parameters of up to $\alpha = 5.2$ for α-KHg and 4.5 for α-TlHg were obtained at the pressures closest to p_c. In spite of these high values no sign of an FFLO state was observed in either of the compounds.

Both compounds show a noticeable inplane anisotropy. The direction of $\varphi \approx 50^\circ \pm 5^\circ$ for the strongest superconductivity in the bulk SC state of both compounds does not seem connected to any of the FS or crystal structure parameters at first glance. However, if we compare this direction with the inplane anisotropy of the inhomogeneous SC state at ambient pressure, where the direction of strongest superconductivity is at $\varphi \approx 30^\circ \pm 5^\circ$, we see a $\sim 20^\circ$ shift in this angle, which is similar to the shift of the direction of the 1D FS sheets, caused by the FS reconstruction in the CDW state. This hints to some connection to the position of the 1D FS sheets. However, for a more clear picture further measurements, especially at slightly undercritical pressures are required.

Even with the very high (for organic charge-transfer salts) inplane coherence length $\xi_\parallel \approx 700$ nm in α-KHg at $p = 4.7$ kbar, which is a result of the very low critical temperature and fields, no indication for a crossover from the type II to the type I

regime of superconductivity was found in our measurements. Estimations of $\xi_{\|}$ and λ_{L} at the highest studied pressure of $p = 4.7\,\mathrm{kbar}$ yield a Ginzburg-Landau parameter κ slightly bigger than $1/\sqrt{2}$. However, with this value of κ our system is not in a strongly type I regime of superconductivity. Further we have to take into account that the crossover into the type I regime will only be realised, if our system is in the clean limit of superconductivity. Our rough estimations of the mean free path ℓ yield a value, which, while slightly higher, lies in the same order of magnitude as $\xi_{\|}$ and λ_{L}. So we have to conclude that our system probably lies in an intermediate regime both concerning cleanness and the GL-parameter κ. Therefore, this may be the reason that we do not see any manifestations of a type I superconductivity regime in our system. Additionally we should keep in mind that maybe the type I nature of superconductivity is hard to detect in interlayer resistance measurements.

In κ-FeCl and κ-FeBr Shubnikov-de Haas (SdH) oscillations were used as a tool to study the FS and the magnetic interactions and their changes at the transition from the AFM to the PM state. The influence of the localised magnetic moments was examined, by tracking nodes in the SdH oscillations. These nodes are caused by a change of the Zeeman-splitting in the presence of an exchange interaction. Thereby the exchange field B_e of κ-FeCl could be experimentally determined for the first time. The resulting value of $B_e = (7.1 \pm 0.3)\,\mathrm{T}$ is in reasonable agreement with theoretical predictions. In κ-FeBr similar studies yielded a value of $B_e = (12.8 \pm 0.3)\,\mathrm{T}$, which is consistent with the value obtained from the center of the field induced SC (FISC) region on the phase diagram. However, for both compounds anomalies in the behaviour of the nodes were observed, which could not be explained yet. For clarifications of these issues, further studies, including measurements of the magnetisation, are necessary.

Inside the AFM state a different set of SdH oscillations was found for both compounds, indicating a FS reconstruction upon the transition into the AFM state. The oscillations are characterised by a strong hysteresis of both the background resistance and the oscillation amplitude. While the exact behaviour of the background resistance is strongly sample dependent, the oscillation amplitude is always lower on the field downsweep. This behaviour can probably be explained by a field induced disorder, maybe some kind of domain structure, which shows a hysteretic behaviour.

An extensive study of the angular dependence of these oscillations inside the AFM state in κ-FeBr revealed the complete absence of the spin-splitting effect inside the AFM state. This result is, in general, in agreement with theoretical predictions. However, the exact conditions for this behaviour specified in the theory are not met in our system. This means that either the FS reconstruction is more complicated than suggested to date or the theory has to be revised.

The magnetic phase diagram of κ-FeCl was established for magnetic field along the three principal axes in the temperature range below $T_N = 473\,\mathrm{mK}$. For magnetic field along the easy axis (the crystallographic a-axis) a spin-flop state was found with a bicritical point of $T = 0.25\,\mathrm{K}$ and $B = 0.28\,\mathrm{T}$. The AFM state is completely suppressed at a field of approximately twice the spin-flop field. For the two hard axes only one AFM

phase was observed as expected. For $B\|b$ the phase line starts with a positive slope at T_N, reflecting a slight enhancement of the transition temperature for small fields. This behaviour is an indication for a rather weak interlayer coupling in the present compound: Due to the low dimensionality of the system T_N is reduced because of phase fluctuations, which become suppressed by magnetic fields.

A comparison of these phase diagrams with the sister compound indicates a stronger magnetic interlayer coupling in κ-FeBr. There also seems to be a smaller anisotropy for the spin orientation between the two hard axes (b and c) for κ-FeBr, since the transition fields for those two axes are very similar, while they are almost a factor of 2 different in κ-FeCl. However, κ-FeCl has a lower inplane anisotropy. This is the reason that the spin-flop phase is observed in a large area of the phase diagram, while in κ-FeBr the existence of a spin-flop state was not yet unambiguously revealed.

The phase diagram of κ-FeBr has been studied under pressure: The SC state is rapidly suppressed while the AFM state shows a clear enhancement under pressure. This is probably caused by the compression of the crystal, resulting in shorter interatomic distances and, therefore, stronger d-d interactions, which are dominant in the present compound. This is a significantly different behaviour than what was observed for λ-FeCl, where a reduction of the AFM state is observed under pressure. The reason for this is the fact that in λ-FeCl the π-d coupling is dominant. For $B\|a$ at $p = 4.5\,\mathrm{kbar}$ a second phase line started to appear at low temperatures seen by a very weak feature in field sweeps. This is the first hint of a spin-flop state in κ-FeBr under pressure. One explanation for this behaviour is that the compression reduces the inplane anisotropy for the spin orientation, making the spin-flop state more energetically favourable.

Appendix

A Sample characterisation

Sample quality was an important issue for the properties studied in this thesis. Especially the SC state proves to be strongly dependent on the specific sample purity. This strong sample dependence of the SC state was also observed in both α-KHg and κ-FeBr. For κ-FeBr the quality was especially important because of the necessity of observing strong SdH oscillaitons as explained in Sec. 6.2. Therefore, in this appendix we show some sets of measurements on both compounds, which were used in order to estimate the sample quality.

A.1 α-(BEDT-TTF)$_2$KHg(SCN)$_4$

A.1.1 Determination of sample quality

A characterisation at ambient pressure was respectively done for both α-KHg and α-TlHg. As the procedure for both compounds is exactly the same we will only present the details on the characterisation measurements on α-KHg here and give a short summary of the characterisation on α-TlHg.

For the characterisation a number of different properties are known to yield information on the crystal quality. We will go through all of them and, at the end, summarise, which samples are thought to be the best.

Temperature dependence of the resistance

Usually the first property one looks at is the temperature dependence of the sample resistance. Figure A.1(a) shows the cooling curves of several samples of α-KHg, where the resistances were normalised to the resistance value at $T = 1.4\,\mathrm{K}$. A part of the samples was from H. Müllerr[1] and another part from N. Kushch[2] (as given in table A.1). One characteristic, which is often used to determine the purity of metals is the residual resistance ration (RRR). In our case we took for RRR the ratio the resistances at $T = 300\,\mathrm{K}$ and $1.4\,\mathrm{K}$. The details are shown in table A.1. As we can see, there is a large difference in the RRR between the different samples, with the best being sample #8 closely followed by #3 with values close to 300. For sample #6, however, the RRR is more than ten times smaller. Another property that is said to be a good indicator for the quality in this class of compounds is the resistance drop below the charge density wave (CDW) transition at $T \approx 8\,\mathrm{K}$, which can be seen in the low part of the $R(T)$ shown in Fig. A.1(b). Therefore, also the ratio $\frac{R(8\,\mathrm{K})}{R(1.4\,\mathrm{K})}$ has been calculated and is given

[1] European Synchrotron Radiation Facility, 38043 Grenoble, France
[2] Institute of Problems of Chemical Physics, 142432 Chernogolovka, Russian Federation

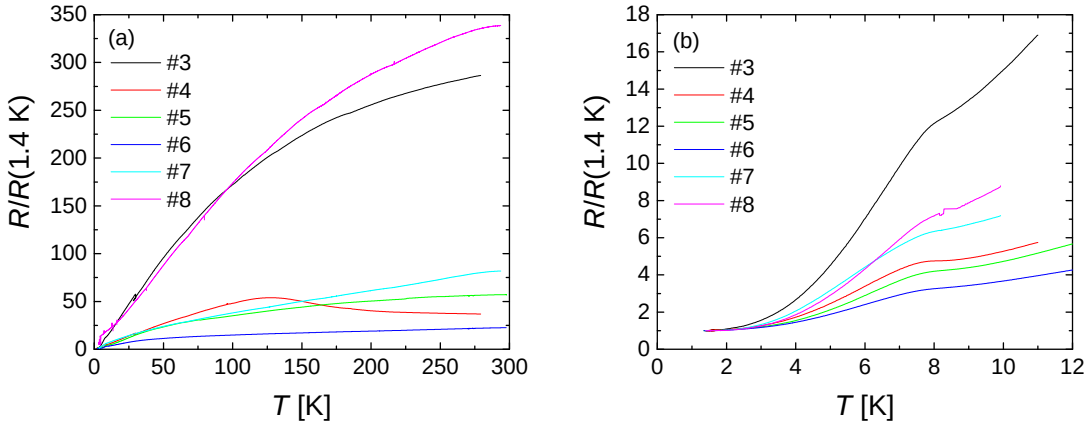

Figure A.1: (a) Interlayer resistance of several samples of α-KHg as a function of temperature. The sample resistances are normalised to $R(T = 1.4\,\mathrm{K})$. (b) The low temperature part of the curves shown in (a). The hump at $T \approx 8\,\mathrm{K}$ is caused by the transition into the CDW state.

in table A.1. The ranking of the samples in this category is almost equal as for the RRR.

Sample	$R(300\,\mathrm{K})$	$R(8\,\mathrm{K})$	$R(1.4\,\mathrm{K})$	$\mathrm{RRR}\left(\frac{R(300\,\mathrm{K})}{R(1.4\,\mathrm{K})}\right)$	$\frac{R(8\,\mathrm{K})}{R(1.4\,\mathrm{K})}$
#3 H. Müller EK39	25.8 kΩ	1.09 kΩ	90 Ω	286	12
#4 H. Müller EK2..	279 Ω	83.6 Ω	17.6 Ω	37	4.75
#5 N. Kushch NKG172	1.05 kΩ	77 Ω	18.4 Ω	57	4.2
#6 N. Kushch NKG163	1.42 kΩ	205 Ω	63 Ω	22.5	3.3
#7 H. Müller EK39	2.14 kΩ	165 Ω	26.1 Ω	82	6.3
#8 H. Müller EK209	3.8 kΩ	80.3 Ω	11.2 Ω	340	7.2

Table A.1: Resistance values of the characterised α-KHg samples at ambient temperature ($T = 300\,\mathrm{K}$), at the charge density wave transition ($T_{\mathrm{CDW}} = 8\,\mathrm{K}$) and at the lowest reached temperature during characterisation ($T = 1.4\,\mathrm{K}$) and their respective rations.

Magnetoresistance and Shubnikov-de Hass oscillations

Some other important properties can be studied by applying a magnetic field perpendicular to the conducting layers. Figure A.2(a) shows the field dependence of the resistance for the same six samples as presented above. The resistances were normalised to the zero field resistance. Therefore, the scale of the y-axis of Fig. A.2(a) directly shows us the relative magnetoresistance. Usually samples with higher quality tend to have a higher magnetoresistance. Again the ranking is very similar to that of the RRR, where the only differences are that #3 and #4 are inverted and that #7 scores significantly

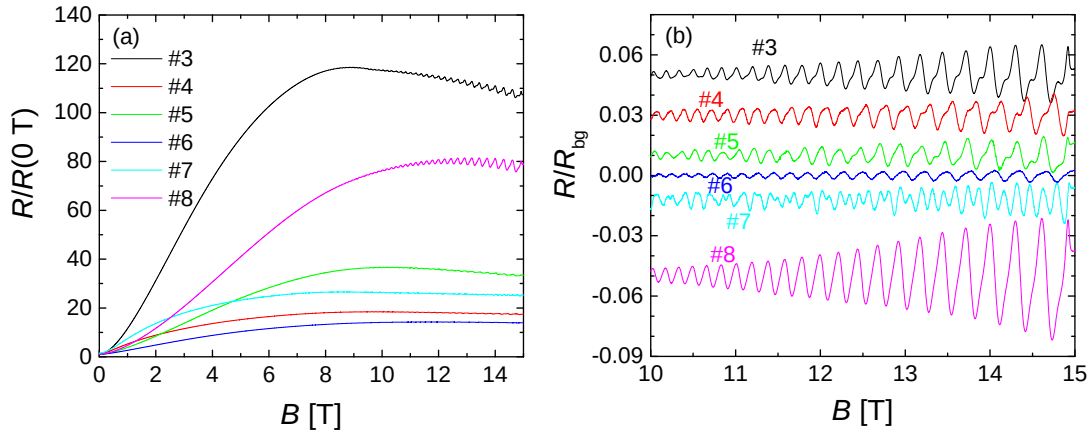

Figure A.2: (a) Resistance as a function of magnetic field perpendicular to the layers, normalised to the resistance at zero field, for several samples. (b) Oscillatory part of the resistance (normalised to the background resistance) of the sweeps shown in (a). The curves are shifted with respect to each other for better visibility.

lower.

Another important criterium is the relative amplitude of the SdH oscillations, which become visible above $B \approx 8\,\mathrm{T}$ in Fig. A.2(a). The reason for this is that, as explained in Sec. 2.1.2, a finite relaxation time of the electrons due to crystal imperfections broadens the Landau tubes and, therefore, decreases the oscillation amplitude. The comparison of the relative amplitudes of the samples can be seen in Fig. A.2(b), where the high field part of the field sweeps normalised to the background resistance is plotted. When looking at the main frequency α, sample #8 clearly has the highest amplitude of about 6% at 15 T, followed by #3. #6 is by far the worst with an amplitude, which is about a factor of 10 smaller than #8. However, we also have to take into account that many samples show a strong second harmonic. In #7 the second harmonic is especially strong and even becomes the dominating component. In #6 and #8 the second harmonic is rather weak. So again samples #3 and #8 look most promising. We do not understand why the second harmonic in #8 is so much weaker, than in the other samples, but it has to be noted that in general it is still unclear, why the second harmonic in this compound is so strong. #7 also shows a special behaviour with its extremely strong second harmonic.

Angular magnetoresistance oscillations (AMRO)

Further conclusions can be drawn from the angular dependence of the magnetoresistance. Figure A.3 shows some examples of θ-sweeps for the six presented samples at different azimuthal angles of φ^*. $\varphi^* = 0°$ is arbitrary. The measurements were performed at $T = 1.4\,\mathrm{K}$ and $B = 15\,\mathrm{T}$. The first point to notice in the presented curves, are the AMRO, which are present in all samples. In fact, the dominating AMRO component is a Lebed-magic-angle (LMA) resonance caused by the q1D parts of the FS (as explained in Sec. 2.2.1). In this respect this class of compounds shows an unusual behaviour. For

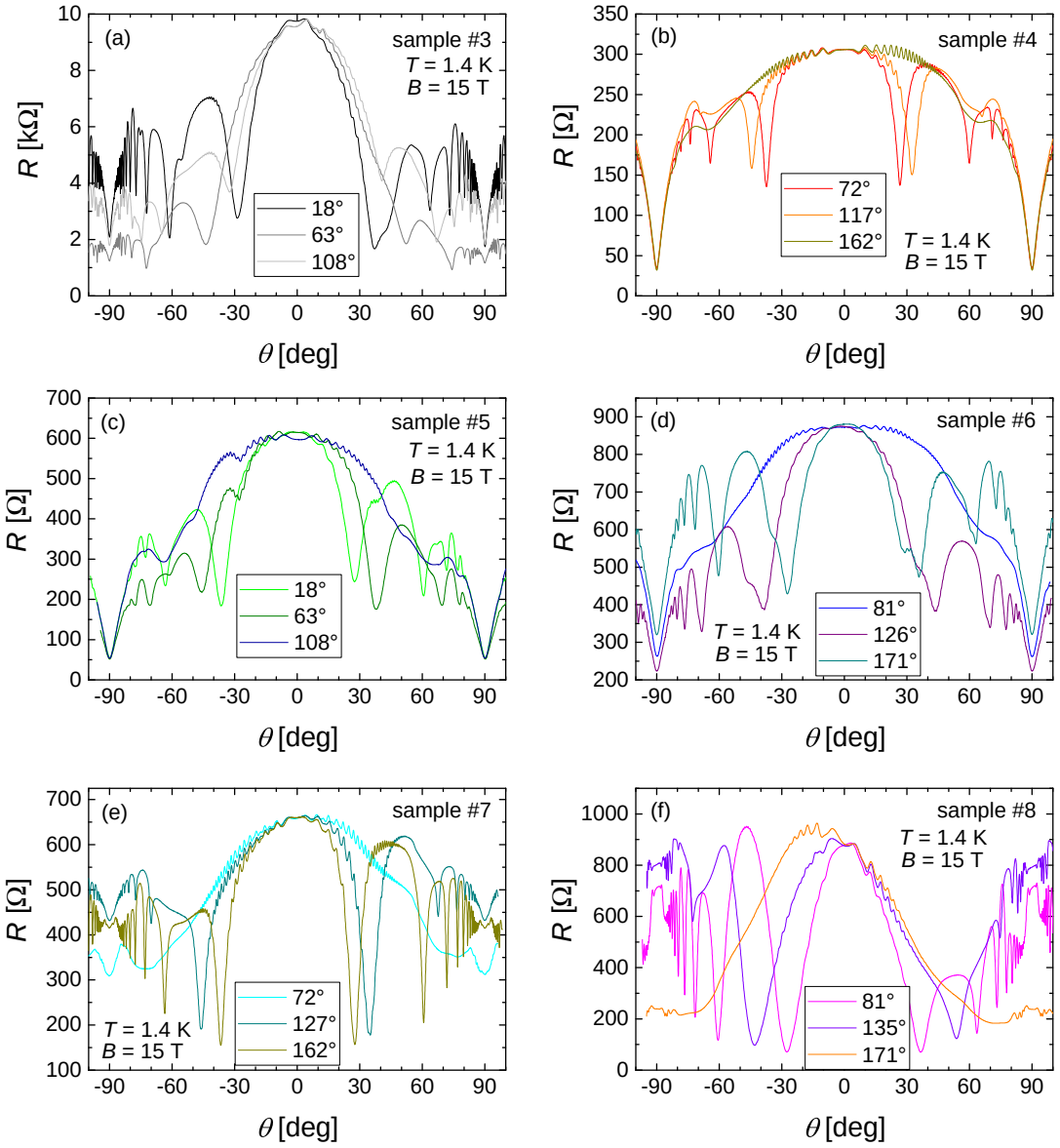

Figure A.3: Examples of θ sweeps at different φ^* for the different measured samples. All the measurements were done at $T = 1.4\,\mathrm{K}$ and $B = 15\,\mathrm{T}$. The φ^*-values are arbitrary and were chosen so that for each sample one curve with a minimum period, a maximum period and one in between are shown.

most compounds the AMRO component caused by the 2D FS are dominating [9] as we have seen on the AMRO of κ-FeCl presented in Sec. 6.1.3. The reason that the LMA are the dominating AMRO component in α-KHg lies in the FS reconstruction due to the CDW state [113]. The φ^*-angles of the presented curves were always chosen to show data with φ^* close to maximum and close to minimum period of the oscillations and one φ^* somewhere in between.

When comparing the relative amplitude of the LMA, we see that samples #4 and #5 (Figs. A.3(b) and (c)) have the smallest amplitude, while sample #8 (Fig. A.3(f)) clearly has the largest. Again, a large amplitude usually is a sign for better quality, since the AMRO are an effect of coherent interlayer transport, which is weakened by high impurity scattering. The effect of a strong or weak incoherent interlayer transport can be seen even stronger, when looking at the $R(\theta)$-dependence in the vicinity of $\theta = \pm 90°$. For low quality samples the angular dependence of resistance near parallel orientation is characterised by a broad dip [107] like it is observed for samples #4, #5 and #6 (Figs. A.3(b), (c) and (d)). In case of high quality samples the structure is more complex, as we can see on samples #3, #7 and #8 (Figs. A.3(a), (e) and (f)).

The exact explanation for the resistance behaviour at parallel field is the existence of two different channels for the interlayer transport [171]: The coherent transport is caused by the Boltzman conductivity, which is dependent on the orientation and strength of the magnetic field, while the incoherent transport is only sensitive to the field component perpendicular to the layers. The incoherent interlayer transport may for instance be caused by electrons being scattered to the adjacent layer by impurities. For lower quality samples the impurity concentration is high and the scattering rate τ^{-1} is large. Under these conditions the charge transfer for B parallel to the layers is mainly due to the incoherent hopping [171]. When the field is tilted away from parallel, the incoherent conductivity decreases and, therefore, the AMRO, which are exclusively caused by the coherent channel, become visible. In the case of a high quality sample, the impurity concentration and, therefore, the scattering rate is low. This strongly suppresses the incoherent transport leaving only the coherent channel. The absence of the incoherent channel leads to higher AMRO and other features for $\theta \approx 90°$ characteristic of the coherent magnetoresistance, which are otherwise shunted by the incoherent channel.

Among the features of the coherent interlayer transport with a field orientation close to parallel, is a peak-like structure centered at $\theta = 90°$, which is called the "coherence peak". As described in Sec. 2.2.2, the coherence peak is caused be the self-touching orbits on the q2D FS and can be used to determine the warping of the cylindrical FS. For α-KHg the coherence peak is known to be visible only in a limited φ region [107] and, since it is a property of the coherent transport channel, it is only visible for high quality samples. In our characterisation only samples #7 and #8 showed a coherence peak. However, the reason for the absence of a coherence peak in sample #3 might be found in its bicrystalline nature. This is because the second crystallite, while having parallel conducting planes, is tilted in φ. Therefore, for each of the crystallites the coherence peak would appear at a different φ and the relative amplitude is expected to be smaller than usual since only a part of the crystal contributes to the coherence peak. This may cause the coherence peak to become unresolvable.

Another significant characteristic of the coherent transport is the φ-dependence of the parallel magnetoresistance $R_\parallel(\varphi)$. In Figs. A.3(b) and (c) we can see that samples #4 and #5 show no φ dependence of $R_\parallel$ at all, which suggests that these are the most incoherent ones measured. By far the highest φ-dependence of $R_\parallel$ is observed in sample #8 (Fig. A.3(f)), where the highest $R_\parallel$ is about 10 times the lowest one.

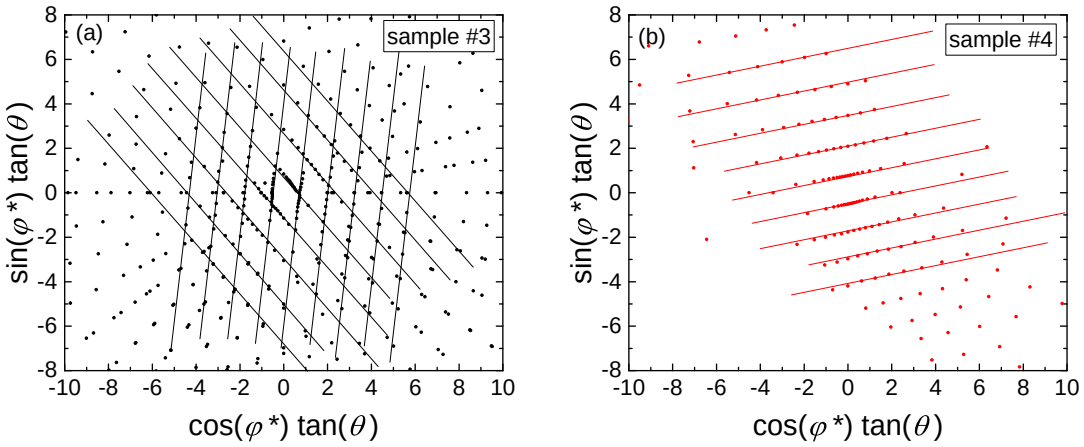

Figure A.4: The position of the LMA dips at different φ and different θ for samples (a) #3 and (b) #4.

Bicrystallinity

For measurements of the critical field anisotropy, it is essential that the used samples are single crystals. While it is usually possible to recognise by the shape of the crystal whether a sample of α-MHg is single- or bicrystalline, AMRO measurements make it possible to verify this. Figure A.4 exemplarily shows the positions of LMA dips in a polar coordinate system of θ and φ for samples #3 and #4. In the case of a single crystalline sample only one set of LMA is observed, where the LMA period depends on the φ angle between the field direction projected onto the plane of the conducting layers and the direction of the 1D FS sheet as explained in Sec. 2.2.1. Therefore, in this coordinate system the positions of the LMA dips lie on straight lines, which are perpendicular to the direction of the nesting vector $\mathbf{Q}$. Such a pattern is seen for sample #4 in Fig. A.4(b), indicating that this sample is a pure single crystal. In a bicrystalline sample we expect two sets of LMA, because each of the crystallites contributes to the total resistance of the sample. This is because, as explained in the last section, the crystallites are stacked on each other and the current has to pass through both of them. For sample #3 clearly two sets of lines are resolved demonstrating that #3 is a bicrystal.

For the other crystals the patterns are not shown due to high similarity. We found out that sample #5 has a very small second crystallite, while all other presented samples were single crystals.

Summary of characterisation

Taking into account all of the presented properties, we can conclude that samples #4, #5 and #6 are of rather low quality while #3, #7 and #8 are of higher quality. Sample #3, however, in the presented characterisation was a bicrystal and after splitting showed a lower quality than before. In the end sample #8 was chosen to be cooled down in the dilution refrigerator, because of its high $R_{\parallel}(\varphi)$. Still the majority of the measurements presented in this thesis were done on sample #1, which is the highest quality sample

of α-KHg found so far, since it still showed significantly higher T_c and a sharper SC transition than sample #8.

As mentioned above, a similar characterisation was performed for different samples of α-TlHg. Also there samples with significant differences in the above mentioned characteristics were found. In the end two samples were chosen for measurements in dilution refrigerator, where again only one sample showed a relatively sharp SC transition allowing detailed studies of the critical field anisotropy. This characterisation is described in detail in the master's thesis of L. Höhlein [41].

A.1.2 Determination of the crystal axes

In order to study the orientation dependence of physical properties it is essential that the orientation of the crystal axes of the samples is known. Commonly this is done by a Laue diffraction, which can be done fast. For some materials like the κ-FeX compounds presented chapter 6 of this thesis the orientation can also be directly seen from the shape of the crystal. This is, however, not possible for the α-MHg compounds: While the crystal structure is triclinic, the inplane lattice constants a and c differ by only 1% and the inplane crystal angle β is almost 90° making it difficult to distinguish the different axes. In this compound the characteristic edges of the "as grown" crystals can be either parallel to the a and c direction or to the diagonals ($a \pm c$ and $a \mp c$) according to earlier test with X-ray diffraction, so that, together with the almost 90° angle, a determination of the crystal axes by the shape of the crystal is impossible.

The routine method in order to obtain the crystal orientation of these compounds

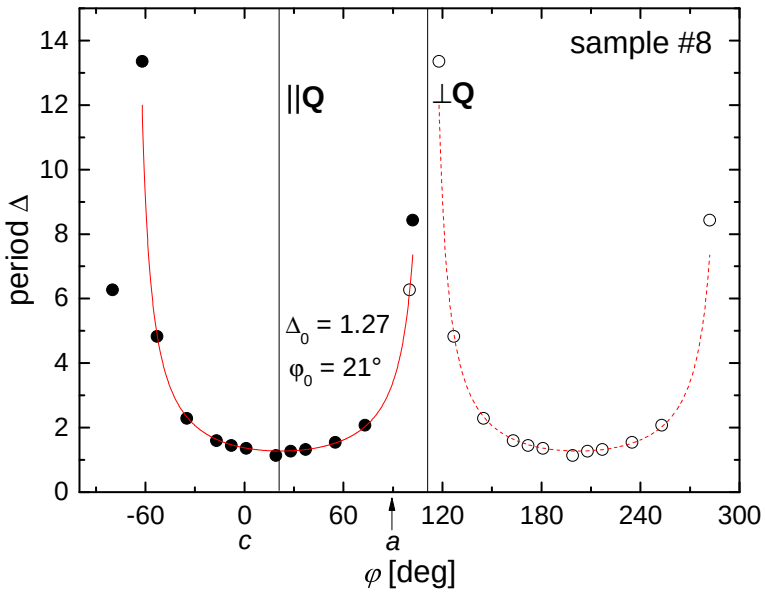

Figure A.5: φ-dependence of the LMA period Δ. The empty circles represent the same data as the filled ones, but are shifted by 180°. Δ_0 is the LMA period and φ_0 is the angle between the LMA minimum (direction of $\mathbf{Q}$) and the c-axis.

would be a full diffraction pattern, which is extensive an costly and was not readily available. Fortunately, a determination of the crystal orientation is also possible from LMA studies. As explained above, the LMA period depends on the φ angle: It becomes minimum, when the magnetic field is rotated in the plane parallel the 1D FS sheet and diverges perpendicular to that direction. In the CDW phase of the present class of compounds the FS sheet is parallel to the direction of the nesting vector $\mathbf{Q}$. Therefore, by looking at the φ-dependence of the period the direction of $\mathbf{Q}$ can be determined [63].

The LMA period Δ for each φ can be estimated by plotting the value of $\tan\theta_p$ against the order number p, where θ_p is the p-th order LMA dip. This period $\Delta(\varphi)$ is then plotted versus φ and fitted with the dependence

$$\Delta(\varphi) = \frac{\Delta_0}{\cos(\varphi - \varphi_0)}, \tag{A.1}$$

where φ_0 is the angle of the minimum period Δ_0.

This procedure has been done for all characterised single crystals. However, here we will only present the results for sample #6 from the characterisation, because it was the only one that was further studied. For this sample the $\Delta(\varphi)$ is shown in Fig. A.5, where the empty symbols are the same data as the filled one, but shifted by 180°. From the fit we obtain $\Delta_0 = 1.27$, which is in reasonable agreement with earlier reports (1.26 ± 0.02) [179]. From Fig. A.5 it is also easy to determine the direction of $\mathbf{B} \perp \mathbf{Q}$, because of

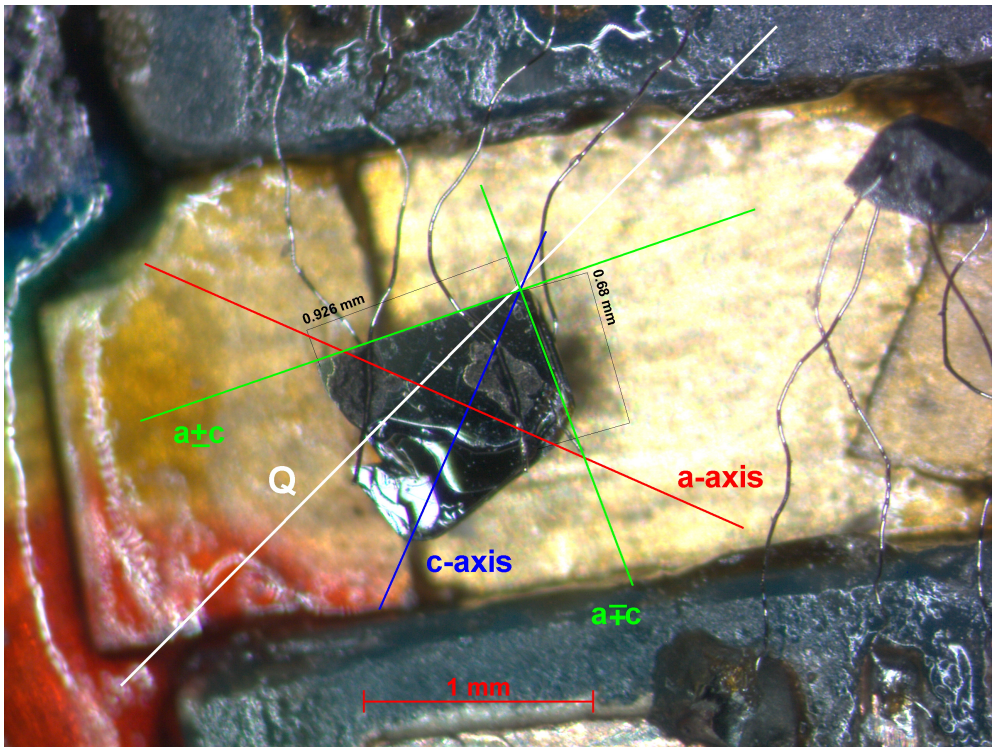

Figure A.6: Photograph of sample #6 containing the directions of the crystal axes and the nesting vector as determined from AMRO.

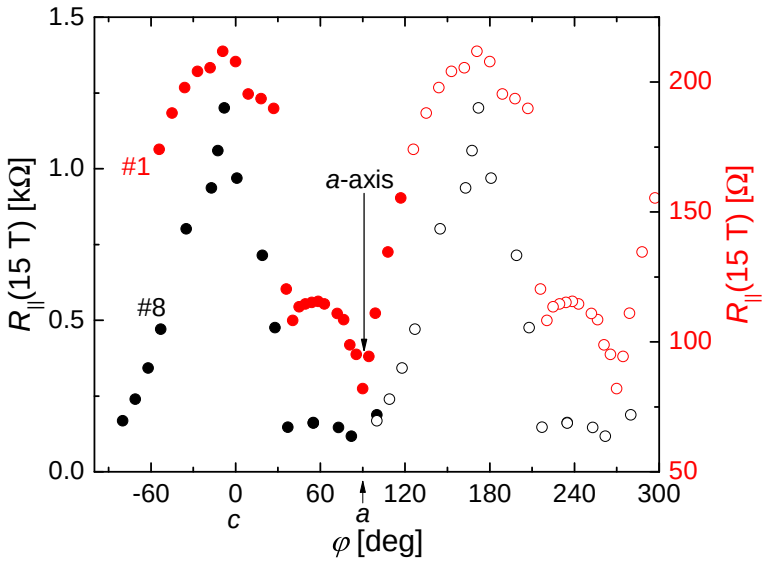

Figure A.7: Interlayer resistance of sample #8 (black) with a magnetic field applied exactly parallel to the conducting layers at $B = 15\,\mathrm{T}$. The red data set is from sample #1, where the orientation was also determined by X-ray.

the extremely strong φ-dependence of Δ in this region. According to literature we can expect an angle between the c-axis and $\mathbf{Q}$ of $\varphi_0 = 20° \pm 2°$. However, we do not have a direct access in which angular direction from $\mathbf{Q}$ we have to expect the c-axis. To this end we look at a phatograph of the sample, as shown in Fig. A.6. Here we have inserted the direction of $\mathbf{Q}$ indicated by the white line. Next we measured the angle between the white line and the closer (upper) crystal edge and the diagonal respectively. Between the crystal edge and $\mathbf{Q}$ we measure 26°and between the diagonal and $\mathbf{Q}$ we get 20°. From that we assume that for this sample, the crystal edges are the diagonals to the crystal axes and vice versa.

For samples with a sufficiently high coherent channel a further option to determine the crystal axes opens up by looking at the angular dependence of the parallel magnetoresistance $R_{\|}(\varphi)$. In the case of α-KHg the direction of the a-axis is known to be connected with a sharp dip in this dependence as we can see in Fig. A.7, where $R_{\|}(\varphi)$ is plotted for $B = 15\,\mathrm{T}$. On sample #8 only a rough $R_{\|}(\varphi)$ can be drawn from the executed measurements. For comparison a similar set of data for sample #1, which was studied by X-ray is also plotted. The φ-stepsize in the measurements on sample #8 is too big to determine the orientation of the a-axis to an accuracy of better than ±5°. However, since the position of the a-axis determined from the photograph lies within this window, we can conclude that obviously the determination from the photograph was correct.

The same procedure of determining the crystal axes was also performed on the characterised α-TlHg samples and can be found in [41].

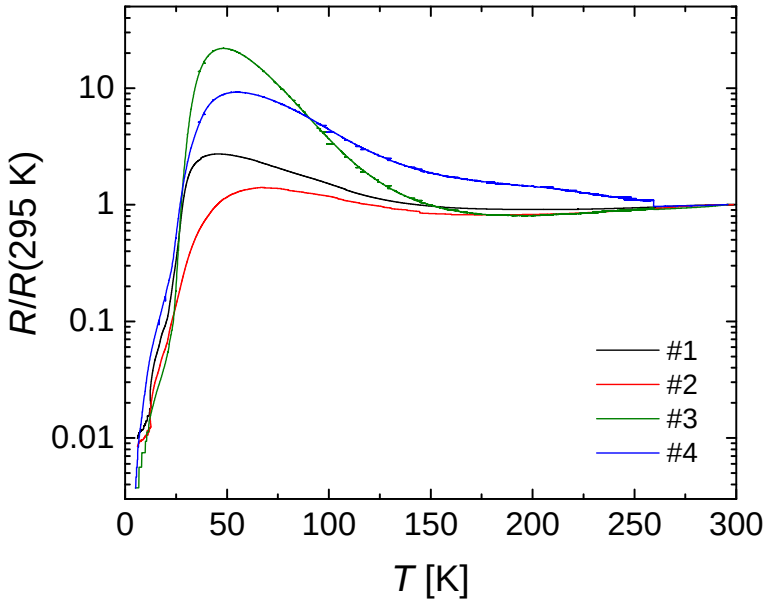

Figure A.8: Interlayer resistance of several samples of κ-FeBr as a function of temperature between 300 and 4.2 K.

A.2 κ-(BETS)$_2$FeBr$_4$

Here we present an overlook over the quality aspects of the different studied samples of κ-FeBr.

Temperature dependence of resistance

Figure A.8 shows cooling curves for the different samples of κ-FeBr normalised to the respective resistance values at $T = 295$ K. Often the cooling behaviour already contains some indication on the sample quality, however, as described in Sec. A.1.1 one has to take care how to interpret the $R(T)$ dependence. A characteristic feature of the cooling curve of κ-FeBr is a broad hump of the resistance at a temperature of around 50 K. Very similar humps were observed in a number κ-(BEDT-TTF)$_2$X salts. There it was shown that the hump height correlates with the crystal quality [180]. The RR of this material usually is in the range of 150 to 300 (measured between ambient temperature and $T = 2.5$ K, which is just above T_N), which is not nearly as high as for κ-FeCl (see Sec. 6.1.1). However, we came to the conclusion that the height of the hump is a better indicator for the sample quality. The values of the resistance ratios between ambient temperature, the maximum of the hump and low temperature values are given in table A.2.

From table. A.2 we see that according to all the ratios sample #3 is clearly the best, followed by the other Fujiwara's sample #4. The two Kushch's samples even have the same RRR showing a difference only in the height of the hump. So from the cooling curves we might expect that #3 is by far the best, #4 somewhat intermediate and the

sample	$R(300\,\mathrm{K})$	$\frac{R(300\,\mathrm{K})}{R(2.5\,\mathrm{K})}$	$\frac{R_{\mathrm{hump}}}{R(2.5\,\mathrm{K})}$	$\frac{R_{\mathrm{osc}}}{R_{\mathrm{bg}}}(B = 14\,\mathrm{T})$
#1 (Kushch AD244)	$152\,\Omega$	160	436	1.4%
#2 (Kushch AD251)	$170\,\Omega$	160	210	0.27%
#3 (Fujiwara)	$51.1\,\Omega$	272	5930	6.7%
#4 (Fujiwara)	$25.8\,\Omega$	160	1460	6%

Table A.2: Resistances of different samples at ambient temperature, the resistance ratios between ambient temperature and the hump compared to low temperature, respectively, and the relative oscillation amplitude at $B = 14\,\mathrm{T}$.

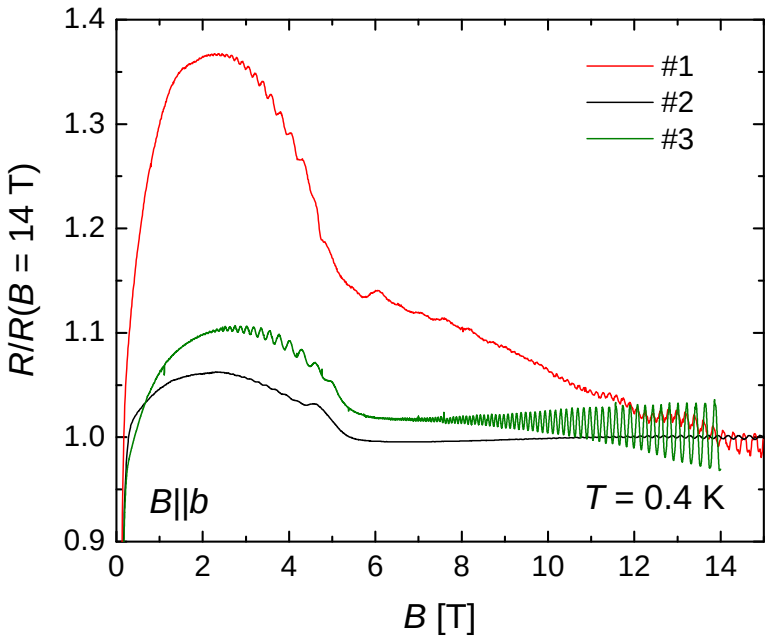

Figure A.9: Resistance as a function of magnetic field featuring SdH oscillations both below and above the AFM transition for three different samples at $T = 0.4\,\mathrm{K}$.

two Kushch samples are rather similar, sample #1 being slightly better than the other.

Shubnikov-de Haas oscillations

Let's next look at the SdH oscillations. Field sweeps with magnetic field perpendicular to the conducting layers for three of the samples shown in the cooling curves are presented in Fig. A.9(a). The temperature was set to $T = 0.4\,\mathrm{K}$. The curves have been normalised to the respective value of the background resistance at $B = 14\,\mathrm{T}$. Also here sample #3 seems to be the best, showing the highest SdH amplitude in both the AFM and the PM states. Sample #4 was not shown because it looks very similar to #3. Sample #1 is clearly the second best. At $B = 14\,\mathrm{T}$ the oscillation amplitude is about a factor 5 smaller than for #3. And here also the difference between the two Kushch's

samples is significant: The amplitude of sample #2 is a factor of 5 smaller.

Summary: Sample quality

In conclusion we observe that for both the α-MHg and the κ-FeX compounds clear differences in the sample quality can be observed by looking at the low-temperature resistance effects. However, all of the samples still had sufficient quality to show quantum effects like the SdH oscillations for fields below 15 T proving them to be significantly cleaner like for example most of the cuprates studied so far.

Bibliography

[1] K. Bechgaard, C. S. Jacobsen, K. Mortensen, H. J. Pedersen & N. Thorup. The properties of five highly conducting salts: $(TMTSF)_2X$, X = PF_6^-, AsF_6^-, SbF_6^-, BF_4^- and NO_3^-, derived from tetramethyltetraselenafulvalene (TMTSF). *Solid State Commun.* **33**, 1119–1125 (1980). URL `http://www.sciencedirect.com/science/article/pii/0038109880910881`.

[2] D. Jérome, A. Mazaud, M. Ribault & K. Bechgaard. Superconductivity in a synthetic organic conductor $(TMTSF)_2PF_6$. *J. Phys. Lett.* **41**, 95–98 (1980). URL `http://dx.doi.org/10.1051/jphyslet:0198000410409500`.

[3] K. Bechgaard, K. Carneiro, M. Olsen, F. B. Rasmussen & C. S. Jacobsen. Zero-Pressure Organic Superconductor: Di-(Tetramethyltetraselenafulvalenium)-Perchlorate $[(TMTSF)_2ClO_4]$. *Phys. Rev. Lett.* **46**, 852–855 (1981). URL `http://link.aps.org/doi/10.1103/PhysRevLett.46.852`.

[4] M. Mizuno, A. F. Garito & M. P. Cava. "Organic metals": alkylthio substitution effects in tetrathiafulvalene-tetracyanoquinodimethane charge-transfer complexes. *J. Chem. Soc., Chem. Commun.* 18–19 (1978). URL `http://pubs.rsc.org/en/content/articlelanding/1978/c3/c39780000018`.

[5] E. B. Yagubskii, I. F. Schegolev, V. N. Laukhin, P. A. Kononovich, M. V. Kartsovnik, A. V. Zvarykina & L. I. Buravov. Normal-Pressure Superconductivity in an Organic Metal $(BEDT\text{-}TTF)_2I_3$ [bis(ethylene Dithiolo) Tetrathiofulvalene Triiodide]. *Jetp Lett.* **39**, 12–16 (1984).

[6] N. Toyota, M. Lang & J. Müller. *Low-Dimensional Molecular Metals*. Vol. 154 of *Springer Series in Solid-State Sciences* (Springer Verlag, Berlin Heidelberg, 2007), 1st edn. URL `http://www.springer.com/us/book/9783540495741`.

[7] T. Ishiguro, K. Yamaji & G. Saito. *Organic Superconductors*. Vol. 88 of *Springer Series in Solid-State Sciences* (Springer Verlag Berlin Heidelberg, 1998), 2nd edn.

[8] A. Lebed, R. Hull, R. M. Osgood, J. Parisi & H. Warlimon (eds.) *The Physics of Organic Superconductors and Conductors*, Vol. 110 of *Springer Series in Materials Science* (Springer Berlin Heidelberg, Berlin, Heidelberg, 2008). URL `http://link.springer.com/10.1007/978-3-540-76672-8`.

[9] M. V. Kartsovnik. High Magnetic Fields: A Tool for Studying Electronic Properties of Layered Organic Metals. *Chem. Rev.* **104**, 5737–5782 (2004). URL `http://pubs.acs.org/doi/pdf/10.1021/cr0306891`.

[10] H. Kobayashi, H. Cui & A. Kobayashi. Organic Metals and Superconductors Based on BETS (BETS = Bis(ethylenedithio)tetraselenafulvalene). *Chem. Rev.* **104**, 5265–5288 (2004). URL http://dx.doi.org/10.1021/cr030657d.

[11] A. Ardavan, S. Brown, S. Kagoshima, K. Kanoda, K. Kuroki, H. Mori, M. Ogata, S. Uji & J. Wosnitza. Recent Topics of Organic Superconductors. *Journal of the Physical Society of Japan* **81**, 011004 (2012). URL http://jpsj.ipap.jp/link?JPSJ/81/011004/.

[12] H. Urayama, H. Yamochi, G. Saito, K. Nozawa, T. Sugano, M. Kinoshita, S. Sato, K. Oshima, A. Kawamoto & J. Tanaka. A New Ambient Pressure Organic Superconductor Based on BEDT-TTF with T_c Higher than 10 K ($T_c = 10.4$ K). *Chem. Lett.* **17**, 55–58 (1988).

[13] H. Urayama, H. Yamochi, G. Saito, S. Sato, A. Kawamoto, J. Tanaka, T. Mori, Y. Maruyama & H. Inokuchi. Crystal Structures of Organic Superconductor, $(BEDT\text{-}TTF)_2Cu(NCS)_4$, at 298 K and 104 K. *Chem. Lett.* **17**, 463–466 (1988).

[14] R. Kato, H. Kobayashi & A. Kobayashi. Synthesis and properties of bis(ethylenedithio)tetraselenafulvalene (BEDT-TSeF) compounds. *Synth. Met.* **42**, 2093–2096. URL http://www.sciencedirect.com/science/article/pii/037967799192024C.

[15] A. Kobayashi, T. Udagawa, H. Tomita, T. Naito & H. Kobayashi. New Organic Metals Based on BETS Compounds with MX_4- Anions (BETS = bis(ethylenedithio)tetraselenafulvalene; M = Ga, Fe, In; X = Cl, Br). *Chemistry Letters* **22**, 2179–2182 (1993).

[16] F. Goze, V. N. Laukhin, L. Brossard, A. Audouard, J. P. Ulmet, S. Askenazy, T. Naito, H. Kobayashi, A. Kobayashi, M. Tokumoto & P. Cassoux. Magnetotransport Measurements on the λ-Phase of the Organic Conductors $(BETS)_2MCl_4$ (M = Ga, Fe). Magnetic-Field-Restored Highly Conducting State in λ-$(BETS)_2FeCl_4$. *EPL* **28**, 427 (1994). URL http://iopscience.iop.org/0295-5075/28/6/009.

[17] L. Brossard, R. Clerac, C. Coulon, M. Tokumoto, T. Ziman, D. K. Petrov, V. N. Laukhin, M. J. Naughton, A. Audouard, F. Goze, A. Kobayashi, H. Kobayashi & P. Cassoux. Interplay between chains of S = 5/2 localised spins and two-dimensional sheets of organic donors in the synthetically built magnetic multilayer λ-$(BETS)_2FeCl_4$. *Eur. Phys. J. B* **1**, 439–452 (1998). URL http://link.springer.com/article/10.1007/s100510050207.

[18] S. Uji, H. Shinagawa, T. Terashima, T. Yakabe, Y. Terai, M. Tokumoto, A. Kobayashi, H. Tanaka & H. Kobayashi. Magnetic-field-induced superconductivity in a two-dimensional organic conductor. *Nature* **410**, 908–910 (2001). URL http://www.nature.com/nature/journal/v410/n6831/full/410908a0.html.

[19] H. Tanaka, T. Adachi, E. Ojima, H. Fujiwara, K. Kato, H. Kobayashi, A. Kobayashi & P. Cassoux. Pressure-Induced Superconducting Transition of λ-$(BETS)_2FeCl_4$ with π-d Coupled Antiferromagnetic Insulating Ground State at

Ambient Pressure [BETS = Bis(ethylenedithio)tetraselenafulvalene]. *J. Am. Chem. Soc.* **121**, 11243–11244 (1999). URL http://dx.doi.org/10.1021/ja992930s.

[20] H. Kobayashi, H. Tomita, T. Naito, A. Kobayashi, F. Sakai, T. Watanabe & P. Cassoux. New BETS Conductors with Magnetic Anions (BETS = bis(ethylenedithio)tetraselenafulvalene). *J. Am. Chem. Soc.* **118**, 368–377 (1996). URL http://dx.doi.org/10.1021/ja9523350.

[21] T. Otsuka, A. Kobayashi, Y. Miyamoto, J. Kiuchi, S. Nakamura, N. Wada, E. Fujiwara, H. Fujiwara & H. Kobayashi. Organic Antiferromagnetic Metals Exhibiting Superconducting Transitions κ-$(BETS)_2FeX_4$ (X=Cl, Br): Drastic Effect of Halogen Substitution on the Successive Phase Transitions. *Journal of Solid State Chemistry* **159**, 407–412 (2001). URL http://www.sciencedirect.com/science/article/pii/S0022459601991728.

[22] T. Konoike, S. Uji, T. Terashima, M. Nishimura, S. Yasuzuka, K. Enomoto, H. Fujiwara, B. Zhang & H. Kobayashi. Magnetic-field-induced superconductivity in the antiferromagnetic organic superconductor κ-$(BETS)_2FeBr_4$. *Phys. Rev. B* **70**, 094514 (2004). URL http://link.aps.org/doi/10.1103/PhysRevB.70.094514.

[23] T. Konoike, S. Uji, T. Terashima, M. Nishimura, S. Yasuzuka, K. Enomoto, H. Fujiwara, E. Fujiwara, B. Zhang & H. Kobayashi. Fermi surface reconstruction in the magnetic-field-induced superconductor κ-$(BETS)_2FeBr_4$. *Phys. Rev. B* **72**, 094517 (2005). URL http://link.aps.org/doi/10.1103/PhysRevB.72.094517.

[24] F. Pratt, S. Lee, S. Blundell, I. Marshall, H. Uozaki & N. Toyota. μSR studies of the interaction between magnetism and superconductivity in κ-$(BETS)_2FeCl_4$. *Synthetic Metals* **133-134**, 489–492 (2003). URL http://www.sciencedirect.com/science/article/pii/S0379677902003946.

[25] L. Schaidhammer. *Magnetotransport studies of the organic superconductor and antiferromagnet κ-$(BETS)_2FeBr_4$*. Masterarbeit, Technische Universität München (2014).

[26] F. Kollmannsberger. *Magnetic Quantum Oscillations in the Organic Antiferromagnetic Superconductor κ-$(BETS)_2FeBr_4$*. Bachelorarbeit, Technische Universität München (2016).

[27] D. Andres, M. V. Kartsovnik, W. Biberacher, K. Neumaier, E. Schuberth & H. Müller. Superconductivity in the charge-density-wave state of the organic metal α-$(BEDT\text{-}TTF)_2KHg(SCN)_4$. *Phys. Rev. B* **72**, 174513 (2005). URL http://link.aps.org/doi/10.1103/PhysRevB.72.174513.

[28] P. Christ, W. Biberacher, M. Kartsovnik, E. Steep, E. Balthes, H. Weiss & H. Müller. Magnetic field-temperature phase diagram of the organic conductor α-$(BEDT\text{-}TTF)_2KHg(SCN)_4$. *JETP Lett.* **71**, 303 (2000).

[29] N. Biskup, J. Perenboom, J. Brooks & J. Qualls. Argument for charge density wave sub-phases in the ground state of α-(BEDT-TTF)$_2$KHg(SCN)$_4$. *Solid State Commun.* **107**, 503 – 507 (1998). URL `http://www.sciencedirect.com/science/article/pii/S003810989800252X`.

[30] N. Harrison, L. Balicas, J. S. Brooks & M. Tokumoto. Critical state in a low-dimensional metal induced by strong magnetic fields. *Phys. Rev. B* **62**, 14212–14223 (2000). URL `http://link.aps.org/doi/10.1103/PhysRevB.62.14212`.

[31] M. V. Kartsovnik, D. Andres & W. Biberacher. Hierarchy of the density-wave states and superconductivity in the organic conductor α-(BEDT-TTF)$_2$KHg(SCN)$_4$. *Comptes Rendus Chimie* **10**, 6 – 14 (2007). URL `http://www.sciencedirect.com/science/article/pii/S1631074806001500`.

[32] M. V. Kartsovnik, D. Andres, W. Biberacher, P. Christ, E. Steep, E. Balthes, H. Weiss, H. Müller & N. D. Kushch. *B-T-P* phase diagram of α-(BEDT-TTF)$_2$KHg(SCN)$_4$. *Synthetic Metals* **120**, 687–690 (2001). URL `http://www.sciencedirect.com/science/article/pii/S0379677900011188`.

[33] D. Andres, M. V. Kartsovnik, W. Biberacher, H. Weiss, E. Balthes, H. Müller & N. Kushch. Orbital effect of a magnetic field on the low-temperature state in the organic metal α-(BEDT-TTF)$_2$KHg(SCN)$_4$. *Phys. Rev. B* **64**, 161104 (2001). URL `http://link.aps.org/doi/10.1103/PhysRevB.64.161104`.

[34] D. Andres, M. Kartsovnik, W. Biberacher, K. Neumaier & H. Müller. Direct evidence for superconductivity in the organic charge density wave compound α-(BEDT-TTF)$_2$KHg(SCN)$_4$ under hydrostatic pressure. *J. Phys. IV France* **12**, 87–88 (2002). URL `http://dx.doi.org/10.1051/jp4:20020364`.

[35] D. Andres, M. V. Kartsovnik, P. D. Grigoriev, W. Biberacher & H. Müller. Orbital quantization in the high-magnetic-field state of a charge-density-wave system. *Phys. Rev. B* **68**, 201101 (2003). URL `http://link.aps.org/doi/10.1103/PhysRevB.68.201101`.

[36] D. Andres. *Effects of High Magnetic Fields and Hydrostatic Pressure on the Low-Temperature Density-Wave State of the Organic Metal α-(BEDT-TTF)$_2$KHg(SCN)$_4$*. Ph.D. thesis, Technische Universität München (2005).

[37] M. V. Kartsovnik, *The Physics of Organic Superconductors and Conductors*. A. G. Lebed (ed.), chap. 8, Layered Organic Conductors in Strong Magnetic Fields, 185–246 (Springer Verlag, 2008), 2nd edn.

[38] S. Jakob. *Magnetic field effects in the layered organic superconductor α-(BEDT-TTF)$_2$KHg(SCN)$_4$*. Diplomarbeit, Technische Universität München (2007).

[39] A. I. Schegolev, V. N. Laukhin, A. G. Khomenko, M. V. Kartsovnik, R. P. Shibaeva, L. P. Rozenberg & A. E. Kovalev. Pressure effect and anisotropy of resistivity in organic metal (ET)$_2$TlHg(SCN)$_4$. *J. Phys. I France* **2**, 2123–2129 (1992). URL `http://dx.doi.org/10.1051/jp1:1992272`.

[40] H. Ito, M. Kartsovnik, H. Ishimoto, K. Kono, H. Mori, N. Kushch, G. Saito, T. Ishiguro & S. Tanaka. Superconductivity in α-(BEDT-TTF)$_2$MHg(SCN)$_4$ (M = K, Rb, Tl, NH_4). *Synthetic Metals* **70**, 899 – 902 (1995). URL `http://www.sciencedirect.com/science/article/pii/037967799402693S`. Proceedings of the International Conference on Science and Technology of Synthetic Metals.

[41] L. Höhlein. *Magnetic field and pressure effects in the layered organic superconductor α-(BEDT-TTF)$_2$TlHg(SCN)$_4$*. Masterarbeit, Technische Universität München (2016).

[42] L. Landau. Diamagnetismus der Metalle. *Z. Physik* **64**, 629–637 (1930). URL `http://link.springer.com/article/10.1007/BF01397213`.

[43] L. Onsager. Interpretation of the de Haas-van Alphen effect. *Phil. Mag.* **43**, 1006–1008 (1952).

[44] W. J. de Haas & P. M. van Alphen. The dependence of susceptibility of diamagnetic metals upon the field. *Proc. Netherlands Roy. Acad. Sci.* **33**, 1106 (1930).

[45] L. W. Shubnikov & W. J. d. Haas. The testing of mono-crystalline wires. *Proc. Netherlands Roy. Acad. Sci.* **33**, 130 and 163 (1930).

[46] D. Shoenberg. *Magnetic oscillations in metals* (Cambridge University Press, 1984).

[47] I. Lifshitz & A. Kosevich. Theory of Magnetic Susceptibility in Metals at Low Temperature. *Sov. Phys.-JETP* **2**, 636 (1956). URL `http://www.jetp.ac.ru/cgi-bin/e/index/e/2/4/p636?a=list`.

[48] E. N. Adams & T. D. Holstein. Quantum theory of transverse galvano-magnetic phenomena. *J. Phys. Chem. Solids* **10**, 254–276 (1959). URL `http://www.sciencedirect.com/science/article/pii/0022369759900022`.

[49] A. B. Pippard. *The Dynamics of Conduction Electrons* (Gordon and Breach, 1965).

[50] R. B. Dingle. Some Magnetic Properties of Metals. II. The Influence of Collisions on the Magnetic Behaviour of Large Systems. *Proc. Roy. Soc.* **211**, 517–525 (1952).

[51] J. Wosnitza. *Fermi Surfaces of Low-Dimensional Organic Metals and Superconductors*. Vol. 134 of *Springer Tracts in Modern Physics* (Springer Berlin / Heidelberg, 1996). URL `http://dx.doi.org/10.1007/BFb0048480`. 10.1007/BFb0048480.

[52] I. J. Lee, V. N. Laukhin, D. K. Petrov, M. Chaparala, N. Kushch & M. J. Naughton. Simultaneous dHvA and SdH studies of ?-(BEDT-TTF)2TlHg(SeCN)4. *Synthetic Metals* **85**, 1559–1560 (1997). URL `http://www.sciencedirect.com/science/article/pii/S0379677997803475`.

[53] S. I. Pesotski?, R. B. Lyubovski?, M. V. Kartsovnik, W. Biberacher, N. D. Kushch, A. Kobayashi & B. Zhou. Possible weakening of the many-body interactions in the organic quasi-two-dimensional metal ?-(BETS)2. *J. Exp. Theor. Phys.* **109**, 664–666 (2009). URL `http://link.springer.com/article/10.1134/S1063776109100124`.

[54] J. Wosnitza, V. M. Gvozdikov, J. Hagel, O. Ignatchik, B. Bergk, P. J. Meeson, J. A. Schlueter, H. Davis, R. W. Winter & G. L. Gard. Spin-zero anomaly in the magnetic quantum oscillations of a two-dimensional metal. *New J. Phys.* **10**, 083032 (2008). URL `http://stacks.iop.org/1367-2630/10/i=8/a=083032`.

[55] M. H. Cohen & L. M. Falicov. Magnetic Breakdown in Crystals. *Phys. Rev. Lett.* **7**, 231–233 (1961). URL `http://link.aps.org/doi/10.1103/PhysRevLett.7.231`.

[56] E. I. Blount. Bloch Electrons in a Magnetic Field. *Phys. Rev.* **126**, 1636–1653 (1962). URL `http://link.aps.org/doi/10.1103/PhysRev.126.1636`.

[57] A. Slutskin & A. M. Kadigrobov. Theory of interband magnetic breakdown in metals. *Fiz. Tverd. Tela (USSR)* **9**, 184–195 (1967). INSPEC:1968B01052.

[58] L. M. Falicov & H. Stachowiak. Theory of the de Haas-van Alphen Effect in a System of Coupled Orbits. Application to Magnesium. *Phys. Rev.* **147**, 505–515 (1966). URL `http://link.aps.org/doi/10.1103/PhysRev.147.505`.

[59] A. B. Pippard. Quantization of Coupled Orbits in Metals. *Proc. R. Soc. London* **270**, 1–13 (1962). URL `http://rspa.royalsocietypublishing.org/content/270/1340/1`.

[60] A. B. Pippard. Quantization of Coupled Orbits in Metals II. The Two-Dimensional Network, with Special Reference to the Properties of Zinc. *Philos. Trans. R. Soc. London* **256**, 317–355 (1964). URL `http://rsta.royalsocietypublishing.org/content/256/1072/317`.

[61] A. G. Lebed. Anisotropy of an instability for a spin density wave induced by a magnetic field in a q1d conductor. *JETP Lett.* **43**, 174–177 (1986).

[62] T. Osada, S. Kagoshima & N. Miura. Resonance effect in magnetotransport anisotropy of quasi-one-dimensional conductors. *Phys. Rev. B* **46**, 1812–1815 (1992). URL `http://link.aps.org/doi/10.1103/PhysRevB.46.1812`.

[63] M. V. Kartsovnik, A. E. Kovalev & N. D. Kushch. Magnetotransport investigation of the low-temperature state of transition (BEDT-TTF)$_2$TlHg(SCN)$_4$: evidence for a Peierls-type transition. *J. Phys. I France* **3**, 1187–1199 (1993). URL `http://dx.doi.org/10.1051/jp1:1993264`.

[64] A. G. Lebed & P. Bak. Theory of unusual anisotropy of magnetoresistance in organic superconductors. *Phys. Rev. Lett.* **63**, 1315–1317 (1989). URL `http://link.aps.org/doi/10.1103/PhysRevLett.63.1315`.

[65] K. Yamaji. On the Angle Dependence of the Magnetoresistance in Quasi-Two-Dimensional Organic Superconductors. *J. Phys. Soc. Jpn.* **58**, 1520–1523 (1989). URL `http://journals.jps.jp/doi/abs/10.1143/JPSJ.58.1520`.

[66] M. V. Kartsovnik, V. N. Laukhin, S. I. Pesotskii, I. F. Schegolev & V. M. Yakovenko. Angular magnetoresistance oscillations and the shape of the Fermi surface in β-$(ET)_2IBr_2$. *Journal de Physique I* **2**, 11 (1992).

[67] V. G. Peschansky, J. A. R. Lopez & T. G. Yao. On galvanomagnetic effects in layered conductors. *J. Phys. I* **1**, 11 (1991).

[68] P. D. Grigoriev. Angular dependence of the Fermi surface cross-section area and magnetoresistance in quasi-two-dimensional metals. *Phys. Rev. B* **81**, 205122 (2010). URL `http://link.aps.org/doi/10.1103/PhysRevB.81.205122`.

[69] A. A. House, N. Harrison, S. J. Blundell, I. Deckers, J. Singleton, F. Herlach, W. Hayes, J. A. A. J. Perenboom, M. Kurmoo & P. Day. Oscillatory magnetoresistance in the charge-transfer salt β''-$(BEDT\text{-}TTF)_2AuBr_2$ in magnetic fields up to 60 T: Evidence for field-induced Fermi-surface reconstruction. *Phys. Rev. B* **53**, 9127–9136 (1996). URL `http://link.aps.org/doi/10.1103/PhysRevB.53.9127`.

[70] M. S. Nam, S. J. Blundell, A. Ardavan, J. A. Symington & J. Singleton. Fermi surface shape and angle-dependent magnetoresistance oscillations. *J. Phys.: Condens. Matter* **13**, 2271 (2001). URL `http://iopscience.iop.org/0953-8984/13/10/319`.

[71] N. Hanasaki, S. Kagoshima, T. Hasegawa, T. Osada & N. Miura. Contribution of small closed orbits to magnetoresistance in quasi-two-dimensional conductors. *Phys. Rev. B* **57**, 1336–1339 (1998). URL `http://link.aps.org/doi/10.1103/PhysRevB.57.1336`.

[72] V. G. Peschansky & M. V. Kartsovnik. Comment on "Contribution of small closed orbits to magnetoresistance in quasi-two-dimensional conductors". *Phys. Rev. B* **60**, 11207–11209 (1999). URL `http://link.aps.org/doi/10.1103/PhysRevB.60.11207`.

[73] R. Gross & A. Marx. *Festkörperphysik* (Oldenbourg Verlag München, (2012)), 1st edn.

[74] W. Buckel & R. Kleiner. *Supraleitung* (Whiley-VCH, (2013)), 7th edn.

[75] M. Tinkham. *Introduction to Superconductivity* (Dover Puplications, Inc., 1996), 2nd edn.

[76] V. V. Schmidt. *The Physics of Superconductors*. P. Müller & A. V. Ustinov (eds.) (Springer Berlin Heidelberg, 1997). URL `http://link.springer.com/book/10.1007/978-3-662-03501-6`. DOI: 10.1007/978-3-662-03501-6_1.

[77] P. W. Anderson. Theory of dirty superconductors. *J. Phys. Chem. Solids* **11**, 26–30 (1959). URL http://www.sciencedirect.com/science/article/pii/0022369759900368.

[78] A. A. Abrikosov & L. P. Gor'kov. *Sov. Phys.-JETP* **12**, 1243 (1061).

[79] M. Sigrist & K. Ueda. Phenomenological theory of unconventional superconductivity. *Rev. Mod. Phys.* **63**, 239–311 (1991). URL http://link.aps.org/doi/10.1103/RevModPhys.63.239.

[80] E. Helfand & N. R. Werthamer. Temperature and Purity Dependence of the Superconducting Critical Field, H_{c2}. II. *Phys. Rev.* **147**, 288–294 (1966). URL http://link.aps.org/doi/10.1103/PhysRev.147.288.

[81] Werthamer, N. R. Helfand & P. C. E. Hohenberg. Temperature and Purity Dependence of the Superconducting Critical Field, H_{c2}. III. Electron Spin and Spin-Orbit Effects. *Phys. Rev.* **147**, 295–302 (1966). URL http://link.aps.org/doi/10.1103/PhysRev.147.295.

[82] W. E. Lawrence & S. Doniach. Theory of layer structure superconductors. In *Proceedings of the 12th International Conference of Low-Temperature Physics* 361–362 (1970).

[83] R. A. Klemm, A. Luther & M. R. Beasley. Theory of the upper critical field in layered superconductors. *Phys. Rev. B* **12**, 877–891 (1975). URL http://link.aps.org/doi/10.1103/PhysRevB.12.877.

[84] L. N. Bulaevskii. Magnetic properties of layered superconductors with weak interaction between layers. *Sov. Phys.-JETP* **37**, 1133–1136 (1973).

[85] L. N. Bulaevskii. Inhomogeneous state and the anisotropy of the upper critical field in layered superconductors with josephson layer interaction. *Sov. Phys.-JETP* **38**, 634–639 (1974).

[86] S. T. Ruggiero, T. W. Barbee & M. R. Beasley. Superconductivity in Quasi-Two-Dimensional Layered Composites. *Phys. Rev. Lett.* **45**, 1299–1302 (1980). URL http://link.aps.org/doi/10.1103/PhysRevLett.45.1299.

[87] B. S. Chandrasekhar. A note on the maximum critical field of high-filed superconductors. *Appl. Phys. Lett.* **1**, 7–8 (1962). URL http://dx.doi.org/10.1063/1.1777362.

[88] A. M. Clogston. Upper Limit for the Critical Field in Hard Superconductors. *Phys. Rev. Lett.* **9**, 266–267 (1962). URL http://link.aps.org/doi/10.1103/PhysRevLett.9.266.

[89] P. Fulde & R. A. Ferrell. Superconductivity in a Strong Spin-Exchange Field. *Phys. Rev.* **135**, A550–A563 (1964). URL http://link.aps.org/doi/10.1103/PhysRev.135.A550.

[90] A. Larkin & Y. Ovchinnikov. Inhomogenous state of superconductors. *Sov. Phys.-JETP* **20**, 762 (1965).

[91] K. Maki & T. Tsuneto. Pauli Paramagnetism and Superconducting State. *Progress of Theoretical Physics* **31**, 945–956 (1964). URL http://ptp.ipap.jp/link?PTP/31/945/.

[92] H. Shimahara. Fulde-Ferrell state in quasi-two-dimensional superconductors. *Phys. Rev. B* **50**, 12760–12765 (1994). URL http://link.aps.org/doi/10.1103/PhysRevB.50.12760.

[93] R. Lortz, Y. Wang, A. Demuer, P. H. M. Böttger, B. Bergk, G. Zwicknagl, Y. Nakazawa & J. Wosnitza. Calorimetric Evidence for a Fulde-Ferrell-Larkin-Ovchinnikov Superconducting State in the Layered Organic Superconductor κ-(BEDT-TTF)$_2$Cu(NCS)$_2$. *Phys. Rev. Lett.* **99**, 187002 (2007). URL http://link.aps.org/doi/10.1103/PhysRevLett.99.187002.

[94] B. Bergk, A. Demuer, I. Sheikin, Y. Wang, J. Wosnitza, Y. Nakazawa & R. Lortz. Magnetic torque evidence for the Fulde-Ferrell-Larkin-Ovchinnikov state in the layered organic superconductor κ-(BEDT-TTF)$_2$Cu(NCS)$_2$. *Phys. Rev. B* **83**, 064506 (2011). URL http://link.aps.org/doi/10.1103/PhysRevB.83.064506.

[95] R. Beyer & J. Wosnitza. Emerging evidence for FFLO states in layered organic superconductors (Review Article). *Low Temperature Physics* **39**, 225–231 (2013). URL http://scitation.aip.org/content/aip/journal/ltp/39/3/10.1063/1.4794996.

[96] S. Blundell. *Magnetism in Condensed Matter* (Oxford Univerity Press, 2001), 1st edn. URL https://global.oup.com/academic/product/magnetism-in-condensed-matter-9780198505914.

[97] S. V. Vonsovskii. *Magnetism.* Vol. 1 (Halsted Press, New York, Toronto, 1974), 1st edn.

[98] T. Mori & M. Katsuhara. Estimation of π-d-Interactions in Organic Conductors Including Magnetic Anions. *J. Phys. Soc. Jpn.* **71**, 826–844 (2002). URL http://journals.jps.jp/doi/abs/10.1143/JPSJ.71.826.

[99] O. Cépas, R. H. McKenzie & J. Merino. Magnetic-field-induced superconductivity in layered organic molecular crystals with localized magnetic moments. *Phys. Rev. B* **65**, 100502 (2002). URL http://link.aps.org/doi/10.1103/PhysRevB.65.100502.

[100] V. Jaccarino & M. Peter. Ultra-High-Field Superconductivity. *Phys. Rev. Lett.* **9**, 290–292 (1962). URL http://link.aps.org/doi/10.1103/PhysRevLett.9.290.

[101] H. W. Meul, C. Rossel, M. Decroux, . Fischer, G. Remenyi & A. Briggs. Observation of Magnetic-Field-Induced Superconductivity. *Phys. Rev. Lett.* **53**, 497–500 (1984). URL http://link.aps.org/doi/10.1103/PhysRevLett.53.497.

[102] R. Rousseau, M.-L. Doublet, E. Canadell, R. P. Shibaeva, S. S. Khasanov, L. P. Rozenberg, N. D. Kushch & E. B. Yagubskii. Electronic Structure of the α-(BEDT-TTF)$_2$MHg(XCN)$_4$ (M = K, Tl, NH$_4$); (X= S, Se) and Related Phases. Synthesis and Crystal Structure of the New Stable Organic Metal α-(BEDT-TTF)$_2$TlHg(Se$_{1-x}$S$_x$CN)$_4$ ($x = 0.125$). *J. Phys. I France* **6**, 1527–1553 (1996). URL http://dx.doi.org/10.1051/jp1:1996172.

[103] N. D. Kushch, L. I. Buravov, M. V. Kartsovnik, V. N. Laukhin, S. I. Pesotskii, R. P. Shibaeva, L. P. Rozenberg, E. B. Yagubskii & A. V. Zvarikina. Resistance and magnetoresistance anomaly in a new stable organic metal (ET)$_2$TlHg(SCN)$_4$. *Synthetic Metals* **46**, 271–276 (1992). URL http://www.sciencedirect.com/science/article/pii/037967799290352J.

[104] R. P. Shibaeva, L. P. Rozenberg, N. D. Kushch & E. B. Yagubskii. The Crystal-Structure of the New Stable Organic Metal α-(ET)$_2$TlHg(SeCN)$_4$. *Kristallografiya(Russ.)* **39**, 825–832 (1994).

[105] H. Mori, S. Tanaka, M. Oshima, G. Saito, T. Mori, Y. Maruyama & H. Inokuchi. Crystal and Electronic Structures of (BEDT-TTF)$_2$[MHg(SCN)$_4$](M = K and NH$_4$). *Bull. Chem. Soc. Jpn.* **63**, 2183–2190 (1990).

[106] P. Foury-Leylekian, J.-P. Pouget, Y.-J. Lee, R. M. Nieminen, P. Ordejón & E. Canadell. Density-wave instability in α-(BEDT-TTF)$_2$KHg(SCN)$_4$ studied by x-ray diffuse scattering and by first-principles calculations. *Phys. Rev. B* **82**, 134116 (2010). URL http://link.aps.org/doi/10.1103/PhysRevB.82.134116.

[107] M. V. Kartsovnik, D. Andres, S. V. Simonov, W. Biberacher, I. Sheikin, N. D. Kushch & H. Müller. Angle-Dependent Magnetoresistance in the Weakly Incoherent Interlayer Transport Regime in a Layered Organic Conductor. *Phys. Rev. Lett.* **96**, 166601 (2006). URL http://link.aps.org/doi/10.1103/PhysRevLett.96.166601.

[108] M. V. Kartsovnik. Shubnikov-de Haas oscillations in the new organic metal (ET)$_2$T1Hg(SCN)$_4$. *JETP Lett.* **55**, 339–342. URL http://www.jetpletters.ac.ru/ps/1273/article_19257.shtml.

[109] J. S. Brooks, X. Chen, S. J. Klepper, S. Valfells, G. J. Athas, Y. Tanaka, T. Kinoshita, N. Kinoshita, M. Tokumoto, H. Anzai & C. C. Agosta. Pressure effects on the electronic structure and low-temperature states in the α-(BEDT-TTF)$_2M$Hg(SCN)$_4$ organic-conductor family (M=K, Rb, Tl, NH$_4$). *Phys. Rev. B* **52**, 14457–14478 (1995). URL http://link.aps.org/doi/10.1103/PhysRevB.52.14457.

[110] H. H. Wang, K. D. Carlson, U. Geiser, W. K. Kwok, M. D. Vashon, J. E. Thompson, N. F. Larsen, G. D. McCabe, R. S. Hulscher & J. M. Williams. A new ambient-pressure organic superconductor: (BEDT-TTF)$_2$(NH$_4$)Hg(SCN)$_4$. *Physica C: Superconductivity* **166**, 57–61 (1990). URL http://www.sciencedirect.com/science/article/pii/092145349090552P.

[111] T. Sasaki, N. Toyota, M. Tokumoto, N. Kinoshita & H. Anzai. Transport properties of organic conductor (BEDT-TTF)$_2$KHg(SCN)$_4$: I. Resistance and magnetoresistance anomaly. *Solid State Commun.* **75**, 93 – 96 (1990). URL http://www.sciencedirect.com/science/article/pii/003810989090348F.

[112] P. Foury-Leylekian, S. Ravy, J.-P. Pouget & H. Müller. X-ray study of the density wave instability of α-(BEDT-TTF)$_2$MHg(SCN)$_4$ with M = K and Rb. *Synthetic Metals* **137**, 1271 – 1272 (2003). URL http://www.sciencedirect.com/science/article/pii/S0379677902010056. Proceedings of the International Conference on Science and Technology of Synthetic Metals.

[113] M. V. Kartsovnik, A. E. Kovalev, V. N. Laukhin, I. F. Schegolev, H. Ito, T. Ishiguro, N. D. Kushch, H. Mori & G. Saito. Magnetic field studies of the peculiar electronic state in the α-(BEDT-TTF)$_2$MHg(SCN)$_4$ family. *Synthetic Metals* **70**, 811–814 (1995). URL http://www.sciencedirect.com/science/article/pii/037967799402660Q.

[114] H. Fujiwara, E. Fujiwara, Y. Nakazawa, B. Z. Narymbetov, K. Kato, H. Kobayashi, A. Kobayashi, M. Tokumoto & P. Cassoux. A Novel Antiferromagnetic Organic Superconductor κ-(BETS)$_2$FeBr$_4$ [Where BETS = Bis(ethylenedithio)tetraselenafulvalene]. *J. Am. Chem. Soc.* **123**, 306–314 (2001). URL http://dx.doi.org/10.1021/ja002439x.

[115] H. Kobayashi, H. Tanaka, E. Ojima, H. Fujiwara, T. Otsuka, A. Kobayashi, M. Tokumoto & P. Cassoux. Coexistence of antiferromagnetic order and superconductivity in organic conductors. *Polyhedron* **20**, 1587–1592 (2001). URL http://www.sciencedirect.com/science/article/pii/S0277538701006581.

[116] N. Harrison, C. H. Mielke, D. G. Rickel, L. K. Montgomery, C. Gerst & J. D. Thompson. Magnetism and fermiology of κ-(BEDT-TSF)$_2$FeCl$_4$. *Phys. Rev. B* **57**, 8751–8754 (1998). URL http://link.aps.org/doi/10.1103/PhysRevB.57.8751.

[117] L. Balicas, J. Brooks, K. Storr, D. Graf, S. Uji, H. Shinagawa, E. Ojima, H. Fujiwara, H. Kobayashi, A. Kobayashi & M. Tokumoto. Shubnikov-de Haas effect and Yamaji oscillations in the antiferromagnetically ordered organic superconductor κ-(BETS)$_2$FeBr$_4$: a fermiology study. *Solid State Commun.* **116**, 557–562 (2000). URL http://www.sciencedirect.com/science/article/pii/S0038109800003744.

[118] S. Uji, H. Shinagawa, Y. Terai, T. Yakabe, C. Terakura, T. Terashima, L. Balicas, J. Brooks, E. Ojima, H. Fujiwara, H. Kobayashi, A. Kobayashi & M. Tokumoto. Two-dimensional Fermi surface for the organic conductor κ-(BETS)$_2$FeBr$_4$. *Physica B: Condensed Matter* **298**, 557–561 (2001). URL http://www.sciencedirect.com/science/article/pii/S0921452601003829.

[119] E. Fujiwara, H. Fujiwara, H. Kobayashi, T. Otsuka & A. Kobayashi. A Series of Organic Conductors, κ-(BETS)$_2$FeBr$_x$Cl$_{4-x}$ ($0 \leq x \leq 4$), Exhibiting

Successive Antiferromagnetic and Superconducting Transitions. *Adv. Mater.* **14**, 1376–1379 (2002). URL http://onlinelibrary.wiley.com/doi/10.1002/1521-4095(20021002)14:19<1376::AID-ADMA1376>3.0.CO;2-Y/abstract.

[120] H. Akiba, S. Nakano, Y. Nishio, K. Kajita, B. Zhou, A. Kobayashi & H. Kobayashi. Mysterious Paramagnetic States of Fe 3*d* Spin in Antiferromagnetic Insulator of λ-(BETS)$_2$FeCl$_4$ System. *J. Phys. Soc. Jpn.* **78**, 033601 (2009). URL http://journals.jps.jp/doi/abs/10.1143/JPSJ.78.033601.

[121] J. C. Waerenborgh, S. Rabaça, M. Almeida, E. B. Lopes, A. Kobayashi, B. Zhou & J. S. Brooks. Mössbauer spectroscopy and magnetic transition of λ-(BETS)$_2$FeCl$_4$. *Phys. Rev. B* **81**, 060413 (2010). URL http://link.aps.org/doi/10.1103/PhysRevB.81.060413.

[122] H. Akiba, K. Shimada, N. Tajima, K. Kajita & Y. Nishio. Paramagnetic Metal-Antiferromagnetic Insulator Transition in π-*d* System λ-(BETS)$_2$FeCl$_4$, BETS = Bis(ethylenedithio)tetrathiafulvalene. *Crystals* **2**, 984–995 (2012). URL http://www.mdpi.com/2073-4352/2/3/984.

[123] K. Shimada, H. Akiba, N. Tajima, K. Kajita, Y. Nishio, R. Kato, A. Kobayashi & H. Kobayashi. Temperature Dependence of Internal Field by Analysis of Specific Heat on an Organic Conductor λ-(BETS)$_2$FeCl$_4$. In *Proceedings of the 12th Asia Pacific Physics Conference (APPC12)* Vol. 1 of *JPS Conference Proceedings*012110 (Journal of the Physical Society of Japan, 2014). URL http://journals.jps.jp/doi/ref/10.7566/JPSCP.1.012110.

[124] T. Konoike, H. Fujiwara, B. Zhang, H. Kobayashi, M. Nishimura, S. Yasuzuka, K. Enomoto & S. Uji. Fermi surface in magnetic-field-induced superconductor κ-(BETS)$_2$FeBr$_4$. *Physica C: Superconductivity* **412-414, Part 1**, 107–110 (2004). URL http://www.sciencedirect.com/science/article/pii/S0921453404006501.

[125] T. Konoike, S. Uji, T. Terashima, M. Nishimura, T. Yamaguchi, K. Enomoto, H. Fujiwara, B. Zhang & H. Kobayashi. Anomalous Magnetic-Field-Hysteresis of Quantum Oscillations in κ-(BETS)$_2$FeBr$_4$. *J Low Temp Phys* **142**, 531–534 (2007). URL http://link.springer.com/article/10.1007/s10909-006-9160-5.

[126] T. Konoike, S. Uji, M. Nishimura, K. Enomoto, H. Fujiwara, B. Zhang & H. Kobayashi. Magnetic properties of field-induced superconductor, κ-(BETS)$_2$FeBr$_4$. *Physica B: Condensed Matter* **359-361**, 457–459 (2005). URL http://www.sciencedirect.com/science/article/pii/S0921452605001018.

[127] L. Balicas, J. S. Brooks, K. Storr, S. Uji, M. Tokumoto, H. Tanaka, H. Kobayashi, A. Kobayashi, V. Barzykin & L. P. Gor'kov. Superconductivity in an Organic Insulator at Very High Magnetic Fields. *Phys. Rev. Lett.* **87**, 067002 (2001). URL http://link.aps.org/doi/10.1103/PhysRevLett.87.067002.

[128] S. Uji, H. Kobayashi, L. Balicas & J. Brooks. Superconductivity in an Organic Conductor Stabilized by a High Magnetic Field. *Adv. Mater.* **14**, 243–245 (2002). URL http://onlinelibrary.wiley.com/doi/10.1002/1521-4095(20020205)14:3<243::AID-ADMA243>3.0.CO;2-F/abstract.

[129] T. Otsuka, H. Cui, H. Fujiwara, H. Kobayashi, E. Fujiwara & A. Kobayashi. The pressure effect on the antiferromagnetic and superconducting transitions of κ-$(BETS)_2FeBr_4$. *J. Mater. Chem.* **14**, 1682–1685 (2004). URL http://pubs.rsc.org/en/content/articlelanding/2004/jm/b404004j.

[130] T. Helm. *Transport measurements in 214 High-temperature superconductors.* Diplomarbeit, Technische Universität München (2009).

[131] S. Oberbauer. *Electronic properties of an organic superconductor in the vicinity of the Mott-insulating transition.* Bachelorarbeit, Technische Universität München (2015).

[132] M. Kunz. *Magnetoresistance in the normal and superconducting states of the layered organic metal α-(BEDT-TTF)$_2$KHg(SCN)$_4$ under pressure.* Diplomarbeit, Technische Universität München (2011).

[133] M. V. Kartsovnik, W. Biberacher, D. Andres, S. Jakob, M. Kunz, K. Neumaier, H. Müller & N. D. Kushch. Magnetic field effects on the charge-density-wave and superconducting states in pressurized. *Physica B: Condensed Matter* **407**, 1919–1922 (2012). URL http://www.sciencedirect.com/science/article/pii/S0921452612000695.

[134] M. Kartsovnik, D. Andres, P. Grigoriev, W. Biberacher & H. Müller. Interplay between the orbital quantization and Pauli effect in a charge-density-wave organic conductor. *Physica B: Condensed Matter* **346-347**, 368–372 (2004). URL http://www.sciencedirect.com/science/article/pii/S0921452604000997.

[135] D. Andres, M. V. Kartsovnik, W. Biberacher, K. Neumaier, I. Sheikin, H. Müller & N. D. Kushch. Field-induced charge-density-wave transitions in the organic metal α-$(BEDT\text{-}TTF)_2KHg(SCN)_4$ under pressure. *Low Temp. Phys.* **37**, 762–770 (2011). URL http://scitation.aip.org/content/aip/journal/ltp/37/10/10.1063/1.3670031.

[136] D. Saint-James, G. Sarm & E. J. Thomas. *Type II Superconductivity.* Vol. 17 of *International series of monographs in natural philosophy* (Pergamon Press, Oxford, 1969), 1st edn.

[137] M. Tinkham. Flux motion and resistance in high temperature superconductors: an overview. *Physica B: Condensed Matter* **169**, 66–71 (1991). URL http://www.sciencedirect.com/science/article/pii/092145269190209W.

[138] M. Chaparala, O. H. Chung, Z. F. Ren, M. White, P. Coppens, J. H. Wang, A. P. Hope & M. J. Naughton. Vortex-state resistance near parallel orientation

in layered superconductors. *Phys. Rev. B* **53**, 5818–5825 (1996). URL http://link.aps.org/doi/10.1103/PhysRevB.53.5818.

[139] M. V. Kartsovnik, G. Y. Logvenov, W. Biberacher, T. Ishiguro, P. Christ, K. Andres, E. Steep, A. G. M. Jansen, N. D. Kushch & H. Müller. Magnetoresistance of κ-(BEDT-TTF)$_2$X in normal and mixed states. *Synthetic Metals* **86**, 2061–2062 (1997). URL http://www.sciencedirect.com/science/article/pii/S0379677997810272.

[140] S. Yasuzuka, S. Uji, T. Terashima, K. Sugii, T. Isono, Y. Iida & J. A. Schlueter. In-Plane Anisotropy of Upper Critical Field and Flux-Flow Resistivity in Layered Organic Superconductor β''-(ET)$_2$SF$_5$CH$_2$CF$_2$SO$_3$. *J. Phys. Soc. Jpn.* **84**, 094709 (2015). URL http://journals.jps.jp/doi/abs/10.7566/JPSJ.84.094709.

[141] A. E. Kovalev, S. Hill & J. S. Qualls. Determination of the Fermi velocity by angle-dependent periodic orbit resonance measurements in the organic conductor α-(BEDT-TTF)$_2$KHg(SCN)$_4$. *Phys. Rev. B* **66**, 134513 (2002). URL http://link.aps.org/doi/10.1103/PhysRevB.66.134513.

[142] M. V. Kartsovnik, P. D. Grigoriev, W. Biberacher, N. D. Kushch & P. Wyder. Slow Oscillations of Magnetoresistance in Quasi-Two-Dimensional Metals. *Phys. Rev. Lett.* **89**, 126802 (2002). URL http://link.aps.org/doi/10.1103/PhysRevLett.89.126802.

[143] I. Luk'yanchuk. Theory of superconductors with κ close to $1/\sqrt{2}$. *Phys. Rev. B* **63**, 174504 (2001). URL http://link.aps.org/doi/10.1103/PhysRevB.63.174504.

[144] F. Mohamed, M. Troyer, G. Blatter & I. Luk'yanchuk. Interaction of vortices in superconductors with κ close to $1/\sqrt{2}$. *Phys. Rev. B* **65**, 224504 (2002). URL http://link.aps.org/doi/10.1103/PhysRevB.65.224504.

[145] J. S. Brooks, S. J. Klepper, X. Chen, P. Henning, P. J. C. Signore, M. p. Meisel, N. Kinoshita, M. Tokumoto & H. Anpai. Superconductivity and localisation in the density pave state of the α-(BEDT-TTF)$_2$MHg(SCN)$_4$ organic conductor family. *Appl. Supercond.* **2**, 759–766 (1994). URL http://www.sciencedirect.com/science/article/pii/0964180794900787.

[146] E. Abrahams, P. W. Anderson, D. C. Licciardello & T. V. Ramakrishnan. Scaling Theory of Localization: Absence of Quantum Diffusion in Two Dimensions. *Phys. Rev. Lett.* **42**, 673–676 (1979). URL http://link.aps.org/doi/10.1103/PhysRevLett.42.673.

[147] S. Hikami, A. I. Larkin & Y. Nagaoka. Spin-Orbit Interaction and Magnetoresistance in the Two Dimensional Random System. *Prog. Theor. Phys.* **63**, 707–710 (1980). URL http://ptp.oxfordjournals.org/content/63/2/707.

[148] A. A. Abrikosov & L. P. Gor'kov. Spin-Orbit Interaction and the Knight Shift in Superconductors. *Sov. Phys.-JETP* **15**, 752 (1962). URL http://www.jetp.ac.ru/cgi-bin/e/index/e/15/4/p752?a=list.

[149] T. Sugano, G. Saito & M. Kinoshita. Conduction-electron-spin resonance in organic conductors: α and β phases of di[bis(ethylenedithiolo)tetrathiafulvalene]triiodide [(BEDT-TTF_2I_3]. *Phys. Rev. B* **34**, 117–125 (1986). URL `http://link.aps.org/doi/10.1103/PhysRevB.34.117`.

[150] B. L. Altshuler, D. Khmel'nitzkii, A. I. Larkin & P. A. Lee. Magnetoresistance and Hall effect in a disordered two-dimensional electron gas. *Phys. Rev. B* **22**, 5142–5153 (1980). URL `http://link.aps.org/doi/10.1103/PhysRevB.22.5142`.

[151] B. Salameh, P. Auban-Senzier, N. Kang, C. R. Pasquier & D. Jérome. Precise texture determination of the spin density wave/superconductivity mixture in the phase separation regime of. *Physica B: Condensed Matter* **404**, 476–478 (2009). URL `http://www.sciencedirect.com/science/article/pii/S0921452608005644`.

[152] C. R. Pasquier, N. Kang, B. Salameh, P. Auban-Senzier, D. Jérome & S. Brazovskii. Evolution of the spin-density wave-superconductivity texture in the organic superconductor $(TMTSF)_2PF_6$ under pressure. *Physica B: Condensed Matter* **407**, 1806–1809 (2012). URL `http://www.sciencedirect.com/science/article/pii/S0921452612000403`.

[153] Y. A. Gerasimenko, S. V. Sanduleanu, V. A. Prudkoglyad, A. V. Kornilov, J. Yamada, J. S. Qualls & V. M. Pudalov. Coexistence of superconductivity and spin-density wave in $TMTSF_2ClO_4$: Spatial structure of the two-phase state. *Phys. Rev. B* **89**, 054518 (2014). URL `http://link.aps.org/doi/10.1103/PhysRevB.89.054518`.

[154] M. Kunz, W. Biberacher, N. D. Kushch, A. Miyazaki & M. V. Kartsovnik. Resistive properties and phase diagram of the organic antiferromagnetic metal κ-$(BETS)_2FeCl_4$. *arXiv:1606.07331 [cond-mat]* (2016). URL `http://arxiv.org/abs/1606.07331`.

[155] N. Doiron-Leyraud, P. Auban-Senzier, S. René de Cotret, C. Bourbonnais, D. Jérome, K. Bechgaard & L. Taillefer. Correlation between linear resistivity and T_c in the Bechgaard salts and the pnictide superconductor $Ba(Fe_{1-x}Co_x)_2As_2$. *Phys. Rev. B* **80**, 214531 (2009). URL `http://link.aps.org/doi/10.1103/PhysRevB.80.214531`.

[156] L. Taillefer. Scattering and Pairing in Cuprate Superconductors. *Annual Review of Condensed Matter Physics* **1**, 51–70 (2010). URL `http://dx.doi.org/10.1146/annurev-conmatphys-070909-104117`.

[157] R. Daou, N. Doiron-Leyraud, D. LeBoeuf, S. Y. Li, F. Laliberté, O. Cyr-Choinière, Y. J. Jo, L. Balicas, J.-Q. Yan, J.-S. Zhou, J. B. Goodenough & L. Taillefer. Linear temperature dependence of resistivity and change in the Fermi surface at the pseudogap critical point of a high-T_c superconductor. *Nat. Phys.* **5**, 31–34 (2009). URL `http://www.nature.com/nphys/journal/v5/n1/full/nphys1109.html`.

[158] S. Lefebvre, P. Wzietek, S. Brown, C. Bourbonnais, D. Jérome, C. Mézière, M. Fourmigué & P. Batail. Mott Transition, Antiferromagnetism, and Unconventional Superconductivity in Layered Organic Superconductors. *Phys. Rev. Lett.* **85**, 5420–5423 (2000). URL `http://link.aps.org/doi/10.1103/PhysRevLett.85.5420`.

[159] S. I. Pesotskii, R. B. Lyubovskii, W. Biberacher, M. V. Kartsovnik, V. I. Nizhankovskii, N. D. Kushch, H. Kobayashi & A. Kobayashi, *Molecular Low Dimensional and Nanostructured Materials for Advanced Applications*. A. Graja, B. Bulka & F. Kajzar (eds.), chap. Quantum Interference in quasi-two-dimensional organic Metals κ-$(BETS)_2FeCl_4$ and κ-$(BETS)_2GaCl_4$, 285–288 (Kluwer Academic Publishers, 2002).

[160] S. Uji, C. Terakura, T. Terashima, T. Yakabe, Y. Terai, M. Tokumoto, A. Kobayashi, F. Sakai, H. Tanaka & H. Kobayashi. Fermi surface and internal magnetic field of the organic conductors λ-$(BETS)_2Fe_xGa_{1-x}Cl_4$. *Phys. Rev. B* **65**, 113101 (2002). URL `http://link.aps.org/doi/10.1103/PhysRevB.65.113101`.

[161] M. V. Kartsovnik, P. A. Kononovich, V. N. Laukhin & I. F. Schegolev. Anisotropy of magnetoresistance and the Shubnikov-de Haas oscillations in the organic metal β-$(ET)_2IBr_2$. *JETP Lett.* **48**, 541 (1988). URL `http://www.jetpletters.ac.ru/ps/1109/article_16777.shtml`.

[162] A. G. Lebed, N. N. Bagmet & M. J. Naughton. Magic Angle Effects and Angular Magnetoresistance Oscillations as Dimensional Crossovers. *Phys. Rev. Lett.* **93**, 157006 (2004). URL `http://link.aps.org/doi/10.1103/PhysRevLett.93.157006`.

[163] P. D. Grigoriev. Theory of the Shubnikov-de Haas effect in quasi-two-dimensional metals. *Phys. Rev. B* **67**, 144401 (2003). URL `http://link.aps.org/doi/10.1103/PhysRevB.67.144401`.

[164] K. Sakurazawa, H. Kontani & T. Saso. Magnetic-Field-induced Antiferromagnetism in Two-dimensional Hubbard Model: Analysis of $CeRhIn_5$. *Journal of the Physical Society of Japan* **74**, 271–274 (2005). URL `http://journals.jps.jp/doi/abs/10.1143/JPSJ.74.271?journalCode=jpsj&quickLinkVolume=74&quickLinkPage=271&selectedTab=citation&volume=74`.

[165] P. Sengupta, C. D. Batista, R. D. McDonald, S. Cox, J. Singleton, L. Huang, T. P. Papageorgiou, O. Ignatchik, T. Herrmannsdörfer, J. L. Manson, J. A. Schlueter, K. A. Funk & J. Wosnitza. Nonmonotonic field dependence of the Néel temperature in the quasi-two-dimensional magnet $[Cu(HF_2)(pyz)_2]BF_4$. *Phys. Rev. B* **79**, 060409 (2009). URL `http://link.aps.org/doi/10.1103/PhysRevB.79.060409`.

[166] L. D. Landau & E. M. Lifshitz. *Electro-dynamics of continuous media*. Vol. 8 of *Course of Theoretical Physics* (Pergamon Press, 1984), 2 edn.

[167] M. E. Fisher. Scaling Axes and the Spin-Flop Bicritical Phase Boundaries. *Phys. Rev. Lett.* **34**, 1634–1638 (1975). URL `http://link.aps.org/doi/10.1103/PhysRevLett.34.1634`.

[168] M. E. Fisher & D. R. Nelson. Spin Flop, Supersolids, and Bicritical and Tetracritical Points. *Phys. Rev. Lett.* **32**, 1350–1353 (1974). URL `http://link.aps.org/doi/10.1103/PhysRevLett.32.1350`.

[169] D. P. Landau & K. Binder. Phase diagrams and multicritical behavior of a three-dimensional anisotropic Heisenberg antiferromagnet. *Phys. Rev. B* **17**, 2328–2342 (1978). URL `http://link.aps.org/doi/10.1103/PhysRevB.17.2328`.

[170] J. Caulfield, W. Lubczynski, F. L. Pratt, J. Singleton, D. Y. K. Ko, W. Hayes, M. Kurmoo & P. Day. Magnetotransport studies of the organic superconductor κ-(BEDT-TTF)$_2$Cu(NCS)$_2$ under pressure: the relationship between carrier effective mass and critical temperature. *J. Phys.: Condens. Matter* **6**, 2911 (1994). URL `http://iopscience.iop.org/0953-8984/6/15/013`.

[171] M. V. Kartsovnik, P. D. Grigoriev, W. Biberacher & N. D. Kushch. Magnetic field induced coherence-incoherence crossover in the interlayer conductivity of a layered organic metal. *Phys. Rev. B* **79**, 165120 (2009). URL `http://link.aps.org/doi/10.1103/PhysRevB.79.165120`.

[172] V. V. Kabanov & A. S. Alexandrov. Magnetic quantum oscillations in doped antiferromagnetic insulators. *Phys. Rev. B* **77**, 132403 (2008). URL `http://link.aps.org/doi/10.1103/PhysRevB.77.132403`.

[173] R. Ramazashvili. Kramers Degeneracy in a Magnetic Field and Zeeman Spin-Orbit Coupling in Antiferromagnetic Conductors. *Phys. Rev. Lett.* **101**, 137202 (2008). URL `http://link.aps.org/doi/10.1103/PhysRevLett.101.137202`.

[174] R. Ramazashvili. Electric excitation of spin resonance in antiferromagnetic conductors. *Phys. Rev. B* **80**, 054405 (2009). URL `http://link.aps.org/doi/10.1103/PhysRevB.80.054405`.

[175] M. R. Norman & J. Lin. Spin zeros and the origin of Fermi-surface reconstruction in the cuprates. *Phys. Rev. B* **82**, 060509 (2010). URL `http://link.aps.org/doi/10.1103/PhysRevB.82.060509`.

[176] R. Ramazashvili. Quantum oscillations in antiferromagnetic conductors with small carrier pockets. *arXiv:1006.0167* (2010). URL `http://arxiv.org/abs/1006.0167`. Phys. Rev. Lett. 105, 216404 (2010).

[177] S. I. Pesotskii, W. Biberacher, unpublished.

[178] S. Uji, K. Kodama, K. Sugii, T. Terashima, T. Yamaguchi, N. Kurita, S. Tsuchiya, T. Konoike, M. Kimata, A. Kobayashi, B. Zhou & H. Kobayashi. Vortex Dynamics and Diamagnetic Torque Signals in Two Dimensional Organic Superconductor λ-(BETS)$_2$GaCl$_4$. *J. Phys. Soc. Jpn.* **84**, 104709 (2015). URL `http://journals.jps.jp/doi/10.7566/JPSJ.84.104709`.

[179] A. Kovalev, M. Kartsovnik, R. Shibaeva, L. Rozenberg, I. Schegolev & N. Kushch. Angular magnetoresistance oscillations in the organic conductor α-(BEDT-TTF)$_2$KHg(SCN)$_4$ above and below the phase transition. *Solid State Communications* **89**, 575 – 578 (1994). URL `http://www.sciencedirect.com/science/article/pii/003810989490166X`.

[180] J. G. Analytis, A. Ardavan, S. J. Blundell, R. L. Owen, E. F. Garman, C. Jeynes & B. J. Powell. Effect of Irradiation-Induced Disorder on the Conductivity and Critical Temperature of the Organic Superconductor κ-(BEDT-TTF)$_2$Cu(NCS)$_2$. *Phys. Rev. Lett.* **96**, 177002 (2006). URL `http://link.aps.org/doi/10.1103/PhysRevLett.96.177002`.

List of publications

M. V. Kartsovnik, W. Biberacher, D. Andres, S. Jakob, M. Kunz, K. Neumaier, H. Müller and N. D. Kushch. Magnetic field effects on the charge-density-wave and superconducting states in pressurized. *Physica B: Condensed Matter* **407**, 1919–1922 (2012).

M. Kunz, W. Biberacher, N. D. Kushch, A. Miyazaki and M. V. Kartsovnik. Resistive properties and phase diagram of the organic antiferromagnetic metal κ-$(BETS)_2$ $FeCl_4$. *arXiv:1606.07331 [cond-mat]* (2016). Submitted to *Phys. Rev. B* July 2016.

unpublished manuscripts

M. Kunz, M. Kartsovnik et al. "Fermi surface studies on κ-$BETS_2FeCl_4$" (2016)

Acknowledgments

At the end of this work I would like to thank all the people, who helped me to make this work possible.

I especially want to express my gratitude to:

- Prof. Dr. Rudolf Gross, for giving me the possibility of doing thesis at the Walther-Meißner-Institut, especially since the finances were not clear from the beginning.
- Dr. Mark Kartsovnik for being my mentor and supervisor, for sharing his knowledge, for helping me along my way and always having an open ear in case of problems. I further thank for always keeping a good mood and raising my spirit even in tough situations.
- Dr. Werner Biberacher for advising me in a lot of situations, for always being ready to help even after the retirement and for reading this thesis time and again in spite of the length.
- My master student Ludwig Schaidhammer for assisting me in a lot of measurements on κ-$(BETS)_2FeBr_4$ in the course of his master's thesis and for developing a new method of analysing AMRO.
- My master student Luzia Höhlein for carrying out all the measurements on α-$(BEDT\text{-}TTF)_2KHg(SCN)_4$ during her master's, for a number of good ideas in our analysis and for providing literature, which otherwise was not accessible.
- My bachelor student Florian Kollmannsberger for doing a very successful last minute experiment on the new samples of κ-$(BETS)_2FeBr_4$ during his bachelor's thesis and for helping me with fitting of difficult functions in Mathematica.
- Toni Helm, for being a good colleague and room mate throughout the first half of my thesis and for always being helpful, when there were problems in the lab.
- My bachelor students Sebastian Oberbauer and Ismail Achmed-Zade and our master student Sergej Fust for broadening my view over the topic of organic superconductors since their experiments were not part of my thesis topic.
- Alma Dorantes for helping me in one of my characterisation measurements as a working student and for listening to several of my concerts.
- Vasislis Tzanos and Ahmed Alshemi for doing their masters' thesis in our group and being nice colleagues.

- Sebastian Jakob, for establishing the measurement setup during his diploma work period and for helping us with advice even though having left the institute four years ago.
- Natalya D. Kushch and Harald Müller for providing the crystals.
- Prof. Dr. Vladimir N. Zverev, Dr. Oleg Vyaselev and Dr. Steven Winter for nice discussions during their times as guests in our institute.
- Joachim Geismann, for building the new gas-handling system for our dilution refrigerator.
- Dr. Karl Neumaier, for his advising us how to operate the dilution fridge.
- Robert Müller, Georg Nitschke, Christian Reichlmeier, Julius Klaus, Helmut Thies and Alex Rössel from the workshop for helping me out a lot of times, especially with "short-term" problems.
- the technical staff of the WMI, for their help in the case of problems with the measurement equipment, especially to Ulrich Guggenberger, who repaired our magnet power supplies several times.
- the other students and scientists at the WMI, for the nice working atmosphere.
- to everyone else whom I have forgotten because of my lack of time while writing this.

In particular, I want to thank my parents, for their support in the course of my study of physics.